Universities of Glasgow and Strathclyde

Department of Naval Architecture and Marine Engineering

AN INVESTIGATION INTO THE APPLICATION OF LES AND DES FOR PREDICTION OF FLOW AND FORCES AROUND AN IACC YACHT KEEL AND MARINE BODIES

by

Dimitrios Mylonas

A thesis presented and submitted in fulfilment for the requirement of the degree of Doctor of Philosophy

Year: 2013

This thesis is the result of the author's original research, carried out in the Department of Naval Architecture and Marine Engineering. It has been composed by the author and has not been previously submitted for examination which has led to the award of a degree.

Summary

In this thesis, an approach into the applicability of Large Eddy Simulation (LES) and Detached Eddy Simulation (DES) for the prediction of forces and flow around marine bodies at high Reynolds number is presented. The main aim of the thesis was to investigate and assess the use of LES and DES based computational fluid dynamics applications as a tool for hydrodynamic prediction. A methodology for addressing the problem was followed based on mathematical models and numerical solutions translated into a three-dimensional commercial Computational Fluid Dynamics (CFD) code. Meshing strategy involved the use of adapted unstructured meshes with local refinement around key areas of the bodies.

The CFD models based on LES and DES are validated against experimental measurements for three different bodies: a NACA 0012 section airfoil, a 6:1 prolate spheroid at angles of incidence and an asymmetric America's Cup yacht keel. Quantitative comparisons included prediction of values of global force coefficients around the geometries, pressure and friction coefficients on the surface, and wake analysis. Qualitative observation focused on flow generation near the bodies such as separation, velocity vectors.

It was found from the study that LES and DES provide two suitable turbulence models that can be implemented for the simulation of the flow around a static airfoil and a static spheroid. However, it is necessary to examine the problem further to have full confidence in their capabilities when applied to yacht hydrodynamics and more challenging flows.

Foreword

Instead of the traditional acknowledgement page, I thought it was more suitable to write some notes and help increase the knowledge and wisdom of people with some quotes that deserve everyone's attention.

The Doctorate of Philosophy is a long and strenuous process, often edging between the limits of fear, uncertainty, difficulties, disbelief, questioning, etc. I would like to thank my family for their support and encouragements throughout this time, especially my sister Irene, a few close friends and colleagues for their advice and experiences, they will recognise themselves.

I would also like to thank any other person, anonymous or not, famous or not, dead or alive, who helped in a way or another. Be it through the music I listened, the online videos I watched, the comments I read, the sporting challenges I followed or took part in, for making life easier sometimes, giving some perspective and taking a bit of the weight off the shoulders, albeit momentarily. The chances are they will never read this thesis, but credit is due where credit is deserved.

Finally, some of my favourite quotes; there are more at the beginning and end of each chapter, not to annoy the reader but to share some more philosophical thoughts that I found worthy of sharing during the course of my Ph.D. studies. Thank You.

«*Au milieu de l'hiver, j'ai découvert en moi un invincible été*.» **Albert Camus**

"*The illiterate of the 21st century will not be those who cannot read and write, but those who cannot learn, unlearn and relearn*." **Alvin Toffler**

"*I was asked once, "You're a smart man. Why aren't you rich?" I replied, "you're a rich man, why aren't you smart?*" **Jacques Fresco**

"*He who does not understand your silence will probably not understand your words*." **Elbert Hubbard**

"*The problem with the world is that the intelligent people are full of doubts, while the stupid ones are full of confidence*." **Charles Bukowski**

"Thinking is the hardest work there is, which is probably the reason why so few engage in it." **Henry Ford**

Table of Contents

List of Figures

List of Tables

Nomenclature

Acronyms

2D	Two-Dimension
3D	Three-Dimension
AC	America's Cup
AMG	Algebraic Multigrid
AoA	Angle of Attack
CFD	Computational Fluid Dynamics
CFL	Courant-Friedrich Levy number
CPU	Central Processing Unit
deg	Degrees (angle)
DES	Detached Eddy Simulation
DNS	Direct Numerical Simulation
DSM	Dynamic Smagorinsky-Lilly
FVM	Finite Volume Method
IACC	International America's Cup Class
ITTC	International Towing Tank Committee
KRISO	Korea Research Institute for Ships and Ocean Engineering
LES	Large Eddy Simulation
NACA	National Advisory Committee for Aeronautics
PISO	Pressure Implicit with Splitting of Operator
PRESTO!	Pressure Staggering Option
RANS	Reynolds Averaged Navier-Stokes
Rκε	Realizable κ-ε
SA	Spalart-Allmaras
SIMPLE	Semi-Implicit Method for Pressure-Linked Equations
SIMPLEC	Semi-Implicit Method for Pressure-Linked Equations Consistent
SM	Smagorinsky-Lilly
VoF	Volume of Fluid

Greek characters

α	Angle of Attack (^{o})
ε	Turbulent dissipation rate per unit mass (m^2/s^3)
κ	Turbulent kinetic energy (m^2/s^2)
μ	Dynamic viscosity (kg/ms)
μ_t	Turbulent eddy viscosity (kg/ms)
ν	Kinematic viscosity (m^2/s)
ρ	Density of fluid (kg/m^3)
τ	Shear stress (Pa or N/ m^2)
ω	Specific dissipation rate per unit mass (1/s)
∂	Partial differential operator
ϕ	Scalar quantity
σ	Stress rate (Pa or N/ m^2)

Roman characters

A	Projected area (m^2)
c	Chord's length (m)
C_D	Drag coefficient (-)
C_{DES}	DES model constant (-)
C_f	Skin-friction coefficient (-)
C_L	Lift coefficient (-)
C_M	Moment coefficient (-)
C_p	Pressure coefficient (-)
C_s	Smagorinsky constant (-)
D	Drag force (N)
g	Gravitational acceleration (m/s^2)
L	Lift force (N), length of body (m)
M	Moment (N/m)
p	Pressure (Pa)
R	Total resistance (N)
Re	Reynolds number (-)

t	Time (s)
U	Freestream velocity (m/s)
u, v, w	Velocity components along x, y, z (m/s)
y^+	Non-dimensional distance of first mesh cell from wall (-)
S	Rate of strain (-), wetted surface area (S)
x, y, z	Cartesian coordinates

Subscripts

ν	Viscous value
w	Wall value
∞	Freestream value

Superscripts

*	Dimensional quantity
¯	Time averaged component or spatial filtered component (LES)
'	Turbulent fluctuation component
º	Degrees (angle)

"A perfection of means, and confusion of aims, seems to be our main problem" **Albert Einstein**

1 Introduction

This opening chapter will reveal the general and specific background rationale behind the pursuance of the research work of the thesis. Moreover, the problem will be formulated for a better understanding of the issue. Concluding this section, an outline of the thesis presents a short summary of the following chapters of the dissertation to help the reader understand the author's ideas and actions performed during this work.

1.1 General perspectives and background

The use of computational fluid dynamics (CFD) in naval architecture is guided by the quest of accurately simulating the performance of a ship or a floating structure under operational conditions and in a controlled environment, using one or a set of computers. Following the boom of the computers in the past 40 years, the development of reliable and efficient numerical methods for flow simulations around a ship's hull or a floating body has been subject to extensive research and development in academia and in the industry.

The push in numerical methods progress has been driven by the urge to diminish the dependence and need of costly and time-consuming experimental procedures, use which will reduce more and more in the coming years should the computational power continues to expand at the current rate and providing trust through validation of numerical methods is assertively achieved.

This shift from experiments to virtual has already fully taken place in industries such as aeronautics and automotive; such an example is the design of the 2010 Formula 1

car VR-01, from Virgin Racing, which was entirely designed, tested and optimised using CFD (Leidel, 2010). Although the team underperformed during their maiden season in the competition, this unique approach constituted a breakthrough for racing cars, and is very likely to influence similar ideas to be implemented in the future. Similarly, CFD has been extensively used in aeronautics for the past 35 years at a research and commercial level, developing its capabilities in parallel with the development of new airplanes (Johnson et al., 2005).

In this context, numerical simulations based on CFD acquire a significant importance in naval architecture and a particular relevance to sailing yacht design and aero-hydrodynamics. Numerical simulations of the flow around sailing yachts are employed to interpret and compare results and data, either between different designs for optimisation and design selection or against towing tank and wind tunnel tests for validation (Porto et al., 2002; Raymond et al., 2008, Viola, 2009).

What makes yacht hydrodynamics an interesting and attractive topic for research is not only the close link shared with the development and use of numerical simulations, but also the following:

- In this discipline, design is critical in making the difference between a winning and a losing yacht. In many cases, due to the tight rules governing the field, room for improvement is small and it is in subtle details that the difference is made in competition. It is considered to be as technically challenging a discipline as one can be.

- Whereas extensive validation has been published in other naval fields, little has been published in comparison for yachts, partly due to its competitive secrecy and partly because of its complexity. There is also a lack of existing database such as there is from the ITTC with the US navy combatant 5415, the KRISO's crude carrier, and container ship models commonly used by most institutions for validation.

- Most of the advances and changes carried out in modern yacht design come from breakthroughs in racing yacht hydrodynamics. The introduction of canting keel, the evolution to winged bulb, the current design/shape of hull and the use of innovative materials are some examples benefited from the developments in yacht racing (Freer, 1987; Lee & Philpott, 1990; Giorgetti, 2007).

- Most yachts must offer elegance in shape, safety in navigation, comfort in cruising and performance in racing, traits that make them very demanding for the naval architect in charge of the design. Hence, yacht designers, for many years, were considered not only bright engineers, but also crafted artists who had to think ahead of their time.

Therefore, one can appreciate the interest there can be, and the potential, for further research in yacht aero-hydrodynamics.

1.2 Specific Issue

The America's Cup is an event where significant milestones are achieved in design and in performance of the boats. A constant evolution and improvement in the design of such yachts is required from event to event and, in order to remain competitive and keep up with the leaders, it is paramount to make use of the technologies available for beneficial purposes.

The design process is subjected to severe constraints and pressures (budget, time, research); meaning there is an increasing demand for accurate and effective numerical tools that could support the ageing, but robust, towing tank and wind tunnel procedures employed up to now. The large R&D budgets invested (no shy of dozens of millions dollars) imply a pressure on the teams 'to deliver' on the water.

The motivation in the competition resides not only in the Defender, who wants to successfully repeat its triumph, but also in the teams vying for the Challenger

position, who need initially to race in a series of regattas, for the chance of disputing the trophy. Those teams need to be challenging not only against each other, but then against the champion who arguably has more time to prepare but who on the other hand lacks competition.

The appropriate use of CFD-related technology is of utmost importance to achieve the best out of the yachts, mount a serious challenge and give a syndicate the best chance to win the event.

A major contributing factor in a successful and winning yacht is its underwater appendages, one of the most significant aspects of which is the good prediction of the forces acting on the body and the flow around the bulb. Model scale testing and potential flow solution have been heavily employed in evaluating such features. Nowadays, the development and rapid growth of computers coupled with advances in numerical methods have led to CFD becoming a useful addition to the above and a powerful tool in hydrodynamics predictions.

Hydrodynamic analysis plays a leading role in the preliminary design stage of an America's Cup yacht. Until the model tests are ready to be analysed, it is often the only way to obtain an estimation of the boat's behaviour at sea. Errors and approximations in design can have expensive consequences through the costs of redesign, manufacturing and loss of time in preparation for the racing events.

A higher level of confidence and a better CFD prediction of the overall forces acting on the yacht would allow the design team of an America's Cup (AC) consortium to improve and optimise its design, as well as potentially reduce the design cost, estimated to be about 25% of the overall budget. This in turn would allow the savings to be transferred to another area of interest, such as marketing, logistics or particularly the weather team, helping them to accurately estimate the wind speed and direction during the race for the chosen location of the event, hence benefiting the sailing team with regard to race strategy and training.

Bruce Farr, chief designer of BMW Oracle for the 2003 and 2007 America's Cup, and of the New Zealand challengers in the nineties, stated that the crew and skipper usually improve a yacht's performance by 10 seconds a mile on average during the preliminary races taking place before the event (what was known as the Louis Vuitton Series). He also added that "*tweaking the hydrodynamics – underwater appendages, might yield 2-3 seconds a mile. Aerodynamics – sails and rigs, should offer a bit more, say 3-4 seconds a mile*" (Scuttlebutt, 2002).

Consequently, one can understand the importance and need of a good prediction of the hydrodynamic forces around the appendages since they represent the part with the least possible gain in performance and the most challenging to optimise. Even if part of the success is relying on the skills of a good competitive crew, the work of the designer and his team is important in searching for small gains that can make the difference. With hulls and bodies having converged towards almost identical shape between the teams, the smallest details' impacts are the ones that make the difference in the overall performance. As reported by Milgram (1998), a 1% change in total drag can affect the race time, with time differentials up to 60 seconds. Given that the best yachts are about 40 seconds faster than the slowest ones over the 20 nautical miles legs; this corresponds to a difference of only 3% (Nicolopoulos et al., 2009), enough to make the difference between a win and a loss.

The 32nd AC was by far one of the most exciting events in the recent history of the competition. It finished with the Swiss defender Alinghi defeating the Challenger Emirates Team New Zealand five legs to two (in the seventh leg). The series were closely fought, and most of the legs finished by a difference of less than half a minute. To highlight the closeness of the summer 2007 event, one can simply focus on the seventh stage of the final.

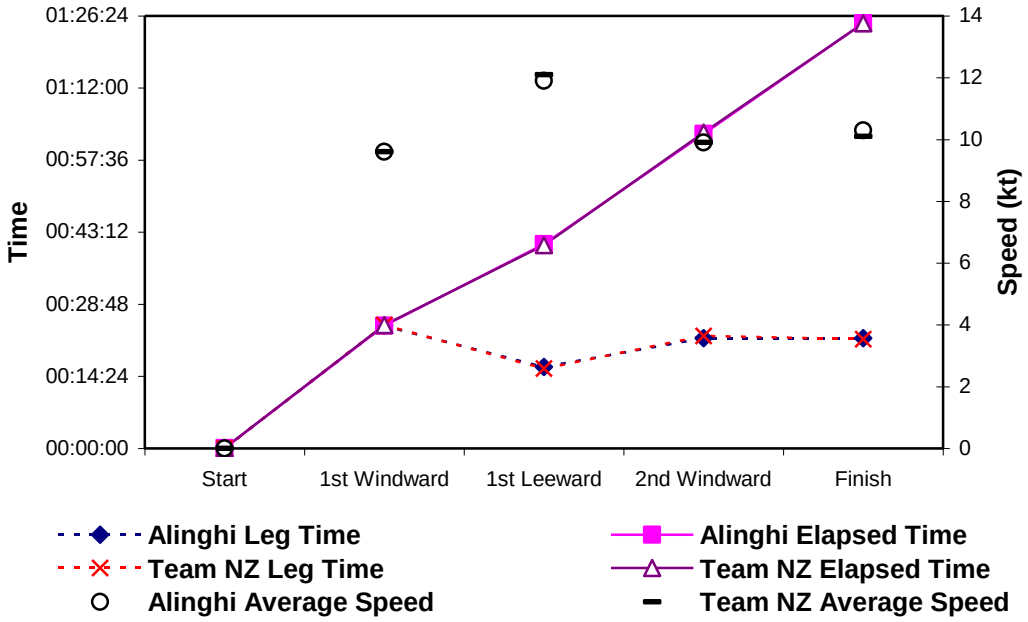

Figure 1. stage 7 of 32nd America's Cup

Figure 1.1 displays the outcome of the seventh leg between the two yachts. As an indication of the closeness of the race, one can observe that both yachts were literally neck-to-neck from start to finish. The slight advantage gained by Emirates Team New Zealand downwind (first Leeward) due to the slender bulb is lost in the upwind segments of the course, from Alinghi's smaller wetter surface bulb. The leg time is also similar for both teams. This ensured a photo finish where the Swiss became victorious, taking a decisive lead of five races to two and effectively ending the hopes of a Kiwi comeback. Figure 1.2 in the now famous picture at the finish line where only a second was separating the two boats.

Figure 1. Photo finish of the seventh race of the 32nd America's Cup, 2007 (source: International Service of the Swiss Broadcasting Corporation, photograph from Reuters)

Arguably, with both teams spending months of research to reach that level of competitiveness, it was always going to be in the details that the difference would be made. Most importantly, both teams used similar numerical tools in performance prediction and calculations of flow around the yachts, from the same provider (Ansys Advantage, 2007). Michael Richelsen, from the Alinghi design team, said following the successful defence of the trophy that:

"*ANSYS software has proven to be a key tool in the design of our winning yacht. (…) The design improvements that we made as a result of the computational fluid dynamics analyses conducted with ANSYS software significantly increased the speed of the boat - and aided us considerably in defending the America's Cup".*

The above quote reflects the importance that CFD had since its introduction into the event and its role in the design and analysis of the winning Alinghi team.

1.3 Importance of flow in accuracy control in America's Cup keel hydrodynamics

Looking at higher competitive issues surrounding the performance of yachts, questions can arise that further rekindle the need for research: How should a yacht designer use the available CFD tools? What can he gain from advanced models in terms of understanding the flow behaviour under specific conditions? Is there a need for further technology development and why? What are the flow features expected to be captured? How important is the numerical prediction in terms of accuracy? What is the current state-of-the-art?

A complete knowledge of the hydrodynamic flow around an America's Cup keel is far from being reached. The complex interactions between the different components of the keel, as well as the constraints imposed by the America's Cup rules, make the design of a performing yacht an extremely difficult task. There is a need for

performance and accuracy control for the flow in order to achieve competitiveness. The keel must be optimised to provide maximum side force (Lift) and minimum drag, to allow the yacht to sail efficiently on the upwind course.

Keel hydrodynamics are studied to gain an understanding of effects and interactions occurring in the near and far field flow, depending on the sailing conditions. Keel, bulb, winglets and rudder design should be developed accordingly in order to guarantee global optimal performances. The advantage of the numerical approach relies on the possibility to test several different configurations and to have a complete picture of the flow behaviour at every time instant.

The viscous hydrodynamic flow around a keel is important for several reasons:

- The transition from laminar to turbulent flow is still a delicate topic in numerical simulation that requires continuous investigation. In presence of slender, streamlined bodies aligned with the velocity, a non negligible part of the flow field around the body can be laminar, and its simulation is crucial to obtain accurate predictions of drag coefficients. The development of numerical models able to predict accurately the laminar-turbulent transition is still an area of active investigation.

- The unsteady flow separation is also a critical aspect that researchers want to grasp to minimise losses and constraints during races. Further problems occur in upwind condition, including changes in velocity and pressure fields giving way to unsteady flow separation and creation of vortices that interact between the components of the yacht and keel. Also, instantaneous effects rather than averaged observations are needed to study the effects of the flow over time.

- Modelling the flow at key locations such as root-junction of keel, bulb and winglets helps understand the creation of vortices, the performance of the keel and the areas where design modifications should be considered. These

locations are difficult to predict because of the complexity of the flow of each component.

- The continuous need for validation of quantitative results for CFD codes is important for high Reynolds number flows. Additionally, more qualitative data that can provide practical help to those involved in yachting is necessary.

1.4 Scope of the research

In order to simulate accurately the hydrodynamic flow around the keel, the numerical models employed nowadays should consider for all of the above. Information about local and global distribution of flow quantities (forces, pressure, velocity, vorticity and turbulence) can be useful to improve the hydrodynamic performances of keels. Creating and computing the flow around the appendages can help understanding the formation of the main flow characteristics and their interaction with the boat components.

Up to now, models based on unsteady Reynolds-Averaged Navier-Stokes equations (URANS) have been extensively used. In the current work, the idea behind the research employs advanced numerical methods based on large eddy simulation and detached eddy simulation (LES & DES) in order assess their impact on the prediction of the unsteady, turbulent flow such as that around an America's Cup keel at angle of yaw, and other bodies considered as test cases for CFD simulations.

The investigation will focus on the use of these CFD methods through mathematical formulations, numerical models assisted by state-of-the-art tools and will look at how sensitive the numerical results are to the geometry complexity, and the nature of the flow encountered in the problems. Hence, the key research questions can be formulated as:

"How beneficial can Large Eddy Simulation and Detached Eddy Simulation models be in understanding, capturing and predicting the flow features around a competitive yacht keel? How do these findings compare to those from other methods and from experimental data? Can we assess the use of such advanced models and propose a generic approach?"

1.5 Aim and Objectives of the thesis

The primary aim of this work is: to investigate the application of advanced numerical methods based on the Large Eddy and Detached Eddy Simulations as a computational tool for the prediction of the hydrodynamic flow around an America's Cup Class keel designed under the version 5 of the rules; discuss their accuracy, complexity, computational cost, advantages and disadvantages and validate against experimental results. The work is realised with the use of commercial state-of-the-art software.

To meet the above scope, the objectives of the work are defined as follows:

- To study and gain knowledge of previous findings in the open literature, regarding the use of technology and current numerical methods relevant to the hydrodynamic flow around yacht appendages in America's Cup.

- To discuss and propose mathematical formulations and numerical approaches relevant to the chosen CFD models for such hydrodynamic studies.

- To investigate the applicability of LES and DES formulations in quantifying the key flow characteristics of America's Cup keel and similar designs validated with experimental data.

- To engage in a discussion of results, key findings, observations, recommendations and concluding remarks drawn from the work.

It should be mentioned that this study does not aim to question the adequacy, performance and design of the tested geometries, but rather to investigate the capabilities of advanced numerical models in capturing the flow features for possible implementation in the future.

1.6 Organisation of the thesis

The thesis is comprised of ten chapters. Following this introduction, chapter 2 is a perusal of the key literature relevant to this study, i.e. on the field of yacht hydrodynamics and current experimental and numerical methods, including the existing use of CFD in America's Cup.

Next, chapter 3 outlines the research methodology and approach adopted in this work.

Chapter 4 presents a detailed account of the mathematical formulation used and the turbulence models involved. The basics of turbulent flow, large eddy simulation and detached eddy simulation are given.

Chapter 5 focuses on the numerical solution utilised for the solution in the computational fluid dynamic simulations.

Validation of the method (model) using standard cases of a NACA profile and an oblate spheroid is covered in Chapters 6 and 7. Firstly, detailing the framework of the simulation (test case, solution domain, grid, boundary condition). Then through comparisons with experimental results on the three-dimensional cases presented in order to validate the reliability and accuracy of the method adopted here in predicting the complexity of the flow.

Further validation and application of the numerical scheme through application to an America's Cup yacht keel is presented in Chapter 8. The upwind condition tested

will be rich in complex flow features that will test the capabilities of LES and DES in grasping the important characteristics.

Findings of this study are discussed in details in Chapter 9, along with the scope for further research and personal contribution.

Finally, the conclusions are given in Chapter 10 of this thesis.

"Do you suppose I could buy back my introduction to you?" **Groucho Marx**

"Twice and thrice over, as they say, good is it to repeat and review what is good." **Plato**

2 Literature Review

This chapter starts with a brief introduction of the America's Cup and its importance in yachting, followed by an insight into experimental techniques used in the field of yacht appendages since their introduction, mainly tank testing and wind tunnel. The chapter then discusses the numerical methods used in America's Cup for prediction of the appendages effects, i.e. potential and viscous flow solutions. Finally, recent work of interest to this study is reviewed and discussed, before closing this section by outlining the research gaps and briefly the current approach.

2.1 Contextual Importance of the America's Cup

The America's Cup is known as the Holy Grail of yacht racing (Time Magazine, 1977). It has been in competition for a period of 160 years now, and is the oldest active and most distinguished competitive trophy in all sports, continuing to draw huge interest from amateurs and enthusiasts. What started as a race around the Isle of Wight contested between the Royal Yacht Squadron and a wealthy syndicate from New York Yacht Club, back in 1851 and won by the schooner '*America*', has now become the main centre of attraction of competitive sailing.

With the exception of certain major modern professional sport, such as motor racing, more talent, technology, effort and money have been devoted to the America's Cup than for any other sport competitions. A number of innovations in current sailing yachts are attributable to the developments that the designers and researchers carried out in the long history of the America's Cup.

From a yacht design point of view, the America's Cup has inspired numerous breakthroughs, fallout from which most, if not all, yachts have taken advantage of. The focus and pursuit of excellence has delivered long-term quality; with the most stylish hull forms, efficient construction and sails, and skilled sailing techniques used in the present day having evolved from America's Cup competition.

As with any marine floating body, an AC yacht embodies many necessary elements, which must dovetail to accomplish its mission. An AC design has as a mission to achieve speed, manoeuvrability and reliability to top a single match race rival around a closed course. In a series of yacht races encompassing generally a variety of wind and sea conditions, an overall good boat wins. Audacious innovation has been rewarded over the years of existence of the competition, but sometimes at the price of failure when extremes have taken place (e.g. Team New-Zealand mast failure in the 2003 finals).

The Cup not only attracts the world's top sailors and yacht designers but also the involvement of wealthy entrepreneurs due to the history and prestige associated with the event. It is often referred to as the "playground of billionaires" because of the considerable sums of money injected (New York Times, 2002). It is not only a test of sailing skills, boat and sail design, but of fund-raising, organisational and managerial skills (Rhyne, 1994).

The financial and economical backlash involved with the event is also of remarkable importance. The teams, knowing that maybe they may not have the opportunity to covet for the trophy, inject millions of dollars into the organisation. Some of the biggest business leaders are always lurking around as major sponsors. Table 2.1 show the total budget for the teams involved in the 32nd America's Cup (Instituto Valenciano de Investigaciones Economicas, 2007). With budgets analogous to those of Formula 1 teams, and the pressure involved, failure is not an option for a race where "there can be no second". In addition, reading from the report the impact it had on the local economy pinpoints that it is more than just a sailing event. Even

King Juan Carlos mentioned the importance of the 2007 America's Cup for Valencia and Spain in front of the world (ThinkSpain portal, 2006).

Table 2. Estimated budget of teams involved in the 32nd America's Cup, in Millions of €

Teams	**Budget**
Team Alinghi (Defender)	120
BMW Oracle Racing	120
Emirates Team New Zealand	110
Luna Rossa Challenge	110
Desafío Español	60
Mascalzone Lsyino-Capitalia Team	60
United Internet Team Germany	55
Victory Challenge	50
Areva Challenge	40
+39 Challenge	40
Team Shosholoza	35
China Team	35
Total	**835**

What is observed from the history of the America's Cup is that, throughout its existence up to today, there has been a close bond between the design evolution (and to a certain extend the rules development) and the advancement of experimental and numerical techniques used in the competition. In particular, one can argue that the appendages currently in use are a direct consequence of the push in development of numerical and computational methods in yacht hydrodynamics. As more rigorous rules were introduced as the Cup entered the turn of the last century, with notably the establishment of the International America's Cup Class (IACC) rule not permitting many differences between the designs, introduction of new CFD methods were developed and used for the competition.

The following sections of the chapter briefly review the experimental and numerical applications on America's Cup appendages related to this thesis.

2.2 Experimental techniques for hydrodynamic prediction of appendages in AC (I): Towing Tank

2.2.1 Procedure for towing tank tests

The tank tests of scaled yachts are a valuable and traditional asset in yacht hydrodynamic prediction and measurement in present days, part of the tradition of measuring the forces applied on the yachts. A carriage is usually driving down the model along the narrow tank at various speeds and conditions. The tests determine the total hydrodynamic components of the hulls. They provide, in a reliable way, information on the following parameters:

- Wave and added-wave resistance for scaled models up to 6 metres long
- Bare hull and appended hull resistance, turbulent wake drag
- Tests performed upright, heeled and yawed. Measure of the overall effort with a 6 Degrees Of Freedom balance
- Trim and sinkage, pitch and dynamic righting moment
- Particle Image Velocimetry (PIV) or Laser Doppler Velocimetry (LDV) of waves and track on and under the water (figure 2.1)

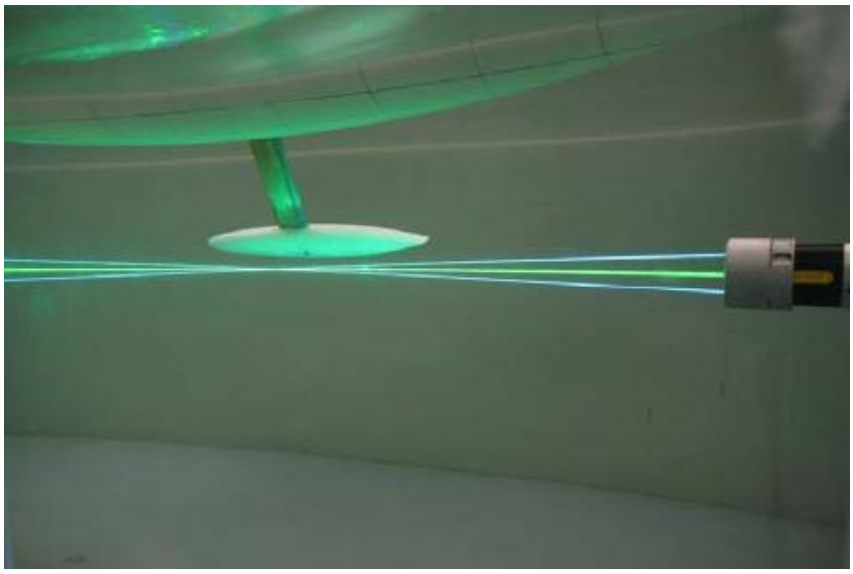

Figure 2.: LDA measurement of flow field in keel plane (Böhm & Graf, 2008)

Forces and moments between the models and the carriage are measured with load cells (dynamometers) to determine the total lift, drag, yaw and heeling moments. In addition, the characteristics of the waves created as the models are towed along the length of the tank are analyzed to determine the component of resistance associated with the wave-making characteristics of the hulls. A towing tank allows investigating the performance of different designs in air-water environment and free-surface interaction effects.

Hydrodynamic facilities around the globe testing yachts have developed and excelled in techniques and methods, from the implementation of models to full results analysis and extrapolation:

- Productions models of fully appended hulls, made from state-of-the-art materials (polystyrene foam, epoxy resin etc…)
- Use of turbulence stimulators for flow transition (to accurately measure drag)
- Optimisation of the grid of test parameters and matrix
- Extrapolation of measurements using preliminary results from the CFD viscous resistance or wetted surface dynamics and performance prediction

A number of combinations of speed, heel, yaw and rudder angles are normally tested, resulting in over one hundred data in the test matrix for each model. Once the data are collected for each model, they are extrapolated to full-scale values for hydrodynamic performance evaluation through a series of corrections for scale effects due to viscosity. The resultant full-scale hydrodynamic data are then fed within a Velocity Prediction Program (VPP), where aerodynamic forces from wind tunnel are applied to predict the overall full-scale sailing performance at various wind speeds and angles.

Definition of the performance tradeoffs available and rapid assessment of alternative design concepts can be carried out using towing tank and wind tunnel test results combined in a VPP to define the performance of different designs.

Although CFD is rapidly establishing itself as a useful and growing tool (cc following sections), tank testing is still regarded by many as the most accurate way of providing reliable results in absolute terms and as the principal verification method of any numerical code. The weakest point of tank testing remains the lack of viscous similitude between model and full-scale forms, which makes it difficult to extrapolate the lift and drag of the appendages due to the low Reynolds numbers. Also, the cost involved in creating the models and setting-up the test can be relatively high. Another limitation is also the number of tests that can be carried out in a short time, since for calm water tests the water needs to settle before the next run can start. These limitations show that wind tunnel tests are important. Wind tunnel procedures complementing the towing tank are discussed later.

For more information on the techniques involved in testing models in a towing tank, the papers from Larsson (1990) and Milgram (1998) offers a greater insight to the interested reader.

2.2.2 Historical Perspective of tank testing

Nearly thirty years after the establishment of the first towing tank in Torquay by W. Froude, Glaswegian designer George L. Watson decided to test several models of his latest AC challenger, *Shamrock II*, in the Dumbarton based Denny tank. Little did he know that he changed the course of history by becoming the first sailing yacht to be designed after towing tank testing. Following nine months of experiments, twelve wax-made models and sixty modifications, the final hull is completed. Unfortunately, the defending champion *Columbia* defeats in three straight races *Shamrock II* in 1901 and the brilliance of Watson fails to be rewarded (Burgess, 1935).

Following this rather unsuccessful first attempt, it took thirty years to see the next tank-oriented design. This time, the effort came from the other side of the Atlantic with the defender of the 15th Cup. The William Burgess-designed *Rainbow* was conceived according to the same principles following two months and a dozen of models tested at the facilities at the University of Michigan in 1931, under the

supervision of Cap. Baier (Burgess, 1935). It overcame *Endeavour* in a close-fought 4-2 overall win, reinstating belief that towing tests are the way forward.

A major step forward came from the *Ranger* campaign, the follow-up to *Rainbow*, which changed the racing philosophy forever. In 1935, the syndicate for the NYYC created the first design team in the history of the America's Cup. Design veteran Burgess and neophyte Olin J. Stephens joined forces, supported by a team from Stevens Institute of Technology, sail & rigging designers and boatbuilders.

The outcome was an innovation savvy yacht. Davidson (1936) modified the experimental approach of the aforementioned cases. Six small models were tank tested, upright then at angles of heel by applying a lateral force at the centre of effort. He also looked at the importance of measuring leeway for side force more accurately. These led to the introduction of performance-prediction, nowadays commonly known as velocity prediction program. Other innovations included the first ever aluminium mast, boom and spinnaker pole, and the first use of synthetic material for the sails. Stephens (2006) attributes to *Ranger* the advent of most yachts since.

From this time up to the mid 1970s, no developments were brought to the science of testing yachts, barring a few advances in techniques of resistance tests and equipment. There were no specific tests carried out for the keel and rudder of the 12-m class yachts during this time, resistance tests were focusing on the canoe body as a whole. A period of stasis and subsequently decline followed then until 1983 when the defender *Liberty* was not tested at all.

The rejuvenation of yacht testing occurred after 1983. Oossanen (1985) reports on the extensive tank tests carried out on the new winged-keel design developed for the *Australia II* challenger of 1983, which won the Cup away from the Americans for the first time it its history. Specific tests focused on the performance of the winglets and the keel. The success of the winning bid was in part due to the design and performance of the keel.

For the following campaign, more emphasis was put into the importance that the appendages bring to the yacht. Debord (1985, 1987) reported on the need of tank testing facilities to adapt to the design changes and to focus on the increased role of the appendages. He also highlighted the necessity of independent measurements of keel lift and drag forces experimentally, as well as researching into flow visualisation of the effect of winglets. Chance (1987) and Salvesen et al. (1988) described the involvement of testing in their winning design but without specific results or comments on the testing of the appendages.

Todter et al. (1993) reported on the importance that tank testing had in designing and analysing the appendages for the then new IACC rule, particularly in comparing various configurations and the final choice. Focus was more on the approach and methodology of the design process rather than actual results of forces and flow field. Oossanen (1992) also reflected on the changes for the new rule and the method for another syndicate, although reference to VPP results is made.

Reichel et al. (1994) mulled over the changing nature of experimental tools in the design of racing yachts and their evolution as a support to numerical tools. They issued a notice for similarity problems in tank testing and the importance to understand appendages drag depending on the model sizes.

DeBord et al. (2004) later reaffirmed this “evolving role” of tank testing and discussed the problems linked to scale effects, which can be understood better using numerical methods. Fassardi (2002) discussed the difficulties in tank testing, and the sensitivity of appendages to changes in the tank (waiting time, temperature, residual turbulence, velocity measurements).

The issues linked to towing tank testing mentioned in the last two papers tend to be tackled and overcome through the use of numerical models. As the authors wrote, numerical tools should take over where the limitations of tank testing are reached. As a general consensus, the testing of appendages experimentally through towing tanks

must rely on computational methods to maintain their importance and continue to provide a meaningful alternative for validation and verification.

2.3 Experimental techniques for hydrodynamic prediction of appendages in AC (II): Wind Tunnel

2.3.1 Procedures involved in wind tunnel testing

Wind tunnel tests are the other major experimental method utilized in America's Cup and the most likely used in relation to keels. Investigations through wind tunnel experiments applied on a yacht's appendages allow the engineer to perform studies where the free-surface flow is not needed, hence helping focusing on the viscous flow and underwater characteristics of the keel. In particular, the following issues are usually observed and obtained for analysis:

- Forces and moments measurements on the keel, rudder and other foils
- Pressures measurements on the surfaces
- Flow visualisation, both on and off the surface, streamlines, wake
- Flow separation and transition (viscous drag shapes of keel, bulb, fin, rudder)
- Interaction between the keel-bulb-winglets or the keel-rudder configurations

The high velocities generated inside the section, the size of the models and the inlet turbulence settings reproduce conditions similar to the actual flow of water around the yacht. The moderate cost of manufacturing the scaled models, the provision of facilities, along with the speed of use and the flexibility of the tool make of the wind tunnel test an affordable and effective procedure. This enables accurate force measurements and small design variations.

The force measurements usually include the lift and drag components of the appendages using velocities up to 60 m/s or more (but under the subsonic limit of 102 m/s or Mach number equal to 0.3 to retain incompressibility), which simulate the equivalent of 9-14 knots of boat speed in water using Reynolds law of similarity. The

surface pressure testing utilizes pressure-sensing devices to determine pressure distributions on the surfaces of the appendages. The flow visualization testing involves using Laser Doppler Anemometry, paint, strand of wool or fumes, which allows the designers to actually see, or visualize, the flow patterns as the air passes over the surfaces of the appendages, for interpretation and validation studies (figure 2.2).

Figure 2. Example of wind tunnel tests for America One challenge (www.americaone.org)

Wind tunnel requires several tests to accommodate the many possible combinations of heel, yaw and trim tab (or flap) deflection. The yaw and flap angles are adjusted in small increments between the tests, then the procedure is repeated over and over again. These tests allow the design team to identify optimum angles and flap deflection, thus reducing the number of tests required in the towing tank. They can then be fed into an optimiser program and a VPP for performance analysis.

As discussed in the previous section, towing tank tests provide an integrated result for the combined hull/appendage system in terms of forces and in terms of free-surface effects. Wind tunnel can determine each component's contribution separately. Combining the two technologies helps in breaking down and understanding the performance of each component. In addition, making use of the wind tunnel's time

efficiency is important since more tests can be run compared to a towing tank in which water requires settling between runs.

2.3.2 Applications to America's Cup Appendages

Many of the competing America's Cup syndicates carry out extensive wind tunnel tests, but these are rarely published due to the confidentiality surrounding the event. Whilst most studies involving wind-tunnel analysis focus on sail and rigging measurements (Flay and Vuletich, 1995, Richards et al., 2001, Viola, 2009 to name but a few) there have been a few directed towards underwater appendages.

Early developments came with Oossanen and Joubert (1986) who reported on the use of wind tunnel experiments for the design of the keel on the groundbreaking *Australia II*, the first yacht ever to use a winged-keel (figure 2.3). Comparison with and without winglets was made, for Reynolds number of 1.7×10^6. The tests showed an increase in lift and performance in the presence of the winglets in heeled and yawed conditions, thus confirming the benefit of including a winged keel in the design of the yacht.

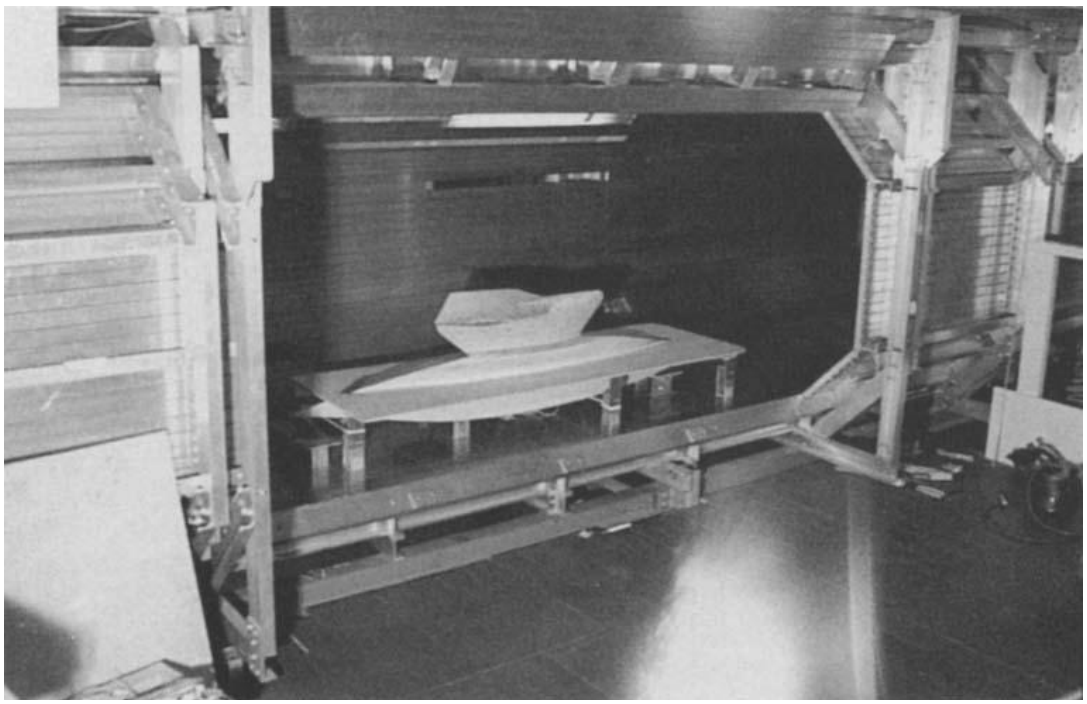

Figure 2. : Model of winged keel of Australia II in wind tunnel (Oossanen and Joubert, 1986)

Todter et al. (1993) reported on the importance that wind tunnel had in designing the appendages for the then new IACC rule, particularly in comparing various configurations. Tests up to Reynolds numbers of 1.3×10^6 were possible.

Tinoco et al. (1993) presented wind tunnel data of generic keels for the 1992 America's Cup campaign. Force polars for two different bulb shapes and two winglet span lengths are given, as well as a description of the model geometries. These data can well be used for CFD validation. However, the geometrical variations are rather large (with/without winglets, long/short winglets). Moreover, no flow measurements are presented.

Turnock et al. (2001) briefly mentioned the successful use of wind tunnel in the Team New-Zealand winning campaign of 2000 but did not give further details concerning results or other findings. Oossanen (2003) referred to the role of the tunnels tests in predicting the induced drag from the keel. He emphasised on the need to use model sizes close to full-scale to ensure a truthful prediction of the induced resistance.

Ranzenbach and Zahn (2005) gave a detailed description of the testing procedures and techniques used for keel flow predictions in the Glenn L. Martin Wind Tunnel. Some force measurements are presented, but unfortunately the tested geometries are not provided.

Werner et al. (2007) presented a case study of a winged keel tested in wind tunnel for validation (figure 2.4). The work was motivated by the lack of public test data suitable for validation of RANS and potential flow code as the main reason to undertake wind tunnel studies. The paper described experimental procedure, uncertainty and presented useful results in terms of force coefficients and wake survey for case of a keel without winglets, and keel with winglets at two locations. The base of the keel is rotating and there is a glass to control the mechanisms during the experiments. The uncertainty reported for the force results was 3%, and for the wake velocities these were 1.3% based on the free-stream velocity. For the cross-flow velocity, the uncertainty was equivalent to 10-15% of the local values. During the testing, a leakage of air occurred and was not taken into account which may well have influenced the data obtained. Most importantly, the database was made available to any interested researcher hereafter.

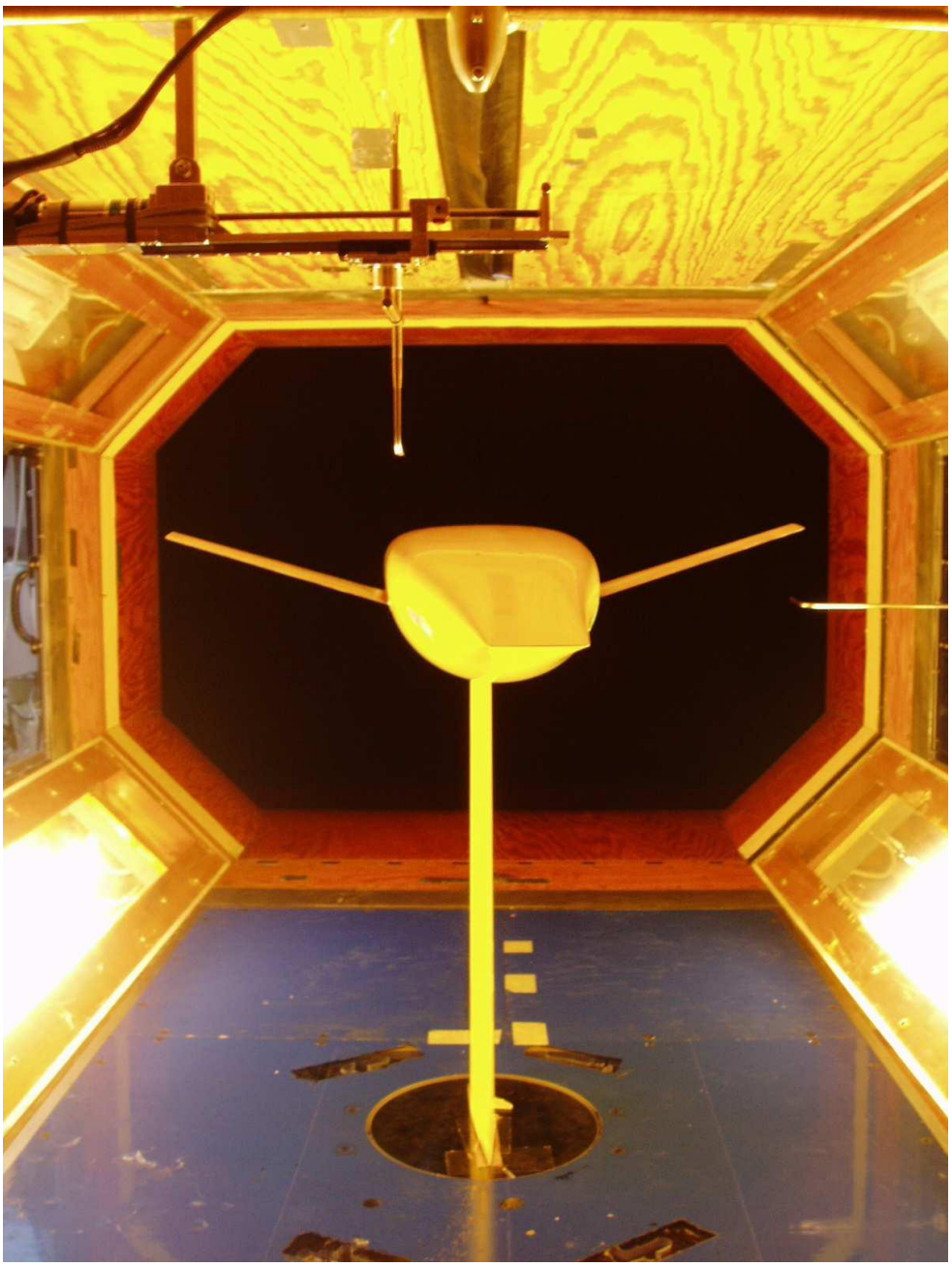

Figure 2. Photograph of the wind tunnel set-up (Werner et al., 2007)

2.4 Computational Methods in America's Cup Appendages

Computational Fluid Dynamics are used for the design and optimisation of America's Cup keels, often as a complement to experimental studies. The ability to predict numerically using CFD the aero and hydrodynamic performance of a chosen design is seen as a potential to offer several benefits. These are:

- Rapid evaluation of design changes
- More cost effective than extensive wind tunnel and towing tank testing: several designs can be modelled and simulated at no manufacture costs
- Greater detail and understanding of the actual flow regime
- Parametric testing more approachable

Hydrodynamic and aerodynamic studies of the underwater appendages of a yacht using numerical methods provide the designer with useful quantitative and qualitative information for analysis and optimisation, in addition to the already mentioned experimental techniques.

2.4.1 Panel Methods and Potential Flow

The first endeavour in computer-aided fluid dynamics came from the introduction of panel codes based on potential flow theory. These were developed in the aeronautics and aerodynamics field, with the pioneering work from Hess and Smith (1967).

They were later extended to the solution of ship hydrodynamic problems (Dawson 1977a, 1977b). Although they are based on a simple irrotational and inviscid flow model, these codes are still nowadays commonly used in the ship hydrodynamics community because of the rapidity of the calculations and relative accuracy of results.

Typically, in panel methods, the appended yacht is assumed to be advancing at a constant and uniform velocity. A Cartesian coordinate system fixed in space is defined. Potential flow panel methods operate under the following assumptions:

- The flow is irrotational (outside the surface of singularities)
- The fluid is inviscid, incompressible and infinite in extent
- The in-stream flow is axially directed parallel to the centreline of the body

Under the assumption of potential flow, a perturbation velocity potential Φ_0 characterises the flow field around the yacht, which satisfies the Laplace equation

$$\nabla^2 \phi_0 = 0 \tag{3.1}$$

The canoe body, appendages and free surface around the hull are divided into a number of panels as shown in figure 2.5. Planar quadrilateral panels are normally used to approximate the surfaces. The drag is computed by taking into account free surface deformation (wave resistance) and induced drag from appendages. Meshes are on the surfaces only; this permits advantageous reduced meshing and computation time.

Potential flow methods give the opportunity to assess wave and pressure fields on and around the surfaces and the water, to get efforts on each mesh element and to optimise shapes through a controlled process. Other studies usually encompassed by panel methods are investigation of keel position, efficiency of lifting foil, winglets and trim tab and comparisons of bulb's dimensions such as width, length and thickness. Effects of heeling on wave resistance and surface flow are also considered.

Numerical codes based on panel codes present some limitations. These are:

- No account of viscous effects (no viscous drag)
- Linear free surface model, wave effects on overhangs cannot be completely taken into account
- Still water modelisation
- Boundary layer prediction sometimes not adequate

Therefore, the following effects cannot be taken into account:

- Flow separation and vortex in viscous wake
- Appendages viscous drag and hull-appendage interaction drag
- Laminarity of flow around foil section
- Added resistance in waves

It was around the mid 1980s that the first serious use of such techniques was applied as a major part of the America's cup challenges.

Oossanen (1985) and Oossanen and Joubert (1986) used a panel code by means of source-sink and vortex distributions with free surface capturing to investigate the use of winglets on a keel and compare with wind tunnel studies mentioned earlier. They used up to 2000 panels; each panel is given pre-determined source strength. On the parts of the yacht developing lift a system of bound and free vortices was superimposed. Their results showed good agreement with the experimental measurements but the computed lift was generally overpredicted by 10%, mainly due to the inability of the potential flow code to model the viscous effects in the keel-hull junction.

Boppe et al. (1987) and Boppe (1988) presented as main application a three-dimensional surface panel method, which was used to examine the upwind performance of the underwater hull and appendages. A boundary layer code was also used for the keel design of Stars and Stripes in 1987. The calculated effective draft was over-predicted compared to towing tank data. This discrepancy was caused by flow separation in the aft-body, which could not be predicted with the potential flow code.

Tinoco et al. (1993) showed good agreement between wind tunnel tests and potential flow/boundary layer computations of generic keels. They concluded that their computational method was well suited for induced drag computations of the keel configurations, but lacked in accuracy in the predictions of the viscous resistance of the bulbs.

Pallu de la Barriere (2000) referred to the use of in-house potential flow code for the design of the keel for the French entry *6e sens*. The dimensions and the winglets were optimised through the REVA code but there was no mention of forces or other calculations, nor comparisons with experimental tests.

Rosen et al. (2000) reported on the use of the potential flow code SPLASH during the 2000 campaign for investigating the side force of the appendages and determine optimum yaw, tab and rudder settings for minimum drag at upwind sailing conditions (figure 2.5). Numerical tests were also run to investigate the trade-offs relating to winglet size and to investigate the effects of keel planform, taper, and the percentage of keel chord to be allocated to the trim tab. A small number of tests were also run to determine the optimum bulb length-to-diameter ratio. SPLASH was found beneficial in all cases. Comparisons with tank test results showed a 20% difference for the potential case.

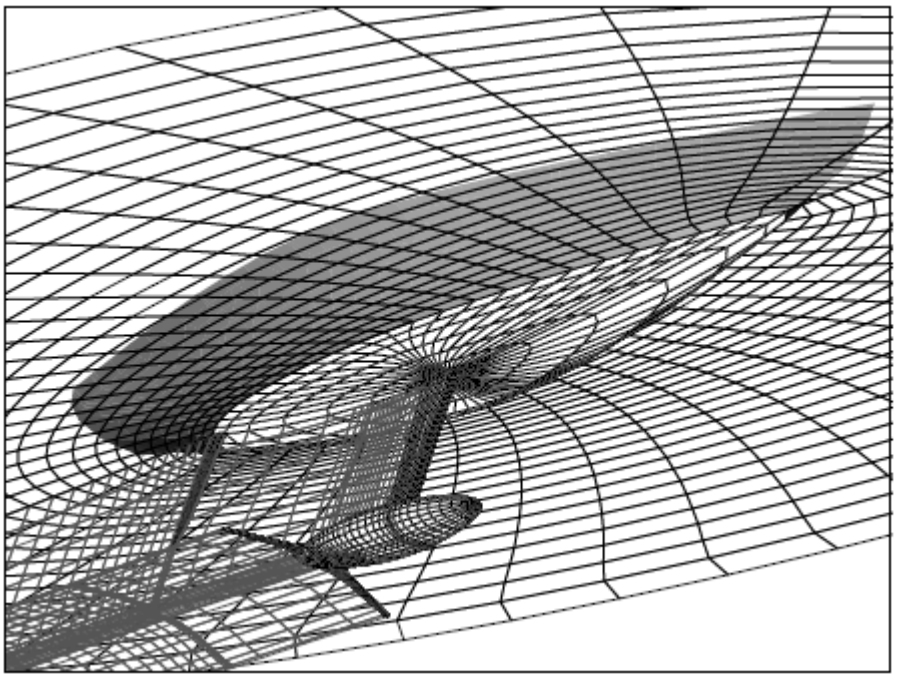

Figure 2. Panel distribution around the underwater of the yacht (Rosen et al., 2000)

Werner et al. (2007a, 2007b) validated a potential flow code (SHIPFLOW) coupled with a boundary layer code against the wind tunnel tests carried by the same authors on an America's Cup keel. Various set-ups for the potential code were used and compared (e.g. direction of wake panels, presence of lifting panels on bulb, no extra strips). Over 8000 panels were used in total for the simulations. The errors in the potential flow code coupled to the boundary layer solution results were within the experimental uncertainty (2% underprediction for both lift and drag), but given that the correct panelisation is used (in some cases, error was as high as 18%).

2.4.2 Reynolds-Averaged Navier-Stokes approach to appendages calculation

Since the early 1990s, and with the increase and advances of available computational power, numerical methods based on the solution of the Navier–Stokes equations became prominent and were initially successfully applied to naval engineering problems. The solution of Navier–Stokes equations has broadened the class of problems that could be faced, including the possibility of treating viscous, turbulent and separated flows which were not possible with panel codes on ships in general and on yachts in particular. Since most races outcome to small details between a winning and a losing yacht, most teams turned to new ways of getting accurate numerical simulations to add to the experimental tests. It soon became obvious that non-viscous, free-surface panel codes based on the potential flow theory were not sufficient anymore, or at least needed further input; as the battle between the boats moved to underwater appendages and sails. Hence, viscous flow solvers appeared and became a useful tool for analysing yacht hydrodynamics.

According to Jones and Korpus (2001), the first serious use of viscous-based numerical simulations, based on the solution of the Navier-Stokes equations appeared with the 30^{th} edition of the America's Cup. However, several studies existed previous to this time. Azcueta (1996, 2002) was one of the first to apply viscous flow calculations to yachts, including free-surface viscous flow and appendages design and performance.

Coudray et al. (1994, 1995) reported on the use of numerical tools for the French Challenge of 1995. Their approach consisted of using mostly numerical tools with experiments used only for validation of the models. For the appendages design, primarily focusing on the bulb and keel rather than rudder, the authors made use of source-dipoles panels, boundary layer and Navier-Stokes codes with various levels of success and at times limited use. The authors recognized the qualitative nature of the numerical tools used which helped in understand the flow but were limited in terms

of quantitative results due to computational power issues involved with higher-order Navier-Stokes problems.

Rosen et al. (2000) reported on some viscous flow calculations using OVERFLOW code that were also performed during this study for the side force of the fully appended yacht, in addition to potential flow runs. Comparisons with tank test results showed an 18% difference for the viscous condition.

Turnock et al. (2001) presented a review of the requirements for the design of appendages for America's Cup, with emphasis on computational fluid dynamics and its capability in helping in the design. Various techniques are presented, with RANS methods in particular. Some qualitative figures from CFD results are included, but without details on calculations. The authors also discuss the experience of Team New Zealand in their successful defence of the 2000 challenge, and the importance of validation of results against proven experimental data. To this mean, a practical RANS example based on a simple NACA 0012 section of a fin keel is presented. The main findings reported that a high quality grid and a systematic approach are required to obtain accurate prediction of lift and drag. Limitations of RANS are also considered but the association of various numerical methods can help in overcoming the issue.

In Jones and Korpus (2001) and Korpus (2004), the CFD work reported from the authors experience in the latest campaigns is presented and has been focused on RANS methods. The role of CFD in yacht design is well described and examples of flow field results are shown, figure 2.6 and figure 2.7. The integrity and ability of RANSE to help in the design of the appendages is explained, applied and discussed in an example for the *AmericaOne* and the *BMW Oracle* challenges in which the authors were involved. An overset grid approach was utilised with an incompressible RANS code, and κ-ε and Spalart-Allmaras turbulence models. Qualitative flow features are shown for some cases for the keel and the winged bulb (streamlines, pressure contours). The integration of RANS helped in selecting the most appropriate design particulars (shaping, winglet's position etc) amongst trade-offs.

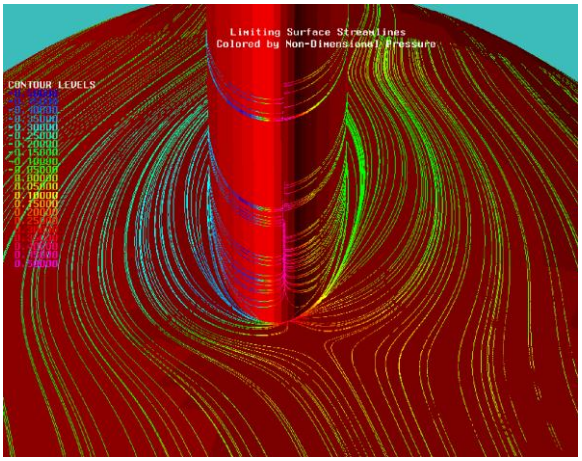

Figure 2. Surface Streamlines around fin keel and bulb junction (Jones & Korpus, 2001)

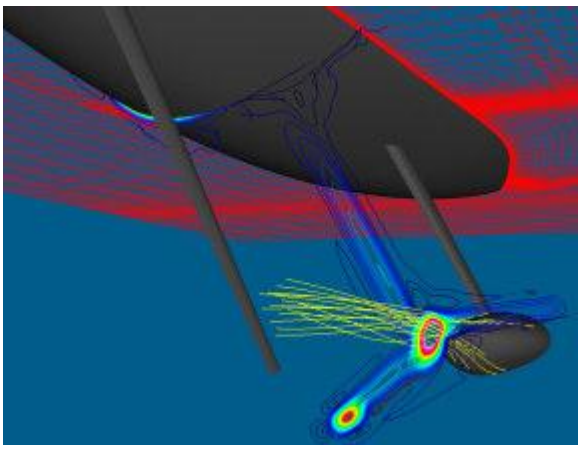

Figure 2. Flow and Vorticity fields behind the keel (Korpus, 2004)

DeBord et al. (2002) presented a general review of available tools for optimisation of America's Cup designs. This encompassed experimental techniques and numerical techniques, all discussed in this chapter. The role of CFD in yacht design is well described, and the authors presented towards the end an advisable procedure for carrying out studies in America's Cup. Navier-Stokes and viscous solvers are recommended for appendages analysis, seconded by experimental tests for validation. However, there were no indications or advice on the required number of cells and on the needs for computational resources for viscous calculations of forces and flow, or results of validated data.

García-Espinosa et al. (2002) presented a finite-element method approach to solving the RANS equations with a validation on AC yachts using unstructured grids of 700,000 cells for upright conditions and of 1,500,000 cells for heel and drift, including hull and appendages. Surface pressures of the keel are shown to be predicted accurately, while global forces for all cases are agreeing with extrapolated experimental data.

Graf and Wolf (2002) reported on CFD investigations applied to the appendages of IACC yachts, carried out for one of the syndicates. The flow simulations for the keel were performed using a RANS solver, on hexahedral and tetrahedral grids of about 1.4 million and 1.75 million cells respectively. A Finite Volume discretization scheme was used for viscous calculations, with a κ-ε and κ-ω turbulence models. The reported accuracy was less than 5% difference with experiments but the authors cautioned that this occurred when using the right parameters. Those were not mentioned. No comparison with experiments in terms of local flow features was presented (contours, pressure, etc...). Viscous calculations helped in finding the optimum configuration and design for the keel (blade profile, bulb shape and length ...).

Böhm and Graf (2008) performed a validation of RANSE simulations against towing tank data for a fully appended AC yacht at model test size and with free-surface effects. Dynamic effects were considered in the computations. The authors followed a volume based method for solving the time-averaged Navier-Stokes equations, with a κ-ω SST model for turbulence. The commercial solved Ansys CFX was chosen for the application. The domain consisted of 4 million cells, with unstructured elements and refinement near the water plane and near the model yacht. The results showed differences of up to 8.5% under prediction in downwind conditions for drag and of 2.5% (under predicted) and 20% (over predicted) for drag and lift in upwind conditions. Flow comparison behind the keel between numerical and LDA measurements yielded similar behaviour/observations.

Graf et al. (2009) presented results based on viscous CFD solver for the hypothetical AC90 Class of America's Cup. Flow simulations around the appended hull of a benchmark design were performed for free-surface issues, but also separately for the underwater appendages without water. An unstructured tetrahedral grid was chosen with 5.7 million elements. The authors focused on flow into the rudder as the rules allowed for one or two rudders, hence forces prediction focused on the tillers rather than the keel.

The work involved around the winning Alinghi team of 2003 and 2007 is also a very good example of successful use of RANS numerical tools in the design and analysis of appendages for an America's Cup bid (Cowles et al, 2003, Parolini and Quarteroni, 2005, Parolini and Quarteroni, 2007, Detomi et al., 2009a and 2009b). Because of the links with the Swiss team, results presented comprise mostly of qualitative images and figures of flow behaviour (contours, streamlines, etc...) but the authors do link the mathematical models behind the CFD methods in more details than other papers (domains, equations of flow, free-surface, turbulence models, fluid-structure interaction for sails, numerical discretization). General description on meshing used is described for all papers, with a progressive approach starting from unstructured grids of around 4.5 million cells for hull, keel and winglets for the early papers to multi-block structured mesh for the latest study consisting of 20 million elements for the complete yacht. Examples of flow near the winglets, the bulb and in the wake are qualitatively reported, which can be useful for researchers to assess similar situations.

As it can be observed, most of the literature on CFD work from the latest campaigns has been focused on RANS methods and the role of CFD in yacht design, with examples of flow field results and most of the time qualitative results but little on available quantitative data that can be used for further research. This is mainly due to the restricted nature of information that can be shared by the teams involved in the competition, hence limiting possible academic work.

Recently, there has been an attempt to validate CFD codes and other numerical methods against experimental data for a fully appended keel configuration, and

several researches have started to look into offering a database (or platform) for yacht hydrodynamics in view of using for possible future works.

Studies have been undertaken at Chalmers University by Werner et al. (2007a, 2007b) on wind-tunnel experiments for a model winged-keel (described earlier), and RANS based calculations were validated against the experimental results in terms of lift and drag forces and wake survey.

The purpose of the study was to find which methods accurately describe forces and flow fields, how the methods can be applied in the most suitable way and how accurately the global forces of the keel can be predicted with CFD. The effects of grid size and turbulence model were considered. The findings included recommendations on best practice to follow for this type of validation studies.

In terms of the RANS methodology, a multi-block structured approach for the grids was adopted, with wall function near the keel as resolution. Grid sizes used ranged from 1 million to 2.6 million cells; the finest mesh was adding up to 3.6 million cells for the case with the winglets, with local refinement set in the wake area in the cross flow plane for the flow comparison. Laminar zones were defined for transition of the flow. Several turbulence models were tested: Spalart-Allmaras, κ-ω SST, κ-ω constrained, standard κ-ω, standard κ-ε and realizable κ-ε.

The errors of the RANS code (FLUENT) were found to be a little higher than the experimental error (uncertainty). The study reported that errors between the measured values and the RANS computations for a wingless keel yielded differences of between 0.4% and 3% for lift, depending on the turbulence model, and between 0.3% and 12% for drag. All values were underpredicted. For a winged-keel, the corresponding discrepancies were around 3% for both lift and drag. Grid size was not found to influence the results (about 0.6% and 0.9% difference in lift and drag respectively). Neglecting the laminar zone gave an error of 5% and 14% in lift and drag. A comparison of the experimental wake flow pattern to the one computed with

RANS was also presented. The standard κ-ω turbulence model was found to give the best predictions of the wake.

2.4.3 Post-Werner work

In addition to the work published by Werner, several other researchers used the keel geometry and database developed at Chalmers University of Technology for further validation studies and flow investigations.

Coiro et al. (2005) used the model in collaboration with Chalmers University to investigate through a numerical analysis the most favourable shape and position of the winglets along the bulb in order to establish set up and experimental test case of the wind tunnel tests for Werner et al described to be used for CFD code validations. A further numerical code, based on the solution of the Poisson's equations for induced drag and on Maskell's method for wake integration and velocities, was developed in order to analyze the experimental data and obtain the performance of the whole fin-bulb-winglet system. The complete methodology of the work is described in the paper, though the final geometry used by Werner was not ready yet.

Thys (2008) used Werner's geometry, along with models of bare hull and fully appended yacht, to test and evaluate the non-viscous, potential flow CFD code RAPID (developed by MARIN), through computing the hydrodynamic forces. Thys also performed an optimisation loop by coupling RAPID to a VPP solver, although the latter was not based on Werner's model. One configuration was tested (winglets in aft position). Forces were found to be in the uncertainty region of the experimental measurements; drag was over predicted, lift was good for one case, but bad for the other. Out of the three lift-prediction methods (pressure integration, Trefftz-plane method and wing theory) used; the pressure integration was found to be the best.

Ambrogi et al. (2008) performed a RANS based numerical simulation of the flow field around the keel using a Spalart-Allmaras turbulence model and a viscous code developed by INSEAN. The computed configurations used were those without and with the winglets in forward position. The study showed differences in terms of

pressure contours, velocity fields, vorticity and comparisons with experiments in terms of non-dimensional global forces and axial velocity for two arrangements. An overgrid, structured mesh of 7 million cells was used. The authors reported quite large errors between numerical results and measured values, of the order of about 8% overprediction in drag and as much as 23% underprediction in lift, for both arrangements tested. The differences were put down as modelling errors. There has been no other published work based on Werner's model to the best of the author's knowledge.

Nicolopoulos et al. (2009) described the CFD based approach used for the design and development of bulbs built by the *AREVA Challenge* on the 32nd America's Cup. The methodology included the use of a RANS based solver for numerical simulations to calculate and compare drag coefficients for a set of three different bulbs, and then combine with experimental results and analytical hypotheses to classify the solutions based on the performance of the designs. The CFD validation is described, although no experimented data appears in the paper, consisting of a FEM solver with a Spalart-Allmaras model for turbulence. General overviews of meshing, domain (incorporated as a virtual towing tank), resolution and boundary conditions are given, and it is assumed a hybrid type of mesh is used for the spatial discretization. The computations were validated for three different speeds, for the three bulb geometries in non-dimensional drag coefficients.
The authors also mention the emergence of DES and LES as new, advanced turbulence models but these were not preferred due to the computational resources available and the large number of simulations needed. However, they conclude on future developments, inclusive of the use of LES and DES to represent flow separations more accurately, which tend to indicate the future lies in these new models.

2.5 Research Gap and Motivation

The opportunity exists to continue the work and trend initiated by the research from Werner and to further develop the use, knowledge and application of advances and

new CFD application on the America's Cup keel developed by Chalmers. Using the geometry of Chalmers and the available database, the main motivation behind the current research is to perform a numerical study using a large eddy simulation (LES) and detached eddy simulation (DES) formulation of the flow around the model yacht keel designed according to the International America's Cup Class (IACC) version 5 of the rules, in order to predict the general forces acting on the model keel and hence to compare against experiments.

Drawing from the above references, the chosen methods go a step further than RANS turbulence models in their capabilities and nature, and it is necessary to examine how well they can predict the forces acting on the keel. There are a few published applications of LES or DES for yachts. Braun and Imas (2008) investigated aerodynamic CFD analysis of racing yachts, including interaction effects with geometry. Wright et al. (2010) evaluated state-of-the-art CFD calculations: they compared DES and RANS for computing force coefficients and surface pressures for VPP and aero-elastic design of sails. To the best of author's knowledge, no other work on the use of LES and DES on America's Cup yachts has been published, which is an additional motivation to fill a gap and continue the research in the field.

This chapter started with a brief overview of the America's Cup's importance, followed by the description of the experimental techniques used in designing and analysing the appendages role, be it towing tank tests or wind tunnel experiments. It then discussed at length, the existing numerical tools which are available to researchers when dealing with the appendages (summarised in table 2.2) followed by the detailed explanation of the latest work on the field. It then skimmed through the recent work of Chalmers and subsequent work from authors based on the keel geometry developed by the Swedish university Finally, the chapter concluded by identifying the research gap and the motivation behind this research. The next chapter is outlining the approach adopted for this research.

Table 2.: Summary of available resources for yacht testing

Model	Strengths	Weaknesses	Introduction	Yacht Design Application
Towing Tank	-Provide accurate data input for VPP -Comparative design decision-making -Multi element testing (hulls, appendages) -Complete picture (wave pattern, forces, coefficients, resistance) -Main technique for verification of CFD codes	-Restricted by Reynolds number -Time consuming to set up and test -Forces on keel and bulb can't be accounted for separately -Appendages sometimes not important	Late 19th century	1930s
Wind Tunnel	-Full scale Reynolds number achievable -Rapid testing -Can focus on appendages -Excellent visualisation of flow and pressure, vel.	-No modelling of wave pattern from appendages -No influence of hull waves -Complicated set up for heel and keel-rudder interaction	1950s	1960s
Potential Flow	-Rapid evaluation of design changes -Cost effective solution -Parametric testing possible	-No viscous effects -Linear free surface model -Boundary layer prediction not adequate	1970s	Mid 1980s
RANS CFD	-Viscous, turbulent and separated flows prediction -Free-surface included -Full scale mod.	-Higher computational resources needed -Longer to calculate	1990s	Circa 1998

"For someone who's had the level of success I've had, there's been very little critical review of my work, which is pretty fascinating"
Billy Corgan

"Stay committed to your decisions, but stay flexible in your approach"
Tom Robbins

3 Approach Adopted

This chapter briefly describes the approach adopted to achieve the aims and objectives of this research project. The mind map of the complete approach is given, which broadly comprises the following: application of a mathematical and numerical model suitable for the current study, validation of the models using existing standard test cases, further validation by appliance to relevant model linked with the America's cup and finally a reflection on the chosen method and the outcome of the project.

3.1 Mapping of the Problem

In order to investigate the use of LES and DES for yacht hydrodynamics problems, it was deemed imperative to establish a simple and clear strategy for achieving the aim and objectives of this research project. Such problems require a plan with various milestones to be completed and with an adequate procedure to follow. A simplified mind map of the approach adopted in this work is depicted in Figure 3.1. It can be seen from the figure that the complete strategy comprised of several major phases / steps that are briefly discussed in the following sections.

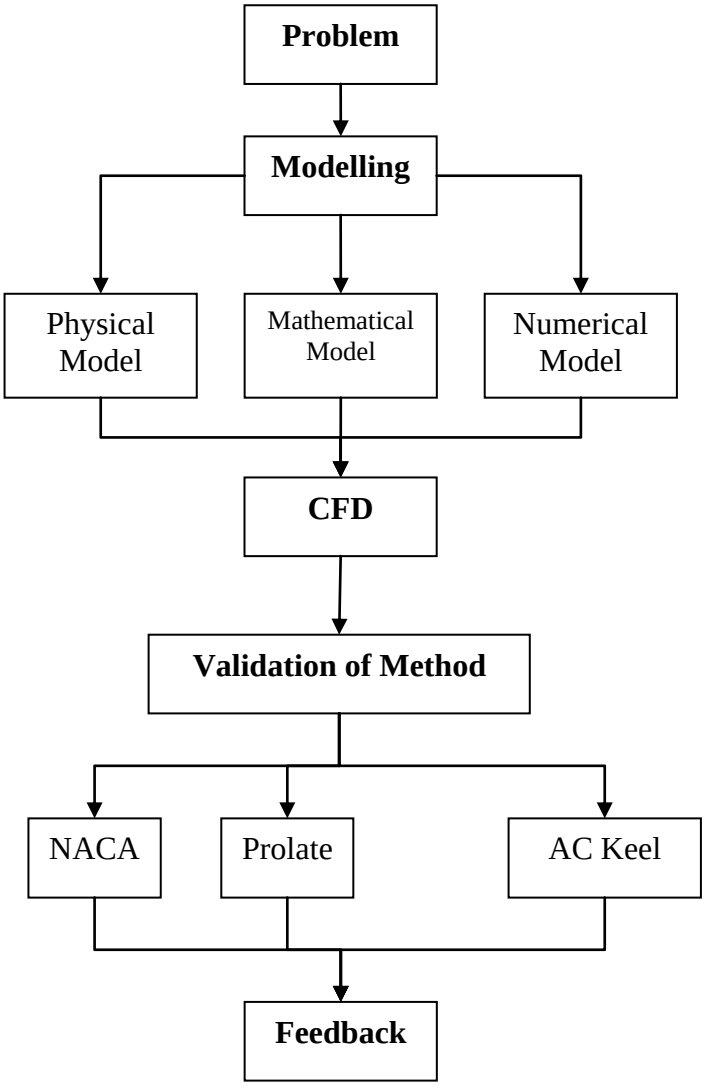

Figure 3. Mapping of the Problem

3.2 Physical, Mathematical and Numerical Modelling

Before embarking on the performance of the numerical simulations, it is essential to gain reasonable appreciation of the modelling aspects involved in the problem. Three aspects linked to modelling of the environment are examined: physical, mathematical and numerical modelling.

The physical background, which is linked to the basics and the physics of the environment around the geometries and with the experimental procedures and results,

is not explicitly defined on its own but rather is incorporated in each section that deals with the application of the numerical solution. For the computational simulations to be accurate and effective, the surroundings from the experiments are expressed in terms of boundary conditions, flow conditions and fluid properties. These are explained at the beginning of each relevant section.

The governing equations of fluid flow (continuity and momentum) are essential in understanding and translating the theoretical notions into a mathematical approach, rendering them more practical for solving marine problems. This study of the equations, along with the fundamental concepts of turbulence and flow, provide important insights into the nature of engineering flow such as the one dealt within this thesis. The mathematical formulation that describes the governing flow is derived. The model is based on the pressure-dependent (homogeneous), incompressible Navier–Stokes equations. The Reynolds numbers associated with yacht hydrodynamics problems are high (order of magnitude of around 10^6 to 10^7). The flow is turbulent around a large portion of the model and suitable turbulence models have to be used to estimate correctly the forces acting on it. An overview of the different turbulence models that are applicable in the framework of a Reynolds Averaged Navier–Stokes solver are given, with particular emphasis on the chosen models for the current thesis (LES and DES) that will be used in the simulations.

Following the mathematical approach, the numerical solution is tackled since it is transposing the flow and turbulence equations into the solver. The numerical discretization of the mathematical model based on the finite volume spatial discretization is presented. The use of LES and DES necessitate more advanced numerical schemes, algorithms and pressure-velocity couplings which are described in details in the relevant chapter. The schemes adopted for the computation of fluxes and for the solution of the Navier–Stokes system, as well as the algorithms used for the solution of the algebraic problems, are explained. The discretizations of the equations associated to the turbulence model are also described.

3.3 Framework of Approach for CFD

Computational Fluid Dynamics transpose the modelling part into components that can be used for analysis in a practical way. The framework of the approach for the CFD simulations is subdivided into the following main stages:

- Grid development for each case using state-of-the-art mesh generator software Gambit 2.4.16 and the tool Tgrid 5.0.6 when required
- Execution of the CFD simulations with the commercial solver FLUENT 6.3.26 which include the mathematical formulation and the numerical solution such as discretization methods, pressure-velocity coupling, turbulence models, fluid properties…forming the backbone of the simulations
- Extraction, processing and analysis of the data
- Validation and verification of the tools, solvers and the method against experimental data and subsequent discussion of the findings

In the initial stage, a mesh for each investigated geometry is created according to the requirements of the physics and selected methods of the mathematical and numerical simulation. The rationale is to create a series of meshes that can correspond to numerical result as close to reality as possible. This is feasible by following some conditions that need to be satisfied:

- Mesh surfaces must be concurrent to geometry surfaces (each node to be positioned on the geometry face harmoniously
- Node distribution must be concurrent to the need of the resolution (e.g. where high flow gradients are expected, resolution needs to be higher)
- Nodes should point in a logical way (right-hand rule)
- Boundary layer must be carefully considered (thickness, layers, ...)

An appropriate balance between sufficiently high calculation accuracy and computational effort that is spent in terms of time has to be found to estimate the number of cells used for the geometry, while bearing in mind the limitations of the

computational capacities of the working computer. This is the main challenge faced when using the mesh generator solver and when dealing with large eddy and detached eddy simulations. Adapted hybrid meshes will be mainly developed herein to give more flexibility with the challenging geometries.

In the second stage, the CFD solver will be set up and the boundary conditions will be defined. The main effort will be put into making sure the problems are solved accurately, predominantly focusing on the global forces and flow features from the various bodies. Advanced turbulence models will be used in the simulations for comparison. When assumptions and/or simplifications will be taken into account, these will be duly mentioned and the thinking behind them explained to the reader.

The third stage will be dominated by post-processing, extraction and data analysis of the results obtained from the simulations. Data first needs to be extracted from the different files and runs obtained. Then it has to be compiled and processed in a form suitable for comparison with experimental values for validation (tabular form, graphs, plots, images).

The last stage make use of the prepared data from phase three, which will be compared with experimental data from wind-tunnel tests mainly (these will be referred to for each case in the relevant chapters later). The practical tests should provide with a good indication as benchmark for the CFD simulations, particularly in regards to the yacht keel simulation. When data are conflicting and do not agree, then discussion and recommendations will ensue to understand the problems and help in future developments and applications to successfully match and agree.

3.4 Test Cases for Validation

Before embarking on the application of the proposed approach to the investigation of the flow around a yacht keel, it is imperative to gain reasonable appreciation and understanding of the numerics past standard cases that are well known and that can

provide a good way to validate and verify the methodology. In the relevant chapter, two applications set-up in wind tunnel configuration and well established within the CFD community are considered: a NACA 0012 profile and a 6:1 prolate spheroid. Both geometries are pertinent for a validation case as they exhibit high Reynolds number flow characteristics.

The NACA 0012 is a simple airfoil geometry and flow but a very good test case for practical reasons. Lift and drag coefficients at various angles of attacks will be investigated, as well as surface pressure coefficient. Well documented experimental tests will provide the comparison with the CFD simulations. A C-type structured grid will be created for the investigation, with a fine near-wall resolution mesh to report the results.

The numerical simulations of the prolate spheroid of length-to-width ratio of 6:1 and at angles of incidence will be validated against the experiments carried out at Virginia Polytechnic Institute (references are included in the relevant chapter of this thesis) in terms of surface integrals, and in terms of normalised lift and moment coefficients monitoring. Flow behaviour at two cross sections along the geometry will also be investigated in terms of separation and other features. The inclined cases are in static condition as per the wind tunnel configuration. Several mesh sizes will be considered, with different near-wall resolutions; and O-type hybrid grids will be created. This slender case is more challenging than the airfoil and widely reported in the field.

3.5 IACC Keel Flow Investigation

The mathematical models, the numerical schemes and the CFD framework introduced earlier will then be used for the numerical simulation of the flow around an America’s Cup scaled keel. A full understanding of the hydrodynamic flow around an America’s Cup yacht is still difficult to grasp and exact representation of the physics is far from being achieved. The complex interactions between the

different components of the appendages as well as the strict constraints imposed by the America's Cup rules make the design of a performing keel an extremely difficult task. By applying the advanced CFD methods described in this thesis, the aim is to find if there could be a better way to predict the forces and the flow around the keel more accurately than existing methods and get contiguous proven experimental tests. In particular, we aim to ascertain if the field of competitive sailing (design and research team) can benefit from the adequate use of these advanced numerical techniques currently available and if they are mature enough to be applied to America's Cup.

Based on the various configurations of the keel being tested (winglets in forward position, winglets in aft position and fin keel with bulb alone), an extensive number of simulations will be carried out in the framework of the thesis using different grid strategies that will be detailed. A simulation procedure for the analysis of several aspects of the design will be set up. The different simulation phases of the CFD framework (geometry reconstruction, grid generation, solution of the flow equation and post-processing of the results) will be described in details with given assumptions, problems encountered, idiosyncrasy of the geometry and other issues faced during this work. In particular, the adopted grid generation approach will be discussed, based on the use of hybrid grids, in order to guarantee an accurate solution of the problem as well as the robustness required when dealing with complex geometries such as the one considered herein.

In this work, we will assess the potential impact that the use of advanced numerical methods can have in the overall prediction of the flow, and bring forward some recommendations related to the application of large eddy and detached eddy simulations on the overall process. We will consider the designed yacht keel appendage from Chalmers Technical University and will investigate the results from global forces and wake flow observation in comparison with the database from Sweden. Other observations not part of the experimental findings such as flow separation, flow transition, pressure distribution will also be mentioned. We will present several numerical investigations based on the influence of critical parameters

linked to the mathematical and numerical models, which are commonly considered as part of a sensitivity analysis of critical factors. We will exhibit how these permutations can influence the results and performance of the models and if some parameters are more beneficial than others. Moreover, there will be a comparison between the turbulence models to find out which one is advantageous and under what circumstances.

Finally, a general discussion will regroup all the findings from the validation cases and the America's Cup keel simulations, lessons from the study will be drawn and taken into account, and conclusions will ensue.

This chapter has briefly presented the approach adopted in this research work. The complete methodology has been outlined in terms of major phases / milestones of the project, beginning with the mapping of the problem solving solution, the modelling approach to the study and, up until the implementation of the CFD to the flow around an America's Cup keel. This has been done to provide an overview and order of the various tasks undertaken in this work to the reader.

"*When you approach a problem, strip yourself of preconceived opinions and prejudice, assemble and learn the facts of the situation, make the decision which seems to you to be the most honest, and then stick to it*"
Chester Bowles

"*Philosophy is a game with objectives and no rules. Mathematics is a game with rules and no objectives*"
Unknown

4 Mathematical Formulation

This chapter introduces the background theory of Computational Fluid Dynamics used in this thesis and the mathematical equations describing fluid flow involved in solving the problem. In the second section, the turbulence models employed for the current study of the flow are detailed.

4.1 Governing Equations of fluid flow

Flow can be defined as laminar or turbulent in nature, depending on the Reynolds number. For engineering applications in naval architecture and marine hydrodynamics, however, most flows are turbulent. The notion of turbulence is defined as the chaotic nature of flow in motion showing random variation in space and time (Pope, 2000). A turbulent flow is characterized by its irregularity, three-dimensionality and dissipative nature.

Turbulence contains eddies with different sizes and scales which are always rotational in motion. Large scale eddies are responsible for the transport of energy and the transfer of momentum in the flow. Smaller scale eddies, where dissipation of energy occurs, are known as the Kolmogorov scale eddies. The larger eddies extract energy from the mean flow and transfer it to the smallest eddies where energy is taken out of the flow through viscosity.

Understanding the dynamics of the flow holds its importance in investigating its influences and impacts on a certain domain, geometry and problem. In order to physically interpret the fluid flow, a series of equations have been developed. The

equations of fluid motion are derived from the fundamental governing equations of fluid dynamics, which represent the conservation laws of physics. These are the continuity, the momentum and the energy equations.

The continuity equation is based on the law of conservation of mass. Applying this concept to fluid flow ensures that the change of mass in a control volume is equal to the mass that enters through its faces minus the total mass leaving its faces.

The momentum equation is based on Newton's Second Law of Motion, expressed in terms of the pressure and viscous stresses acting on a particle in the fluid. This ensures that the rate of change of momentum of the fluid particles is equal to the total force due to surface stresses and body forces acting in an aligned direction of a chosen coordinate axis.

The energy equation is based on the First Law of Thermodynamics: the rate of change of energy of a fluid particle is taken to be equal to the net rate of work done on that particle due to surface forces, heat and body forces such as gravitational force. The energy equation describes the transport of heat energy through a fluid and its effects. For incompressible flows, such as those considered in this thesis, this is not applicable.

Combining these fundamental principles, the physics of fluid flow is expressed in terms of a set of partial differential equations, more commonly known as the Navier-Stokes equations. By solving these equations, the pressure and velocity of the fluid can be predicted throughout the flow. Assuming that the latter is incompressible, the following equations are used to describe the fluid flow:

$$\frac{\partial u_i}{\partial t} + u_j \frac{\partial u_i}{\partial x_j} = -\frac{1}{\rho}\frac{\partial p}{\partial x_i} + \frac{\partial}{\partial x_j}\left(\nu \frac{\partial u_i}{\partial x_j}\right) \tag{4.1}$$

for conservation of momentum and

$$\frac{\partial u_i}{\partial x_j} = 0 \tag{4.2}$$

for conservation of mass,

where u is the velocity in the streamwise direction, p is the pressure, ρ is the fluid density and v is the kinematic viscosity of the flow. The Navier-Stokes equations are usually solved numerically for fluid flow using computers. Advances in computer technology over the past decade have enabled the researcher, engineer and scientist to apply CFD to complex flow field and has become a vital tool in naval architecture.

4.2 Turbulence Modelling and DNS

As mentioned earlier in this chapter, turbulent flow is highly unsteady and irregular, and current available computer power is not yet sufficient to represent all the eddies from the smallest scale corresponding to the dissipative motions, to the largest dimension responsible for most of the momentum transport at high Reynolds Number flows or flows of industrial interest. Hence, turbulence models are employed to describe the turbulence based on some simplified assumptions.

In theory, it is possible to resolve the whole spectrum of turbulence directly using direct numerical simulation (DNS). DNS solves the entire Navier-Stokes equations in the domain, and all the scales of motion in the flow (up to the Kolmogorov scales) without any averaging or approximations, other than the ones implicit within the numerical discretizations. DNS is used for flow simulations, centred mostly on theoretical flows at low Reynolds number such as for example backward facing step (Le et al., 1997), channel flow (Moser et al., 1999) or airfoils (Shan et al., 2005).

Some recent studies of DNS have shifted to naval interest, especially the prediction of cavitation in propeller flow (Hsiao and Chahine, 2004, 2008) and ship breaking waves (Weymouth et al., 2007). However, DNS is computationally intensive and therefore is often not practical for engineering problems at high Reynolds number.

The cost required by DNS to resolve the entire range of scales is proportional to Re_t^3 in terms of time requirements and $Re_t^{9/4}$ in terms of spatial resolution, where Re_t is the turbulent Reynolds number (Blazek, 2001). Clearly, the cost becomes prohibitive unless a considerable amount of computational power is available for generating high-resolution grids at this scale, which is not available yet.

With this in mind, the current study has focused on establishing the level of accuracy achievable by less intensive computational methods, but innovative enough to instil interest to the research in the field of yacht-related fluid dynamics. Hence the decision to use Large Eddy and Detached Eddy Simulation which are described in the following part.

4.3 Large Eddy Simulation

In large eddy simulation (LES) the large(r) three-dimensional unsteady turbulent motions are directly resolved (momentum, energy), while the smaller scale motions are modelled (dissipation, isotropy). LES can be expected to be more accurate and reliable than Reynolds-stress models for flows where large-scale unsteadiness is significant (e.g. highly separated flow); LES thus falls between RANS and DNS in terms of modelling resolution (figure 4.1). Resolving only the large eddies allows LES to use coarser meshes and larger time-steps than in DNS. However, LES still requires substantially finer meshes than those that are typically used for RANS calculations.

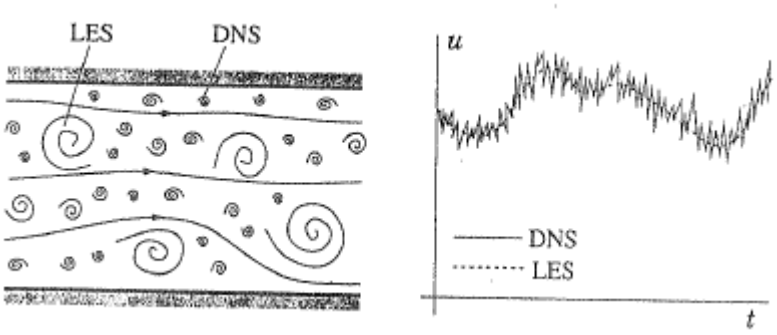

Figure 4. range of eddy sized for LES and DNS (left) and time history for a velocity component at a point (right), from Ferzinger and Peric, 2002

In addition, LES has to run for a sufficiently long flow-time to obtain stable statistics of the flow being modelled. Thus, the computational cost for LES is normally a few orders of magnitude higher than for steady RANS calculations in terms of both RAM and CPU time. Therefore, high-performance parallel computing is required for LES, especially in industrial applications, due to the number of calculations and the size of the required grids to solve for the laminar sublayer.

4.3.1 Filtering of the Navier-Stokes Equations

The governing equations employed for LES are obtained by filtering the time-dependent Navier-Stokes equations in either Fourier (wave number) space or configuration (physical) space. The filtering process removes eddies having scales smaller than the filter width or grid spacing used in the computations. The resulting equations thus govern the dynamics of large eddies.

In LES, the flow velocity U is separated into a filtered, resolved part $\bar{U}$ and a sub-filter, unresolved part, u':

$$U = \bar{U} + u' \tag{4.3}$$

The general filtering operation discretises the flow spatially. The general filtering operation for a variable Φ is denoted by an overbar and is defined by the equation

$$\overline{\Phi}(x) = \int_D \Phi(x')G(x,x')dx' \tag{4.4}$$

where D is the entire fluid domain, G(x, x') is the localized filter function, Φ(x') is the original unfiltered variable and $\bar{\Phi}$ is the filtered variable.

As mentioned, the filter function dictates the large and small scale eddies in the flow (Fluent, 2005). For the current application, a top-hat or box filter function is applied for LES computations:

$$G = \begin{cases} 1/\Delta, \text{if } |x - x'| \le \Delta/2 \\ 0, \text{otherwise} \end{cases} \tag{4.5}$$

The top-hat filter is used in finite volume implementations such as the examples used in the current thesis (finite volume approach will be further discussed in chapter 6). It is the most common and applied filter function in three-dimensional LES computations. Other examples are shown in the Appendices. Filtering the Navier-Stokes equations, and assuming incompressible flow, leads to the filtered equations formulation:

$$\frac{\partial}{\partial x_i}(\overline{u_i}) = 0 \tag{4.6}$$

and

$$\frac{\partial}{\partial t}(\overline{u_i}) + \frac{\partial}{\partial x_j}(\overline{u_i u_j}) = \frac{\partial}{\partial x_j}(\mu \frac{\partial \sigma_{ij}}{\partial x_j}) - \frac{\partial \overline{p}}{\partial x_i} - \frac{\partial \tau_{ij}}{\partial x_j} \tag{4.7}$$

Where μ and p are the fluid's dynamic viscosity and pressure respectively, σ_{ij} is the stress tensor due to molecular viscosity and τ_{ij} is the subgrid-scale stress that represents the interactions between two small scale-eddies, defined by

$$\tau_{ij} = \overline{u_i u_j} - \overline{u_i}\,\overline{u_j} \tag{4.8}$$

4.3.2 Subgrid-Scale Models

The subgrid-scale stresses (SGS) resulting from the filtering operation are unknown, and require modelling. To approximate the SGS Reynolds stress, a SGS model is employed. The SGS turbulence models employ the Boussinesq hypothesis (Boussinesq, 1877), as in the RANS models, and subgrid-scale turbulent stresses are computed from:

$$\tau_{ij} - \frac{1}{3}\tau_{kk}\delta_{ij} = -2\mu_t \overline{S_{ij}} \tag{4.9}$$

where μ_t is the subgrid-scale turbulent dynamic viscosity. The isotropic part of the SGS stresses τ_{kk} is not modelled, but added to the filtered static pressure term. $\overline{S_{ij}}$ is the rate-of-strain tensor for the resolved scale defined by

$$\overline{S_{ij}} = \frac{1}{2(\frac{\partial \overline{u_i}}{\partial x_j} + \frac{\partial \overline{u_j}}{\partial x_i})} \tag{4.10}$$

Various models exist for subgrid-scale (SGS) turbulent viscosity. For the purpose of the present study, the two models of interest were the Smagorinsky-Lilly model (referred to as SM hereafter: (Smagorinsky, 1963 and Lilly, 1967)) and the dynamic Smagorinsky-Lilly model (henceforth referred to as DSM) for comparison. In the SM model, the eddy-viscosity is modelled by

$$\mu_t = \rho L^2{}_S \left|\overline{S}\right| \tag{4.11}$$

where L_S is the mixing length for subgrid scales and $\left|\overline{S}\right| = \sqrt{2\overline{S_{ij}S_{ij}}}$. L_S is computed from

$$L_S = \min(\kappa d, C_S V^{1/3}) \tag{4.12}$$

where κ is the von Kármán constant, d is the distance to the closest wall, C_S is the Smagorinsky constant, taken as a value of 0.1, and V is the volume of the

computational cell. The Smagorinsky SGS model simulates the energy transfer between the large and the subgrid-scale eddies. Energy is transferred from the large to the small scales but backscatter (reverse of cascade process) sometimes occurs where flow becomes highly anisotropic, usually near to the wall.

The Smagorinksy model has been successfully applied to various flows as it is relatively stable and demands less computational resources among other SGS models. However, some disadvantages of the model have been reported (Blazek, 2001, Constantinescu, 2004):

- Too dissipative in laminar regions
- Requires special near wall treatment and laminar turbulent transition
- C_S is not uniquely defined and varies depending on flow type
- Backscatter of flow is not properly modelled

Ferzinger (1993) pointed out that C_S is not constant in a flow and it is a function of the subgrid scale eddies and Reynolds number. The value of C_S varies between 10%-20% depending on the regimes of flow (wall-bounded flow or transition flow) to achieve optimum prediction.

As a way to improve the model, Lilly (1992) and Germano et al. (1996) proposed an approach in which the Smagorinsky model constant, C_S is computed dynamically and locally as a function of time and space, from information provided by the resolved scales of motion. In the dynamic SGS model, another filter is introduced which takes into account of the energy transfer in the dissipation range. The dynamic procedure thus obviates the need for users to specify C_S in advance.

Details of the model implementation in the solver and its validation can be found in Kim (1995). Some of the advantages and disadvantages of the dynamic model over the normal Smagorinsky model are (Ferzinger and Peric, 2002, Constantinescu, 2004):

- Dynamic SGS automatically uses a smaller model parameter in isotropic flows
- Near the wall, the model parameters need to be reduced; the dynamic SGS model adapts these parameters accordingly
- Definition of length scale is always an issue in LES, the dynamic model compensates for the error in length scale by changing the value of the parameters used
- Parameter variation too large
- Variance is ten times the mean
- Produced large negative values of μ_t
- Can be negative for long time, over sizeable region
- Numerical instability

The value of C_S obtained using the Dynamic SM model varies in time and space over a wide range, up to ten times the value of the Smagorinsky constant taken for the previous subgrid-scale model. It is thus know to be more unstable than the SM model.

4.4 Detached Eddy Simulation

Another way to simulate turbulence through advanced modelling is by using the Detached Eddy Simulation method (DES). DES is a modification of a RANS model in which the model switches to a subgrid-scale formulation in regions away from an object for LES calculations. DES employs the RANS models near to the wall and the LES approach in the wake region of a flow where unsteady and chaotic motion of flow is usually found.

Regions near solid boundaries and where the turbulent length scale is less than the maximum grid dimension are assigned the RANS mode of solution. The LES region is normally associated with the core turbulent region where large turbulence scales play a dominant role and unsteady and chaotic motion of flow is usually found. In

this region, the DES models recover the respective subgrid models. In the near-wall region, the respective RANS models are recovered. DES is often referred to as a hybrid LES/RANS approach. The grid resolution is not as demanding as in the pure LES, thereby considerably reducing computational requirements.

Nevertheless, the application of DES may still require significant CPU resources and therefore, as a general guideline, it is recommended that the conventional turbulence models employing the Reynolds-averaged approach be used for practical calculations.

4.4.1 Spalart-Allmaras model

The main DES formulation used in this paper is based on a modification to the Spalart-Allmaras model, the so-called one-equation DES model, (Spalart and Allmaras, 1994), such that it reduces to its RANS formulation close to the wall, while using LES in other regions of the flow (Spalart et al., 1997). The one-equation model is computationally undemanding compared to other more complex RANS models. The model bears the name of its conceiver (Spalart, 2000).

In the Spalart-Allmaras RANS model, a transport equation is used to compute a working variable used to form the turbulent eddy viscosity:

$$\begin{aligned}\frac{D\tilde{\nu}}{Dt} &= C_{b1}\left[1-f_{t2}\right]\tilde{S}\tilde{\nu}-\left[C_{w1}f_w-\frac{C_{b1}}{\kappa^2}f_{t2}\right]\left[\frac{\tilde{\nu}}{d}\right]^2 \\ &+\frac{1}{\sigma}\left[\nabla\cdot\left(\left(\nu+\tilde{\nu}\right)\nabla\tilde{\nu}\right)+C_{b2}(\nabla\tilde{\nu})^2\right] \\ &+f_{t1}\Delta U^2\end{aligned} \tag{4.13}$$

where $\tilde{\nu}$ is the working variable, C_{b1}, C_{b2}, C_{w1} and κ are model constants.

The standard Spalart-Allmaras model uses the distance to the closest wall as the definition for the length scale, d, which plays a major role in determining the level of production and destruction of turbulent viscosity. The DES model, as proposed by

Shur et al. (1999) and used in the paper, replaces *d* everywhere with a new length scale, $\tilde{d}$, to dictate which approach to use during a simulation, defined as:

$$\tilde{d} = \min(d, C_{des}\Delta) \tag{4.14}$$

where the local grid spacing, *Δ*, is based on the largest grid space in the x, y or z directions forming the computational cell. If the turbulent length scale is greater than the grid spacing, which is common in regions with large eddies and chaotic flow nature, LES is activated in the DES formulation. The empirical constant C_{des} has a value of 0.65.

4.4.2 Realizable κ-ε model

Though DES was initially formulated for the Spalart-Allmaras model, it can be implemented with other RANS models, by appropriately modifying the length scale, which is explicitly or implicitly involved in the RANS model. Therefore, while the Spalart-Allmaras model based on DES acts as a LES with a wall model, DES methods based on two-equation models behave as a hybrid RANS-LES model.
Such a case is that of the 'Realizable' κ-ε model. This RANS model is similar to the well-known Realizable κ-ε model with the exception of the dissipation term in the κ equation. In the DES model, the Realizable κ-ε RANS dissipation term is modified such that

$$Y_k = \frac{\rho\kappa^{3/2}}{l_{des}} \tag{4.15}$$

where

$$l_{des} = \min(l_{rke}, l_{les}) \tag{4.16}$$

$$l_{rke} = \frac{k^{3/2}}{\varepsilon} \tag{4.17}$$

$$l_{les} = C_{des}\Delta \tag{4.18}$$

where C_{des} is a calibration constant used in the DES model and has a value of 0.61 and Δ is the maximum local grid spacing ($\Delta x, \Delta y, \Delta z$). For the case where $l_{des} = l_{rke}$, one obtains the expression

$$Y_k = \rho\varepsilon \tag{4.18}$$

The background of computational fluid dynamics, turbulent flow and the mathematical aspects of the numerical simulation discussed in this chapter provide the reader with basic knowledge for understanding the simulated results presented later in the thesis. This chapter also presented the turbulence models used for the current work, and the sub-grid model associated with them.

The following chapter explains the numerical method, the schemes and algorithms associated with the use of LES and DES and applied to the solver.

"*The usual approach of science of constructing a mathematical model cannot answer the questions of why there should be a universe for the model to describe. Why does the universe go to all the bother of existing?*"
Stephen Hawking

"*I believe that the brain has evolved over millions of years to be responsive to different kinds of content in the world. Language content, musical content, spatial content, numerical content, etc*"
Howard Gardner

5 Numerical Solution

Following the description of the mathematical model, the author's attention is turned on the numerical models involved in the CFD calculations. The objective of this chapter is to present the numerical schemes that are used in the simulations. The following paragraphs will cover the algorithms, the discretization of the method, the coupling between the flow variables that are part of the problem and that are used for the application and the solution of fluid flow problem, in relation to LES and DES, in the present thesis. The chapter will end with an explanation of the near-wall approach to turbulent flow and the parallel computational approach of the solver.

5.1 Solver Algorithm and Solution Method

The numerical model described in this chapter is the one implemented in the commercial software Fluent 6.2.36, a general-purpose CFD code that has been used to address a wide range of problems in fluid mechanics. The solver uses a finite volume method (FVM) to formulate the solution of the governing equations. The algorithm consists of three parts (Versteeg and Malalasekera, 2007):

- Formal integration of the governing equations of fluid flow over each and all of the finite control volumes of the solution domain
- Discretization involving the substitution of a variety of approximations for the terms in the integrated equation representing flow processes such as convection, diffusion and sources. This converts the integral equations into a system of algebraic equations
- Solution of the algebraic equations by an iterative method

The numerical algorithm applied is the pressure-based solver. In the past, this solver was initially developed for low-speed incompressible flows, as opposed to the density-based solver, which was used for high-speed compressible flows (above Mach number). Since then, both methods have been adapted and reformulated to operate on a wide range of flow conditions outwith their original configuration.

In the pressure-based algorithm, the pressure field is obtained from the equation of state by solving a pressure or pressure correction equation (Poisson equation). The velocity fields are obtained from the momentum equations. Equations for the conservation of mass, momentum, and other scalars (e.g. turbulence) are solved using the control-volume approach implemented in Fluent that consists of:

- Division of the domain into discrete control volumes using a computational grid
- Integration of the governing equations on the individual control volumes to construct algebraic equations for the discrete dependent variables ("unknowns") such as velocities, pressure, temperature, and conserved scalars
- Linearization of the discretized equations and solution of the resultant linear equation system to yield updated values of the dependent variables

The governing equations of fluid flow are solved separately from each other. Two different pressured-based variants can be distinguished: the segregated and the coupled algorithm. In the current thesis, a segregated approach is used.

In the pressure-based segregated algorithm, the governing equations are solved sequentially, all solution variables one after another, because they are non-linear, in an iteratively way. This procedure makes the solution convergence process relatively slow. It consists of the following steps:

- Fluid properties are updated. Solution is initialised at first iteration
- The x-, y- and z- momentum equations are each solved using current values for pressure and face mass fluxes, in order to update the velocity field

- Since the velocities obtained in step 2 may not satisfy the continuity equation locally, a Poisson equation for the pressure correction is derived from the continuity equation and the linearized momentum equations. This pressure correction equation is then solved to obtain the necessary corrections to the pressure and velocity fields and the face mass fluxes such that continuity is satisfied
- Equations for scalars, turbulence are solved using the previously updated values of the other variables
- Convergence is checked. If successful, the solution ends. If not, the solution method restarts from step 1 and a loop is reinitiated.

On the other hand, the coupled algorithm solves a coupled system of equations implying the momentum equations and the pressure-based continuity equation. All the other equations are solved in a decoupled manner similar to the segregated method. The solution convergence is improved and the process is accelerated.

5.2 Discretization

5.2.1 Scalar-transport equation

A control-volume based technique is used to convert the governing general scalar transport equation to an algebraic equation that can be solved numerically. This consists of integrating the governing equations about each control-volume. It results in discrete equations that conserve each quantity on a control-volume basis.

Discretization of the governing equations can be illustrated most easily by considering the unsteady conservation equation for transport of a scalar quantity ϕ. This is demonstrated by the following equation written in integral form for an arbitrary control volume V as follows:

$$\int_V \frac{\partial \rho \phi}{\partial t} dV + \oint \rho \phi \vec{v} \cdot d\vec{A} = \oint \Gamma_\phi \nabla \phi \cdot d\vec{A} + \int_V S_\phi dV \tag{5.1}$$

where: ρ is the density of fluid, v is the velocity vector, A is the surface area vector, Γ_ϕ is the diffusion coefficient for ϕ and S_ϕ is the source of ϕ per unit volume.

Equation (5.1) above is then discretized and gives the following equation on any given cell:

$$\frac{\partial \rho \phi}{\partial t} dV + \sum_f^{N_{faces}} \rho_f \vec{v}_f \phi_f \cdot \vec{A}_f = \sum_f^{N_{faces}} \Gamma_\phi \nabla_{\phi f} \cdot \vec{A}_f + S_\phi V \tag{5.2}$$

where: N_{faces} is the number of faces enclosing the cell (or control-volume), ϕ_f is the value of ϕ convected through face f, $\rho_f v_f$ is the mass flux through the face, A_f is the face area vector in 3D, $\nabla_{\phi f}$ is the gradient of ϕ at face f and V is the cell volume. The diffusion terms are central-differenced and are always second-order accurate.

The discretized scalar transport equation contains the unknown scalar variable ϕ at the cell centre as well as the unknown values in surrounding neighbour cells. This equation will, in general, be non-linear with respect to these variables. A linearized form of equation (5.2) can be written as:

$$a_p \phi = \sum_{nb} a_{nb} \phi_{nb} + b \tag{5.3}$$

where: the subscript nb refers to neighbour cells and a_p and a_{nb} are the linearized coefficients for ϕ and ϕ_{nb}.

5.2.2 Discretization in Space (Spatial)

The discrete values of the scalar ϕ are typically stored at the cell centres. Conversely, face values ϕ_f are required for the convection terms in equation (5.2) and must be

interpolated from the cell centre values. This is accomplished using an upwind scheme.

Upwinding means that the face value ϕ_f is derived from quantities in the cell upstream, or "upwind", relative to the direction of the normal velocity v_n in equation (5.2). The use of LES and DES imply the application of high-order upwind schemes for the simulation, which are described in the current section.

5.2.2.1 Second-Order Upwind Scheme for DES

First order schemes are normally very stable, but they also tend to become prone to numerical diffusion errors. Such errors can be avoided by introducing a higher, second-order upwind discretization which involves the multidimensional linear reconstruction approach proposed by Barth and Jespersen (1989). In this approach, higher-order accuracy is achieved at cell faces through a Taylor series expansion of the cell-centred solution about the cell centroid. Thus when second-order upwinding is selected, the face value ϕ_f is computed using the following expression:

$$\phi_{f,SOU} = \phi + \nabla\phi \cdot \vec{r} \tag{5.4}$$

where: SOU means second-order upwind, ϕ and $\nabla\phi$ are the cell-centred value and its gradient in the upstream cell, and $\vec{r}$ is the displacement vector from the upstream cell centroid to the face centroid. This formulation requires the determination of the gradient in each cell, which is discussed in details further down in the chapter.

6.3.2.2 Bounded Central-Differencing Scheme for LES

A second-order-accurate central-differencing discretization scheme is available for the momentum equations and preferred when using the LES turbulence model. This scheme provides improved accuracy for LES calculations.

The central-differencing scheme calculates the face value for a variable ϕ_f as such:

$$\phi_{f,CD} = \frac{\phi_0 + \phi_1}{2} + \frac{\nabla\phi_0 \cdot \vec{r}_0 + \nabla\phi_1 \cdot \vec{r}_1}{2} \tag{5.5}$$

where: the indices *0* and *1* refer to the cells that share the common face *f*, $\nabla\phi_0$ and $\nabla\phi_1$ are the reconstructed gradients at the cells and *r* is the vector directed from the cell centroid toward the face centroid.

Central-differencing schemes can produce unbounded solutions that can lead to stability problems for the numerical procedure. These stability problems can often be avoided by using a deferred approach for the algorithm. In this approach, the face value is calculated as:

$$\phi_f = \phi_{f,UP} + (\phi_{f,CD} - \phi_{f,UP}) \tag{5.6}$$

where: UP stands for upwind and CD for Central-Differencing. The upwind part is treated implicitly while the difference between the central-difference and upwind values is treated explicitly. If the numerical solution converges, this approach leads to pure second-order differencing.

The central differencing scheme is a suited choice for LES in view of its low numerical diffusion. However, it often leads to unphysical oscillations in the solution fields. In LES, the situation is exacerbated by usually very low subgrid-scale turbulent diffusivity. Hence, a more robust version is applicable to remediate with this issue.

The bounded central-differencing scheme is based on the normalized variable diagram approach by Leonard, 1991, in conjunction with a convection boundedness criterion. The bounded central differencing scheme is a composite scheme that

consists of a pure central differencing, a blended scheme of the central differencing and the second-order upwind scheme, and the first-order upwind scheme. The first-order scheme is used only when the CBC is violated.

5.2.3 Discretization in Time (Temporal)

For unsteady simulations, the governing equations must be discretized in both space and time. Temporal discretization involves the integration of every term in the differential equations over a time step *Δt*. The integration of the transient terms is shown below.

A generic expression for the time evolution of a variable ϕ is given by:

$$\frac{\partial \phi}{\partial \mathrm{t}} = \mathrm{F}(\phi) \tag{5.7}$$

where: the function *F* comprises any spatial discretization. The first-order accurate temporal discretization is given by:

$$\frac{\phi^{\mathrm{n+1}} - \phi^{\mathrm{n}}}{\Delta \mathrm{t}} = \mathrm{F}(\phi) \tag{5.8}$$

and the second-order is given by:

$$\frac{3\phi^{\mathrm{n+1}} - 4\phi^{\mathrm{n}} + \phi^{\mathrm{n-1}}}{2\Delta \mathrm{t}} = \mathrm{F}(\phi) \tag{5.9}$$

where: ϕ is the scalar quantity, *n+1* is the value at the next time level *t+Δt*, *n* is the value at the current time level *t* and *n-1* is the value at the previous time level, *t-Δt*. Second-order is used for the needs of the thesis.

When the time derivative has been discretized, F(ϕ) can be evaluated by using a future time level with implicit time integration:

$$\frac{\phi^{n+1}-\phi^{n}}{\Delta t} = F(\phi^{n+1}) \tag{5.10}$$

This is referred to as "implicit" integration since ϕ^{n+1} in a given cell is related to ϕ^{n+1} in neighbouring cells through $F(\phi^{n+1})$:

$$\phi^{n+1} = \phi^{n} + \Delta t F(\phi^{n+1}) \tag{5.11}$$

This stable approach can be solved iteratively at each time level before moving to the next time step. The advantage of the fully implicit scheme is that it is unconditionally stable with respect to time step size.

5.2.4 Gradients and Derivatives

Gradients are used to compute values of a scalar at a cell's faces. In addition, gradients such as $\nabla\phi$ can also be used for the calculation of secondary diffusion terms and velocity derivatives. The following two methods are considered in this thesis for the various simulations:

- Green-Gauss Cell-Based
- Green-Gauss Node-Based

Using the Green-Gauss theorem the gradient of the scalar ϕ at the cell centre c_0 can be written as follows:

$$(\nabla\phi)_{c0} = \frac{1}{\nu}\sum_{f}\bar{\phi}_{f}\vec{A}_{f} \tag{5.12}$$

where ϕ_f is the value of ϕ at the cell face centroid

The Green-Gauss Cell-Based approach enables the method where cell centre values are considered for computing the gradient. The face value is taken from the arithmetic average of the values at neighbouring cell centres; this method is usually chosen for structured grids and is considered for the airfoil simulations:

$$\bar{\phi}_f = \frac{\phi_{c0} + \phi_{c1}}{2} \tag{5.13}$$

On the other hand, the Green-Gauss Node-Based enables the face value to be calculated by the arithmetic average of the nodal values on the face; this method is preferred when using unstructured or hybrid meshes, such as the ones dealt in this thesis for the spheroid and the keel simulations:

$$\bar{\phi}_f = \frac{1}{N_f} \sum_{n}^{N_f} \bar{\phi}_n \tag{5.14}$$

Where N_f is the number of nodes on the face

5.2.5 Discretization of the Momentum Equation

The discretization of the momentum equation can be obtained by using the schemes introduced earlier in the chapter. The equation in its general form is expressed as:

$$a_p \phi = \sum_{nb} a_{nb} \phi_{nb} + \sum p_f A \cdot \hat{i} + S \tag{5.15}$$

The pressure field and face mass fluxes are not known, a priori, and must be obtained as a part of the solution by using a pressure interpolation scheme, to compute the face values of pressure from the cell values. The scheme interpolates the values at the faces using momentum equation coefficients outlined by Rhie and Chow (1983):

$$P_f = \frac{\frac{P_{c0}}{a_{p,c0}} + \frac{P_{c1}}{a_{p,c1}}}{\frac{1}{a_{p,c0}} + \frac{1}{a_{p,c1}}} \tag{5.16}$$

Standard pressure interpolation scheme method works well with a consistent pressure variation between cell centres and cannot be used on momentum terms with jumps or large gradients which can cause high pressure gradients at the cell faces. If this scheme is used, the discrepancy shows up in overshoots and undershoots of cell velocity. Standard scheme is used for the large eddy simulation computations for all case studies.

When this becomes an issue, a higher scheme is applied for the pressure interpolation. The PRESTO! (Pressure Staggering Option) scheme uses the discrete continuity balance for a "staggered" control volume about the face to compute the "staggered" (i.e., face) pressure. This procedure is similar in spirit to the staggered-grid schemes used with structured meshes (Patankar, 1980). The PRESTO! scheme is available for all meshes and makes it more reliable than standard scheme for more complex problems. This was used for the detached eddy simulation runs.

5.2.6 Discretization of the Continuity Equation

The equation of the steady-state continuity integrated over a control volume will give the following:

$$\sum_{f}^{N_{faces}} J_f A_f = 0 \tag{5.17}$$

where: J_f is the mass flux through face *f*. the face values of velocity must be related to the stored values of velocity at the cell centres. A linear interpolation of the cell-centre velocities to the face centroids by a momentum-weighted averaging algorithm is introduced, using weighting factors based on the a_p coefficients from equation (5.15). Using this procedure J_f can be written as:

$$J_f = \rho_f \frac{a_{p,c0} v_{n,c0} + a_{p,c1} v_{n,c1}}{a_{p,c0} + a_{p,c1}} + d_f ((p_{c0} + (\nabla p)_{c0} \cdot \vec{r}_0) - (p_{c1} + (\nabla p)_{c1} \cdot \vec{r}_1)) = \hat{J}_f + d_f (p_{c0} - p_{c1}) \quad (5.18)$$

where: p_{c0}, p_{c1} and $v_{n,c0}$, $v_{n,c1}$ are the pressures and normal velocities, respectively, within two cells on either side of the face; $\hat{J}_f$ contains the influence of velocities in these cells and d_f is a function of the average of the momentum equation coefficient a_p for the cells on either side of face *f*.

5.3 Pressure - Velocity Coupling

Pressure-velocity coupling is achieved by using Equation (5.18) to derive an additional condition for pressure, by reformatting the continuity equation (5.17). As mentioned earlier, the pressure-based solver used in this thesis solves the flow in a segregated way; hence, several pressure-velocity couplings algorithms, which are described in this section, can be applied.

5.3.1 SIMPLEC Algorithm

The SIMPLE-Consistent algorithm is a variant of the basic SIMPLE scheme available in the solver. The Semi-Implicit Method for Pressure-Linked Equations algorithm was developed by Caretto et al. (1972) and uses a relationship between velocity and pressure corrections to enforce mass conservation, update the velocities and obtain the pressure field. The resulting face flux from equation (5.18) above does not satisfy the continuity equation if the momentum equation is solved with a presumed pressure field *p**:

$$J_f^* = \hat{J}_f^* + d_f (p_{c0}^* - p_{c1}^*) \quad (5.19)$$

Consequently, a correction term $J_f^{'}$ is added to the face flux so that the corrected face flux, J_f satisfies the continuity equation:

$$J_f = J_f^* + J_f^{'} \tag{5.20}$$

The SIMPLE algorithm then proposes that $J_f^{'}$ is to be written as:

$$J_f^{'} = d_f (p_{c0}^{'} - p_{c1}^{'}) \tag{5.21}$$

where: *p'* is the cell pressure correction. The SIMPLE algorithm then substitutes the flux correction equations (5.20) and (5.21) into the discrete continuity equation (5.17) to obtain the equation for the pressure correction *p'* in the cell:

$$a_p p' = \sum_{nb} a_{nb} p_{nb}^{'} + b \tag{5.22}$$

where: b is the net flow rate into the cell, defined as:

$$b = \sum_{f}^{N_{faces}} J_f^* A_f \tag{5.23}$$

The pressure-correction equation (5.22) can then be solved by using the algebraic multigrid (AMG) method, described later in the chapter. Therefore, a solution is obtained, and the cell pressure and the face flux are corrected using:

$$p = p^* + \alpha_p p' \tag{5.24}$$

$$J_f = J_f^* + d_f (p_{c0}^{'} - p_{c1}^{'}) \tag{5.25}$$

where: α_p is the under-relaxation factor for pressure. The corrected face flux, J_f, satisfies the discrete continuity equation identically during each iteration. In the

SIMPLEC procedure developed by Vandoormaal and Raithby (1984), the SIMPLE procedure outlined above is used but the expression employed for the face flux correction, $J_f^{'}$ is different. The correction equation (5.25) remains the same but the coefficient d_f is redefined as a function of $[\overline{a_p - \sum_{nb} a_{nb}}]$. The SIMPLEC algorithm is known to accelerate convergence in problems where pressure-velocity coupling is causing issues in obtaining a solution. It is also the preferred method for LES-based simulations.

In addition, a skewness correction factor is also introduced for further helping convergence in some meshes. For grids with some degree of skewness, the approximate relationship between the correction of mass flux at the cell face and the difference of the pressure corrections at the adjacent cells is coarse. Since the components of the pressure-correction gradient along the cell faces are not known in advance, an iterative process is desirable. After the initial solution of the pressure-correction equation, the pressure-correction gradient is recalculated and used to update the mass flux corrections. This process significantly reduces convergence difficulties associated with highly distorted meshes. The skewness correction allows the solver to obtain a solution on a highly skewed mesh in approximately the same number of iterations as required for a more orthogonal mesh.

5.3.2 PISO Algorithm

The Pressure-Implicit with Splitting of Operators (PISO) scheme, part of the SIMPLE family of algorithms, is based on the higher degree of the approximate relation between the corrections for pressure and velocity. One of the limitations of the SIMPLEC algorithm is that new velocities and corresponding fluxes do not satisfy the momentum balance after the pressure-correction equation is solved. As a result, the calculation must be repeated until the balance is satisfied. To improve the efficiency of this calculation, the PISO algorithm performs an additional adjustment on top of the skewness correction: the neighbour correction.

The main idea of the PISO algorithm, introduced by Issa (1986) is to move the repeated calculations required by SIMPLEC inside the solution stage of the pressure-correction equation. After one or more additional PISO loops, the corrected velocities satisfy the continuity and momentum equations more precisely. This iterative process is called a momentum or neighbour correction. The PISO algorithm takes a little more CPU time per solver iteration, but it can decrease the number of iterations required for convergence, especially for transient problems.

5.4 Linearization & Under-Relaxation

For the iterative solution of the linearized equations, a point implicit, Gauss-Seidel linear equation solver is used in conjunction with an algebraic multigrid (AMG) method to solve the resultant scalar system of equations for the dependent variable in each cell.

The multigrid scheme accelerates the convergence of the solver by computing corrections on a series of coarse grid levels then fed into finer grid. The use of this multigrid scheme can greatly reduce the number of iterations and the CPU time required to obtain a converged solution, particularly when the model contains a large number of control volumes.

Considering the set of linearized equations given by:

$$\mathrm{A}\phi_{\mathrm{e}} + \mathrm{b} = 0 \tag{5.26}$$

where: ϕ_{e} is the exact solution, valid when the problem is converged. Before the solution has converged, there will be a defect *d* associated with the approximate solution ϕ:

$$\mathrm{A}\phi + \mathrm{b} = \mathrm{d} \tag{5.27}$$

The exact solution is given by:

$$\phi_e = \phi + \psi \tag{5.28}$$

where: ψ is the correction to ϕ. Substituting equation (5.28) into equation (5.26) and using equation (5.27) gives:

$$A\psi + (A\phi + b) = A\psi + d \tag{5.29}$$

This is an equation for the correction in terms of the original fine level operator *A* and the defect *d*. Assuming the local (high-frequency) errors have been sufficiently damped by the relaxation scheme on the fine level, the correction ψ will be smooth and therefore more effectively solved on the next coarser level.

Using the AMG method, the coarse level equations are generated without the use of any geometry or re-discretization on the coarse levels. No coarse grid is constructed or stored and no fluxes or source terms need to be evaluated on the coarse level. Once the system is linearized, the solver does not "feel" non-linearities until the fine level operator is next updated.

The pressure-based solver uses under-relaxation of equations to control the update of computed variables at each iteration. This means that all equations solved using the pressure-based solver will have under-relaxation factors associated with them.

The default under-relaxation parameters for all variables are set to values that are near optimal for the largest possible number of cases. These values are suitable for many problems, but for some particularly nonlinear problems (e.g., some turbulent flows or high Rayleigh number natural convection problems) it is prudent to reduce the under-relaxation factors initially.

The under-relaxation of variables is used because of the nonlinearity of the equation set being solved by the solver, and it is necessary to control the change of ϕ during

each iteration. The new value of the variable ϕ within a cell depends upon the old value, ϕ_{old}, the computed change $\Delta\phi$, and the under-relaxation factor, α, as such:

$$\phi = \phi_{old} + \alpha\Delta\phi \tag{5.30}$$

The under-relaxation of equations is used in the pressure-based solver to stabilize the convergence behaviour of the nonlinear iterations by introducing selective amounts of ϕ in the system of discretized equations:

$$\frac{a_p\phi}{\alpha} = \sum_{nb} a_{nb}\phi_{nb} + b + \frac{1-\alpha}{\alpha} a_p\phi_{old} \tag{5.31}$$

The Courant-Friedrichs-Lewy number (CFL) is a solution parameter in the pressure-based coupled algorithm and can be written in terms of α:

$$\frac{1-\alpha}{\alpha} = \frac{1}{CFL} \tag{5.32}$$

The dimensionless CFL number is defined as:

$$CFL = \frac{\upsilon \cdot \Delta t}{\Delta x} \tag{5.33}$$

where: υ is the velocity, Δt is the time step and Δx is the smallest length interval of the grid.

5.5 Near-Wall Approach to Turbulence

Turbulent flows are significantly influenced by the presence of walls. The mean velocity field is affected through the no-slip condition that has to be satisfied at the

wall. However, the turbulence is also changed by the presence of the wall in non-trivial ways. As the flow approaches near to the wall, it is influenced by viscous effects and does not depend anymore on the free stream parameters. The mean flow velocity only depends on the distance y from the wall, fluid density, ρ and viscosity ν and the wall shear stress τ_w.

The boundary layer of the near-wall region can be subdivided into two main regions: the inner layer and the outer layer. Within the inner layer, three other zones dominate the near-wall:

Firstly, there is the viscous sub-layer, which corresponds to the innermost layer, i.e. the fluid level in contact with the wall. In this region the flow is behaving in almost a laminar way, with the viscous effects dominating the momentum and mass transfer. The viscous sub-layer is in practice extremely thin ($y^+<5$) and assumes that the shear stress is approximately constant and equal to the wall shear stress τ_w. In the viscous sub-layer, the following relation is valid:

$$u^+ = y^+ \tag{5.34}$$

where: u^+ stands for the non-dimensional velocity of the wall-bounded flow and y^+ is the non-dimensional wall distance near the wall-bounded flow. The two are defined in the following way:

$$u^+ \equiv \frac{U}{u_\tau} \tag{5.35}$$

$$y^+ \equiv \frac{u_\tau y}{\nu} \tag{5.36}$$

where: U is the local velocity, u_τ is the friction velocity close to the wall, y is the distance to the wall and ν is the kinematic velocity of the fluid. The friction velocity is defined as:

$$u_\tau \equiv \sqrt{\tau_w / \rho_w} \tag{5.37}$$

where: τ_w is the wall shear stress and ρ_w is the density of the fluid at the wall (assumed to be equal to the density of the fluid since it is constant). Because of the linear relationship between velocity and distance from the wall the fluid layer adjacent to the wall is also known as the linear sub-layer.

Secondly, there is the buffer layer, or blending/intermediate region. In this zone, viscous and turbulent stresses are of similar magnitude. This corresponds to values of the dimensionless wall distance of: $5 < y^+ \leq 30$.

Thirdly, there is the log-law region, which corresponds to the fully turbulent region close to a smooth wall. In this area viscous effects tend to diminish in front of the turbulent effects which start to dominate. The shear stress varies slowly with distance from the wall, and within this inner region, it is assumed constant and equal to the wall shear stress. The relationship between u+ and y+ in the log layer can be estimated with the log law (also called law-of-the-wall):

$$u^+ = \frac{1}{\kappa} \ln(E y^+) \tag{5.38}$$

where: κ is the Von Kármán constant, equal to approx 0.42 and E and empirical constant equal to approx 9.8. The values of κ and E are universal constants valid for all turbulent flows past smooth walls at high Reynolds number.

The logarithmic law of equation (6.34) is valid for $y^+ > \sim 30$ and in the Fluent solver, it is employed when $y^+ \geq 11.225$. When the mesh is such that $y^+ < 11.225$ at the wall adjacent cells, Fluent applies the laminar sub-layer relationship of equation (6.30).

Finally, there is the outer layer, which corresponds to the fully turbulent layer, the inertia-dominated region far from the wall. The lower limit of the outer layer is dependent upon the Reynolds number. For larger values of *y*, the velocity-defect law

provides the correct form. In the overlap region the log-law and velocity-defect law have to equal and overlap is obtained by assuming the following logarithmic form:

$$\frac{U_{max} - U}{u_\tau} = -\frac{1}{\kappa}\ln(\frac{y}{\delta}) + A \tag{5.39}$$

where: A is a constant, δ is the boundary layer thickness. The velocity-defect law is often called the law of the wake. It is applicable when values of y^+ exceed 500; such values of y^+ are not achieved in this thesis since it would not be permissible with LES and DES where values of the near-wall distance must be as small as possible to resolve for the viscous sub-layer.

5.6 Parallel approach

The numerical simulations that are presented in the following chapters have been carried out with the numerical schemes introduced on computational grids of large sizes (up to 4.2 million elements). In a node-centred finite volume approach, the solution of the Reynolds Averaged Navier–Stokes equations coupled with the Finite Volume, and the LES and DES turbulence models comprises of a number of variables (three velocity components, pressure, continuity and turbulence) which are defined as piecewise constant on each grid element. This means that the discrete problems solved in the larger simulations performed involve millions of unknowns.

The solution of such large-scale problems demands for a parallel implementation of the numerical method. In the Fluent solver, parallelism is based on a domain decomposition technique. The computational grid is decomposed in a number of partitions corresponding to the number of processors on which the simulation will be carried out. In order to minimize communication between processors, optimal surface-volume ratios are achieved using the Metis graph-partitioning scheme. The number of processors to use should ideally be chosen according to the size of the simulation; however, limitations imposed by the computing facilities of the Faculty of Engineering, University of Strathclyde did not allow for maximum usage of the

available nodes, hence possibly minimizing the impact or efficiency of parallel processing on the problem.

Once the partition of the grid has been performed, a host process assigns each division to one processor. Each processor simultaneously executes the same operation on its own data and is connected virtually to the other processors through a communicator. The communicator, based on a message passing interface (MPI) system, is devoted to the exchange of boundary information between partitions as well as to keep the synchronization between processors.

The simulations have been carried out on different computer systems:

- An Intel® Core 2 Duo CPU of 3.00 GHz with 2 GB of RAM
- A Linux Cluster with 8 AMD Opteron Dual Core of 2.0 GHz and with 32Gb of RAM
- Intel Xeon 2 CPUs with eight cores, 24 GB Ram capacity and of processing power equal to 3.2 GHz.

The numerical methods used to simulate the flow with CFD and to assist the mathematical models of LES and DES have been presented in this chapter. The pressure-based solver algorithm was discussed and explained, followed by the discretization schemes and the pressure-velocity coupling algorithms. Furthermore, a presentation of the treatment of near-wall turbulent flow was reviewed. Finally, reference to parallel processing was made. In the following chapter, the validation test cases of a NACA foil and a spheroid shaped object are presented.

"*I regard it in fact as the great advantage of the mathematical technique that it allows us to describe, by means of algebraic equations, the general character of a pattern even where we are ignorant of the numerical values which will determine its particular manifestation*"
Friedrich August von Hayek

"*Thinking is easy, acting is difficult, and to put one's thoughts into action is the most difficult thing in the world.*" **Johann Wolfgang von Goethe**

6 Case Studies: Implementation

The physical, mathematical and numerical background introduced in the previous chapters are used to carry out the simulations on two sets of case studies for validation. The current chapter describes the implementation of the methods and techniques and gives information about the procedure and set-up of the simulations.

The two case studies chosen are the flow around a NACA 0012 section and the flow around a 6:1 prolate spheroid at angles of attack. The basic structure of the CFD routine applied to both cases (and to the simulations of the yacht keel introduced later in the thesis) is presented in the flow chart of figure 6.1 below. The CFD analysis passes through the basic steps shown in the chart. The steps and the structure of the CFD modelling will be discussed in the following sections of this chapter for each case study.

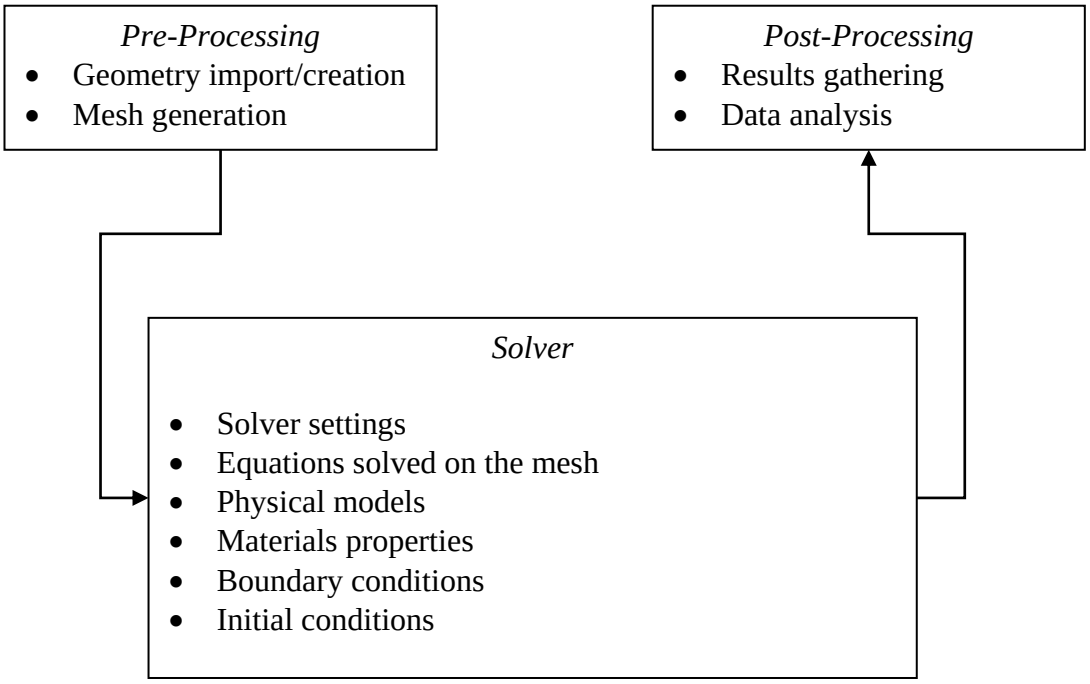

Figure 6.: Structure of the CFD modelling

6.1 Case 1: NACA 0012 Foil

6.1.1 Contextual Backdrop/Overview

The NACA 0012 is amongst the most used foil sections and numerous tests have been perfomed on them, originally in wind tunnel experiments then by using CFD codes, often as a benchmark for validation. It belongs to the symmetric NACA 00xx series foils.

Although the NACA sections were initially developed for aeronautical and flight purposes, their application in the marine field is with no discussion as valid as applying it to an airplane. The use of symmetric foils is abundantly made in rudders, deep fin keels and blades, thus providing the desired characteristics for lift and drag especially on sailing yachts but also in renewable energy applications. The NACA 0012 section offers a maximum thickness ratio of 12% for a keel and/or a rudder section for efficient under water performance.
The geometry is known to have low drag at zero angles of attack equivalent to downwind sailing and will generate high lift equally well with negative or positive angles of incidence in upwind sailing.

Flow past a NACA section foil has been the subject of both experimental and numerical studies for decades. Most of the work performed on airfoils is based on supersonic flow theory. In the present case, however, the NACA 0012 is run in an incompressible, low-speed (i.e. subsonic) condition, with inlet velocities well below Mach number. This is in concordance with the experiments used for our validation and introduced in the following sections, so the assumption is reasonably correct.

6.1.2 Computational details and model geometry

To determine the prediction robustness of the code and the method, two sets of experimental data are investigated and used for validation, focussing on the flow around the NACA 0012 at various angles of attack and Reynolds numbers. For the first case, the Reynolds number based on the chord length and freestream velocity is equal to 2.88 Million, which corresponds to the experimental measurements from

Gregory and O'Reilly, 1970. Their main interest was in recording surface pressure but they also recorded lift and drag values for several Reynolds numbers.
For the second set of simulations, the work from Ladson, 1988, is considered, where measurements based on Reynolds numbers ranging from 0.7 to 6 million of lift and drag coefficients are reported. Both cases are considered incompressible, making them a suitable application for investigation herein. In the latter report, the simulations were performed for both fully turbulent and tripped flow conditions, depending on the Reynolds number the authors investigated. One of the assumptions for the current work is the use of fully turbulent flow only for the CFD simulations.

The geometry was imported as a set of vertices defining the shape of the airfoil into the meshing software GAMBIT. The tip of the profile was modified to come to a same end vertex, to facilitate the mesh creation and avoid small edges and high-clustered cells during meshing. There was no transition set between laminar and turbulent flow on the surface of the airfoil (no tripped conditions).

The conditions investigated are ranging from low to high lift conditions. The challenge for each case is associated with the high Reynolds numbers encountered and the flow regimes around the airfoil. As the angle of incidence increases, flow separation occurs on the trailing edge and there is unsteadiness in the flow near the stall condition. Boundary layers are expected to be fully turbulent over parts of the airfoil. Both cases help towards estimating the capability of LES and DES for simple shape at Reynolds number equivalent to those found in yacht hydrodynamics applications.

The numerical solution of the flow is obtained using the commercial CFD code FLUENT. In the 3D code, discretization is done based on a finite-volume approach. In the tables 6.1 and 6.2, the various CFD settings, schemes and parameters introduced in the previous chapter are summarized as applied selected for the simulations of the current airfoil flow. The residuals convergence criteria considered was 1.0×10^{-5} for these runs.

Table 6.: Simulation set-up for flow around airfoil with LES model

Parameter	***Setting***
Solver	Pressure-based Implicit
Temporal discretization	2nd Order
Pressure-Velocity coupling	SIMPLE-C
Pressure	Standard
Momentum	Bounded Central Differencing
SGS models	Smagorinsky-Lilly (SM) & Dynamic Smagorinsky-Lilly (DSM)

Table 6.: Simulation set-up for flow around airfoil with DES model

Parameter	***Setting***
Solver	Pressure-based Implicit
Temporal discretization	2nd Order
Pressure-Velocity coupling	PISO
Pressure	PRESTO!
Momentum	2nd Order upwind
Turbulent kinetic energy (R κ-ε)	1st Order upwind
Turbulent dissipation rate (R κ-ε)	1st Order upwind
Modified turbulent viscosity (SA)	2nd Order upwind
RANS models	Spalart-Allmaras (SA) & Realizable κ-ε (R κ-ε)

The velocities based on the freestream value U_∞ and the angle of attack α are defined as $U_\infty(\cos \alpha)$ in the x-direction, positive in the longitudinal direction and $U_\infty(\sin \alpha)$ in the y-direction, positive upwards. Velocity is the z-direction was set to zero. Pressure condition inside the domain was assumed equal to atmospheric pressure.

6.1.3 Solution domain of the CFD simulations

The solution domain extended to 10 chord lengths radially forward of the foil and 13 chords downstream in the longitudinal direction. 10 chords separated each side in the vertical direction and 0.1 chord in the transverse direction to give it a three-dimensional effect necessary to apply our turbulence model (this is believed to have little effect on the results in comparing with existing data). These dimensions were sufficient to avoid any effects of interference of the boundaries on the results of the forces. Figure 6.2 below shows the extent of the computational domain, with the foil

located at the centre. The origin of the coordinate system is located at the fore tip of the foil, with the abscissa positive along its length and the ordinate positive upwards.

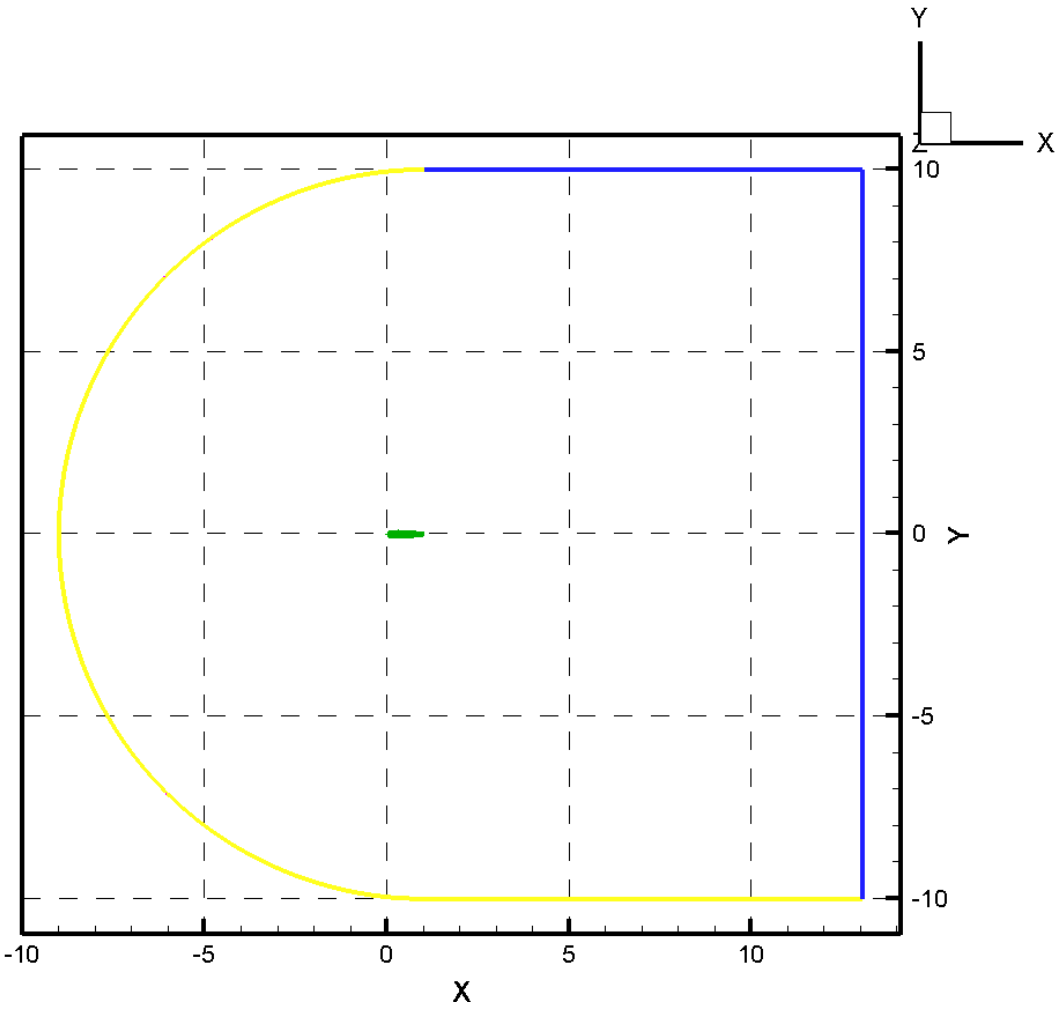

Figure 6.: Domain extent around the NACA 0012

6.1.4 Mesh generation

A fully structured, hexahedral mesh was developed for the simulations using the GAMBIT software. The topology is that of a C-type grid: the mesh is wrapped around the airfoil starting from the downstream outlet boundary, around the upper surface to the lower side of the NACA wing, and then back to the downstream far-field again; the grid meets up with itself in the wake. There is symmetry either side of the surface of the foil along the origin of the coordinate system. Moreover, the grid is stretched in the normal direction away from the wall, and the clustering of cells is maintained in the wake region where vortices and flow changes are expected

to appear with increasing angle of attack. Each row was increased at a ratio of 12% with respect to the previous one away from the airfoil's surface.

There are 398 faces on the surface of the airfoil, 199 along the wake from the trailing edge to the boundary outlet and 69 cells either side of the wake on the vertical edge. In total, the grid is equivalent to a 398 x 138 cells domain or a 796 x 69 mesh (depending on the counting of the cells) which totals to 54,924 cells as seen in figure 6.4. The mesh was adapted to a near-wall approach and has a minimum spacing at the wall of $y = 1.45 \times 10^{-5}$ m, resulting in an approximate average value of y^+ in the range of 0.5 to about 3.5 over the surface at the equivalent Reynolds numbers run in the CFD, which solves & computes with a sufficient accuracy the laminar sublayer of the turbulent boundary layer. The figures below show two views of the grid.

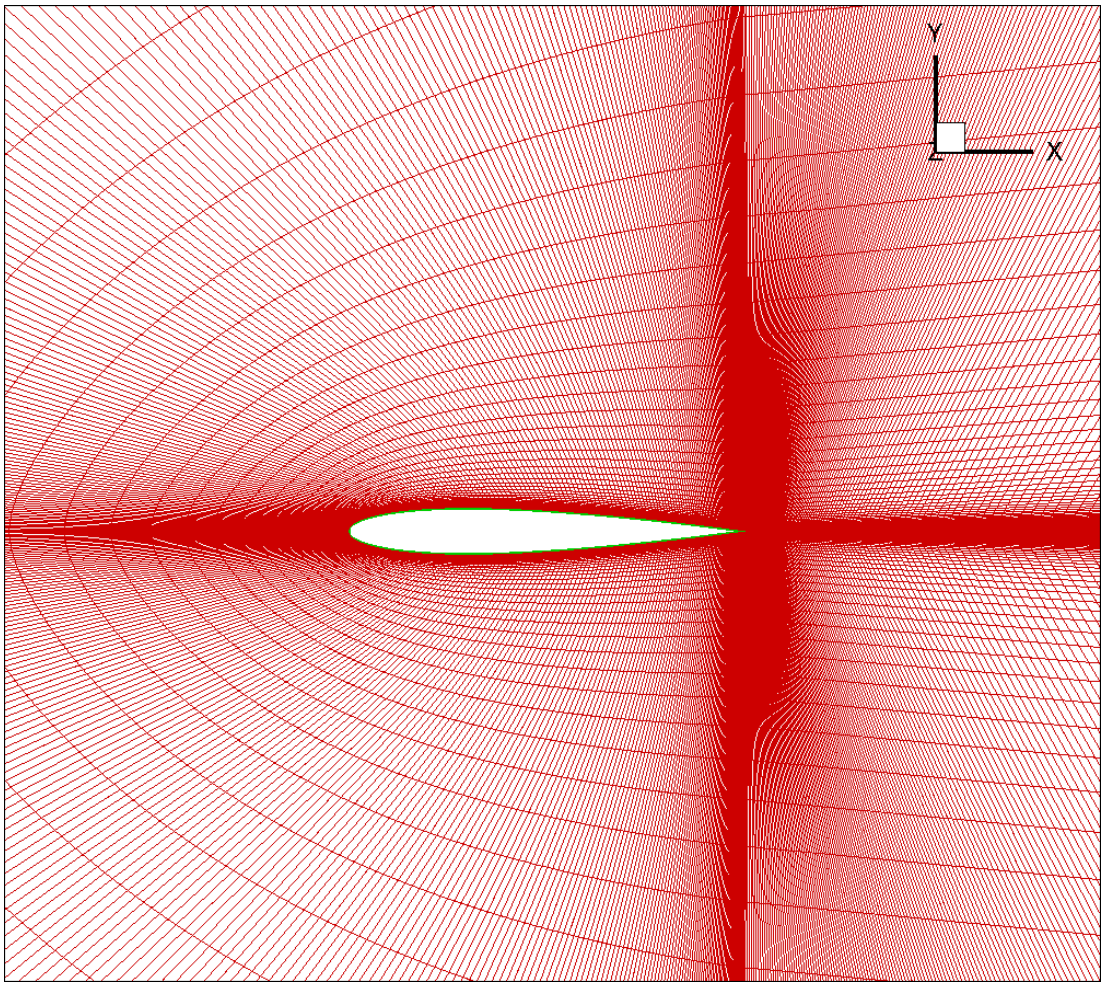

Figure 6.: Grid, close-up with near-wall resolution around airfoil

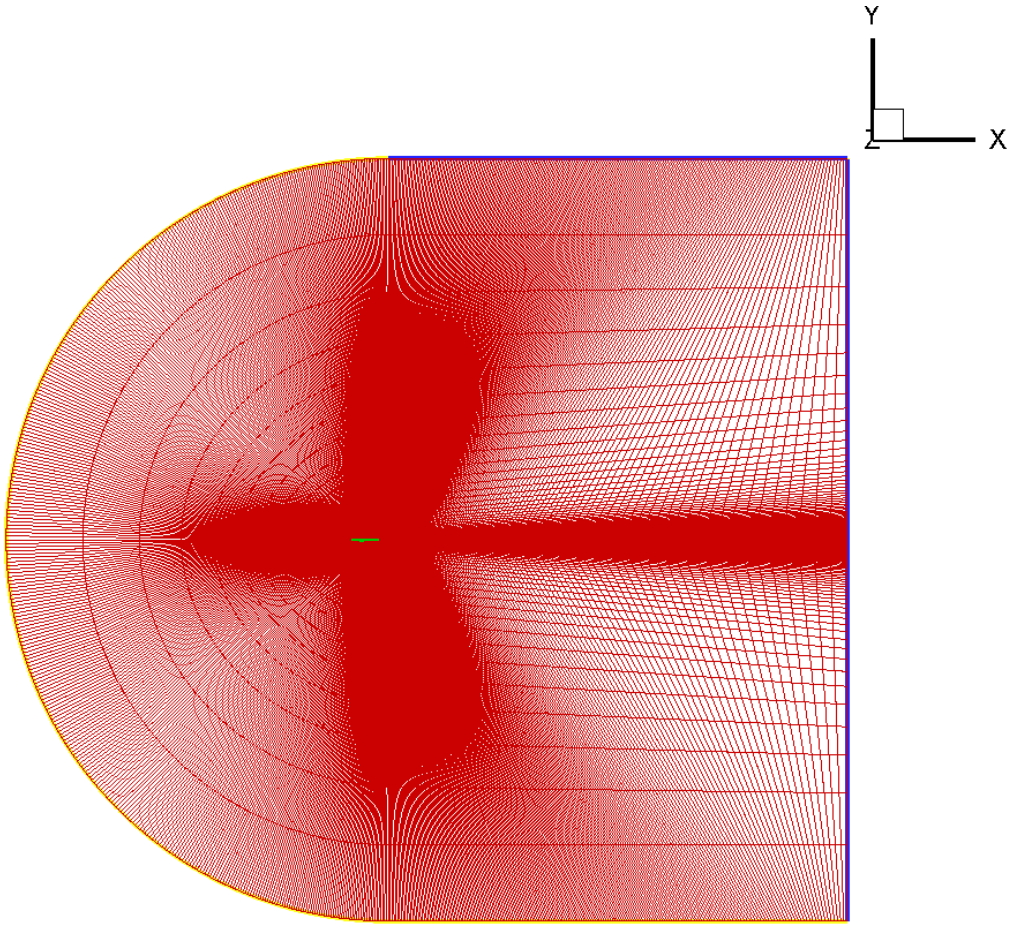

Figure 6.: Grid, overall view of the meshed domain

6.1.5 Boundary conditions

With regard to the definition of boundary conditions in the computations, table 6.3 summarises the application of them on the problem. A no-slip condition was applied on the foil surface. The inflow was defined over the curved area of the mesh as well as the bottom part of the domain as shown in figure 6.2 above (as velocity inlet). A pressure outlet condition is prescribed in the outflow, with a Neumann boundary condition. In the spanwise direction, a symmetry boundary condition is used on both ends of the foil.

The values of inlet turbulent intensity and length scale are assumed from literature review and are believed to be acceptable for low-speed wind tunnels with capabilities at the time of the experiments.

Table 6.: Boundary conditions for airfoil simulations

Domain Boundary	***Condition***
Inlet	Velocity inlet
Outlet	Pressure outlet
Airfoil	Non-slip wall
Side walls	Symmetry
Inlet turbulent intensity (%)	0.1
Inlet turbulent length scale (m)	0.01

6.2 Case 2: Prolate Spheroid at ratio 6:1

6.2.1 Contextual Backdrop

The second relevant case study for the validation of the methodology, and before the specific application carried out on the America's Cup keel, focuses on the flow around a 6:1 prolate spheroid at angles of attack and high Reynolds number. With a simple geometry to create and mesh, the flow around an inclined prolate spheroid exhibits nonetheless a range of intricate three dimensional flow features.

The complex interaction occurring through the flow, inside the boundary layer and between the main vortices, is strongly linked to the angle of attack and the Reynolds number, according to observations made during experiments. As the structure is tilting and with increasing angle of attack, an attached three-dimensional boundary layer is formed on the pressure side. On the suction side, the flow detaches from the hull caused by of the circumferentially adverse pressure gradient and creates a counter-rotating pair of longitudinal strengthening vortices on the back of the body. These unsteady effects make the prediction of three-dimensional separation and the other features associated with the spheroid flow difficult to grasp, and that is one of the main obstacles and challenges faced by the use of CFD in analysis and design and one of the reason it is used for validations of CFD codes and numerical methods.

Two main research groups have reported an extensive series of wind tunnel measurements of the flow past a prolate spheroid: Prof. Simpson and his team from

Virginia Polytechnic Institute (VPI hereafter) (Chesnakas and Simpson, 1996, 1997a, 1997b; Wetzel and Simpson, 1998) and Meier, Kreplin and associates at the Gottingen wind tunnel in Germany (Meier and Kreplin, 1980; Kreplin et al., 1982; 1984 to name a few). Both detailed in a dedicated manner the following features: surface properties in terms of pressure and skin friction, mean flow and turbulence profiles, and development of the vortical structures characterizing the separated region at various angles of attack.

Most of the experimental studies focused on static cases, with a few concentrating on manoeuvring and pitching of the prolate spheroid by means of moving with a sting attached in the back (e.g. Wetzel et al., 1998). As a matter of fact, the sting was also present in the static cases to support the body mounted on to the mechanical arm of the tunnel. The current study focuses also on static body inside the wind tunnel, as this was our principal interest in line with the simulations of the keel presented later in the thesis.

CFD onwards from the mid-nineties supported the experimental measurements. Simulations based initially on RANS codes (e.g. Piquet and Queutey, 1992) then on advanced turbulence modelling using LES (Wikström et al., 2004) and DES techniques have been performed (Constantinescu et al., 2002; Kotapati-Apparao and Squires, 2003). Numerical investigations of static-geometry spheroids have yielded many of the same effects observed in experiments, e.g., fairly accurate predictions of the location of primary and secondary separation for the spheroid at 20 degrees angle of attack, acceptable level of accuracy for surface pressure and wall shear stress , etc.

6.2.2 Computational details and model geometry

The numerical simulations produced in the thesis are based on the experiments carried out at VPI. A 6:1 prolate spheroid model of length L = 1.37 m is considered in the computations inside a wind tunnel with rectangular cross section. The Reynolds number based on the freestream velocity U_∞ and the body length l is 4.2 million.

Several measurements by the research group in the nineties, of the flow over prolate spheroids, have documented surface and flow properties: pressure and skin friction, mean flow, turbulence profiles and development of the vortical structures that characterizes the separated region. These detailed measurements have been carried out at angles of attack between 0 and 30 degrees. Here we focus on the conditions monitored at 10 and 20 deg for the flow properties but we did compare results of lift and moment coefficient for values up to 30 deg in the next chapter.

As mentioned above, during the experiments, the spheroid was supported by a sting mounted at the end of the body to hold it and to control the change in angle of attack. One of the assumptions for the presented simulations was to ignore the existence of the sting for simplification of the problem; thus, it was not modelled and it was not meshed in the domain. Moreover, the blocking effects are neglected, but these are usually considered small in comparison to the effects of the freestream wind tunnel inlet specific flow.

Secondly, to account for the laminar region, the flow was tripped at 20% of the prolate's length to trigger the transition from laminar to turbulent flow. This assumption was applied to the DES calculations only, based on similar decision of the wind tunnel experiments. Laminar zones were created around the region of interest, to investigate the effect of this on the flow and on the predictions, and results were compared with fully turbulent simulations from LES, as discussed in subsequent sections of the thesis accordingly.

As per the previous case, the numerical solution of the flow is obtained using FLUENT. Discretization is done based on a finite-volume approach. The node-centred based method is used to calculate gradients. In the tables 6.4 and 6.5, the various CFD settings, schemes and parameters introduced in the previous chapter are summarized as applied selected for the simulations of the prolate spheroid flow. The convergence criteria considered was again 1.0×10^{-5} for these runs. The numerical solutions were deemed converged when scaled residuals for all solution variables

drop by the order of magnitude defined. The lift and pitching moment were also monitored to ensure full convergence of the solutions.

Table 6.: Simulation set-up for flow around 6:1 prolate spheroid with LES model

Parameter	***Setting***
Simulation mode	3D, Unsteady
Solver	Pressure-based Implicit
Temporal discretization	2nd Order
Pressure-Velocity coupling	SIMPLE-C
Pressure	Standard
Momentum	Bounded Central Differencing
SGS model	Smagorinsky-Lilly (SM) & Dynamic Smagorinsky-Lilly (DSM)

Table 6.: Simulation set-up for flow around 6:1 prolate spheroid with DES model

Parameter	***Setting***
Simulation mode	3D, Unsteady
Solver	Pressure-based Implicit
Temporal discretization	1st Order
Pressure-Velocity coupling	PISO
Pressure	PRESTO!
Momentum	2nd Order upwind
Turbulent kinetic energy (R κε)	1st Order upwind
Turbulent dissipation rate (R κε)	1st Order upwind
Modified turbulent viscosity (SA)	2nd Order upwind
RANS model	Spalart-Allmaras (SA) & Realizable κ-ε (R κ-ε)

6.2.3 Solution domain of the CFD simulations

The solution domain extended to 2.5 m forwards of the prolate and 3.5 m after in the streamwise direction and 2.8 m either side of the body in both the vertical and transverse directions. These dimensions were sufficient to avoid any effects of interference of the boundaries on the results of the forces. This configuration was used for the first four grids created. A perspective view of the domain is shown on figure 6.5 with the squared cross-section of the virtual wind tunnel visible and the location of the spheroid with respect to the environment. The coordinate system adopted in the study is such that the positive x-axis is pointing in the streamwise

direction, y points to the upward vertical direction, and the x-y plane and the y-z plane make the symmetry planes. The origin of the coordinate system is located at the fore-end of the spheroid for all grids.

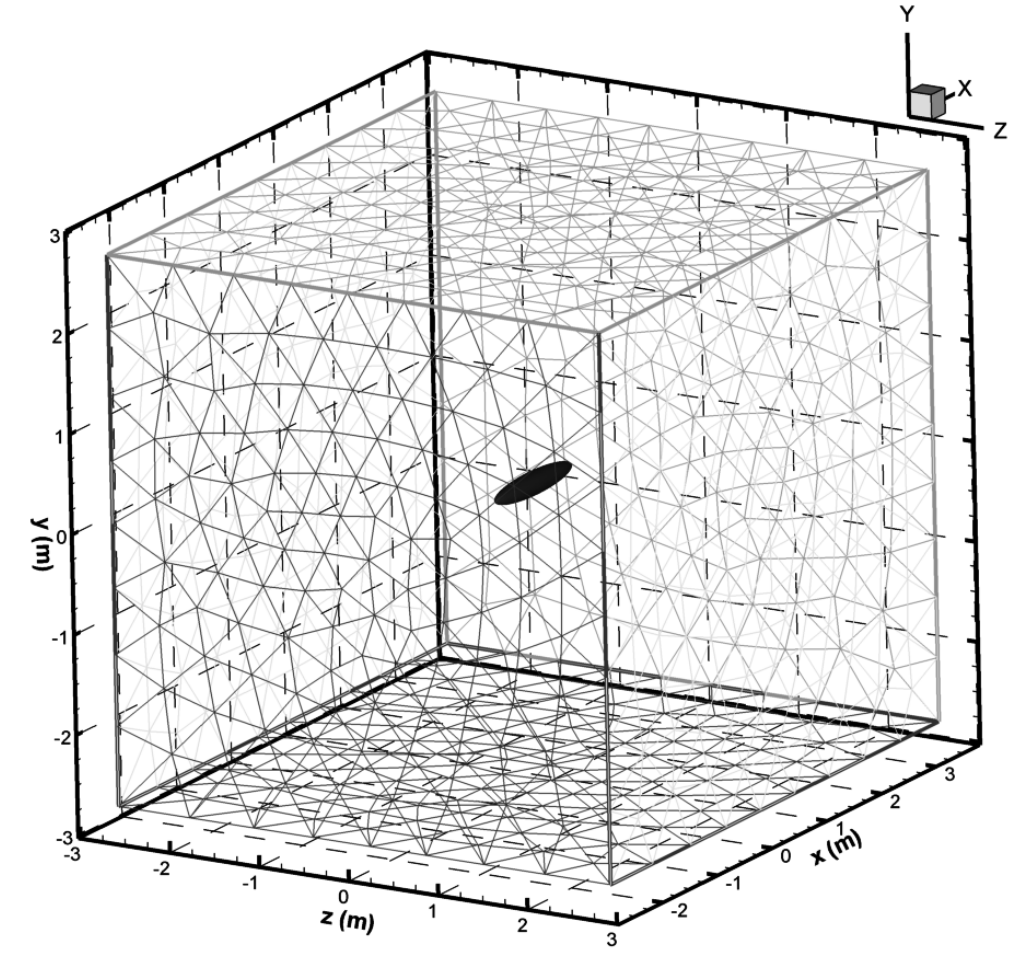

Figure 6.: Domain boundary for meshes A to D

For the fifth and sixth grids, the prolate was rotated 10 and 20 degrees respectively from the origin of the coordinate system around the z-axis as if the body has been moved in a static position. The origin and direction of the coordinate system remained unchanged for the last two meshes. A side view of these configurations is illustrated in figure 6.6.

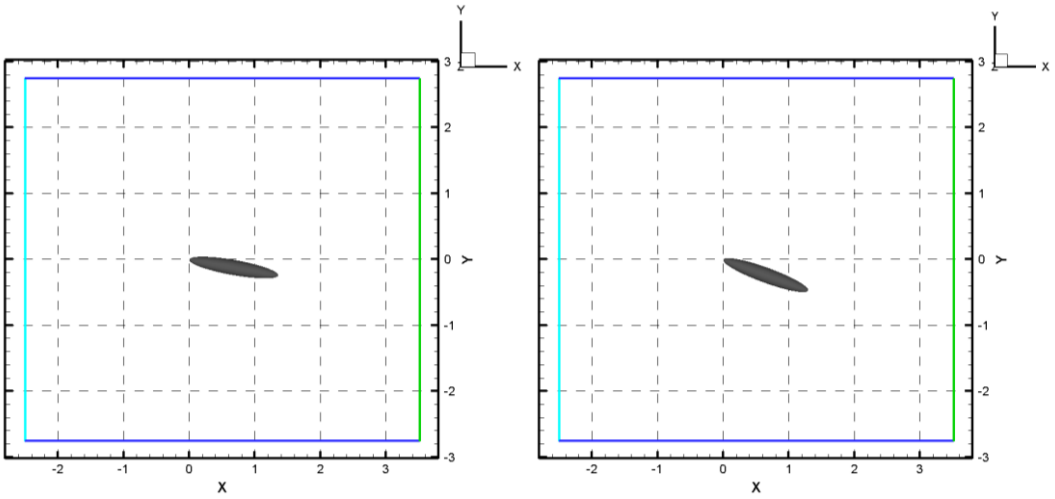

Figure 6.: Configuration for static position of prolate spheroid at 10 deg (left) and 20 deg (right) for meshes E and F respectively

6.2.4 Mesh generation

The meshing strategy consisted of creating for each case a single-block, hydrid mesh around the prolate spheroid to fill the volume. As mentioned, six different meshes were created, divided in two categories: three considered coarse-to-medium and three considered fine. The different mesh sizes were used to investigate the effect of grid dependency on the results.

The grid topology for all meshes consisted of the following: first a structured surface grid was developed, after importing the IGES geometry of the prolate spheroid into GAMBIT. An example of a typical surface mesh created is shown in figure 6.7. There were slightly more cells at the fore and aft were curvature is highest. Then a structured, O-type mesh forming from the surface of the body to the end of the boundary layer zone was generated (figure 6.8). The rows inside the O-grid were expanding at a rate of 1.1, and most of them were adding up to 25 rows. Finally, an unstructured mesh filling the outer volume from the external boundary layer up to the domain boundaries was introduced; with higher number of cells near the last layer of the inner mesh and coarser near the outer boundaries (figure 6.9).

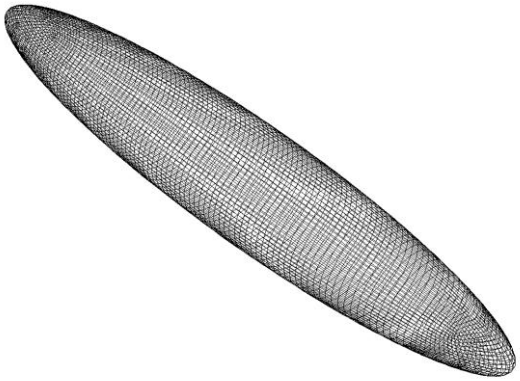

Figure 6.: Structured surface mesh on spheroid body

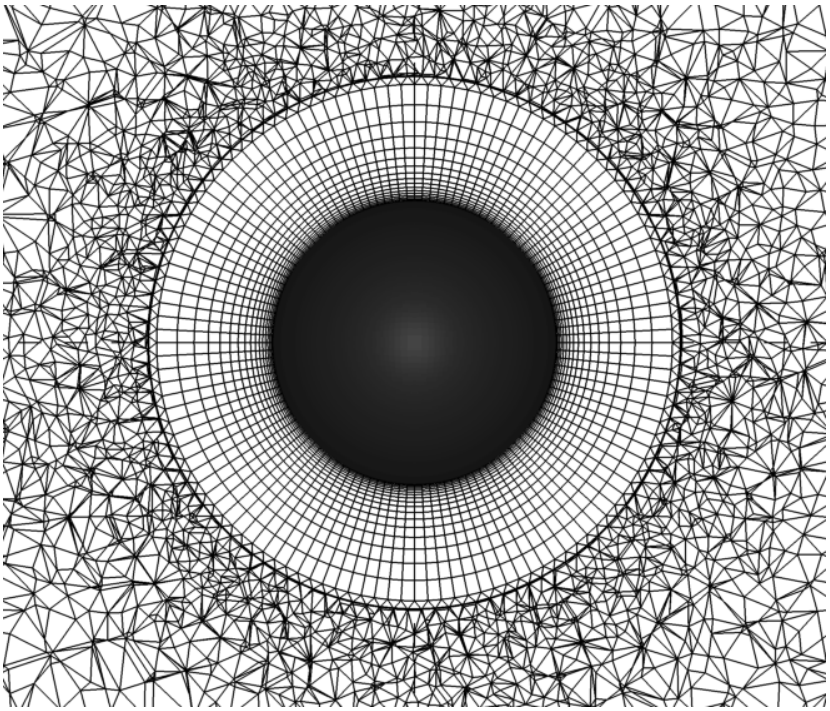

Figure 6.: Inner O-grid around prolate spheroid

The set of six different grids developed are summarised in table 6.6, in order to investigate the effects of the resolution on the results and the flow features. Grids A and B are used exclusively for DES calculations and are incorporating a laminar zone extending until x/L = 0.2, as shown in figure 6.10. The laminar zone comprised of 30,000 cells in total. Grid A is the coarsest of all in terms of cell number. The average y^+ for mesh A is close to the limit of the viscous sublayer range. Mesh B has

about 1.8 times more surface faces and boundary layer cells than mesh A. The y^+ is also lower, expected to give more accurate results. Mesh C can also be considered relatively coarse. It is quite similar to mesh A but has a higher boundary layer.

Mesh D was created based on mesh C and has 2 times more cells in all the different mesh components inside the domain. Mesh D is the finest of all in terms of overall size. Finally meshes E and F were the ones developed for the case of the prolate spheroid inclined at 10 and 20 degrees. They are very similar, the only difference is in the number of cells generated in the outer volume, with mesh F having slightly more than mesh E. The average y^+ is about 65 which means that walls functions were used inside FLUENT.

Table 6.: Meshes for 6:1 prolate spheroid case study

Mesh	Size	Surface	B.L.	Lam Zone	L.Z. cells	y^+ ave
A	633,752	8,290	198,960	y	30,000	5.7
B	683,025	14,680	367,000	y	30,000	3.2
C	674,751	8,800	255,200	n	-	3.6
D	1,312,962	19,800	574,200	n	-	3.6
E	1,215,419	35,200	704,000	n	-	65
F	1,216,322	35,200	704,000	n	-	65

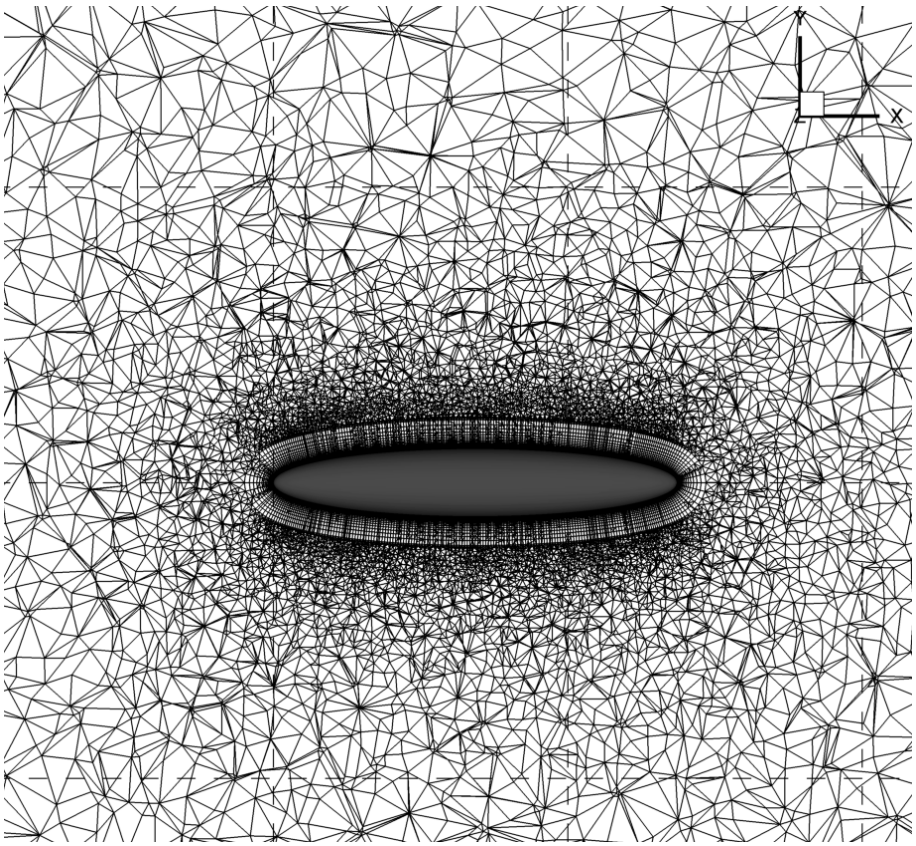

Figure 6.: Plane through the spheroid showing longitudinal mesh (mesh C)

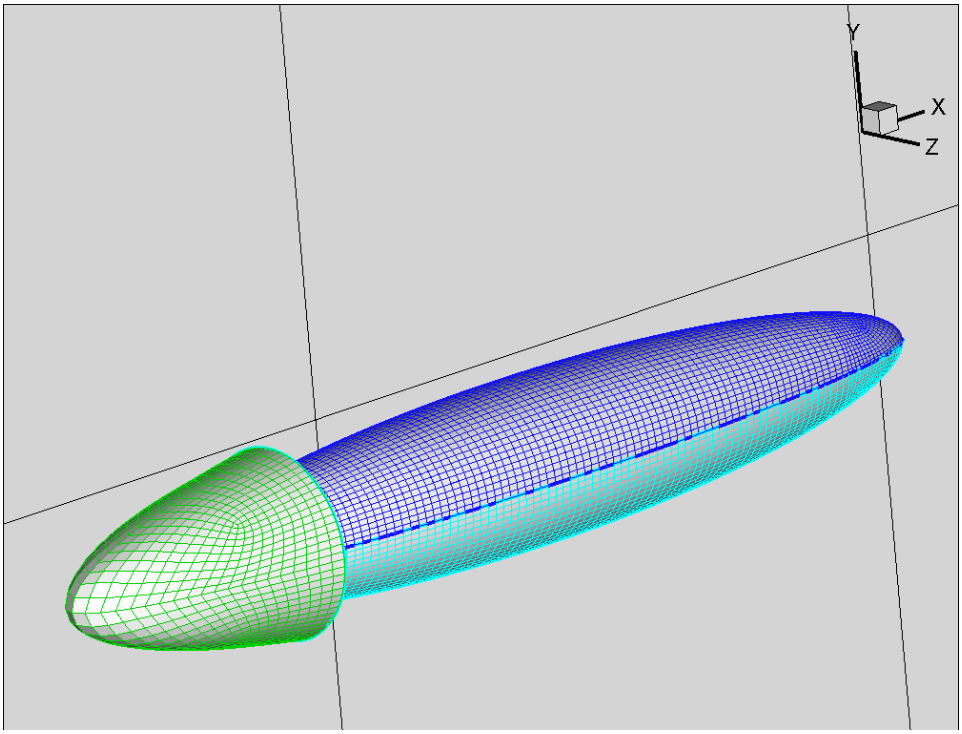

Figure 6.: : surface mesh on the body and around the laminar zone (mesh A)

6.2.5 Boundary conditions

The domain boundaries consisted of the surface of the spheroid, the velocity inlet located in the upstream of the body, the pressure outlet condition downstream and the symmetry planes vertically and horizontally. A no-slip wall is defined on the body surface. On the inlet boundary, the freestream conditions were specified along with the values of turbulence intensity and length scale. On the outlet boundary, the solutions variables were extrapolated and static pressure was set to zero.

Table 6.: Boundary conditions for 6:1 prolate spheroid simulations

Domain Boundary	***Condition***
Inlet	Velocity inlet,
Outlet	Pressure outlet
Prolate surface	Non-slip wall
Top walls	Symmetry
Side walls	Symmetry
Inlet turbulent intensity (%)	0.5
Inlet turbulent length scale (m)	0.01

"*A good idea is about ten percent and implementation and hard work, and luck is 90 percent.*"
Guy Kawasaki

"*The logic of validation allows us to move between the two limits of dogmatism and scepticism.*"
Paul Ricoeur

7 Case Studies: Results

7.1 Case 1: NACA 0012 foil

7.1.1 Overview

Forty-eight computations were carried for this section. For the data compared with Ladson (1988), there were 36 runs in total, corresponding to three Reynolds numbers, three angles of attack each and the four models of LES and DES used. For the comparisons with Gregory and O'Reilly (1970), there were 12 simulations: three angles of attack and four turbulence models at one Reynolds number.

Critical flow parameters, which are non-dimensional, time-averaged drag coefficient and lift coefficient, have been predicted with each turbulence model and calculated values are compared with experimental values. In addition, the time-averaged pressure distribution was calculated around the airfoil surface with the same turbulence models for the second case. The time-step for the simulations corresponding to a CFL number around one was equal to $0.001 \cdot {}^{c}/_{U_\infty}$ for each case. The number of time-steps was at least 25,000 to gather sufficient and reliable data for the results.

7.1.2 Comparisons of lift and drag coefficients

The simulations are conducted for three Reynolds numbers: 7.0×10^5, 2.0×10^6 and 3.94×10^6. The choice of the Reynolds numbers for the simulations was quite large because of the number of experimental data available from Ladson (values up to 6×10^6). It was decided to choose three different Re numbers tested in the wind tunnel with a range of conditions (tripped and free transition). Time-averaged lift and drag coefficients are calculated at three angles of attack (4, 10, 15 degrees). Results are compared against experimental values; the coefficients are defined as:

$$C_L = \frac{L}{0.5 \cdot \rho \cdot A \cdot V^2} \tag{7.1}$$

and

$$C_D = \frac{D}{0.5 \cdot \rho \cdot A \cdot V^2} \tag{7.2}$$

where *L* is the lift force, *D* the drag force, *A* the projected area and *V* the velocity.

The figures below show the lift coefficient as a function of the angle of attack. Simulation results are compared against experimental results reported by Ladson. All solutions are without defining a trip where transition from laminar to turbulent flow occurs. The computational results are reported only for the angles that were used in the simulations. The experimental results are reported over the entire range of values given from the wind tunnel tests, though negative values were omitted. For further information, and for tabular results of results with a refined mesh, please refer to the relevant sections in Appendix A.

Results are in good agreement with the experiments at the low-to-moderate angles of attack. Simulation results deviate from experiments as the critical angle of attack (or stall) is approached and as the Reynolds number increases. This is due to the fact that an accurate prediction of the critical point largely depends on a finer mesh. Hence, simulation results can be considered quite good taking this into account.

The result of lift force against drag coefficient also compared relatively well. The results at the lower angles of attack matched the experimental data within a few percent. As the AoA increased, the discrepancy was higher. This was also the case when the Reynolds numbers tested were augmenting. Drag was over predicted with increasing Reynolds number; both LES models tend to over predict drag whereas the DES models were closer to the measurements. Values of experimental uncertainty were not found so there was no possibility to quantify the error in lift and drag coefficient with the experiments.

At Re equal to 700,000, the difference between the experimental values and the CFD was found to be between 0.4% - 7% for LES SM; 0.25% - 8.5% for LES DSM; 1% - 6% for DES Rκε and 0.5% - 8% for DES SA. Most of the differences for LES were in the drag prediction, whereas for DES it was regarding the lift force. At 15°, the critical angle of attack reflects the change in flow due to stall. Lift is decreasing and there is a sharp increase in drag.

At higher Reynolds numbers, the critical angle of attack has not yet been reached, but the flow exhibits turbulence, separation and vortices as seen in the figures below reporting some qualitative data. At 2.0 million Re, error in force prediction was 0.37% - 5% for LES SM; 0.4% - 7% for LES DSM; 0.2% - 7.5% for DES Rκε and 0.3% - 5% for DES SA. The trend in lift and drag is quite satisfactory for this case; as previously the LES SGS models were predicting lift better than drag; for the RANS models of DES there was a change compared to the lowest Re, with drag not predicted as good as the lift.

Finally, at Reynolds number of 3.94 million, the differences were as follow: LES SM between 0.5% - 2.6%; LES DSM between 0.3% - 3.5%; DES Rκε 0.2% - 4.5% and DES SA between 0.2% - 7%. It must be noted that in figure 7.6, the isolated point corresponds to the Lift-to-Drag ratio at 18° angle of attack which is not shown in figure 7.3. It corresponds to the force after the critical angle of stall.

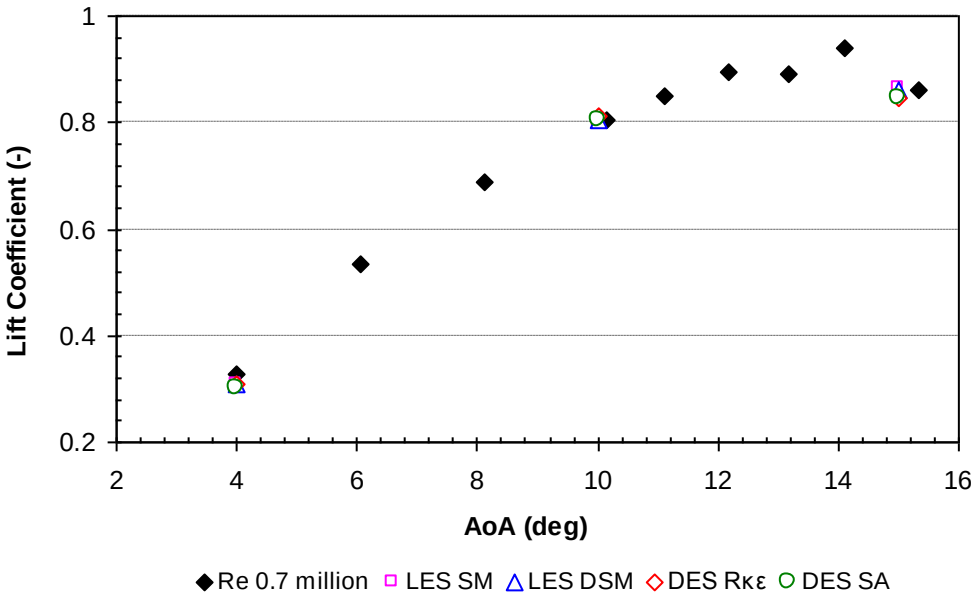

Figure 7.: Lift force vs. AoA for Re 0.7 million

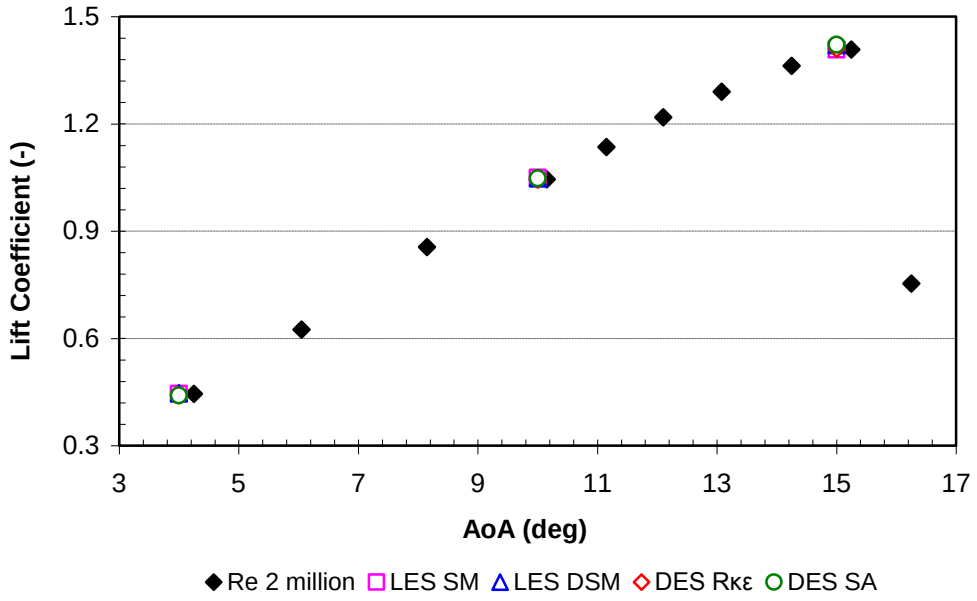

Figure 7.: Lift force vs. AoA for Re 2 million

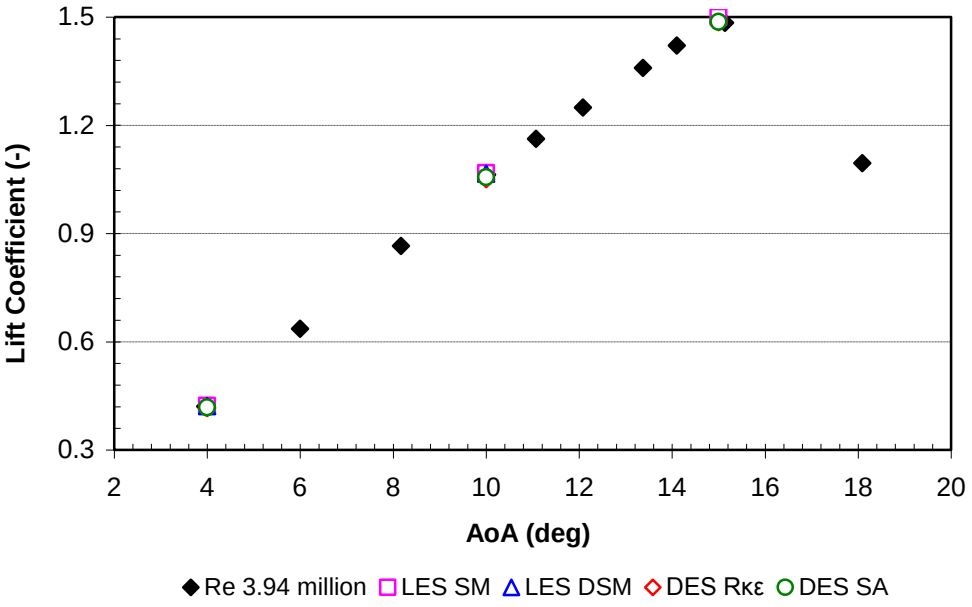

Figure 7.: Lift force vs. AoA for Re 3.94 million

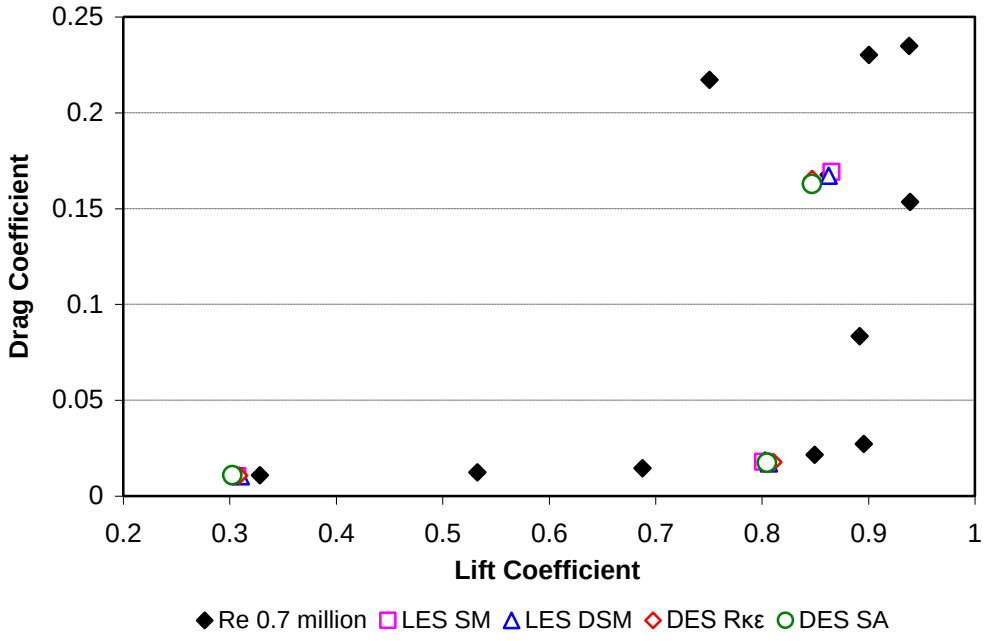

Figure 7.: C_D vs. C_L at Re = 0.7 million

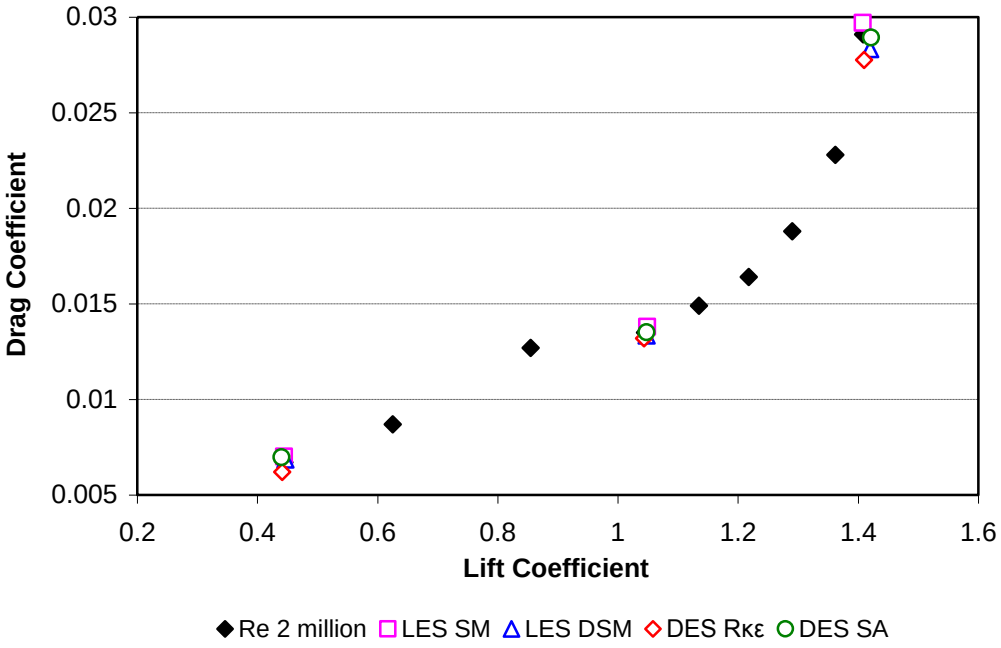

Figure 7.: C_D vs. C_L at Re = 2 million

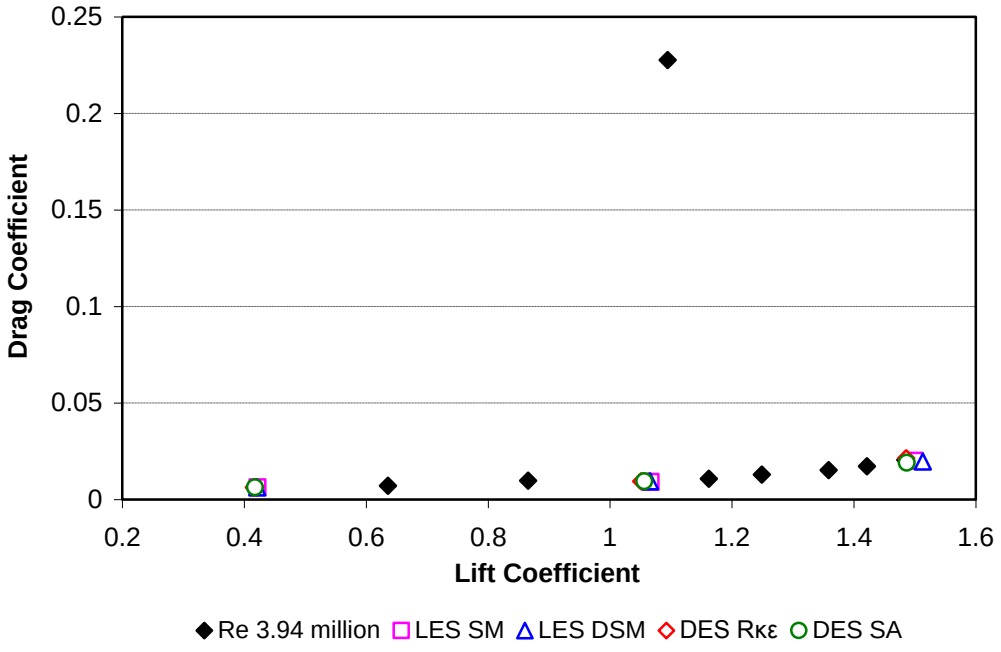

Figure 7.: C_D vs. C_L at Re = 3.94 million

The contours of the instantaneous transverse vorticity at t = 1.92s for the case of Re = 0.7 million at 15° AoA for LES and DES are shown in figure 7.7. The presence of the flow transition, separation and vortex shedding is visible on the upper surface of the airfoil. The separation starts at about x/c = 0.2 for LES and x/c = 0.3 for DES

near the leading edge of the airfoil. It then creates a separated shear layer, which becomes unstable near the mid-chord and leads to the shedding of large-scale vortical structures detaching at around x/c = 0.8. It is believed that the values of the inlet turbulence intensity and length scale are not influencing the vortices but most likely these are generated through streamwise growth of the disturbance in the separated shear layer. The large vortices are carried downstream flow along the airfoil surface. A vortex pairing can also be observed. There are also vortices created at the trailing edge at the end of the airfoil. There is evidence of small-scale vortical structures inside the turbulent layer towards the trailing edge, more visible with LES.

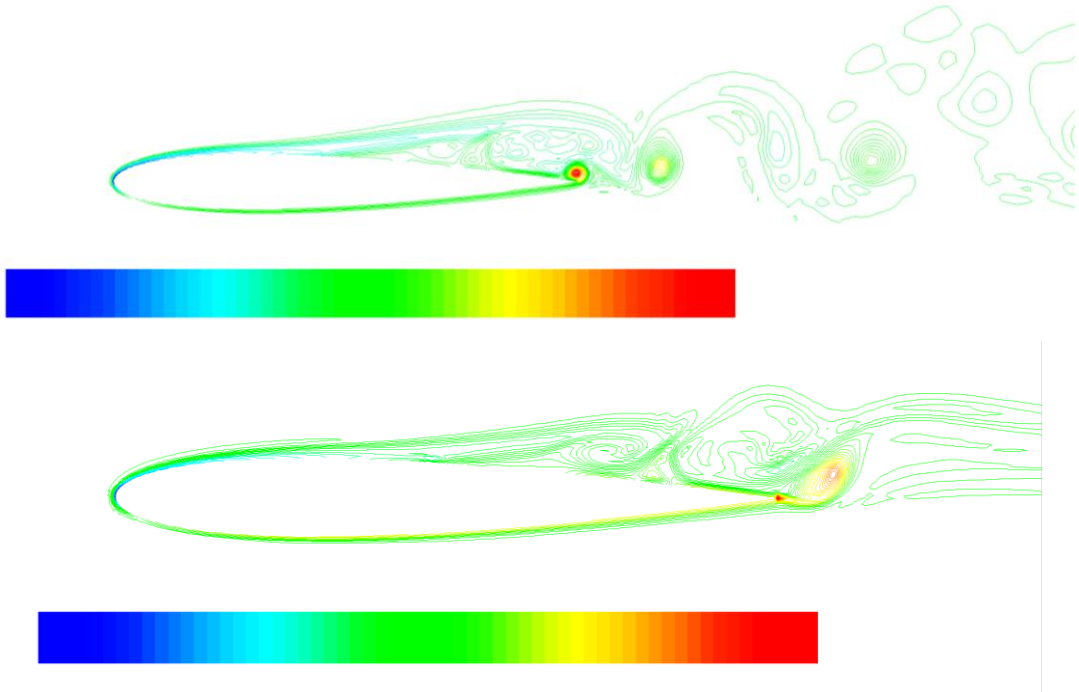

Figure 7.: Contours of instantaneous transverse vorticity, 15°, Re = 0.7 million. Top: LES, bot: DES

Calculations were also done on a refined mesh, of about 525,000 cells, including 6368 faces on the airfoil, to investigate the mesh sensitivity and also the 3D effects in the spanwise direction. Results for lift and drag coefficients are shown in Appendix A. A brief look of some findings is shown here. Compared to the initial grid, the contours of vorticity exhibit a much more complex flowfield.

Figures 7.8 to 7.10 display the instantaneous vorticity magnitude vorticity contours taken at mid-span (z = 0.05) at the same time of t = 0.255s with LES SM at angles of attack of 5, 10 and 15 degrees. The pictures are at 3 million Reynolds number.

Unsteady instability and flow separation are more visible at the higher angles of attack on the refined mesh and at higher Reynolds numbers, as the airfoil is approaching stall. The vortices are formed around the leading edge and travel along the airfoil surface as they develop, separating from the airfoil surface near the trailing edge. The figures show more realistic and turbulent vortical flow structures in the regions of massive separations than the initial mesh. Flow separation occurs on the upper surface near leading edge as shown by the vorticity streaks.

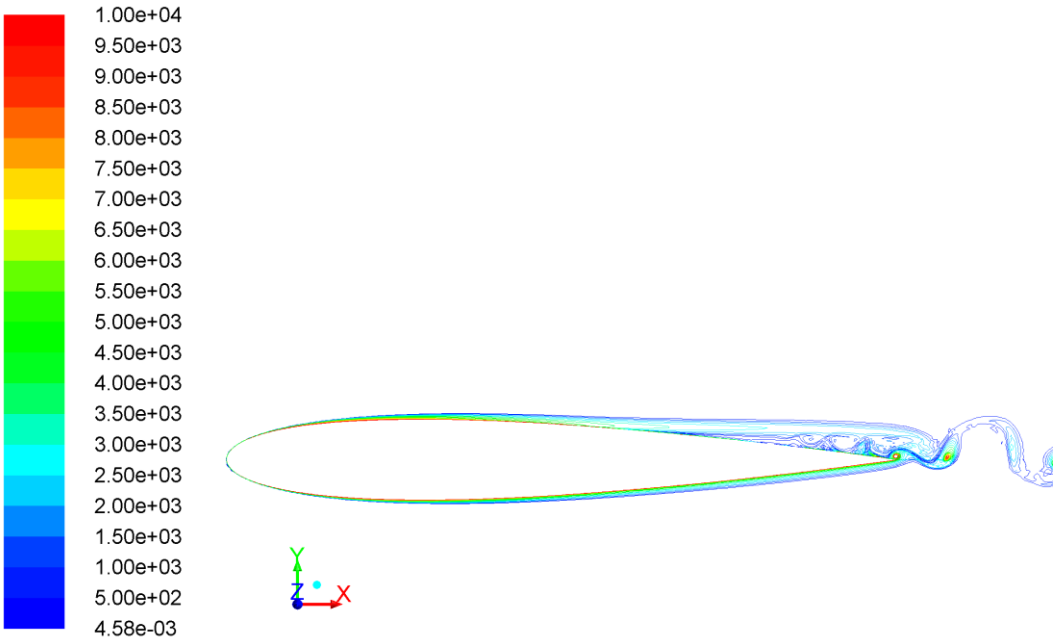

Figure 7.: Contours of vorticity magnitude, refined mesh, 5°, LES SM

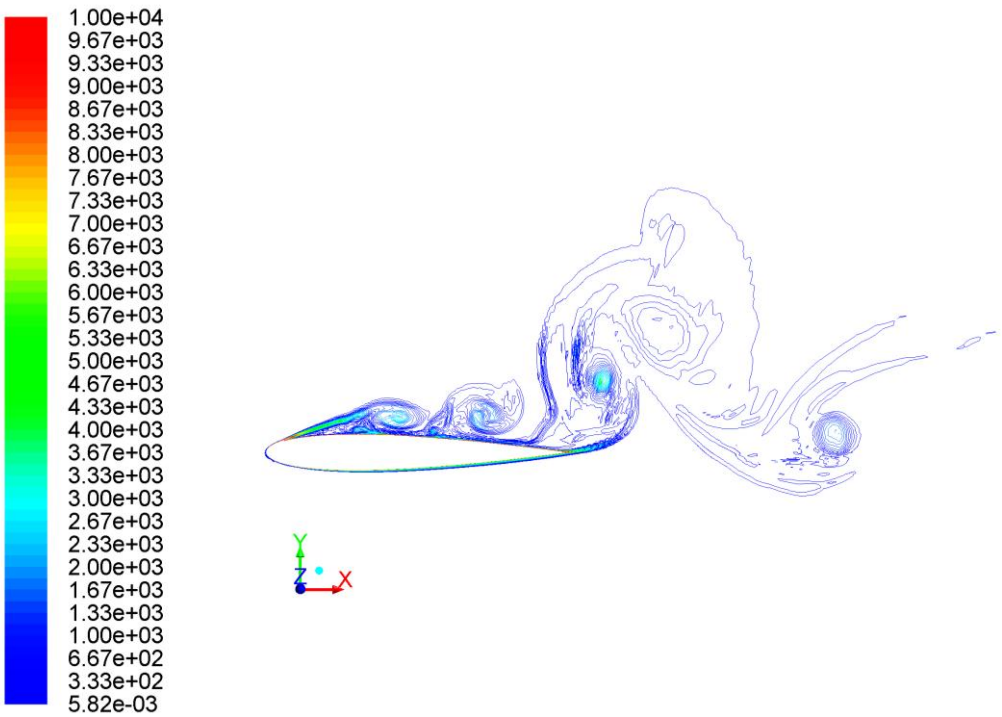

Figure 7.: Contours of vorticity magnitude, refined mesh, 10°, LES SM

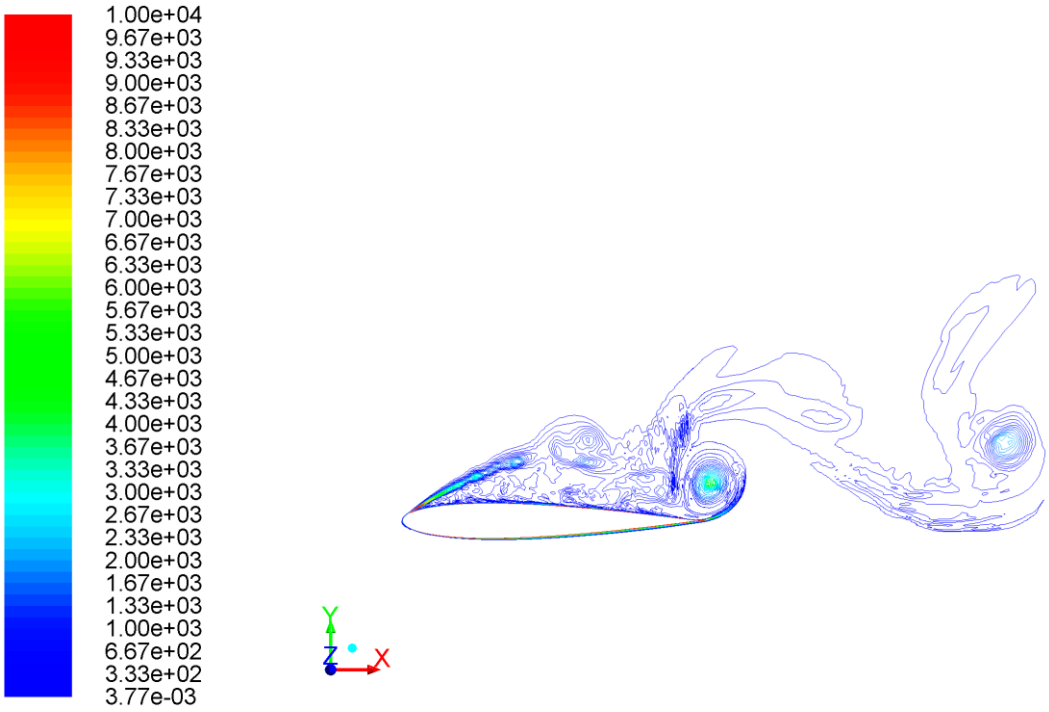

Figure 7.: Contours of vorticity magnitude, refined mesh, 15°, LES SM

The separation zone can also be observed from the time-averaged velocity vectors shown in Figure 7.11 where a very strong reversed flow region can be found at the leading edge in the laminar sublayer. Separation takes place at about same point where adverse pressure gradient appears for all cases.

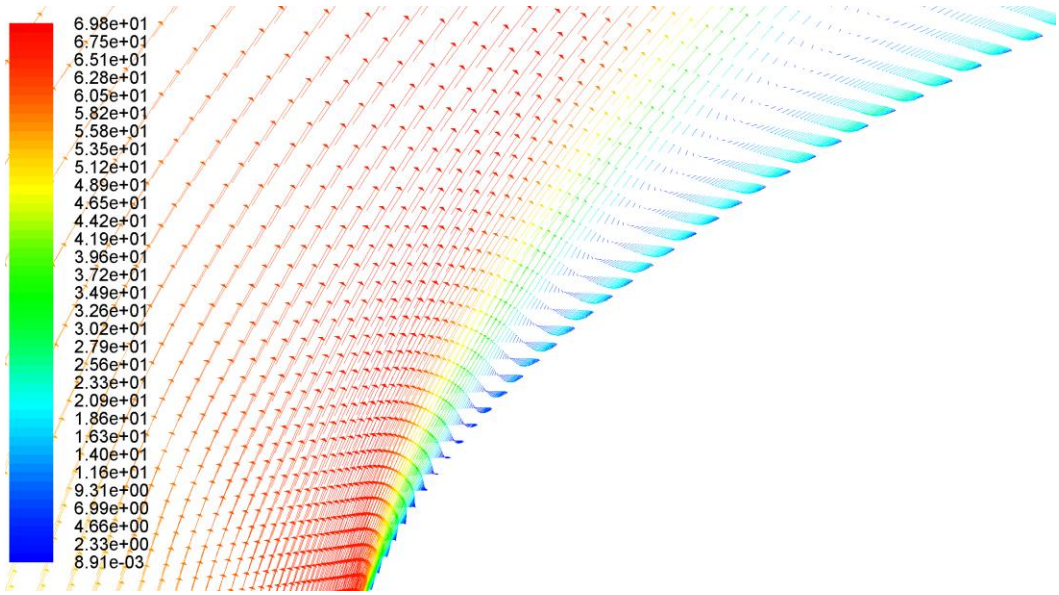

Figure 7.: Laminar bubble separation at leading edge

Finally, streamlines for one case with the refined mesh at Re = 3.94 million and 10° are shown in Figure 7.12. The view highlights the separation bubble at x/c = 0.1. Two large vortices are visible near the surface of the foil. The turbulent flow reattaches at x/c = 0.8. Unfortunately there were no experimental measurements to compare with, but these figures show the unsteady and complex nature of the flow captured with LES and DES.

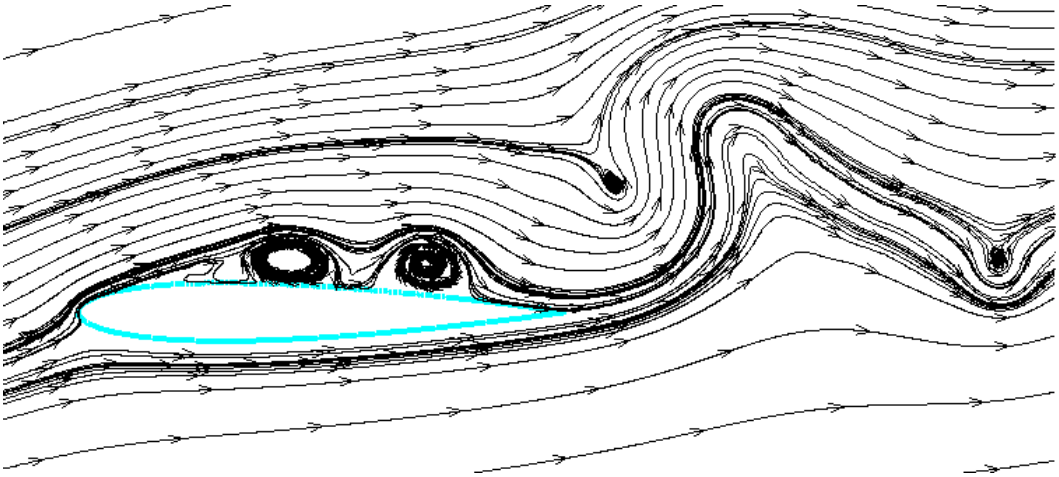

Figure 7.: streamlines at Re = 3/94 x 10^6, 10°

7.1.3 Comparisons of surface pressure coefficient

The mean pressure distribution on the upper and lower sides of the airfoil is obtained from the simulations and compared against the experiments at Reynolds number equal to 2.88 million. The pressure coefficient Cp is defined as follows:

$$C_p = \frac{p - p_\infty}{0.5 \cdot \rho \cdot V^2} \tag{7.3}$$

Where p is the pressure at the evaluated point, p_∞ is the freestream pressure in the far-field. The figures below show the pressure coefficient distributions along the chord for the three angles of attack reported by Gregory & O'Reilly: 0, 10 and 15 deg. Only values for the upper surface are available from the experiments. The overall results show that the trends are in good agreement with the experiments in the entire range of angles of attack under analysis in the test case, over most of the airfoil surface. The results of the simulations accurately reproduced the airfoil surface-pressure fields, including the pressure spike at the airfoil's leading edge; however, the LES models exhibit some strong influence due to the trailing edge separation at 15º for both models and at 0º for the DSM. The latter may require further investigation at zero angle because of the high irregularity of the flow at the trailing edge.

The mismatch between the LES and the measurements illustrates one of the outcomes of the differences in the separation prediction. Differences in the location of separation and in the characteristics of the separated flow region both may contribute to the less negative *Cp* predicted by the RANS models of DES along the suction surface. The SA model is a bit erroneous at the lowest angle but the error reduces at 10 degrees and it correlates very well at the highest angle investigated. The figures show that compared to the experimental measurements, the overall pressure distribution is adequately captured by fully turbulent solutions over the the suction side upstream of the region at least until the region strongly influenced by separation at the trailing edge (x/c > 0.8).

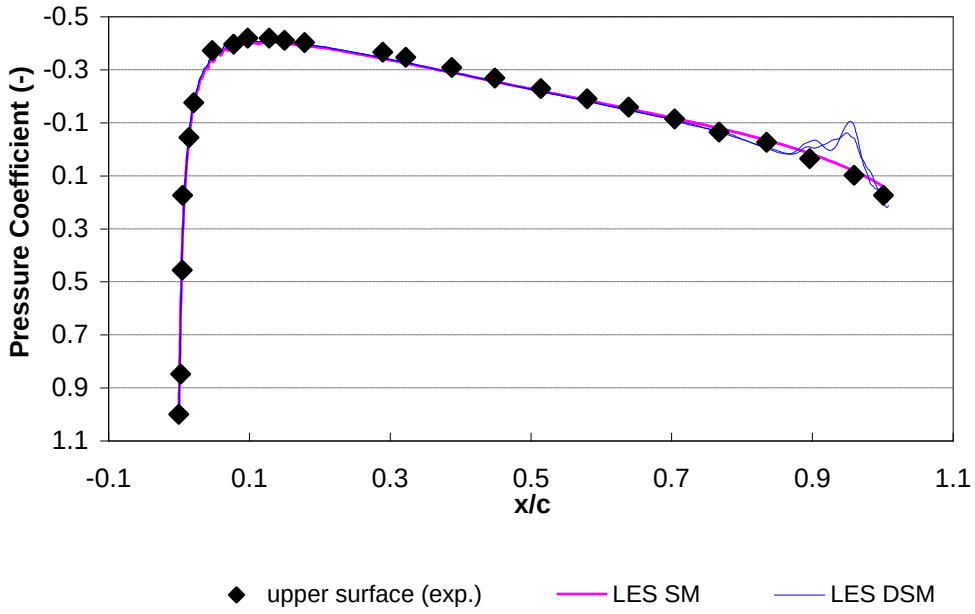

Figure 7.: Surface pressure coefficient with LES at 0 degrees AoA

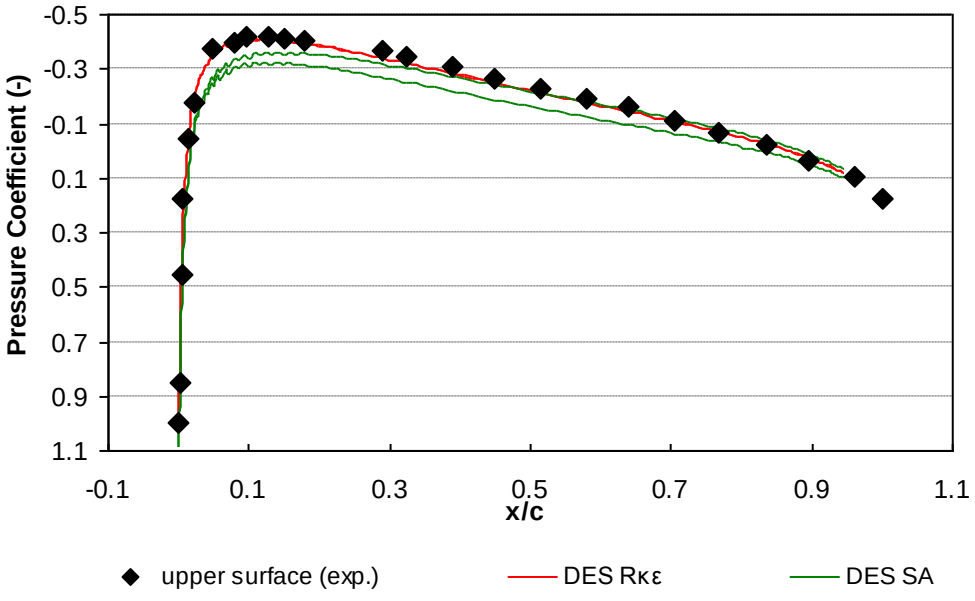

Figure 7.: Surface pressure coefficient with DES at 0 degrees AoA

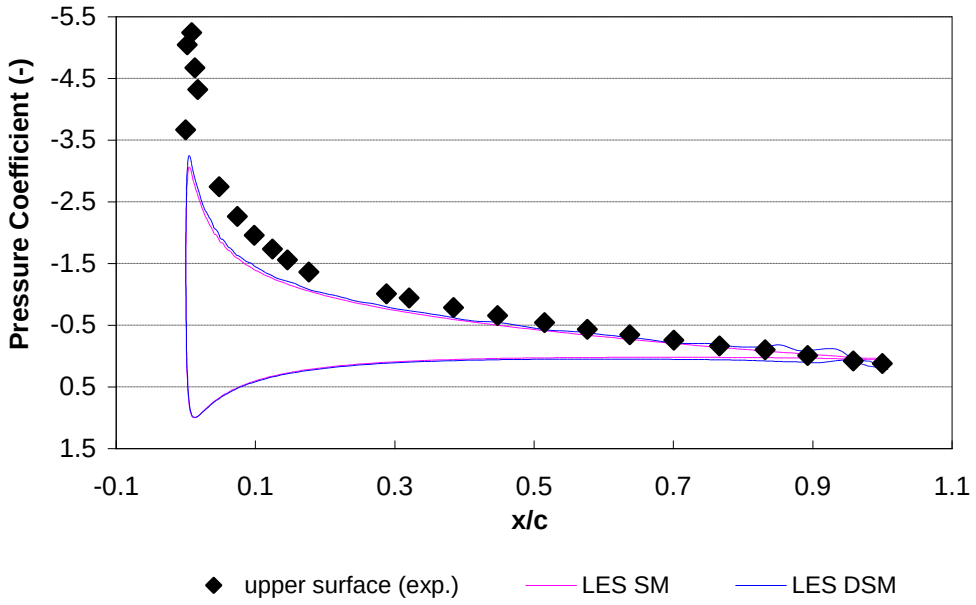

Figure 7.: Surface pressure coefficient with LES at 10 degrees AoA

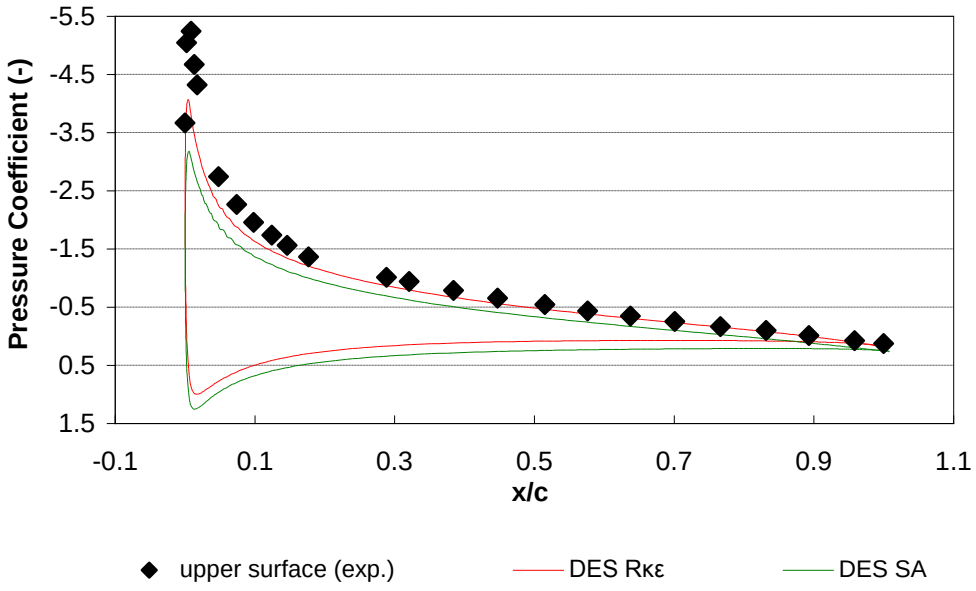

Figure 7.: Surface pressure coefficient with DES at 10 degrees AoA

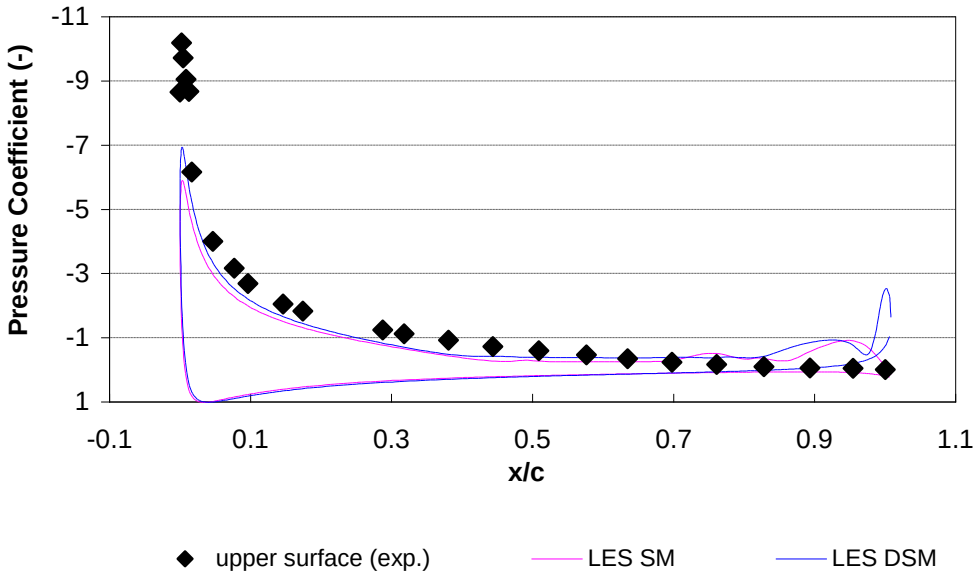

Figure 7.: Surface pressure coefficient with LES at 15 degrees AoA

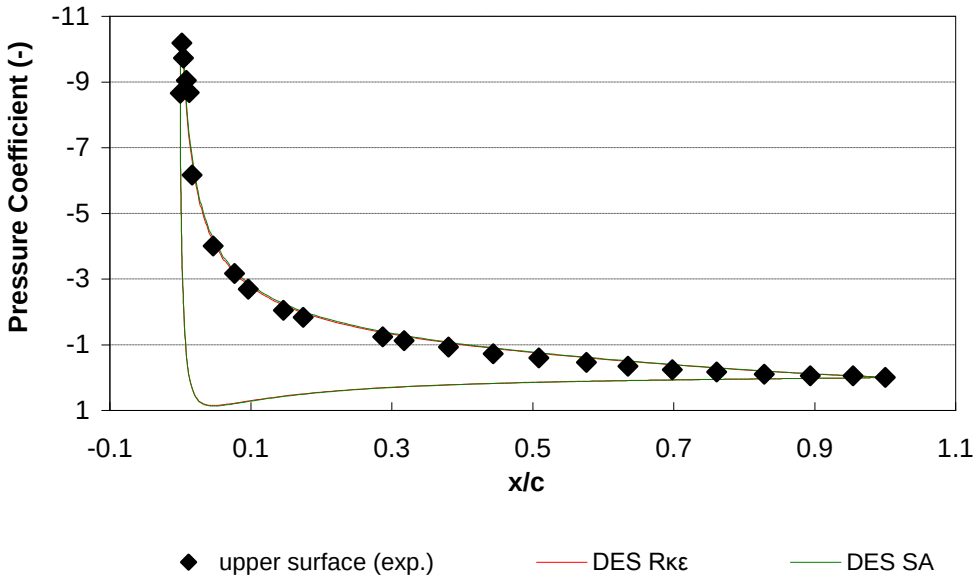

Figure 7.: Surface pressure coefficient with DES at 15 degrees AoA

At 10 degrees, all models yield a peak pressure near the leading edge of the leeward side higher than the measure values from the experiments. This is repeated for the LES models at 15 degrees. The turbulence models do not appear to resolve the

leading edge upper surface pressure peak well. It may be linked to the changes in the airfoil flow circulating near the surface or the laminar bubble separation. Also the 3D effects are not accounted for in the experiments, hence another reason for this difference.

The DSM model exhibits the strangest behaviour at 0 and 15 degrees at the trailing edge, the pressure distribution looking like and instantaneous value rather than an average value. Again, this is likely due to the separation at the trailing edge, and the vortices from the flow as stall condition is approached. The LES SM model is also more unpredictable at 15 degrees. Both LES models slightly overestimate the pressure on the upper surface. This may be due to a number of possibilities:

- longer simulation time needed to capture mean values and ensure the peak is in agreement with the data
- the mesh in the region is skewed with high aspect ratio cells not simulating the flow properly
- Too strong features in the flow and influence of the instantaneous fluctuations over the range of averaged values of pressure contours
- Time-scale too fast in experiments to catch these separations
- Two-dimensionality of experiments does not capture the changes at the trailing edge.

Two enlarged views of the trailing edge region for this model are reported in Figures 7.19 and 7.20. They show the LES SM solution is closer to the experimental measurements than the DSM prediction. They also illustrate one of the effects of the differences in separation predictions.

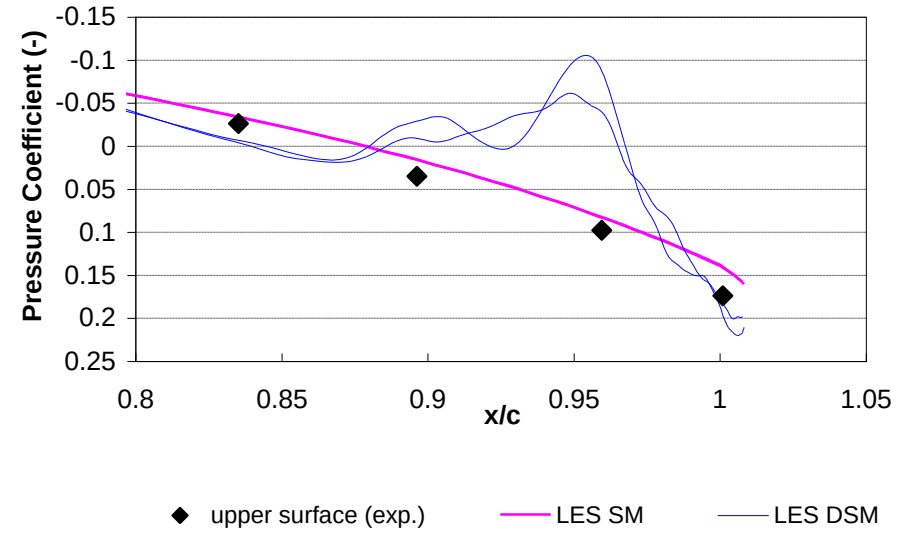

Figure 7.: Enlarged view of the trailing edge region, Cp, LES, 0 deg

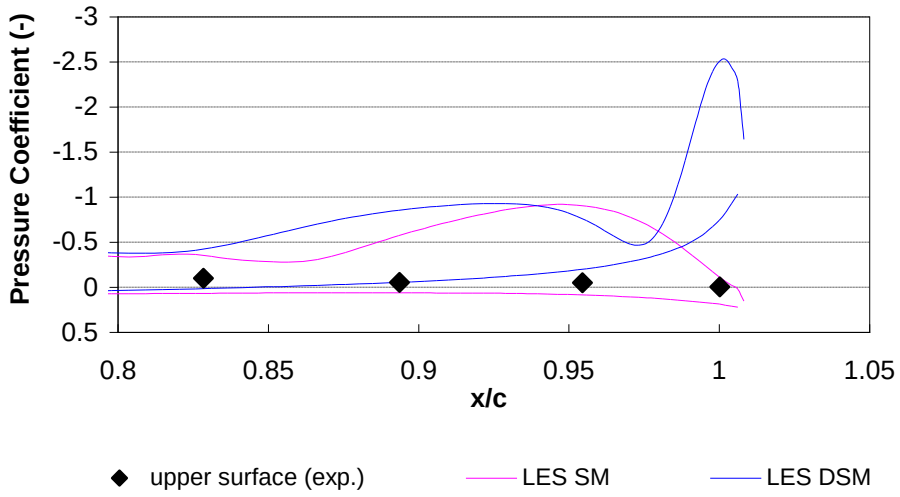

Figure 7.: Enlarged view of the trailing edge region, Cp, LES, 15 deg

7.2 Case 2: Prolate spheroid at ratio 6:1

7.2.1 Overview

Critical flow parameters reported are the non-dimensional, time-averaged lift and pitching moment coefficient, the surface pressure and skin-friction coefficient, the mean velocity profiles and some features of the flow. The current results are an array of all the calculations obtained, some more can be found in Appendix C. The time-step for the simulations corresponding to a CFL number around one was equal to $10^{-4} \cdot L_p / U_\infty$ for each case, where L_P is the length of the prolate spheroid, U_∞ the freestream velocity.

After the initial transients vanishes, the statistical sampling was started, and sufficient time (25,000 time-steps) was allowed for each of the runs to develop time-averaged data for the first and second-order statistical moments of pressure and velocity. As an example, for a time step of the order of 10^{-5} this was equivalent to about one second in simulation time. A statistically stationary solution was obtained when the residuals dropped below the criterion and convergence was estimated when the monitored local quantities and integrals were not differing by more than 3-5% with respect to the previous sample's statistics (as recommended by Constantinescu and Squires, 2003; Radhakrisnan et al., 2006; Xing et al., 2007 in similar LES/DES procedures).

Measurements of pressure and skin-friction coefficients and velocity profiles on the body are taken over a longitudinal axis (for C_p and C_f) and two circumferential planes reported by VPI (for C_p and C_f and the velocities). Figure 7.21 shows the location of these lines.

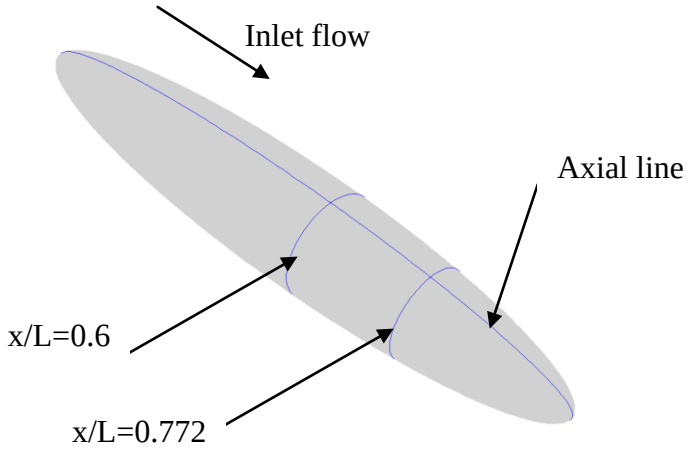

Figure 7.: location of measurement lines on the spheroid surface

Similarly for the velocity profiles, five different angles were used on the leeward side of the spheroid to measure the axial, tangential and radial velocities at the two circumferential lines of *x/L = 0.6* and *0.772*.

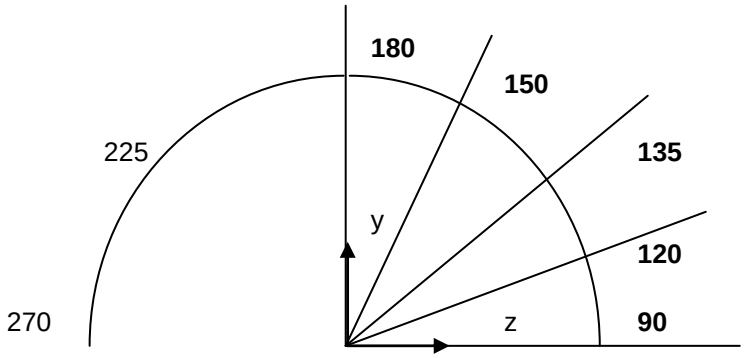

Figure 7.**:** Leeward side locations for velocity profiles

7.2.2 Visualisation on the flow behaviour

Figure 7.23 and Figure 7.24 show the surface shear flows along the prolate geometry at 20° and 30° angle of attack, respectively. Both side view and top view are detailed. Surface streamlines diverge from the windward plane of symmetry around the spheroid, separation is marked by the convergence of the surface flows, and reattachment is identified by the divergence of the surface flows. In the suction side, streamlines from the windward and leeward sides converge to form the primary

separation line. For the geometry at 20°, the primary separation is initiated at an axial location around x/L = 0.4.

At 30° angle of attack, the primary separation is initiated quite early, before the boundary layer trip used for simulations at x/L = 0.2. Increase in the angle of attack leads to more substantial divergence of the flow from the windward plane of symmetry along almost the entire length of the body. For both 20° and 30°, a secondary separation and reattachment is apparent in the aft part of the leeward side. Fluid particles experience adverse pressure gradients with the boundary layer.

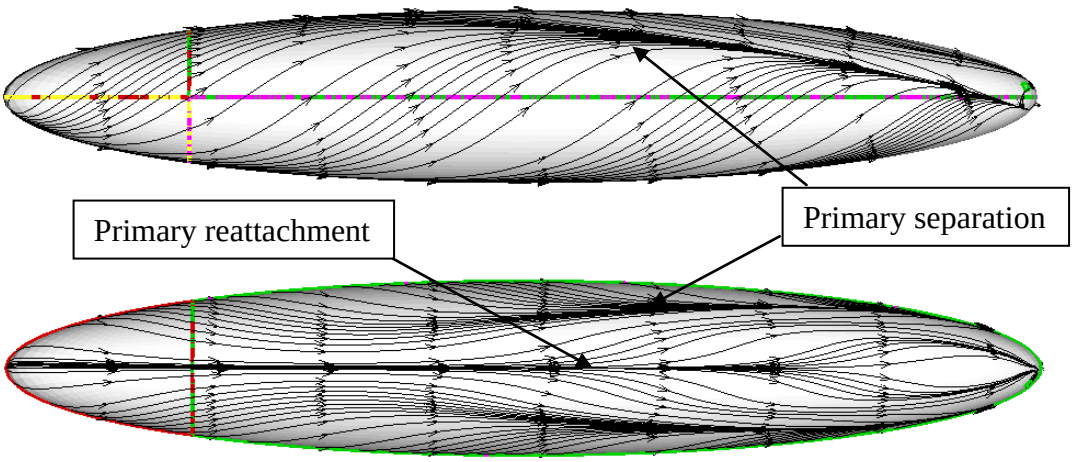

7.: Surface shear lines for DES 20 deg AoA with laminar zones, side view and top view

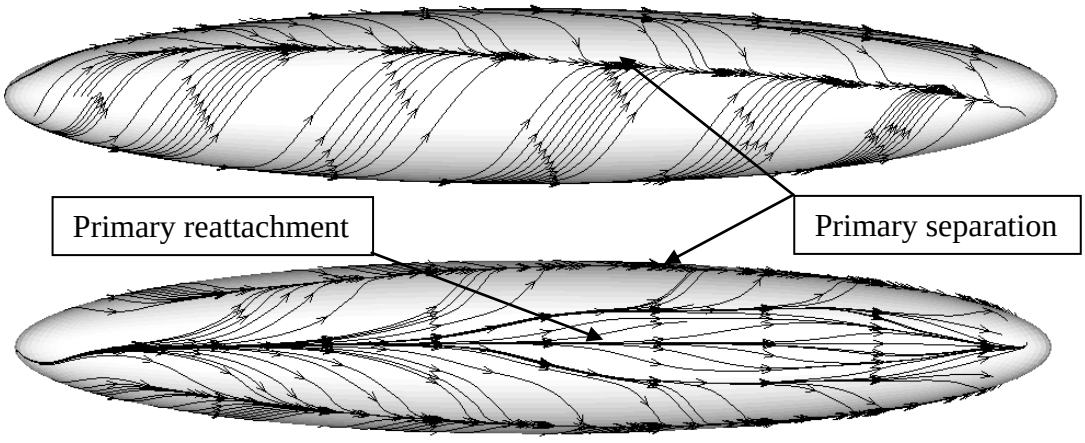

7.: Surface shear lines for LES 30 deg AoA, side view and top view

Figures 7.25 and 7.26 show the contours of velocity magnitude at 20° taken at the plane x/L = 0.772 for the DES case. The first picture is for the mesh A (high near-wall resolution, y^+=5.7, 24 layers in the boundary) while the second is for the mesh F (low near-wall resolution, y^+=65, 20 layers within the boundary). Flow separation for both cases appears between 115°-120°. The only noticeable difference is in the outer boundary layer regarding the strength of the rotating flow but it looks like the RANS model of the DES computations is predicting accurately the flow.

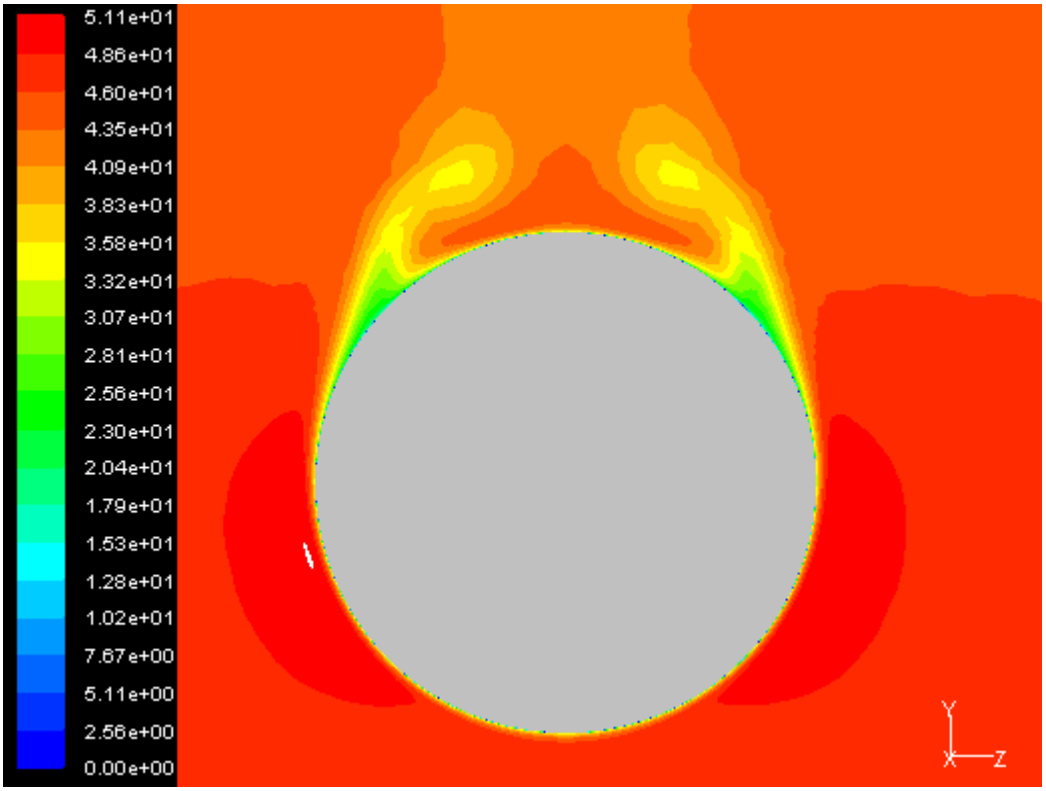

7.: Contours of Velocity Magnitude at x/L=0.772 and 20 deg AoA, mesh A

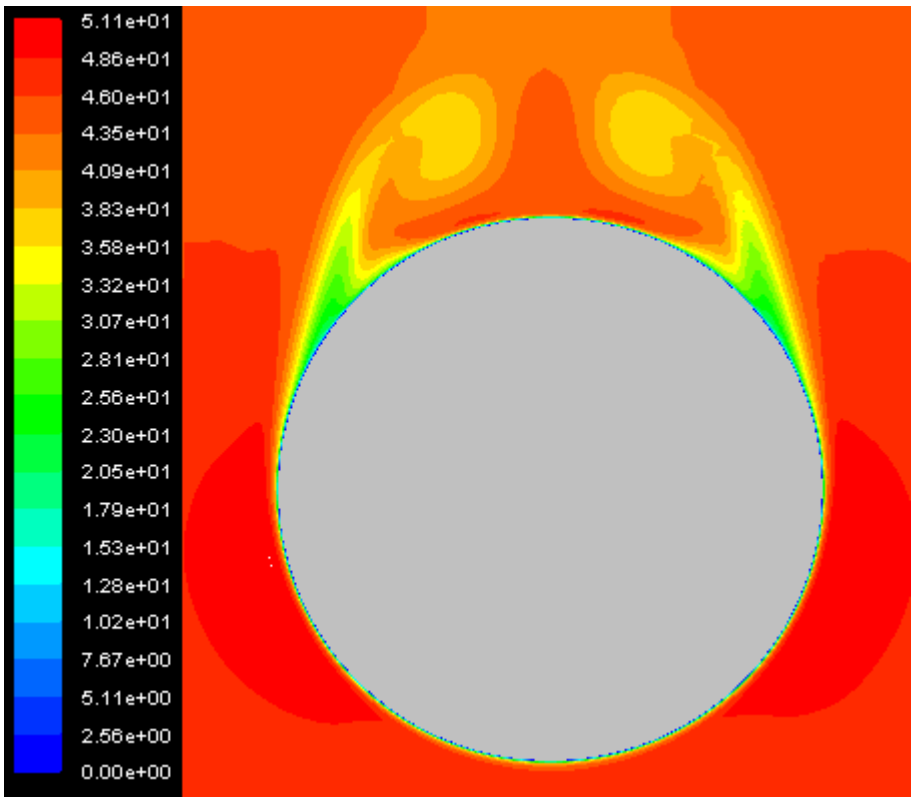

7.: Contours of Velocity Magnitude at x/L=0.772 and 20 deg AoA, mesh F

Figures 7.27 to 7.30 show a perspective view of the crossflow separation and the associated longitudinal vortices on the 6:1 prolate spheroid at 20 deg. The flow is represented by the pathlines from the surface. We can observe the flow detaching on the leeward side. All models predict the outcome of the flow well and capture the key features, and from the pictures it appears that LES DSM is the one that captures qualitatively better the swirling and the vortices.

7.: Pathlines of flow separation LES SM, AoA 20 deg, mesh F

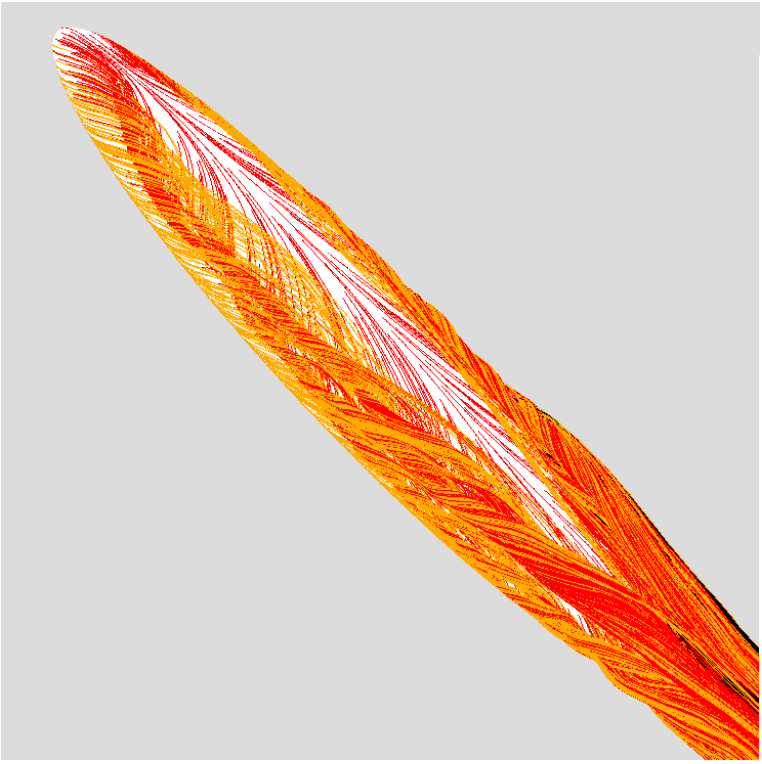

7.: Pathlines of flow separation LES DSM, AoA 20 deg, mesh F

7.: Pathlines of flow separation DES Rκε, AoA 20 deg, mesh F

7.: Pathlines of flow separation DES SA, AoA 20 deg, mesh F

The vorticity contours show the development of the structures from the primary separation along the leeward side at 20° angle of attack. The time-averaged skin friction contours on the spheroid surface show the influence of the free turbulence model on the boundary layer and the flow. The vortex develops further downstream in size becoming more circular and in the aft cross-sections the vortex detaches completely from the body surface.

A longitudinal band of minimum C_f extends from x/L = 0.2 for the DES case or from about x/L = 0.1 for the LES case to the rear of the spheroid. The windward edge of this band corresponds to the primary separation lines while the leeward edge to the secondary separation line in the static flow. The Dynamic Smagorinsky-Lilly appears to have the most unsteady behaviour. This is also observed from the results in the next section.

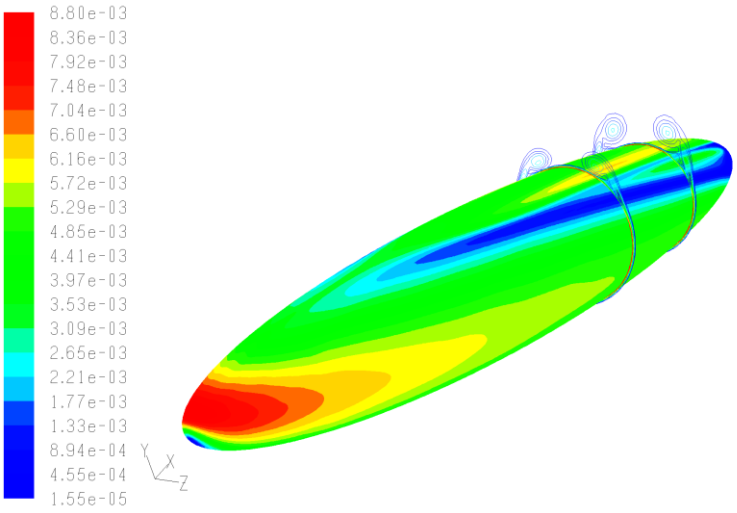

7.: Mean surface skin friction coefficient and vorticity magnitude contours, LES SM, AoA 20 deg

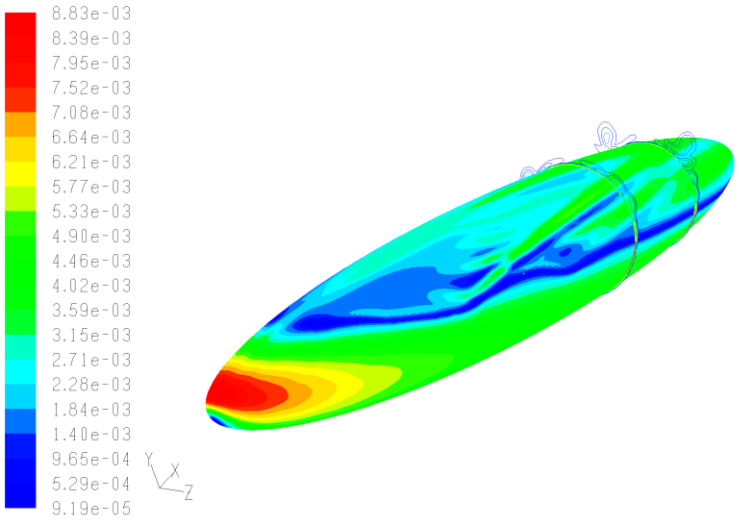

7.: Mean surface skin friction coefficient and vorticity magnitude contours, LES DSM, AoA 20 deg

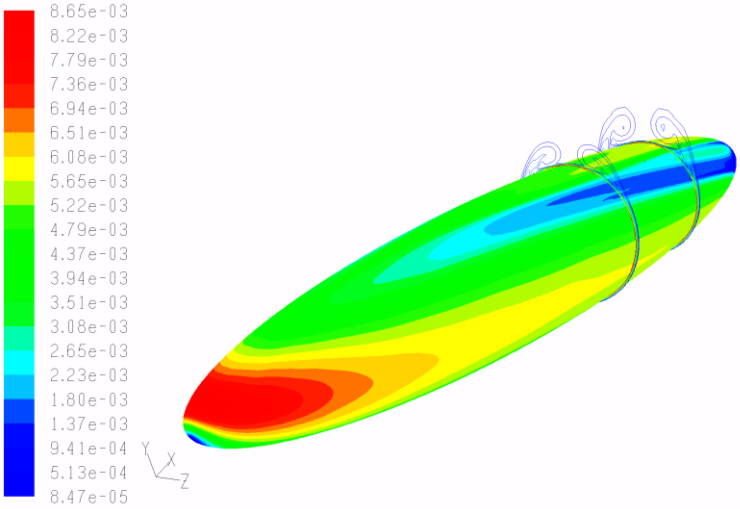

7.: Mean surface skin friction coefficient and vorticity magnitude contours, DES Rκε, AoA 20 deg

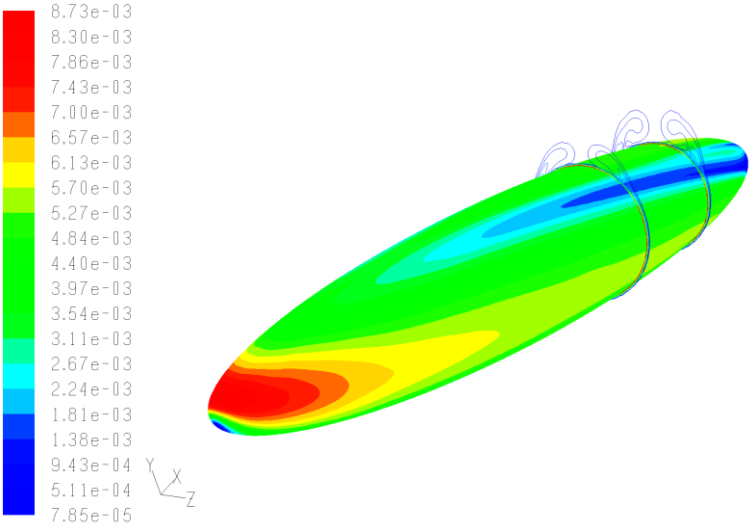

7.: Mean surface skin friction coefficient and vorticity magnitude contours, DES SA, AoA 20 deg

7.2.3 Pressure and skin-friction coefficients

Figures 7.35 and 7.36 show the static pressure coefficient along the axial line for meshes A & C (low y^+), defined as equation (7.3) above. The agreement between simulations and experiments is very good, especially on the leeward side, over the majority of the body's length. LES seem to be predicting the pressure slightly better than DES. The jump in values at x/L = 0.2 for DES corresponds to the end of the laminar zone created in the mesh. Along both sides in the stern, there is some discrepancy, more visible for the LES models; one contributor could be the presence of the support sting used in the experiments and not included in the CFD and the other reason is the high curvature in the shape resulting in a more stretched mesh around this region than at mid-body. Moreover, as experienced for the NACA airfoil, the LES models do give the instantaneous fluctuation changes in the flow and this can be a third reason for the slight jump in the values. But overall, the predictions are satisfactory.

Similarly, figures 7.39 and 7.40 indicate the surface pressure for mesh E (high y^+) for all models. Both DES models are showing excellent correlation with the measurements, inclusive the stern of the body. LES models are also as accurate, if not better, over most of the windward side (over prediction of the pressure up to x/L=0.7) and near the end of the leeward side. The main differences between SM and DSM are in the stern, where the flow has separated. However near the expected region of flow separation between x/L = 0.5 and x/L = 0.8, all models are close to the experiments. There is a wobble showing at x/L = 0.2 for the DSM model, may be linked to the flow transition.

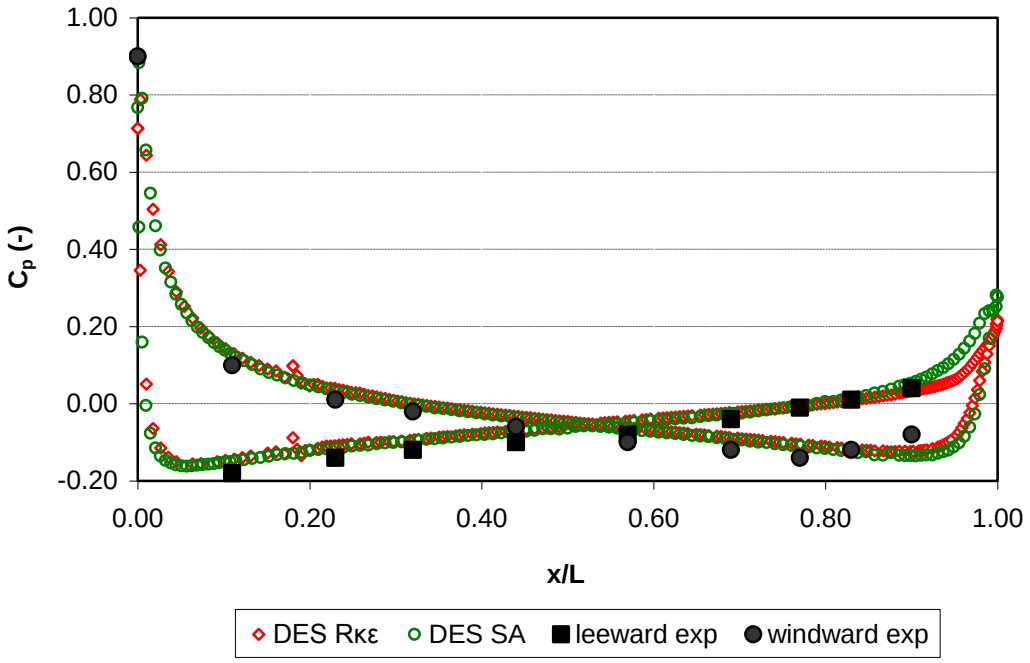

Figure 7.: Axial pressure coefficient on the surface of the prolate at 10 deg AoA, DES, mesh A

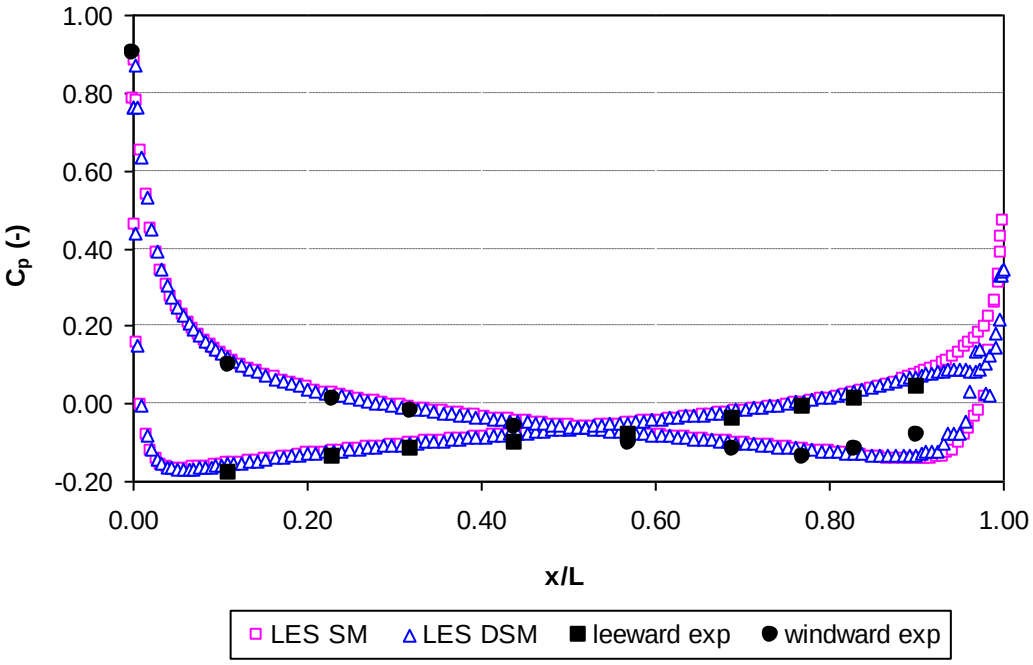

Figure 7.: Axial pressure coefficient on the surface of the prolate at 10 deg AoA, LES, mesh C

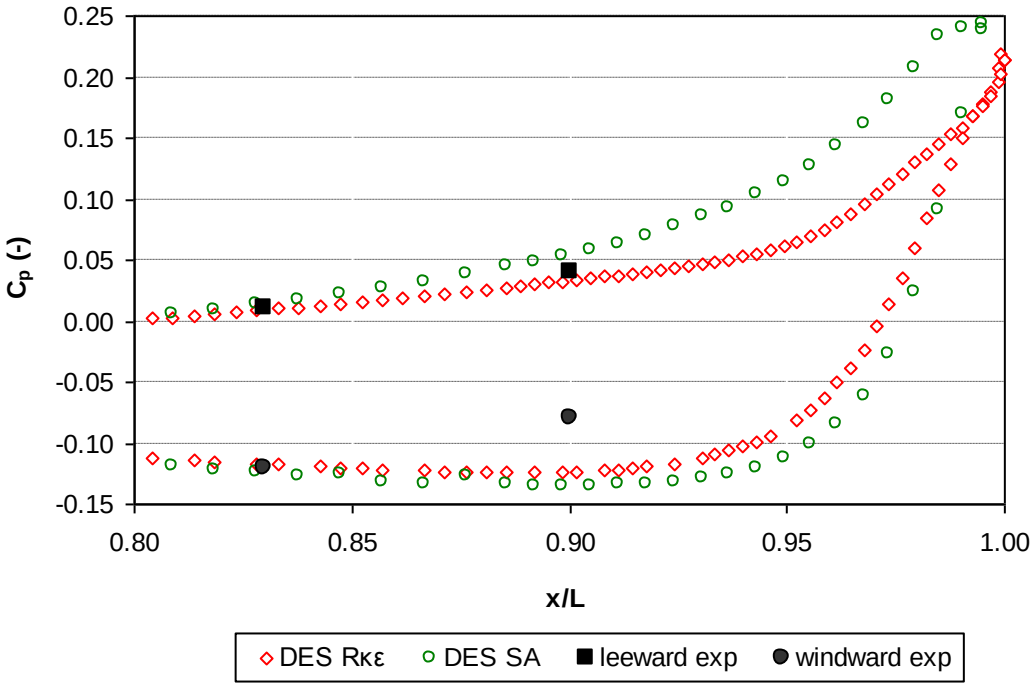

Figure 7.: Close-up view of C_P at the trailing edge region, DES, mesh A

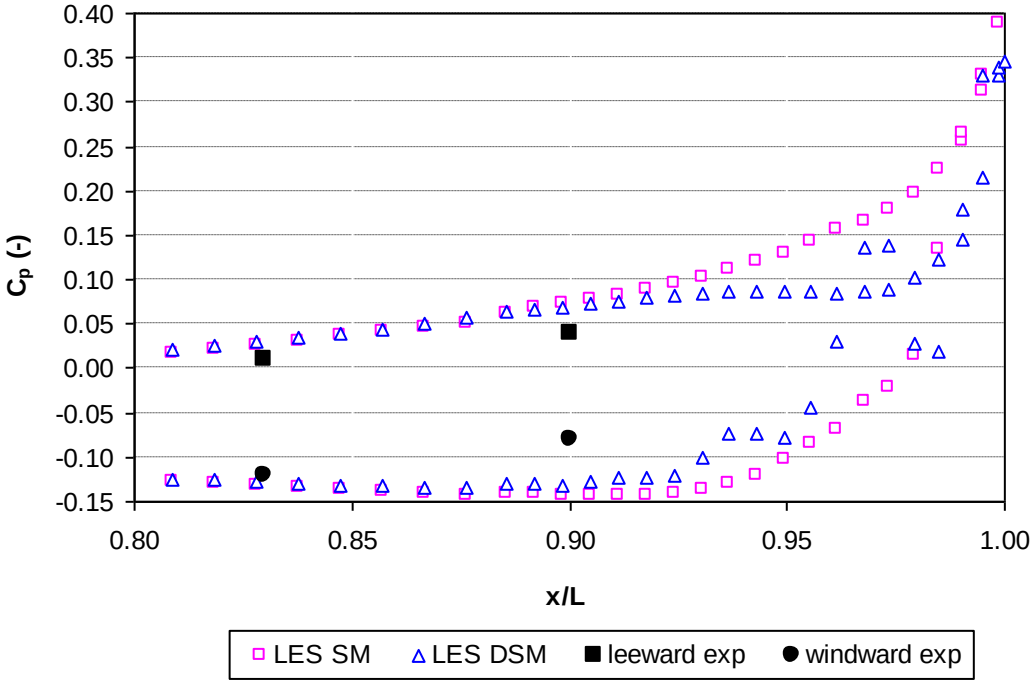

Figure 7.: Close-up view of C_P at the trailing edge region, LES, mesh C

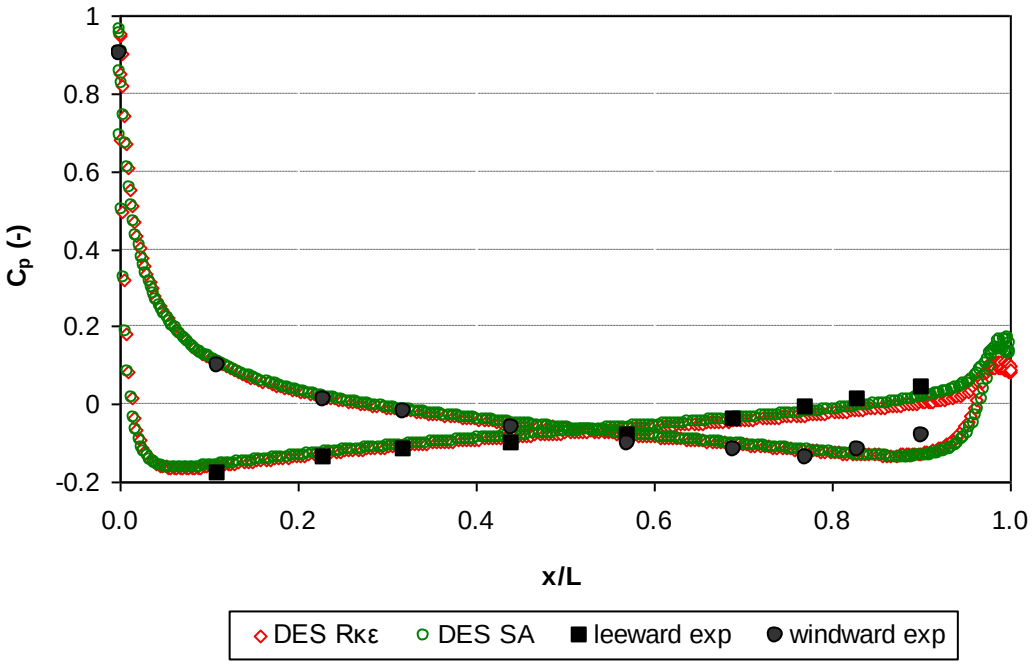

Figure 7.: Axial pressure coefficient on the surface of the prolate at 10 deg AoA, DES, mesh E

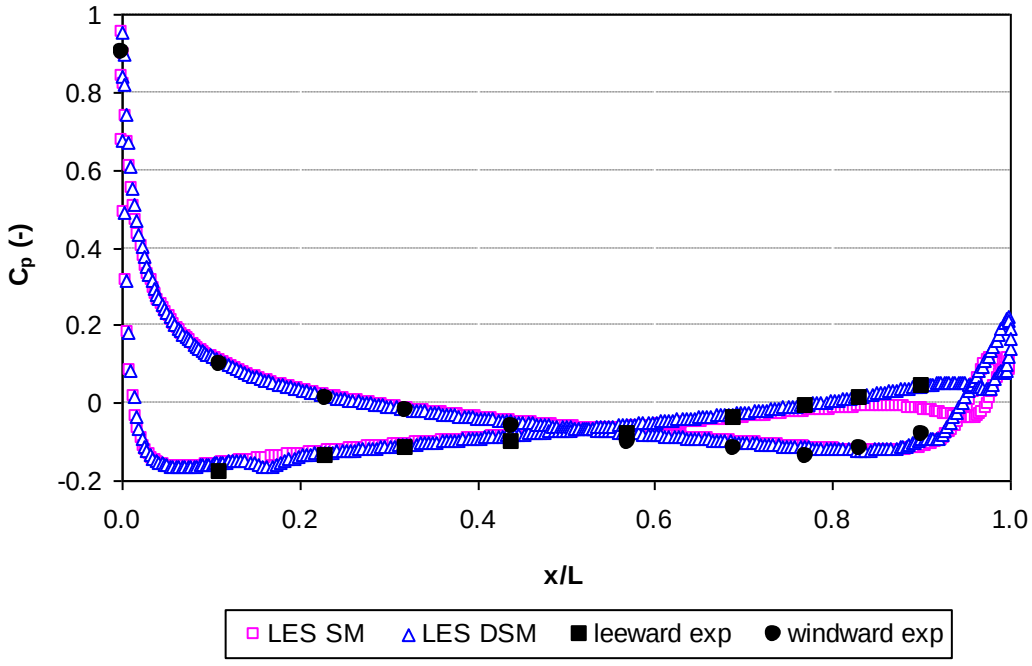

Figure 7.: Axial pressure coefficient on the surface of the prolate at 10 deg AoA, LES, mesh E

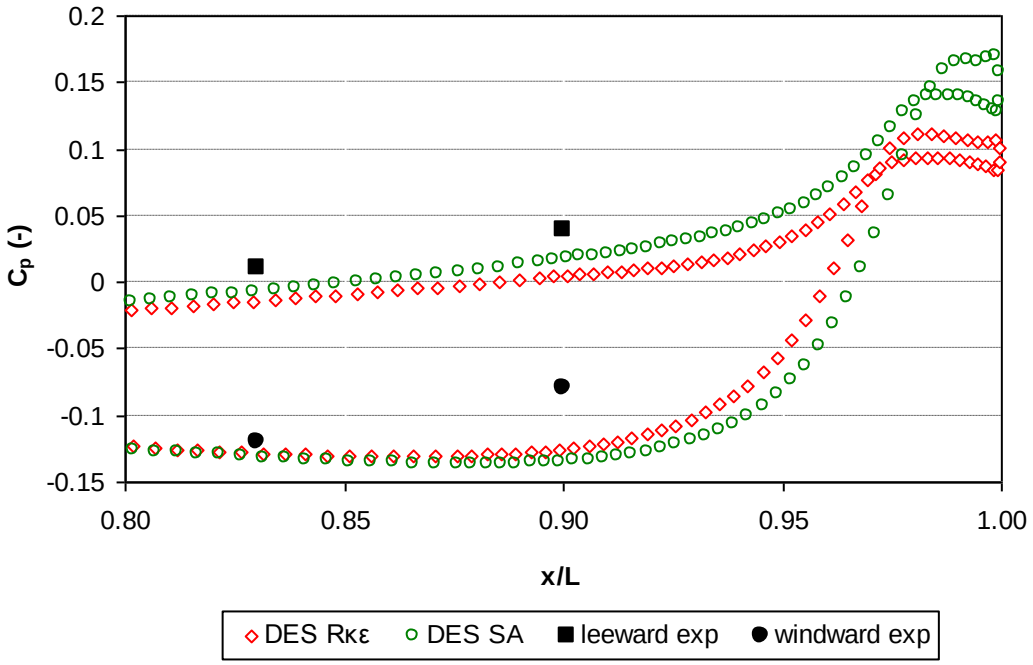

Figure 7.: Close-up view of C_P at the trailing edge region, DES, mesh E

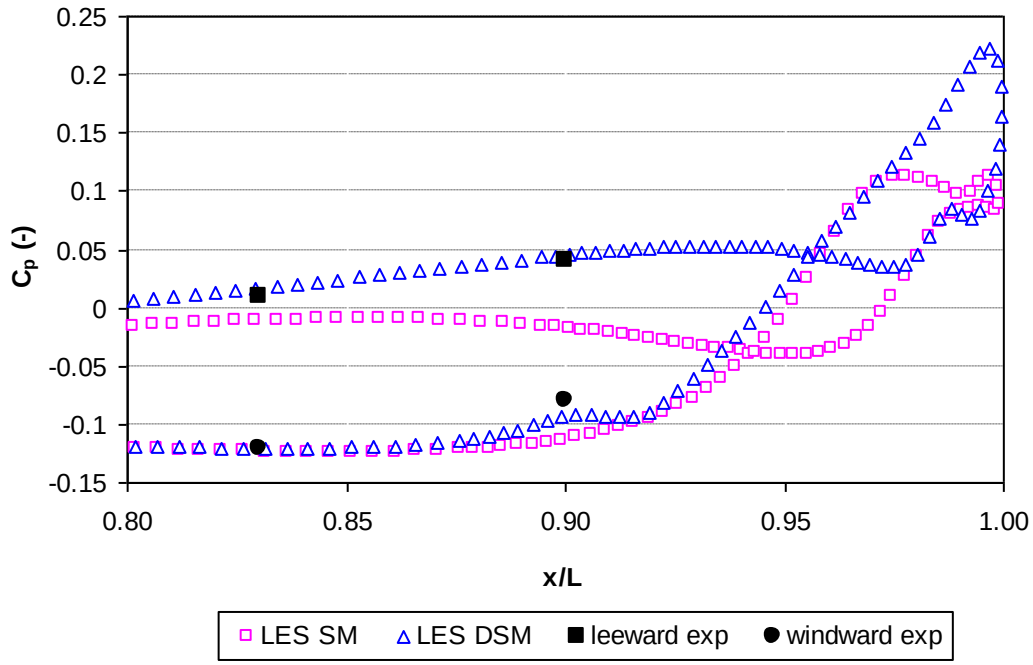

Figure 7.: Close-up view of C_P at the trailing edge region, LES, mesh E

In figures 7.43 and 7.44, C_p is shown as a function of the circumferential angle at the location x/L = 0.772, on the leeward side from 90 to 180 degrees on mesh F for 10 and 20 degrees angle of incidence respectively. For the case of the AoA = 10 deg,

the agreement between all the CFD predictions and the experimental data is good between 90 and 130 degrees; the SM model in particular is very good up to 150 degrees. Then the DES calculations are the most accurate, though the LES SM is also correct with the exception of a small lag at 150 degrees. The LES DSM is under predicting the pressure coefficient for most of the surface but particularly between 120 and 140 degrees, then it is over predicting like the other models.

The range between 120 and 150 degrees is the region linked to the primary vortex creation, with low pressures associated on that region. It is likely that the LES DSM is the most sensitive model over this region. As mentioned above, the mesh is also liable to influence the results of the two LES models; although the SM method is showing very good correlation with the data from VPI.

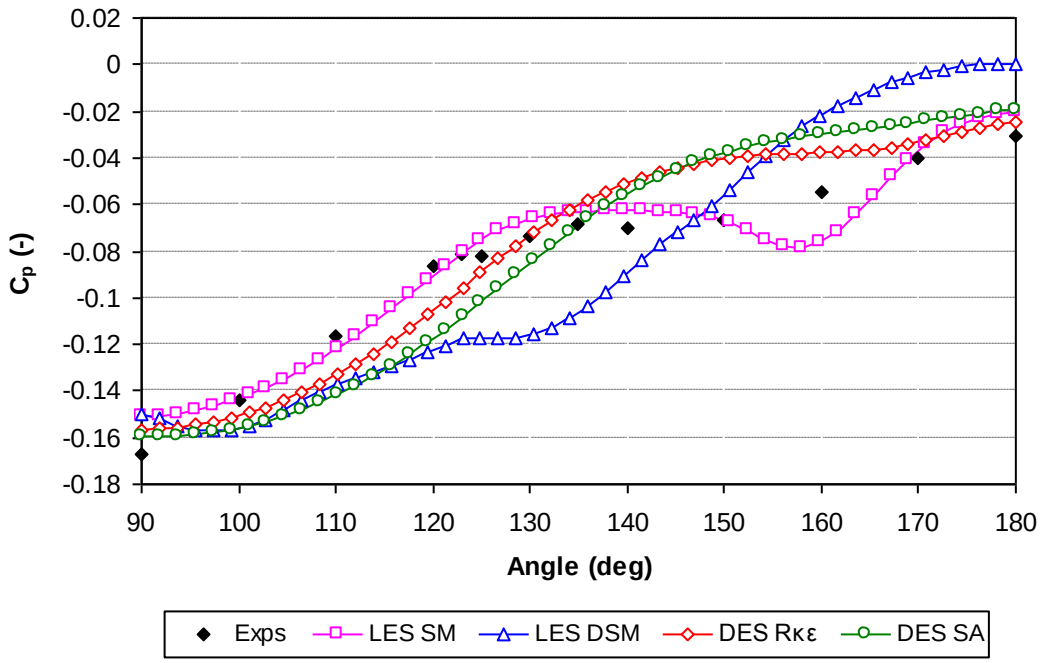

Figure 7.: Circumferential pressure coefficient at AoA 10 deg and x/L 0.772

For the 20 deg case, C_p shows the existence of a primary and a secondary separation on the body, and the agreement between experimental data and CFD runs is excellent for LES SM and reasonable for runs DES Rκε and DES SA. Although all models seem to predict the minimum C_p at 90 degrees, only the LES SM is the closest one for the second minima at 165°. The predictions by LES DSM diverge considerably

from the other models and the experimental data from 140 to 180 deg. This is in accordance to the flow observations, and the dynamic nature of the model. These results show the sensitivity of the predictions to the models and the grid and suggest that the LES DSM requires finer resolution; whereas the two DES models are more adaptable with the use of wall-models in the CFD.

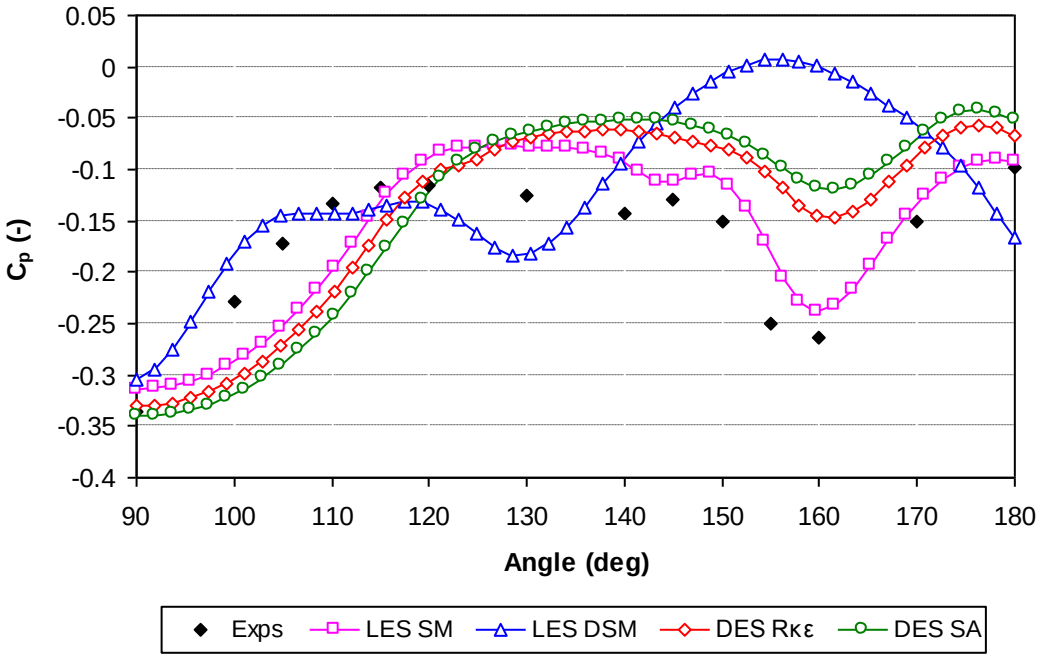

Figure 7.: Circumferential pressure coefficient at AoA 20 deg and x/L 0.772

The skin friction coefficient at a longitudinal location of x/L = 0.6 and x/L = 0.772 is given in fig. 7.45 and fig. 7.46, respectively at 10 deg and at 20 deg angle of attack, for meshes A and C. For both examples, the trend in prediction of the skin friction is good, particularly for the first example. With the angle increasing, the flow becomes more interesting and from experimental observations, it is the locating plane for flow separation. The first separation at 90 deg is well covered by all models; however, the DES models predict the second one at 150 deg better. This could be due to instability or the influence of the turbulent flow, since no laminar zone was defined in LES. Nonetheless, the latter models accurately describe the flow in other locations around the plane. The results are quite good because of the fine mesh near the surface.

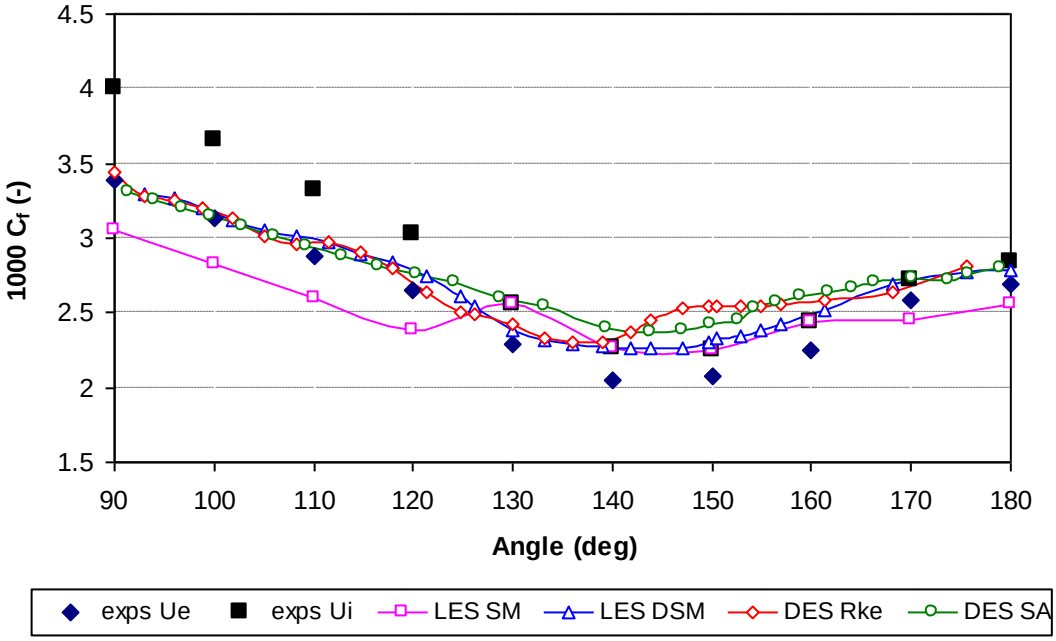

Figure 7.: Skin friction distribution at plane x/L = 0.6 and 10 deg angle of attack, mesh A

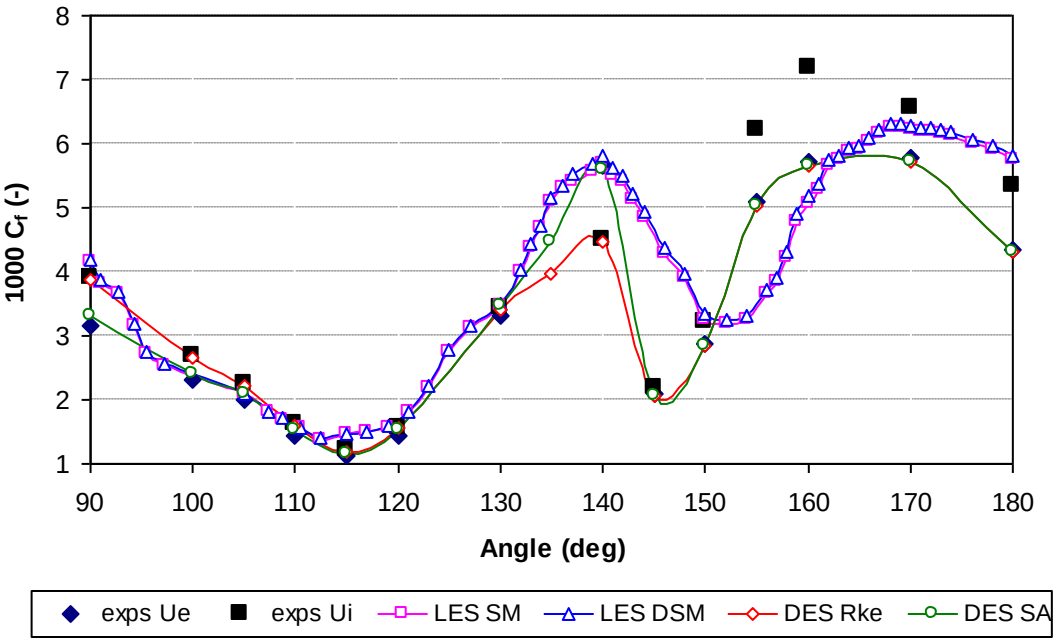

Figure 7.: Skin friction distribution at plane x/L = 0.772 and 20 deg angle of attack, mesh C

The skin friction coefficient at a longitudinal location of x/L = 0.6 and x/L = 0.772 is given in fig. 7.47 and fig. 7.48, respectively at 10 deg and at 20 deg angle of attack, for meshes E and F. For the first case, the trend in prediction of the skin friction is good. Both DES models over predict the friction coefficient until after separation,

where as the LES models are close until 130 deg leeward, then they under predict C_f at separation to return to the correlation at 180 deg.

For mesh F the predicted skin-friction is more interesting. In terms of trend of the curves, all models are in accordance with the experimental data. The values of minimum and maximum C_f are also within the range of validity. The differences appear in the values at certain points, with quite large errors.

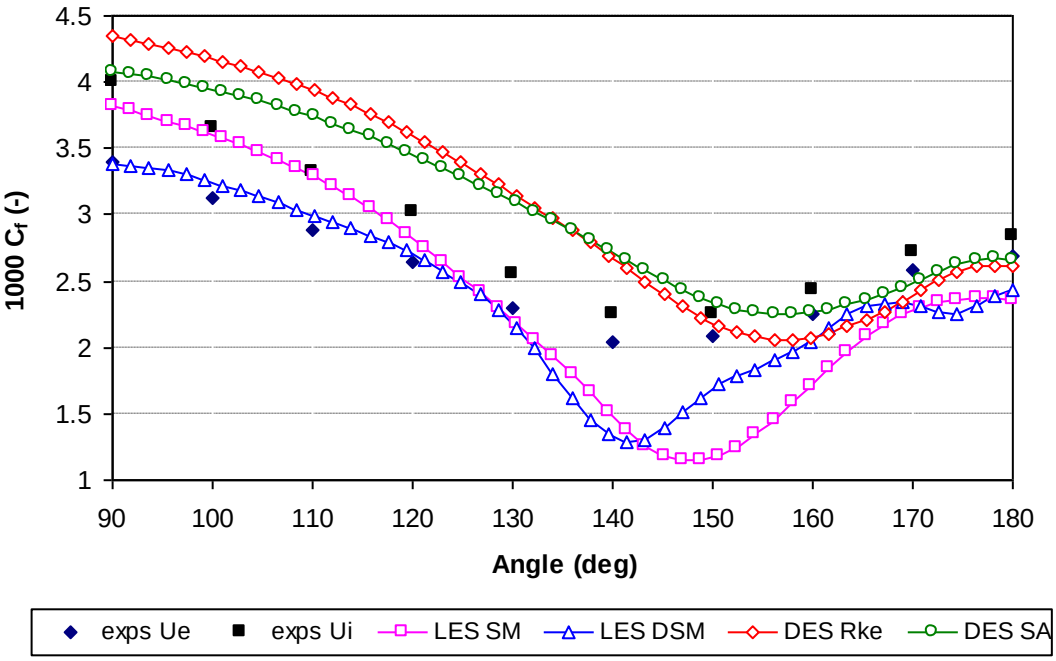

Figure 7.: Skin friction distribution at plane x/L = 0.6 and 10 deg angle of attack, mesh E

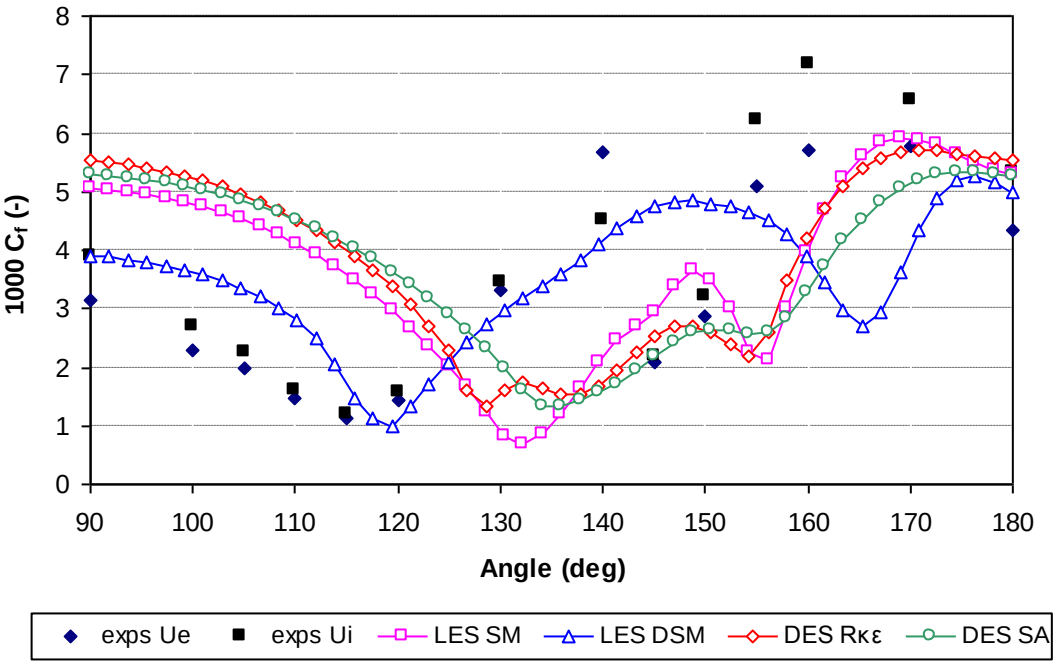

Figure 7.: Skin friction distribution at plane x/L = 0.772 and 20 deg angle of attack, mesh F

7.2.4 Mean Velocity Profiles

Figures 7.49 to 7.57 show the normalized time-averaged boundary-layer velocity profiles at *x/L=0.6*, for the circumferential angle of 90 deg for AoA of 10 and 20 deg. The velocity components are presented in the body-surface coordinate system. Here, *U* is tangent to the body and point toward the tail of the model, *V* is normal to the body (positive outwards), and *W* is tangent to the body and forms a right-handed coordinate system. The letters A to F correspond to the grids presented in the previous chapter. The other letters correspond to the turbulence model applied for that specific case. Only a sample is shown here, but graphs have been generated for the circumferential angles introduced above and are all presented in Appendix C with relevant explanations on the coding used in the graphs.

LES qualitatively captures the influence of the angle of attack that is evident from the increase in *V* in the outer part of the boundary layer. This increase in *V* is caused by fluid being extracted from the boundary layer into the primary vortices on the back of the body. For the normal (or *V*) component good agreement with experimental data is obtained for quasi all the models irrespectively of grid

resolution and for both angles of attack. For the tangential (or W) component we observe that all LES models reproduce the experimental data fairly well. For the axial (or U) component we find reasonable agreement between predictions and good curve correlation with the data. In general, the agreement between the LES, the DES and the experimental data is reasonable considering the complexity of the flow and this is also highlighted in the remaining velocities profiles.

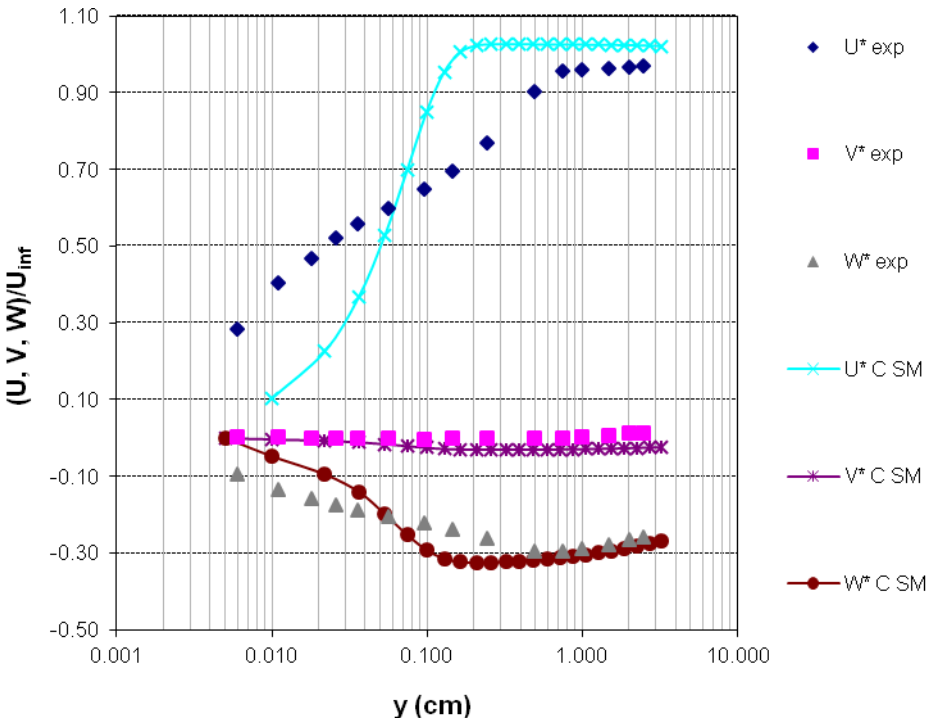

Figure 7.: Mean velocity profile on the body surface x/L = 0.600, φ= 90 deg, AoA 10 deg, mesh C

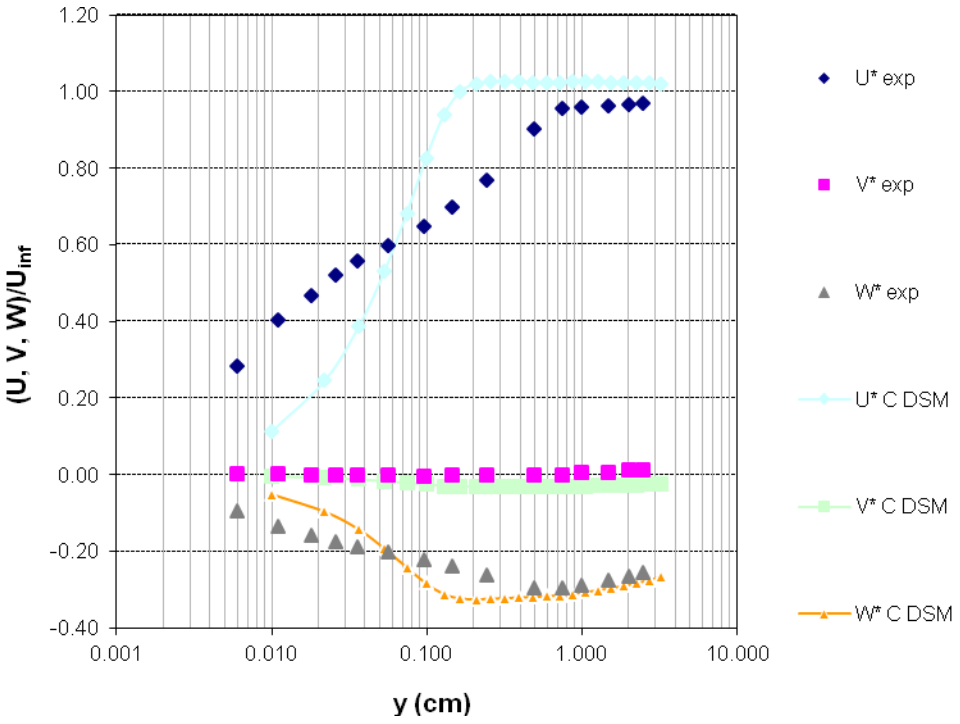

7.: Mean velocity profile on the body surface x/L = 0.600, φ= 90 deg, AoA 10 deg, mesh C

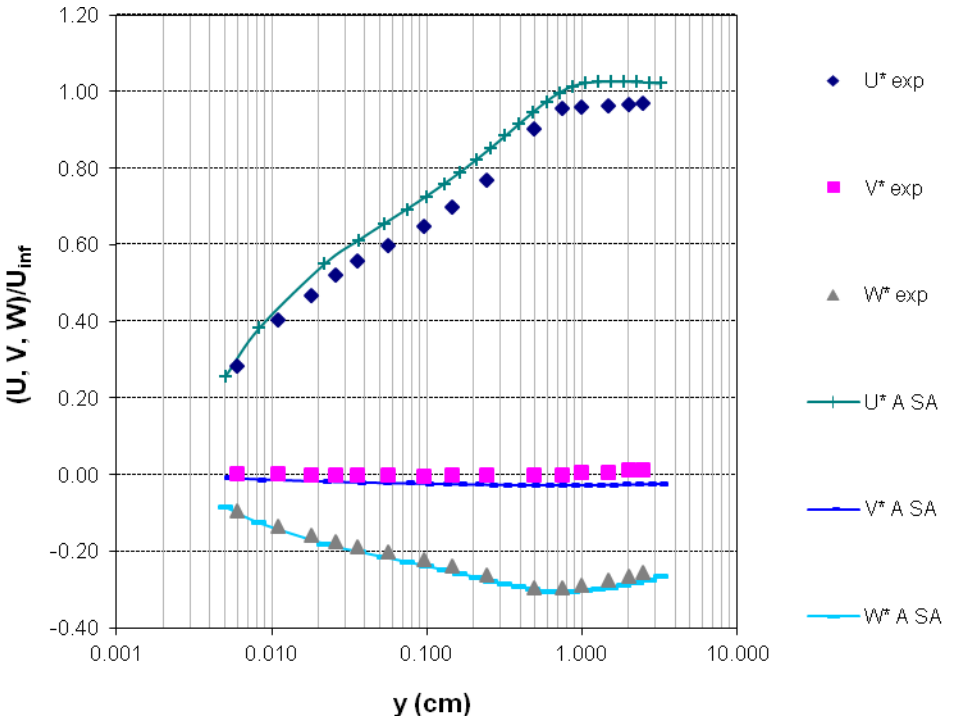

7.: Mean velocity profile on the body surface x/L = 0.600, φ= 90 deg, AoA 10 deg, mesh A

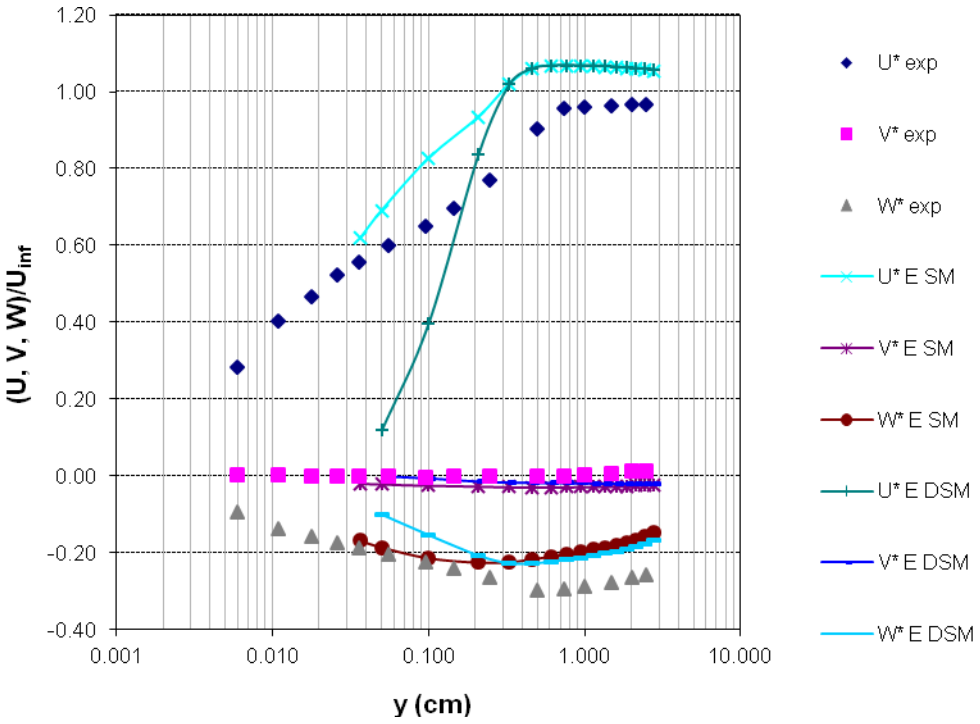

Figure 7.: Mean velocity profiles on the body surface x/L = 0.600, φ= 90 deg, AoA 10 deg, mesh E

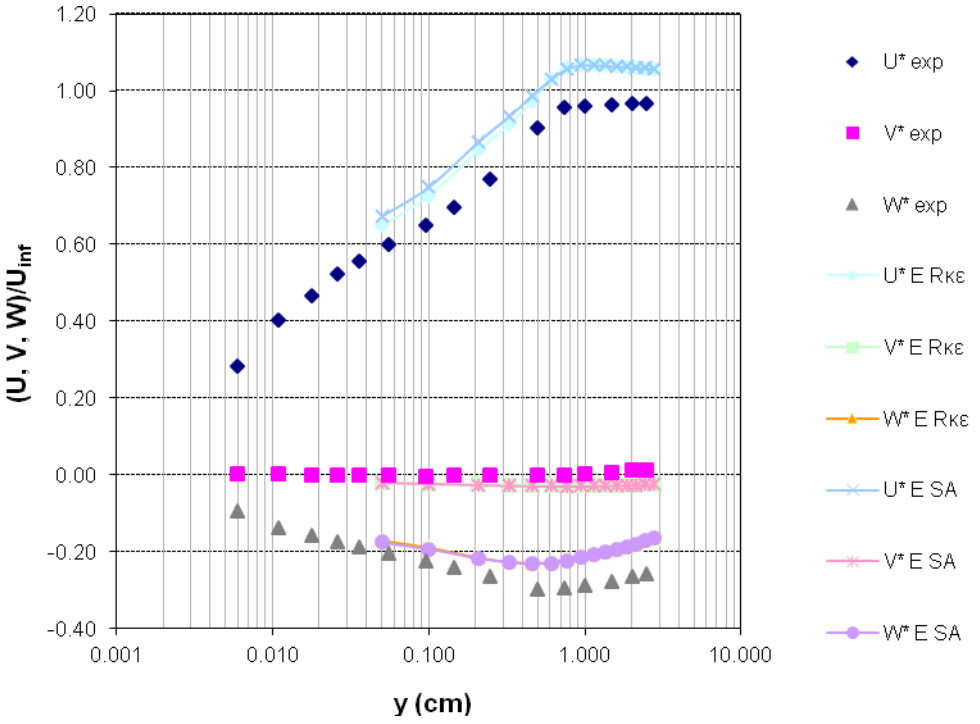

7.: Mean velocity profiles on the body surface x/L = 0.600, φ= 90 deg, AoA 10 deg, mesh E

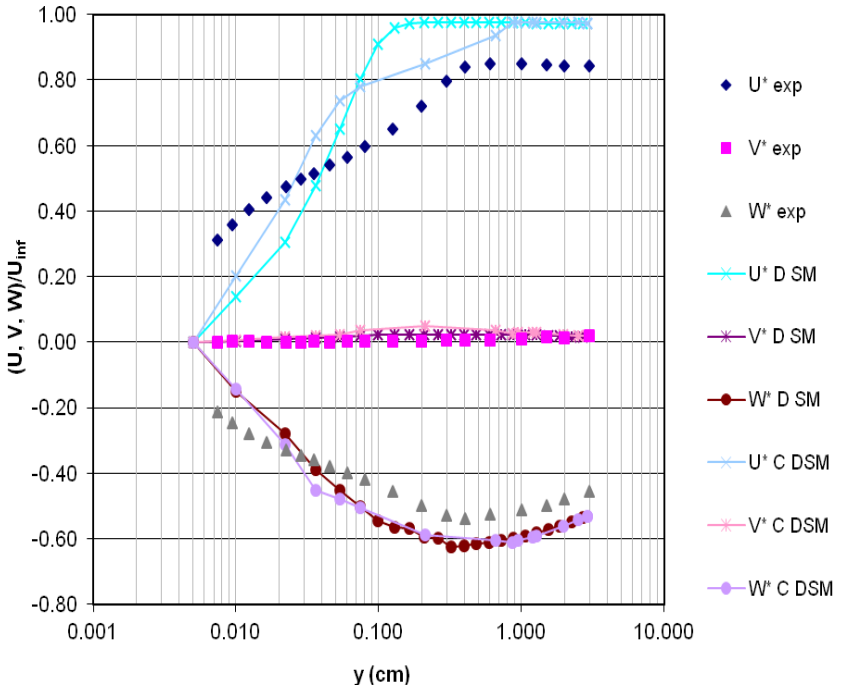

7.: Mean velocity profiles on the body surface x/L = 0.600, φ= 90 deg, AoA 20 deg, mesh D

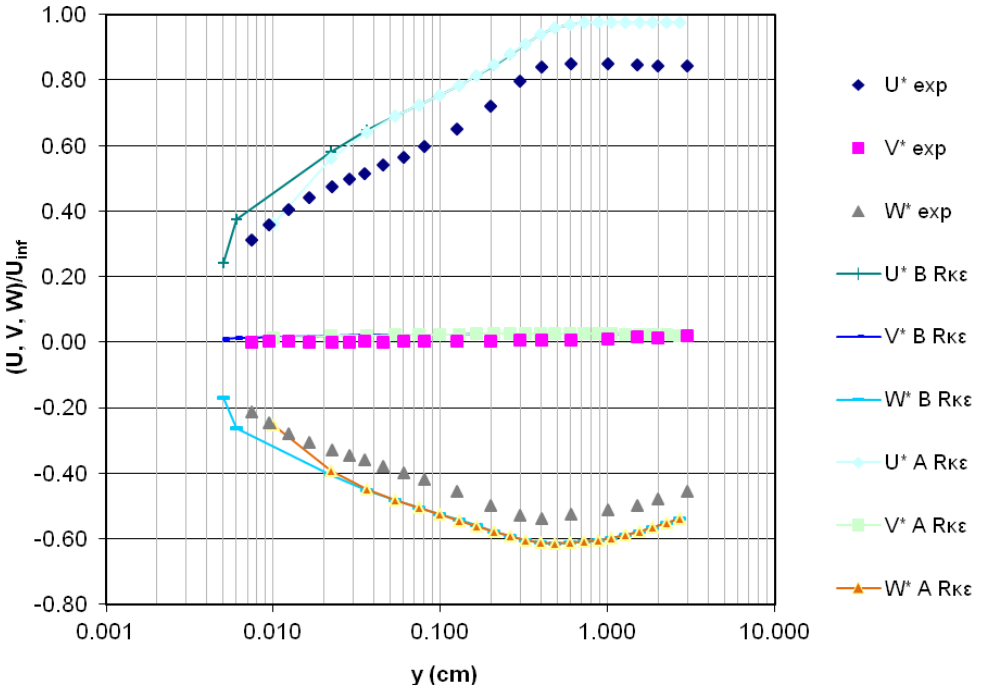

7.: Mean velocity profiles on the body surface x/L = 0.600, φ= 90 deg, AoA 20 deg, mesh A & B

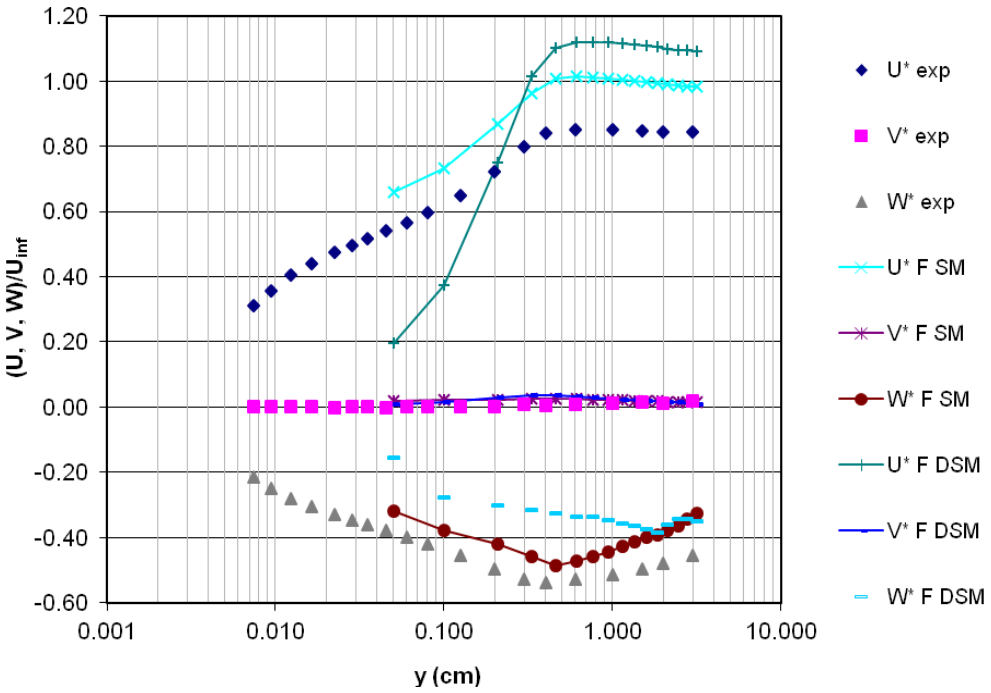

Figure 7.: Mean velocity profiles on the body surface x/L = 0.600, φ= 90 deg, AoA 20 deg, mesh F

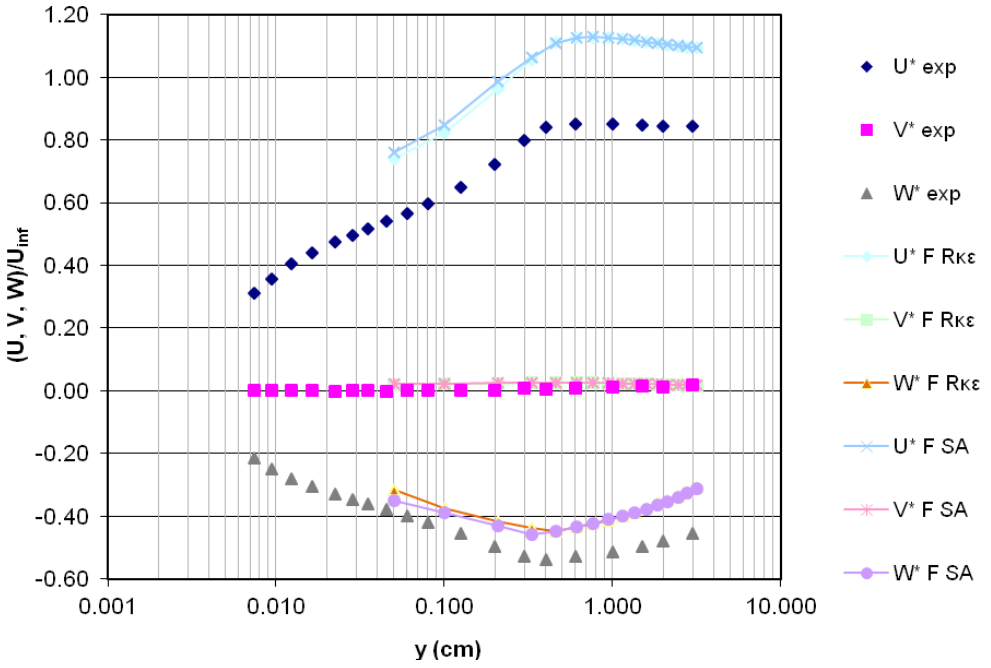

7.: Mean velocity profiles on the body surface x/L = 0.600, φ= 90 deg, AoA 20 deg, mesh F

7.2.5 Lift force and pitching moment

The non-dimensional lift and moment coefficients at angles of attack are shown in the figure below, compared with measurements from Wetzel et al. (1998). The time-averaged values are defined as:

$$C_L = \frac{L}{0.5 \cdot \rho \cdot L_p^2 \cdot V^2} \tag{7.4}$$

and

$$C_M = \frac{M}{0.5 \cdot \rho \cdot L_p^3 \cdot V^2} \tag{7.5}$$

where L is the lift force, M the moment, A the projected area L_p the length of the body and V the velocity. The experimental uncertainty was found to be 1.5% for both lift and moment.

The lift is characterized by a nonlinear increase with incidence angle. This is due to the low pressure near the core of the vortices which is impressed upon the nearby body surface. The predictions vary in a wide range. Observations show that the differences among the models increase with the incidence. Most models under predict the lift, but at low angles of incidence, the correlation between experiments and simulations is very good. The lift predictions show some correlations with the behaviours of the surface quantities discussed before. The errors are higher for the moment coefficient. At high angles of attack, more differences occur, especially at 30°: the refinement near the spheroid was insufficient to account for high angles, and hence some differences occur.

Table 7.: Lift Coefficient at various angles of attack

AoA	5 deg	Abs. Error (%)	10 deg	Abs. Error (%)	20 deg	Abs. Error (%)	30 deg	Abs. Error (%)
Exp.	0.0015	-	0.0032	-	0.0132	-	0.0268	-
LES SM	0.001482	1.20	0.003514	9.81	0.012089	8.42	0.02365	11.75
LES DSM	0.001491	0.60	0.00318	0.62	0.013376	1.33	0.0246	8.21
DES SA	0.0014	6.67	0.002917	8.84	0.011359	13.95	0.021362	20.29
DES Rκε	0.001521	1.40	0.00318	0.63	0.0133	0.76	0.02598	3.06

Table 7.: Moment Coefficient at various angles of attack

AoA	5 deg	Abs. Error (%)	10 deg	Abs. Error (%)	20 deg	Abs. Error (%)	30 deg	Abs. Error (%)
Exp.	-0.0019	-	-0.0035	-	-0.0056	-	-0.0072	-
LES SM	-0.0021	10.53	-0.00387	10.57	-0.00497	11.25	-0.0073	1.39
LES DSM	-0.002	5.26	-0.00357	1.86	-0.00519	7.32	-0.00692	3.89
DES SA	-0.00224	17.89	-0.00378	8.00	-0.00507	9.46	-0.00712	1.11
DES Rκε	-0.00213	12.11	-0.0036	2.86	-0.00544	2.80	-0.00686	4.72

"Let us beware of saying there are laws in nature. There are only necessities: there is no one to command, no one to obey, no one to transgress. When you realize there are no goals or objectives, then you realize, too, that there is no chance: for only in a world of objectives does the word "chance" have any meaning." **Friedrich Nietzsche**

"Statistics are like a bikini: what they show can be exciting but what they hide is essential. The same is true for CFD. It is very easy to get colourful pretty pictures that look correct; the problem lies in making sure that what you see is really what happens in nature"
Jim Bungener, Chief CFD Analyst, Alinghi team

8 Investigation of the flow past the IACC yacht keel with LES and DES

8.1 Contextual overview of the investigation

An America's Cup yacht is a very sophisticated system that should operate optimally in a wide range of sailing conditions. The different mechanisms (over and under the water surface) that compose a sailing yacht act together through several complex relations. The design of an America's Cup yacht must account for this complexity and requires suitable (experimental and numerical) tools able to describe as accurately as possible the system, in order to achieve an optimal configuration.

The challenge faced by any AC team in producing a competitive yacht is double. On one hand, it must be able to perform optimally under any given sailing condition, but particularly under those experienced during racing at the location of the event. On the other hand, the yacht has to ward off the challenge of the other teams in order to win the races and lift the trophy. Over the years, the evolution in the design of the yachts turned them into sophisticated and state-of-the-art boats, so technologically acute that cometh the hour, there are marginal differences between them and little possibility to modify drastically any design feature, should something go wrong.

Since the last edition and onwards for the forthcoming two America's Cups, multi-hulled bodies have taken over. However, this trend in design was initiated by the IACC class, which restricted the differences between the boats (converging them towards a standard configuration), and pushed for the increased use of new technologies, such as CFD, to complete the final configuration of the optimal designs. This push started during the nineties and nowadays more than ever technology is present at all stages of the design.

The role of implementing advanced CFD modelling in the competition is to provide accurate estimates of the forces acting on the boat, in different sailing conditions, in order to improve the reliability of the prediction of the overall performance associated to a given design configuration.

Numerical predictions with near perfect level of accuracy on absolute force estimates are still difficult to obtain (at least for this class of engineering problems). The challenge that was aimed to be met during this thesis was to investigate if there can be an increase in accuracy of numerical predictions by applying the latest available turbulence models in CFD. Although this is more appropriate and in a way easier to achieve when data for different design configurations are considered and available (by design configuration in this case we mean various shapes, properties and parameters), it is still possible to estimate, on a relative basis, which model performs better on the design that was studied herein.

In this chapter, the focus is on the prediction of some of the global force components on the keel contributing to the global balance in one equivalent sailing configuration as tested inside a wind-tunnel section. We present the numerical simulations that have been carried out to estimate the forces acting on the yacht appendages and to investigate the role of the different turbulent models, on some design parameters.

8.2 Assumptions and simplifications of the problem

The overall complexity and the time constraints have prompted the application of a hierarchy of steps characterized by different levels of accuracy, difficulty, computational cost and ease of use. A number of assumptions and simplifications were made in order to reduce the intricacy of the problem:

- The experimental setting of the wind-tunnel was to be reproduced as precisely as possible.
- It was assumed the body was not subject to deformation or modification of the structural integrity; hence fluid-structure interaction was neglected.

- The use of laminar zones around the regions of laminar flow had to be abandoned due to modelling and computational resources issues. This is further explained in the relevant section further below.
- Simulations for LES were fully turbulent.
- From the experimental data available, only one pitch angle was investigated for the winglets (at 0°) for the two winglets location available.
- Most of the calculations, due to the long computing time, were done for a simulation time of about 0.3-0.5 seconds. This is equivalent to 3-5 flow-through times inside the domain in CFD terms for the 36.27 m/s inlet velocity.
- Some grid assumptions/problems were also addressed.
- No mesh sensitivity analysis carried out due to large meshes
- Blockage effects of tunnel walls are ignored

Following this initial clarifications, the numerical simulations still hold a computational intricacy, since they require:

- The importation and manipulation of the geometry from IGES to a format usable for the pre-processor
- The generation of three dimensional grids capable of capturing the important flow features
- The solution of the RANS equations and turbulence models by means of parallel computing in the computational domain
- The data gathering and post-processing of the results

Finally, the results from the other numerical studies using the same data and introduced in the literature review were correlated to the original values for a combined comparison.

8.3 Computational details & model geometry

The geometry of interest for our study is that of a model (scale 1:4 with respect to full-scale size) of an IACC yacht keel fixed in the wind tunnel. The fin and the winglets have a NACA 0012 profile. The bulb has a flat bottom and a beaver tail tip;

this is known to produce minimum drag by extending the effective span of the keel and ensuring that the wetted area is not increased excessively (Axfors and Tunander, 2011). Three main configurations formed the basis of our study of the global force coefficients: bulb and fin without winglets; appended keel with winglets in forward position; and appended keel with winglets aft, as shown in the figure 8.1 below. (Further information on the experimental setup can be found in Werner et al. (2006)).

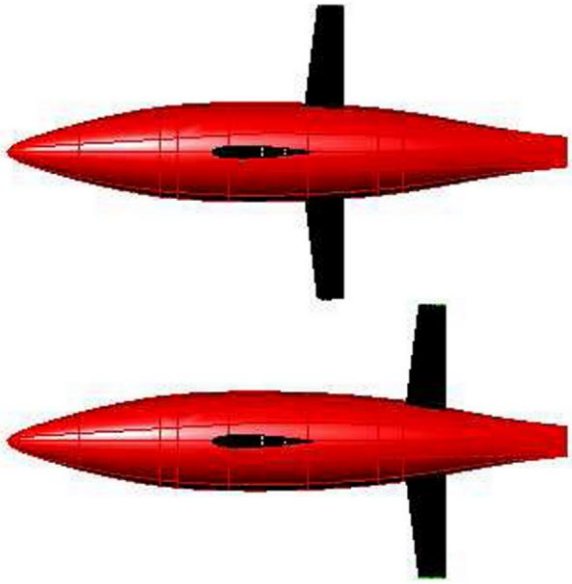

Figure 8.: Positions of the winglets in fore and aft configuration

For the wake flow comparison, and the sensitivity analysis of numerical parameters, only the case of the keel without winglets is presented. Future work proposed includes a numerical sensitivity study with the wings and an extended domain size.

Constraints in the experimental wind tunnel set-up of the keel led to a leeway angle fixed at 4 degrees since it was not possible to keep the keel upright (figure 8.2). Thus, it was decided that the same arrangement would be tested in the CFD runs.

The Reynolds number based on the freestream inlet velocity and the bulb's length was 3.2×10^6, in agreement with the experiments. For the fin and the winglets, this equalled to $Re_f = 5.04 \times 10^5$ and $Re_w = 1.8 \times 10^5$ respectively. The two SGS models for LES and the two RANS models for DES were considered when running the

simulations for the case when winglets are positioned forward. For the other two cases (winglets aft and no winglets), only one SGS model and one RANS model were considered for each. In the experiments, transition from laminar to turbulent flow was forced by attaching a strip of tape to the surface of the bulb and the fin, located at 25% of the chord length for each, and for the winglets fixed at 10%. This was not included in the current numerical simulations because of mesh issues when this was undertaken. Instead, calculations were performed without laminar zones and there were no constrains on forcing the turbulent transition. Hence, the simulations were performed freely. Table 8.1 summarises the main dimensions of the keel.

Table 8.: model keel dimensions (all in mm unless stated)

Bulb Chord	1365
Bulb Max Thickness	176
Fin Mean Chord	216
Fin Max Thickness, Mean Chord	26
Fin Span	613
Winglet Mean Chord	77
Winglet Max Thickness, Mean Chord	9
Winglet Span	252
Winglet Dihedral (deg)	17°
Winglet Pitch (deg)	0°

The numerical solution of the flow is obtained using the commercial CFD code FLUENT. Discretization is done based on the finite-volume approach. In the tables 8.2 and 8.3, the various CFD settings, schemes and parameters are summarized as applied selected for the simulations of the current airfoil flow. The convergence criteria considered was 10^{-3} for most of the runs. These simulations were much more demanding than those in the previous chapter were.

Table 8.: Simulation set-up for flow around America's Cup keel with LES model

Parameter	***Setting***
Simulation mode	3D, Unsteady
Solver	Pressure-based Implicit
Temporal discretization	2nd Order
Pressure-Velocity coupling	SIMPLE-C
Pressure	Standard
Momentum	Bounded Central Differencing
SGS model	Smagorinsky-Lilly (SM) & Dynamic Smagorinsky-Lilly (DSM)

Table 8.: Simulation set-up for flow around America's Cup keel with DES model

Parameter	***Setting***
Simulation mode	3D, Unsteady
Solver	Pressure-based Implicit
Temporal discretization	2nd Order
Pressure-Velocity coupling	PISO
Pressure	PRESTO!
Momentum	2nd Order upwind
Turbulent kinetic energy (R κε)	1st Order upwind
Turbulent dissipation rate (R κε)	1st Order upwind
Modified turbulent viscosity (SA)	1st Order upwind
RANS model	Spalart-Allmaras (SA) & Realizable κε (R κε)

8.4 Solution domain of CFD simulations

The domain was reproduced to copy the experimental wind tunnel: length L of 2.7 m and cross section B x H of 1.8 m x 1.25 m. The complete wind tunnel test section was modelled from the inlet plane, where the wind tunnel contraction ends, to the outlet plane, where the expansion begins. The model is shown in fig. 8.2 sitting in the wind-tunnel section, with the winglets under a forward configuration. The coordinate system was defined at the inlet base of the tunnel, the x-axis streamwise, positive from bow to stern, the y-axis positive upwards, and the z-axis forming a mutually orthogonal right-handed set of axes.

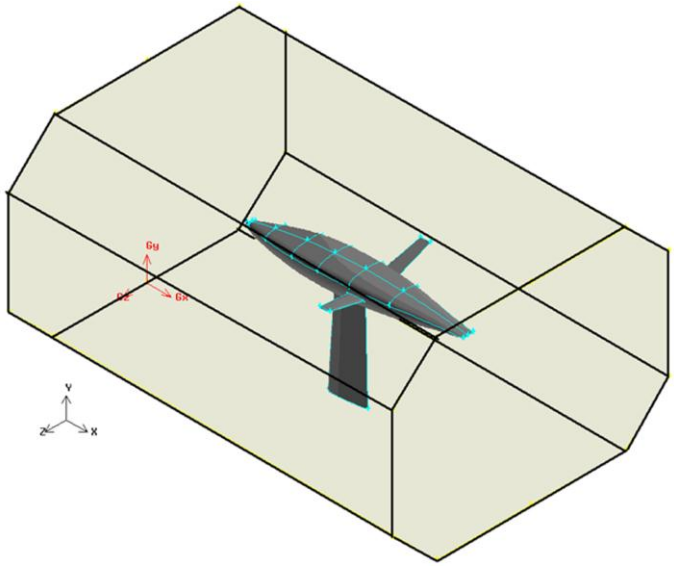

Figure 8.: Computational domain for model keel with coordinate system, example of winglets in forward position

8.5 Grid Generation

One of the challenges of the study was to be able to create a series of grids ranging in size and nature in order to get a range of meshes and assess how each one was contributing to the prediction of the forces on the keel. Although there exists a common pattern followed by all engineering problems requiring a mesh generation, for the current example some levels required a more thorough investigation and problem-solving.

8.5.1 Geometry cleaning

As the geometry was imported, the CAD was rigorously examined to ensure that it met the constraints of the grid generation software in terms of surface tolerance. CAD geometries that are unsuitable for CFD analysis (due to the presence of irregularities) can be a major bottleneck in the grid generation process; and unfortunately this was the case with the geometry used in the thesis as shown in the pictures below. The initial CAD file was created from the model of the wind tunnel, through measuring main dimensions and then generating the surface as closely as possible in CAD software, similar to Rhino and MaxSurf (private conversation with S. Werner, 2008). This resulted in gaps, overlaps, small edges, double vertices for the

same surfaces and superimposed faces. This was visible when creating the surface mesh. The figure below shows two examples of these issues: the first is depicting a very small face at the stern of the bulb, and the second the face mesh near the bow of the bulb incorrectly following the curvature and creating a gap and discontinuity with the adjacent meshed face.

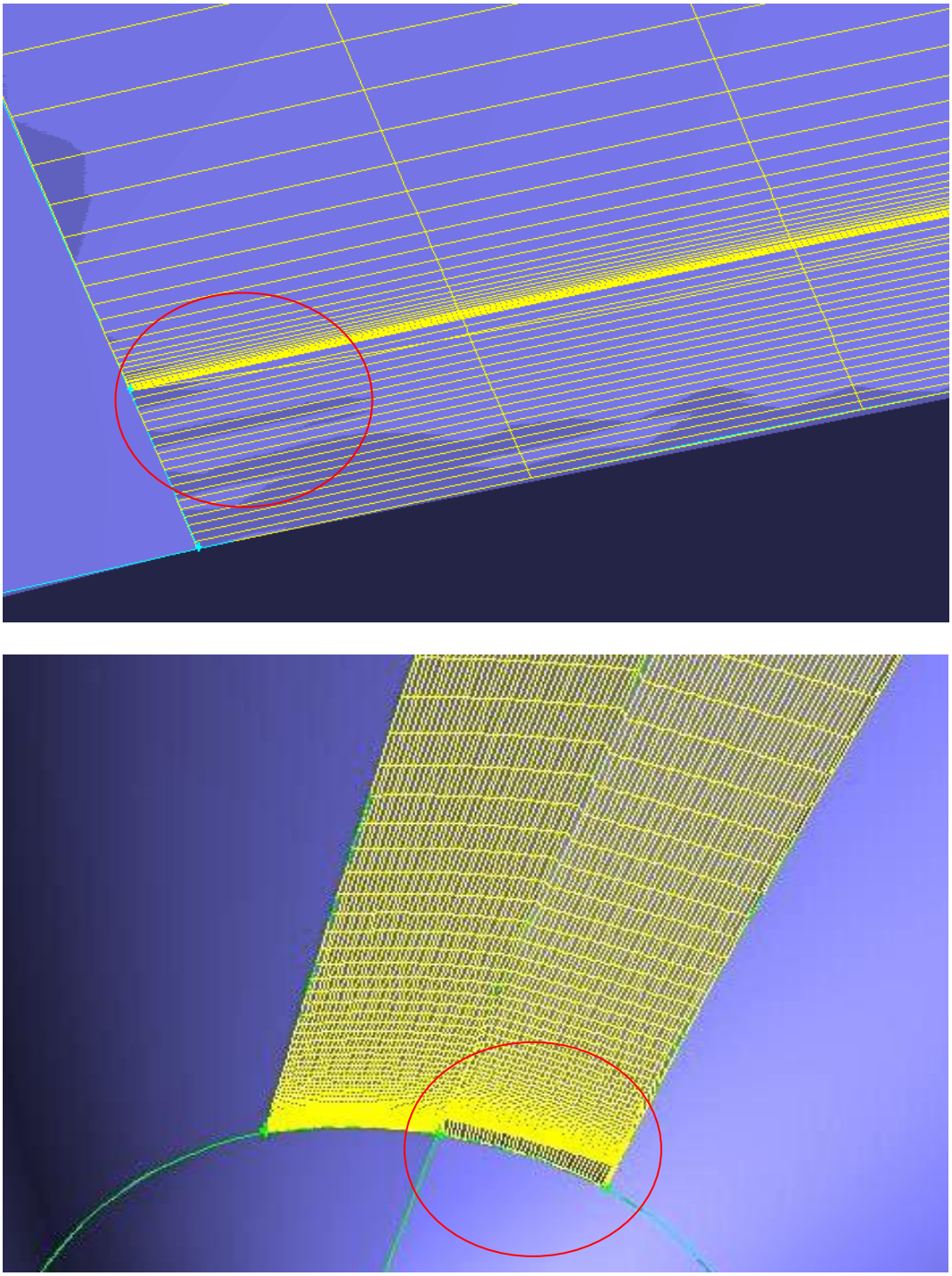

Figure 8.: Examples of issues encountered with the CAD geometry

The main problems were encountered on the bulb, particularly in areas of high convection, and near the intersections with the fin and the winglets. The repair and the manipulation of the geometry was a difficult task in GAMBIT and took a lot of time, but was necessary. The problems encountered with the geometry did to some extend influence the results. This will be discussed in the following chapter. When all geometry cleaning and repairing was performed, the surface was giving a very smooth shape over the keel.

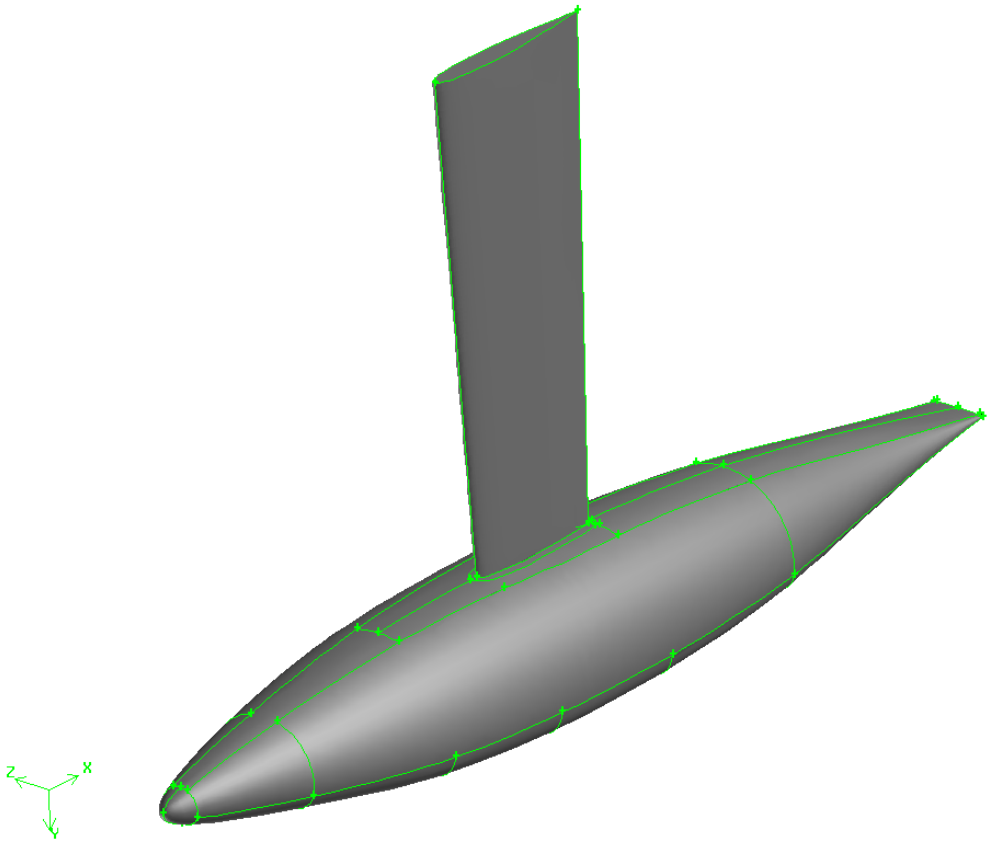

Figure 8.: Example of repaired and cleaned surface for the bulb

8.5.2 Surface meshing

Following the careful examination and repair of the geometry, the surface mesh was created. Flexibility in the grid topology is critical for treating complex geometries such as underwater region of an IACC yacht. Bearing this in mind, the choice of mesh type was towards unstructured facets. Tri/tetrahedral grids are used because of their ability to model complex three-dimensional geometries. When using

unstructured mixed element grids to resolve high-Reynolds-number viscous flow, the surfaces are meshed with triangles and where permitted quadrilaterals, followed by layers of prisms and hexahedral cells extruded from the surface to produce a region to capture the boundary layer. In the final step, tetrahedral cells are generated to fill the remaining volume of the computational domain.

When the surface curvature of critical components is high, such as the fin's and the winglets leading edges, triangulation of the surface is difficult because it causes an uncontrollable number of elements that can at times abort the mesh. The aspect ratio of the facelets must remain small. For these regions, adaptation through refinement was used to avoid further problems, either in GAMBIT or with the intermediate tool TGrid. Hence the aim for 'adapted unstructured grids' mentioned at the beginning of this thesis. On other particular areas of interest, such as the root of the winglets and the root of the fin where flow is expected to be important, the mesh was also denser and finer.

For a couple of meshes, a quadrilateral surface grid was used in these areas since element aspect ratios could be controlled better. The surface grids contained between 36,500 and 150,000 elements. Figure 8.5 shows examples of surface mesh for each configuration tested, with refinement near the winglets and the fin for the winged condition, and higher face density mesh for the case of the non-winged keel. Figure 8.6 is a close-up of the surface grid for one of the meshes.

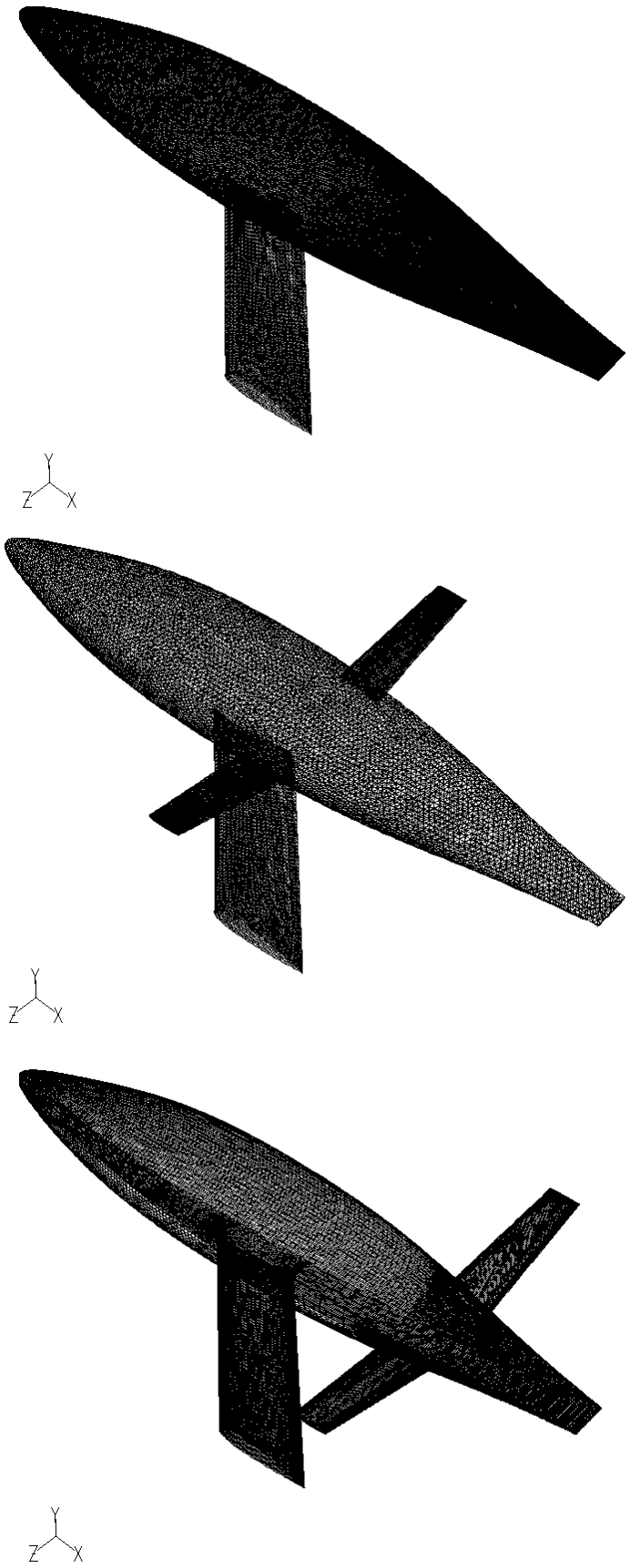

Figure 8.: Surface triangular mesh on the keel for each of the configurations

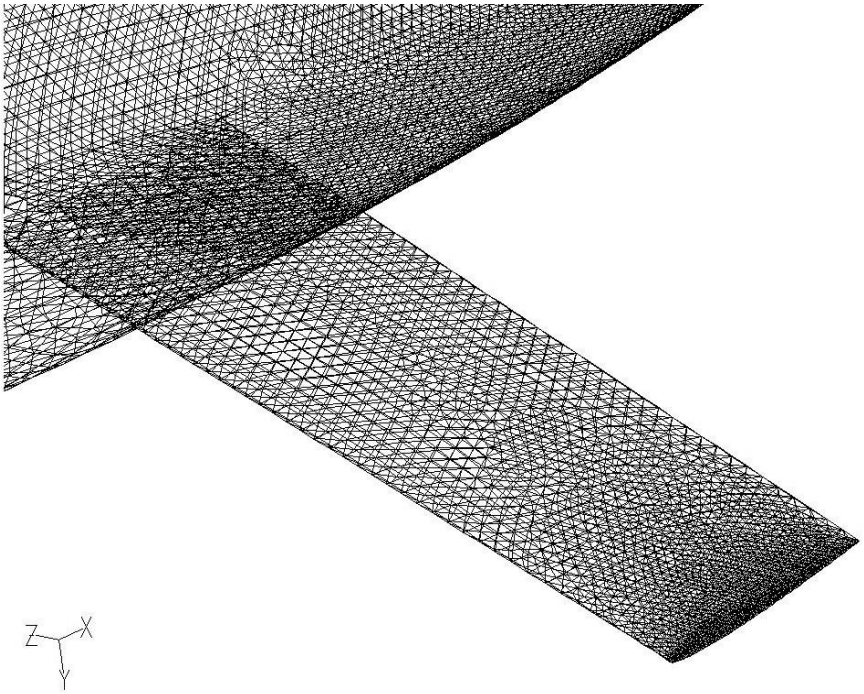

Figure 8.: Close-up of surface grid for one of the meshes

8.5.3 Volume meshing

After completion of the surface meshing, the boundary layer is created. The Reynolds number, the spatial accuracy of the solver, the turbulence model, and the method used to resolve the inner region of the turbulent boundary layer dictate the layer's spacing, stretching, and thickness inside that region.

For DES, the SA and R κ-ε models are flexible and use a wall function scheme when y^+ is over about 50 and a near-wall treatment scheme when y^+ is smaller than about five. For LES simulations, the target for near-wall resolution was to achieve a y^+ value close to unity. This was equivalent to the first cell distance to be of the order of magnitude of 10^{-5} m. In several grids this proved to be quite difficult if not impossible at times, particularly in regions of high concavity around the winglets/bulb intersection, the tail of the bulb and the base of the fin/bulb intersection, and because of the number of surface triangles (surface mesh elements). The growth process often failed and alternative parameters were chosen.

For high convexity regions, the local wall normal must be very accurate, in particular when generating boundary layers. This accuracy is achieved imposing very low tolerances for the geometrical description of wall surfaces, and increasing the number of facets discretising each surface. In convex regions where curvature suddenly increases (example: winglet tip), a too high boundary layer can lead to discontinuous changes in cell dimensions. The grid spacing on the body surface was modified when necessary, in order to obtain more uniform outer layers.

Again the TGrid tool was used in numerous occasions to solve these issues and allowed a more powerful boundary layer extrusion, continued by the remaining volume creation. In a few occasions when the tool could not perfume, size functions were used in GAMBIT, creating a thinner boundary layer than initially desired. In the simulations, the prismatic boundary layer was grown from the bulb, keel and winglets surfaces. The height of the first layer for the finest mesh was of the order of 0.001 mm. The number of layers in the prismatic grid varied between 4 and 20. The thickness grew at a ratio of 1.1 or 1.2. The maximum thickness of boundary layers was limited by overlapping problems in some regions. This had some effect on the results of the forces; these are highlighted in the next section. Two examples of boundary layers are shown in figures 8.7 and 8.8 for different conditions described above.

In the last step of the grid generation procedure, the remaining volume is filled with tetrahedrons. The grid sizes ranged from 550,000 for the coarsest to about 4 million cells for the finest case. No formal grid sensitivity study is presented here because of time pressure but this will be part of a future study. Fig. 8.9 shows the computational domain meshed around the keel for the case with winglets at the aft position.

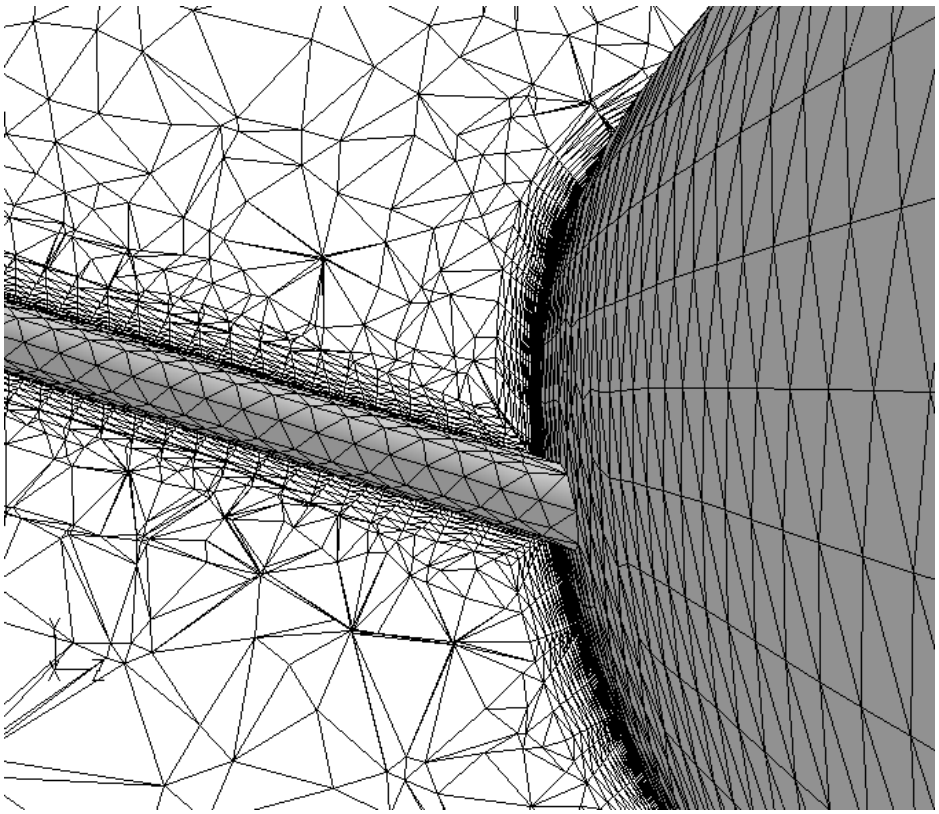

Figure 8.: Highly resolved boundary layer around winglets-bulb intersection

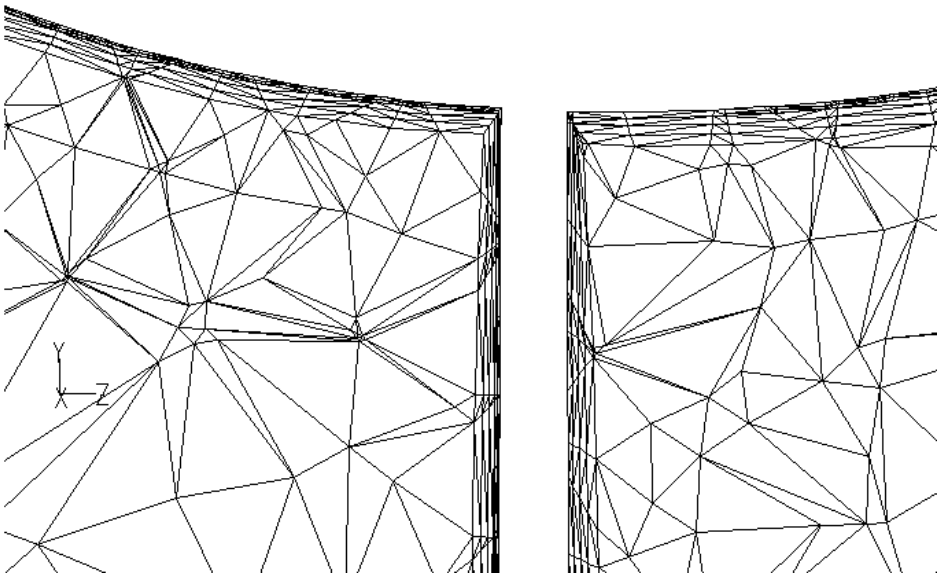

Figure 8.: Example of low boundary layer creation around junction of fin and bulb for one of the coarse meshes

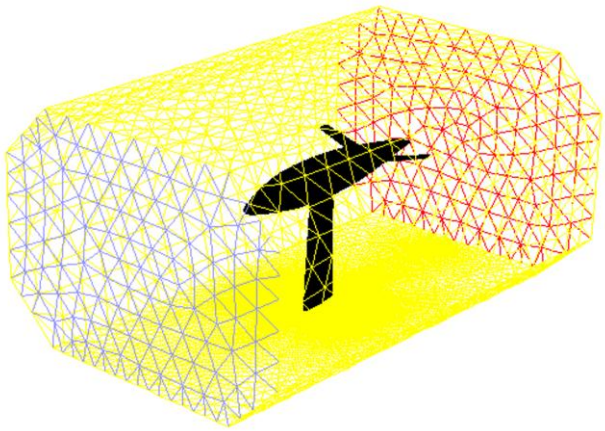

Figure 8.: Meshed computational domain, example for winglets located aft: blue is the inflow, red is the outflow, yellow is the slip-condition walls and black shows the keel in no-slip condition

8.6 Boundary conditions

No-slip conditions were employed on the surface of the keel. The inlet boundary conditions were constant freestream velocity and turbulence settings according to the experiments with a constant inlet turbulence length scale; the latter is directly linked to the dissipation. The values for the inlet condition are shown in table 8.4. The outlet boundary condition was a value of zero for the normal gradient for all flow variables except the pressure. To reduce computational time, the tunnel walls were defined as slippage surfaces (zero shear stress). No-slip condition was also considered, but the results were not influenced; so it was decided to opt for the slip

Table 8.: Boundary and Inlet flow conditions, America's Cup keel simulations

Domain Boundary	***Condition***
Inlet	Velocity inlet
Outlet	Pressure outlet
Keel surface	Non-slip wall
Top & bottom walls	Slip-condition
Side walls	Slip-condition
Atmospheric pressure (kPa)	100.9
Inlet velocity (m/s)	36.27
Dynamic viscosity (kg/ms)	$1.84 \cdot 10^{-5}$
Inlet turbulent intensity (%)	0.1
Inlet turbulent length scale (m)	0.001

8.7 Numerical Results

8.7.1 Global Hydrodynamic Forces

The current section summarises the results obtained from the present CFD calculations; comparisons are included for the experimental values of Werner and the other CFD studies from Werner, 2007; Ambrogi et al., 2008, and Thys, 2008. Lift (L) and drag (D) are expressed in terms of averaged non-dimensional coefficients, and rendered dimensionless by wetted surface area *S*, velocity *V*, density of fluid ρ and force. Drag coefficient is taken longitudinally in the direction of the undisturbed flow and lift coefficient is taken perpendicular to the wind, along the z-axis:

$$C_L = \frac{L}{0.5 \cdot \rho \cdot S \cdot V^2} \tag{8.1}$$

and

$$C_D = \frac{D}{0.5 \cdot \rho \cdot S \cdot V^2} \tag{8.2}$$

Table 8.5 gives a comparison of the results for the forward winged keel. It can be seen that the present values differ from the experimental data depending on the method used and on the value of the near-wall distance. However, with the exception of a few cases, the numerical results are considered good for the lift, with a maximum error of less than 9%, and acceptable for the drag, with errors less than 15%. By looking more closely, a trend is observed in the values predicted by LES. The DSM model is particularly erroneous and does not predict the forces well: the percentage error is high (around 19% for the lift). This is likely due to the instability of the model, because for the run with $y^+ = 3$, the model was expected to perform adequately based on the results from the previous chapter. It is however the only model that predicts drag better than lift in all simulations.

The SM model, on the other hand, predicts lift with an error of only about 6% on average. Drag is generally poorly predicted, with additional discrepancies for values of y^+ around 0.55: here, good agreement with the experimental values should be

expected; this behaviour is not yet explicable and further insight into the issue is needed.

For the DES runs, the Realizable κ-ε model is more accurate than the SA model, and close to LES predictions in terms of forces. Refining the mesh and increasing its size has a beneficial effect for this method. Again, drag is too far from the correct values, and this is something that needs to be looked at; the lack of laminar region may be responsible for this error. Fully turbulent flow usually overestimates the drag, and its effect is more perceptible in the downwind sailing compared to an upwind condition. In the present calculation however all models underestimate that same force.

Table 8.: Comparison of results for forward configuration

Study	***Model***	***Sub model***	***Mesh Size***	C_L	C_D	y^+	***%err L***	***%err D***
Exps.	-	-	-	0.0617	0.0057	-	-	-
Werner et al.	RANS	κ-ω	3600000	0.0598	0.0055	30	3	3
Ambrogi et al.	RANS	S-A	7000000	0.047	0.00524	Unknwn	23.8	7.97
Current	LES	SM	550159	0.0569	0.0047	0.57	7.78	16.71
	LES	SM	958585	0.0584	0.0048	99	5.22	14.77
	LES	DSM	958585	0.05	0.0051	99	18.91	9.84
	DES	S-A	958585	0.0583	0.0044	182	5.46	22.22
	DES	R κ-ε	958585	0.0599	0.0048	154	2.88	14.95
	LES	SM	1044303	0.0577	0.0052	0.53	6.42	8.43
	DES	R κ-ε	1215401	0.0591	0.0046	85	4.08	19
	LES	DSM	1268321	0.0494	0.0051	3	19.93	9.84
	LES	SM	1339420	0.058	0.0053	2.8	5.93	7.38
	LES	SM	1742961	0.0565	0.0044	0.56	8.37	21.82
	LES	SM	1902269	0.0594	0.0053	2.8	3.65	6.5

From table 8.6, which presents the computed force coefficients for the winglets positioned aft, one can observe that LES is accurately predicting the lift generated by the keel, and this for relatively high values of y^+. It is possible that there is an activation of standard wall model for LES, because our values of y^+ are larger than 30. Drag though is still over or under predicted between 15% and 19% but the error diminishes with greater mesh refinement near the model. The DES Realizable κ-ε model is reasonably accurate, with maximum errors in lift and drag of about 6% and

11% respectively. The SA model generates acceptable results for lift, but those for drag are rather over-predicted. Drag is better estimated for some of the DES cases compared to LES; this is due to the RANS near-wall model more adapted to higher y^+ values.

Table 8.: Comparison of results for aft configuration

Study	***Model***	***Sub model***	***Mesh Size***	C_L	C_D	y^+	***%err L***	***%err D***
Exps.	-	-	-	0.0606	0.0056	-	-	-
Thys	Potential	-	1046				3-23	7-12
Current	LES	SM	1071858	0.0619	0.0065	62	2.3	17.63
	DES	R κ-ε	1366237	0.0624	0.0062	56	2.99	10.97
	DES	S-A	1571178	0.0567	0.0064	56	6.44	15.29
	LES	DSM	1792778	0.0587	0.0045	56	3.12	19.06
	LES	SM	3908847	0.062	0.006	31	2.39	7.91

Table 8.7 shows results for the non-winged keel. Although fewer runs were performed for this case, it gives the most satisfactory results for LES. The first LES run is the best one, with the closest match to any experimental values. It seems that the viscous sublayer is correctly resolved, and for a relatively medium mesh size, the values of lift and drag are very close to the wind tunnel values. However, coarsening the mesh in the vicinity of the keel does immediately increase the errors in computed values: drag in particular is affected. It would be worthwhile to use the 1.5 million mesh, with a finer near-wall resolution, to establish whether improvements are obtained. DES yields good agreement for the lift coefficient with a difference of less than 6.5% in comparison with experimental data, but is unsatisfactorily underestimating the drag coefficient by about 18.5%, although y^+ is located in the range of the wall function used by the model for these values. Again, it would be prudent to further refine locally the mesh.

Table 8.: Comparison of results for no winglets configuration

Study	*Model*	*Sub model*	*Mesh Size*	C_L	C_D	y^+	*%err L*	*%err D*
Exps.	-	-	-	0.063	0.0058	-	-	-
Werner et al.	RANS	S-A	2600000	0.0617	0.0051	30	2	12
	RANS	SST κ-ω	2600000	0.0611	0.0055	30	3	6
	RANS	κ-ω	2600000	0.0617	0.0058	30	2	0.3
	RANS	R κ-ε	2600000	0.0624	0.0056	30	1	4
	RANS	S κ-ε	2600000	0.0627	0.0056	30	0.4	4
Ambrogi et al.	RANS	S-A	7000000	0.0481	0.0053	Unknown	23.66	7.86
Current	LES	SM	1403067	0.0634	0.0057	5	0.67	2.08
	DES	R κ-ε	1481017	0.067	0.0047	68	6.38	18.48
	LES	SM	1505097	0.06	0.0048	13	4.83	17.47

8.7.2 Wake survey

To assess the accuracy of the methods in terms of flow field, a comparison of the wake at a given plane behind the keel has been carried out for the simplest case (no wings). This type of comparison is instructive in cases when data such as surface pressure, skin-friction (shear stress), velocity measurements on or near the body are not obtained or not available from experiments. Observing the wake of the flow is thus important in assessing a CFD code in terms of level of accuracy, by comparing the two LES and DES predictions, and conclusions can be drawn from possible differences against experiments.

The LES SM model with 1.4 million cells and the DES Realizable κ-ε model with 1.5 million cells from table 8.7 are compared in terms of non-dimensional velocity components in the streamwise, vertical and lateral directions (i.e. along x-, y- and z-axes) to the same contours obtained in the experimental measurements. The wake plane is located at a distance of 2.375 m from the tunnel inlet as per the wind tunnel set-up. The grid in this location comprised of about 2,000 cells in the area where the core vortices were expected to appear.

In Fig. 8.10 and Fig. 8.11, a comparison between experimental and numerical solutions in terms of axial, radial and tangential velocity contours is shown. From the

observations, it can be concluded that overall shape of contours and vortices is present; both DES and LES seem to capture the main bulb tip vortex, as described by Werner et al. (2007); however the resolution and the intensity of the vortex differs between the two models. The position of this vortex is well predicted. For the remaining vortices, the global shape of the 'bilge' vortex in the DES calculation is discerned, in LES it is not developed yet, which means that either more simulation time might be needed to get a satisfactory result or either the resolution in the cross section needs to be higher for LES. Another explanation is the switch from the RANS model near the keel to the LES in the farfield is taking place for the DES simulation; and the results are thus good in the LES region of the flow. In the radial and tangential directions, LES is matching the experiments better than DES. Both models though slightly underestimate the values of normalised velocities. An explanation to the differences occurring is brought forward in the discussion section, which follows this chapter.

In addition, figure 8.12 shows the contours of vorticity magnitude (Units: 1/s) of the experimental results calculated at the same wake plane, compared to LES and DES predictions. The vorticity shows the complexity of the turbulent flow in the wake of the bulb, with the interaction of the various vortices created along the length of the keel and from the separation in the flow. The areas of large vorticity magnitude coincide with areas of low velocity. Flow analyses using vorticity are essential in the development of new keel designs. This study shows that wake measurements from the wind tunnel are useful for evaluating the LES and DES results, so that it can be used as a reliable tool for detailed flow analysis.

Looking more into detail between the two, the prediction obtained with LES is disappointing. Although the core vortices and outline are present, the model underpredicts the high vorticity. There is either not enough resolution in the wake or the mesh is too coarse upstream near the keel. The DES computation is on the opposite very successful in predicting the main vortices. The range of values agree well with the experiments, and a similar pattern can be distinguished. The overall wake shape and position is in fair agreement with the experimental data. Vortex

shape and intensity in the bulb wake can be considered satisfactory; there is some lack of resolution in the bottom part of the vortex for most but the overall trend is reasonable.

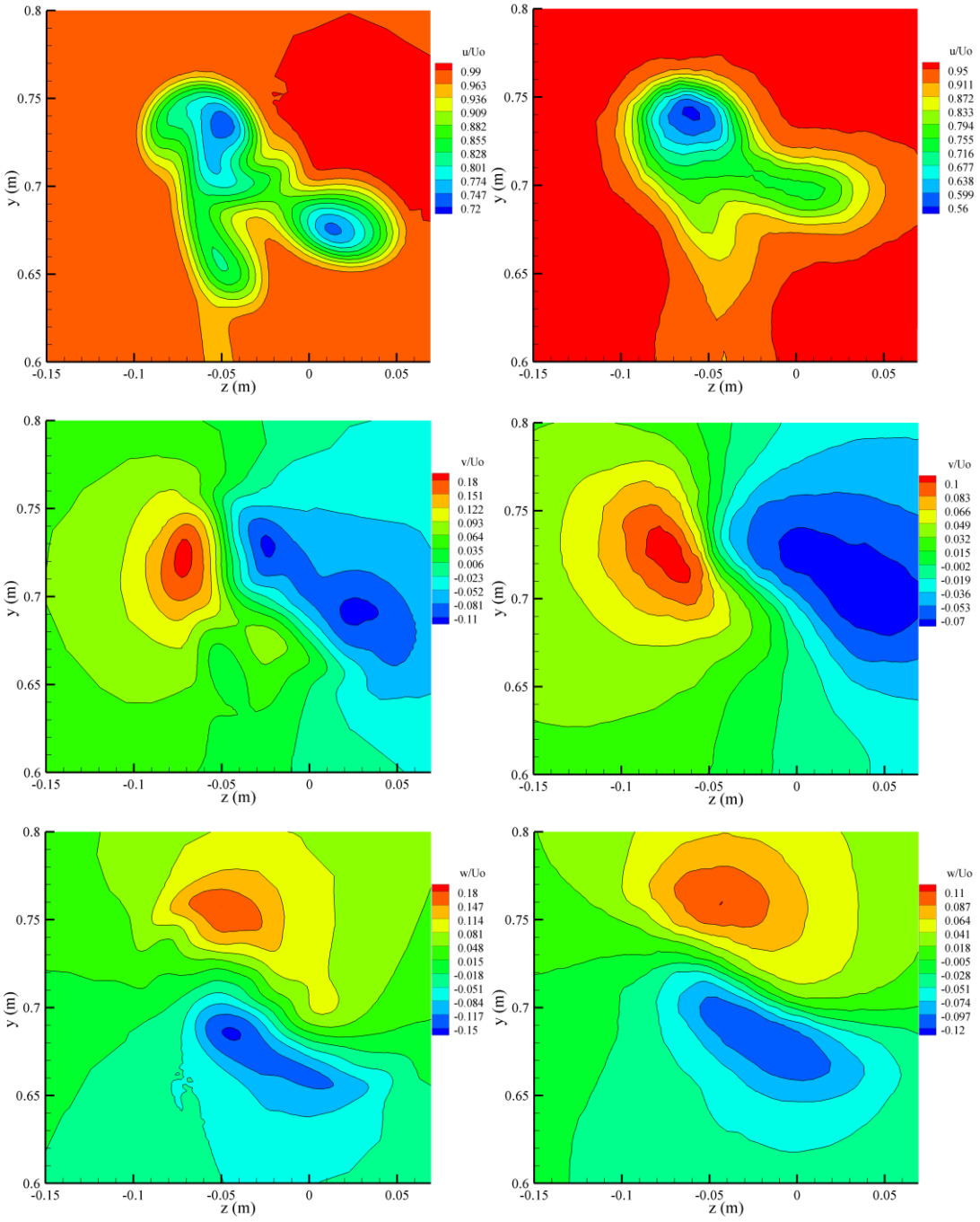

Figure 8.: Contours of axial, radial and tangential velocities at wake plane. Left: experimental results, right: DES results

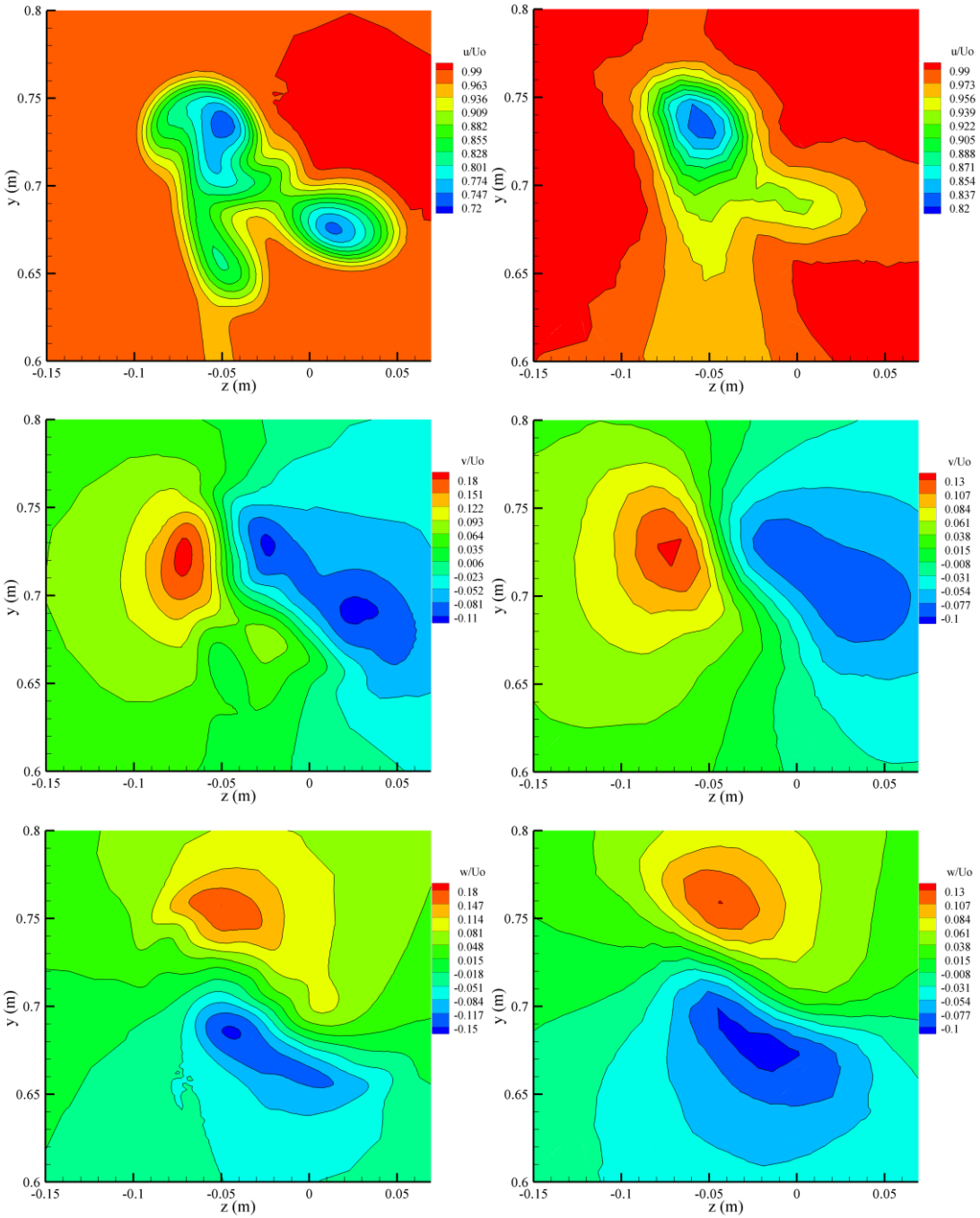

Figure 8.: Contours of axial, radial and tangential velocities at wake plane. Left: experimental results, right: LES results

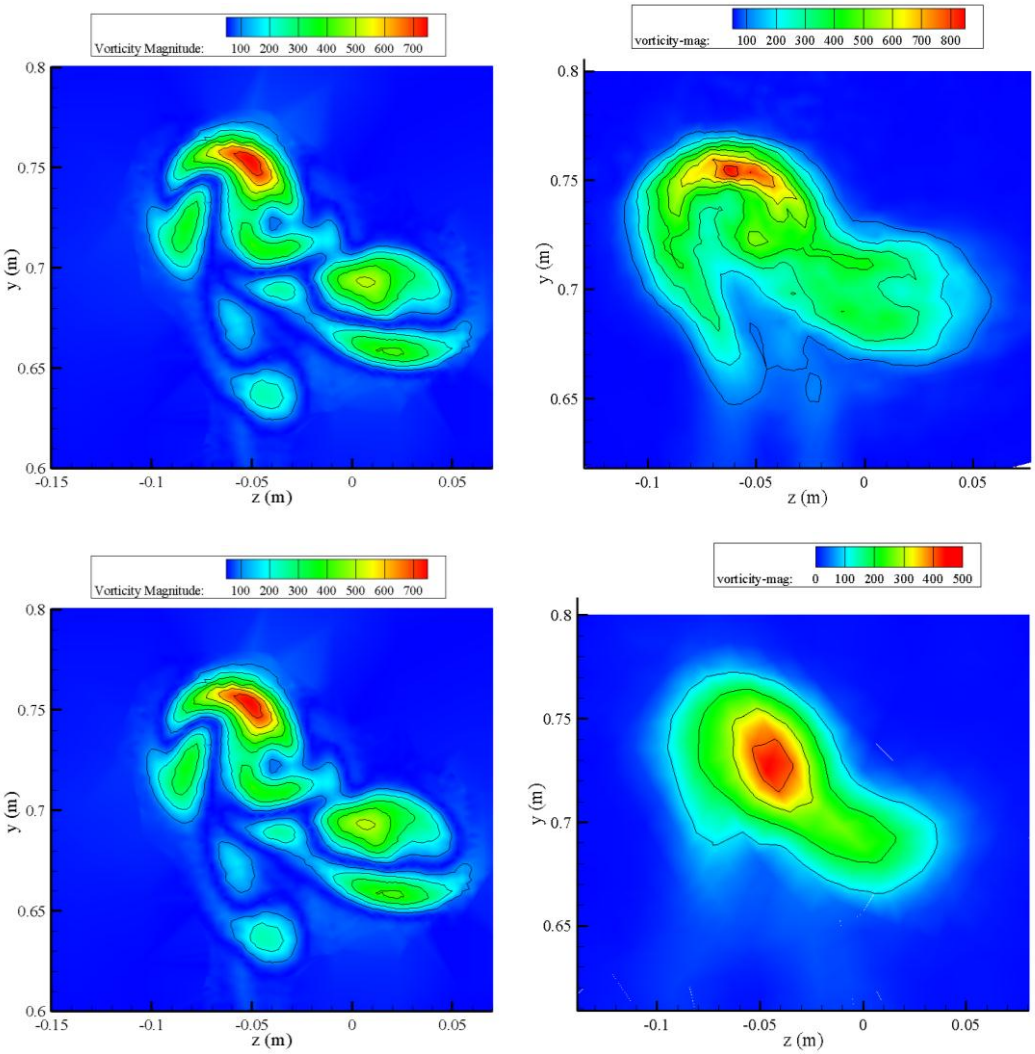

Figure 8.: Contours of vorticity magnitude (1/s). Left: Experiments, top right DES, bot right LES

8.7.3 Unsteady flow features

Flow past an appended keel is a challenging case for CFD because of the different flow regimes around the body; including the laminar boundary layer, the transition region, the turbulent boundary layer, separation point, and separation region as well as wake region as seen above. There were no other formal observations during the experiments of the flow to report but important features captured by LES and DES are presented in this section. At the yaw angle of the measurements, separation is expected to occur at the trailing edge of the suction side of the model. Although it can be argued that there is no massive separation to justify the use of LES or DES

(i.e. large angles of attack or high pressure gradient changes), the models nonetheless predict the flow unsteadiness in a characteristic manner.

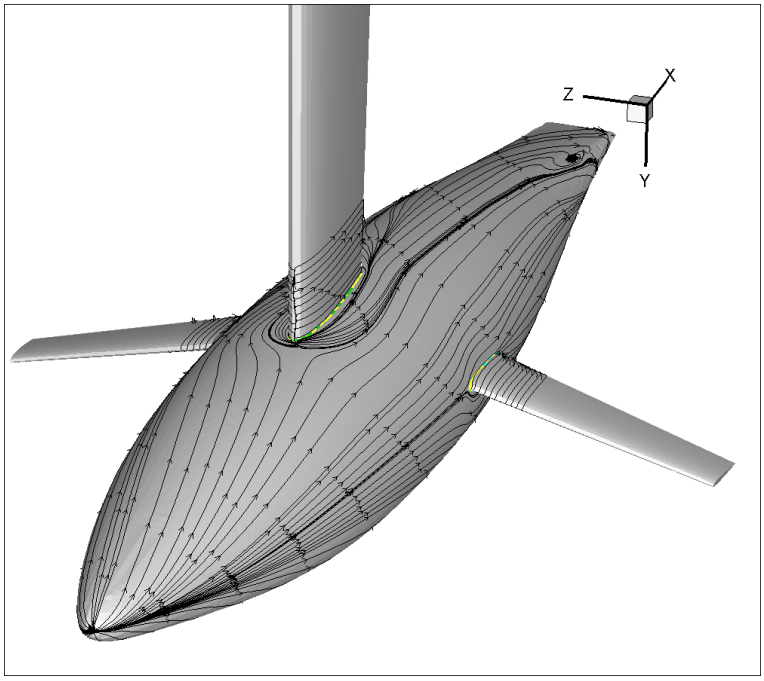

Figure 8.: Surface shear lines, windward side

The surface shear lines on the keel show the presence of a horseshoe vortex when the undisturbed flow reaches the fin at the junction with the bulb; figures 8.13 and 8.14. On the trailing edge, reattachment occurs. The flow remains unsteady and turbulent in the aft part, inducing further separation down the keel. In the pressure side, the flow is less disturbed, due to the yaw angle, pressure transfers from the windward to the leeward side. The surface streamlines show that the numerical simulations capture the important features of the recirculation zone.

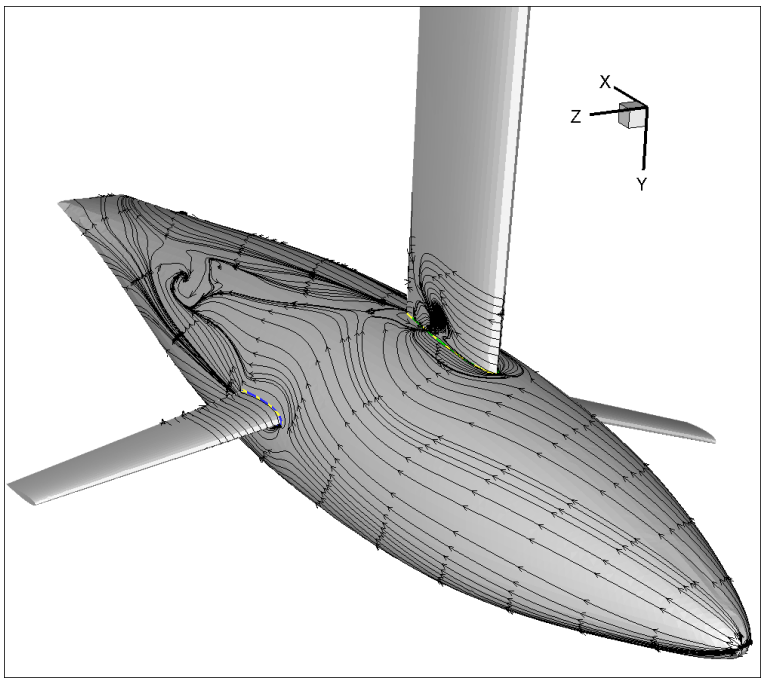

Figure 8.: Surface shear lines, leeward side

A close-up of the leeward side shows the reattachment occurring between around 50-60% of the bulb-fin root. A large vortex is visible on the surface of the keel along with a smaller one at the intersection with the bulb. Then further separation occurs behind the fin, with generation and evolution of coherent structures in turbulent flows. Figure 8.16 shows the instantaneous flow pathlines at the intersection close of the fin with the bulb. The vortical structures emanate from the junction towards the end of the trailing edge and from the bulb. The rotation in the flow carries on further down the length of the bulb and in the wake; these vortices, move towards the starboard side, as expected.

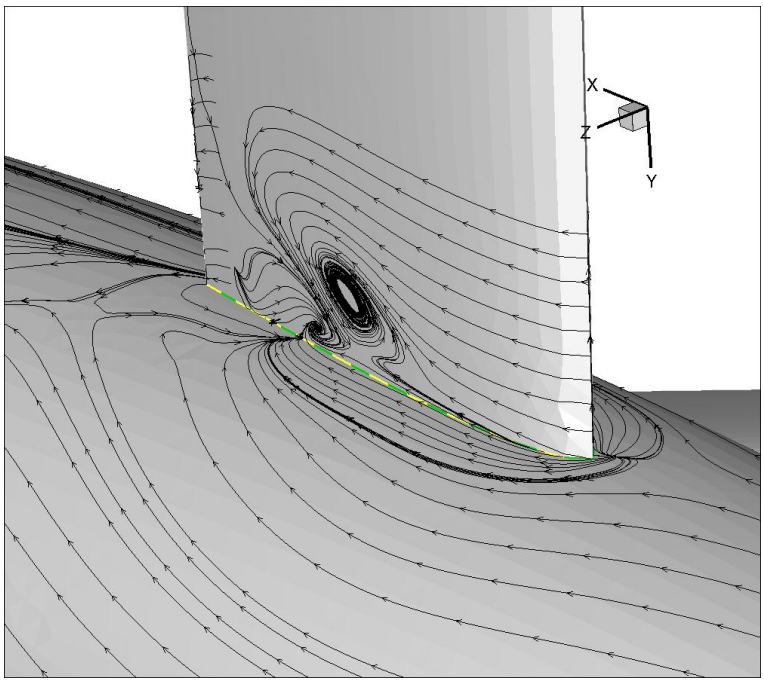

Figure 8.: Close-up of the windward side at the bulb-fin junction

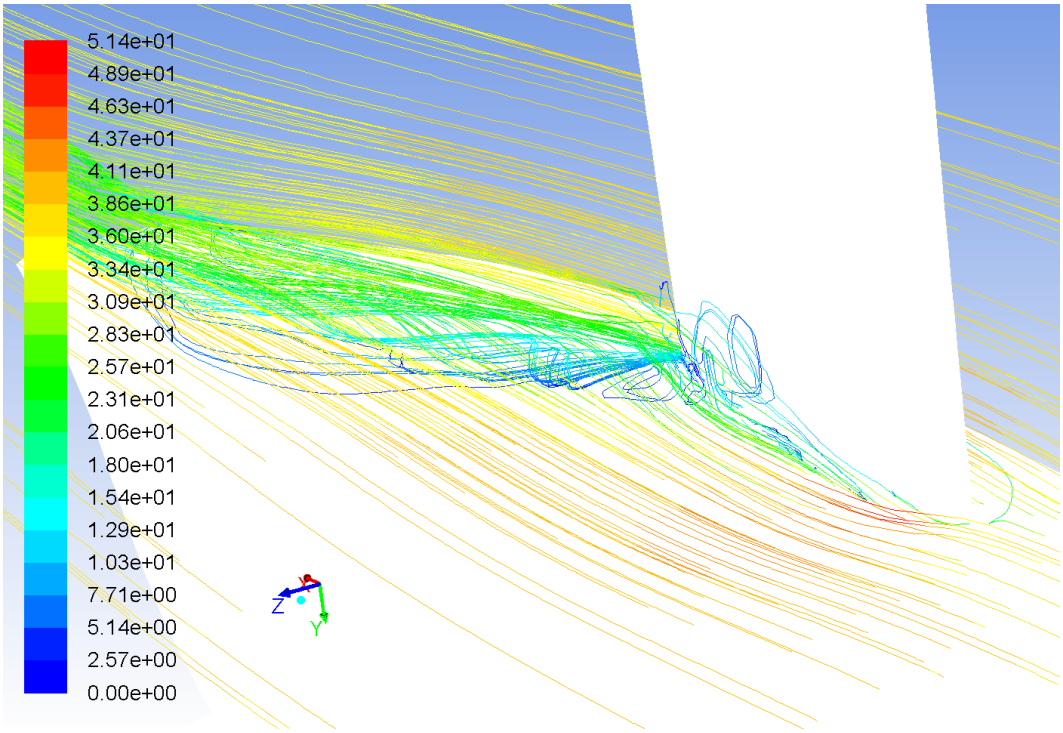

Figure 8.: Close up of turbulent and separated flow at the fin-bulb trailing junction

Regarding the winglets, similar behaviour was reported for the flow near the root of the wings, but not as pronounced in the forward position because the winglets' pitch was zero degrees. There were more effects occurring for the winglets in the aft

position. Figure 8.17 shows the surface flow streamlines and the turbulent boundary layer separation behind the winglets, which in this case are placed aft of the model. The picture on the left shows the windward side; results for the leeward side are depicted in the right illustration. Both pictures are extracted for a run with LES model. At the root of the winglets (and similarly at the root of the fin) junction flow is developing. Separation occurs at the trailing edge on both sides. On both sides flow seems to be re-circulating in an anticlockwise direction in the trailing edges of the winglets, although the eddies on the pressure side are larger than those on the suction side. On the leeward region smaller eddies are developing below the winglet. Similar behaviour is observed for winglets in forward location. LES resolves the complex flow pattern near the keel to a high degree of accuracy. Also, tip vortices were observed for the cases with the winglets on both positions (forward and aft).

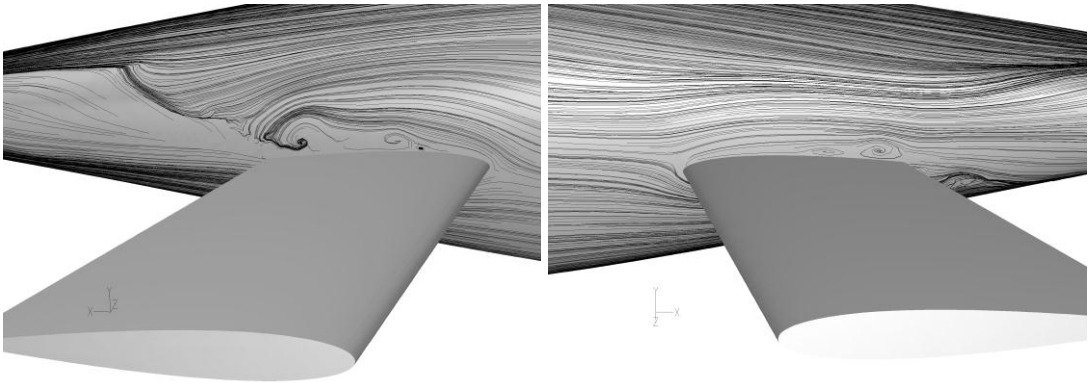

Figure 8.: Surface Streamlines on the bulb at the winglets junction, showing boundary layer separation and vortices in the aft configuration. Left: windward side, right: leeward side

Another advantage of LES is the possibility to evaluate the instantaneous fluctuations in the flow. Figure 8.18 depicts the contours of instantaneous vorticity strength, for the case with no winglets, at three planes located behind the geometry, set at a distance of 2.125, 2.25 and 2.375 m respectively from the entrance of the wind tunnel. The bulb vortices are well defined as the mesh resolution near the keel increases, and one can appreciate the various vortex structures that come from the pressure side (left), the tip vortex (top) and the bilge vortex.

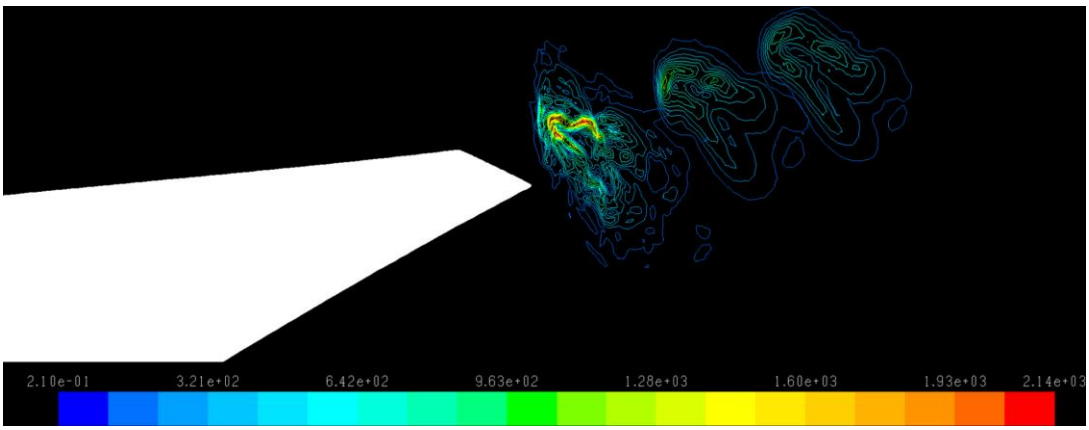

Figure 8.: Contours of instantaneous vorticity magnitude for case with bulb and fin only with LES

Figure 8.19 illustrates the flowlines behind the fin on the suction (leeward) side of the model. The contours of mean pressure coefficient are superimposed on the surface of the keel and the range of values are displayed on the left. Recirculation is evident on the trailing edge along the span of the fin, as is separation, due to the leeway angle. The root flow is developing at the base of the fin, and similarly at the connection between the fin and the wind tunnel wall. The transition between laminar and turbulent flow seems to be accurately modelled, the observed streamlines on the leading edge of the fin in the laminar region become turbulent in the trailing edge. Transition appears to occur slightly behind the location of the forced transition from the experiments. By predicting the natural transition, the resultant forces can be more accurately accounted for and variations during the race minimised in order to maximise the laminarity.

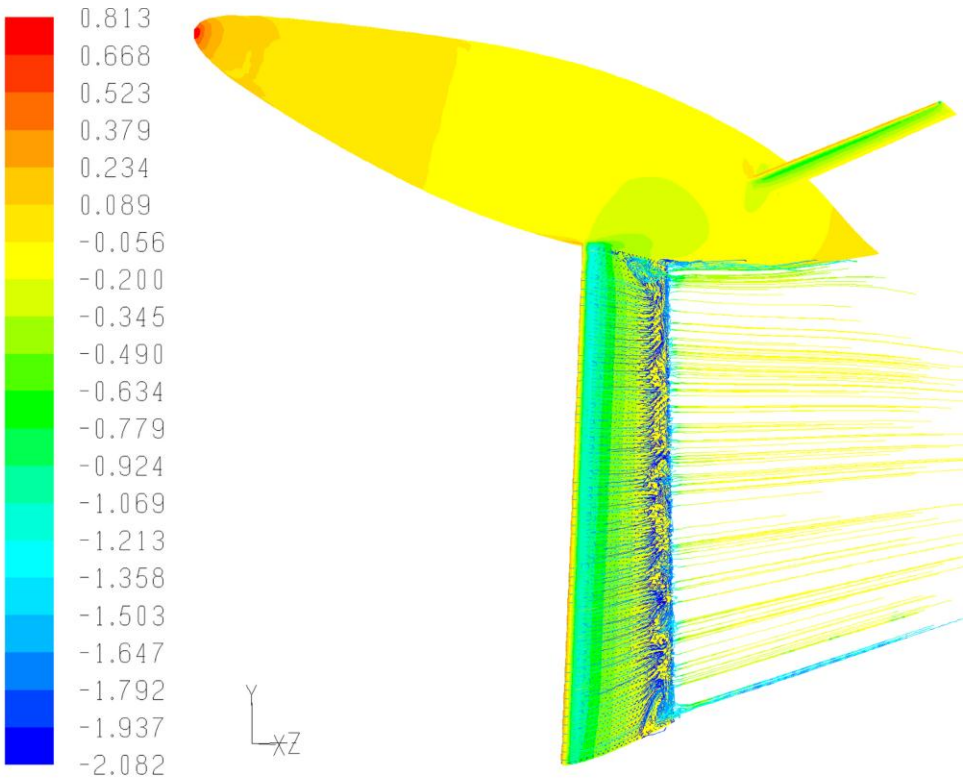

Figure 8.: Mean pressure coefficient contours on keel, with flow pathlines behind the fin's suction side, coloured by velocity magnitude

Turbulence is expected around the fin and the winglets over most part of the structures. Based on the inlet flow, their Reynolds number is equal to Re_f = 5.04 x 10^5 and Re_w = 1.80 x 10^5 respectively, which means transition will occur sooner than for the bulb. In computational terms, this means that further resolution may be necessary near the wall of these lifting surfaces to fully grasp the unsteadiness and the transition from laminar to turbulent flow. The flow around the bulb is laminar over a longer part, whereas the turbulence on the fin and the winglets is much more pronounced.

As an example, figures 8.20 to 8.22 show the instantaneous velocity vectors near and in the boundary layer of the fin at the plane y = 0.61, over a part of the cross section near the intersection with the bulb. The top picture shows the trailing edge on the leeward side, and the bottom is the leading edge on the windward side. A vortex structure can be identified on the trailing edge, with separation and turbulence occurring on the viscous sublayer. The flow then reattaches after the vortex. On the

pressure side, there is less relevant turbulent effect and the flow exhibits a laminar regime over a longer range. It appears more energized; as a result, the boundary layer thickness in the pressure side is much thinner than in the suction side. The regions of stagnation points, reattachment and separation on the suction side correspond to changes in the surface pressure of the fin, due to the flow unsteadiness.

The streamlines and vectors show that the numerical solution captures the important features of the boundary layer including separation, recirculation zone and turbulent boundary layer. Further insight into these complex phenomena is required, with the investigation of parameters influencing the turbulence for LES and DES, such as intensity and turbulent viscosity at the inlet.

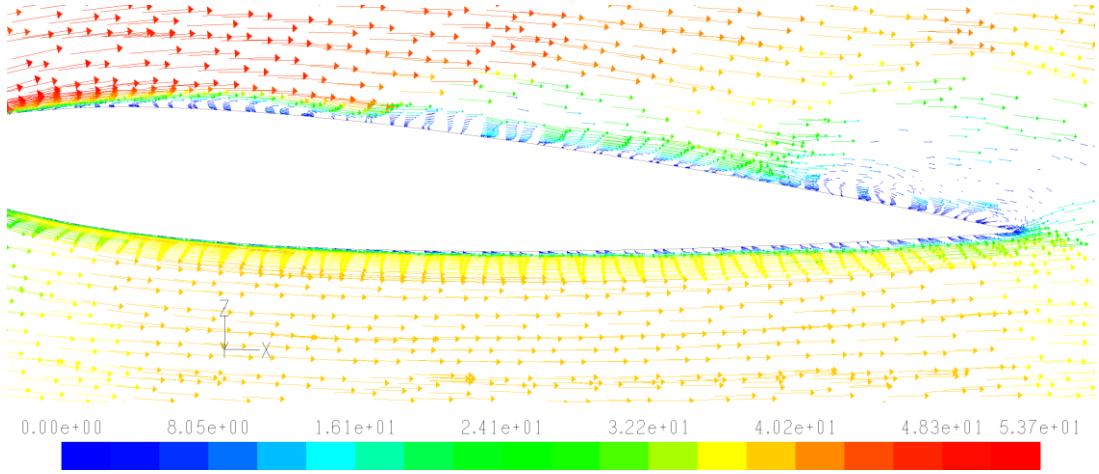

Figure 8.: Velocity vectors at plane y = 0.61

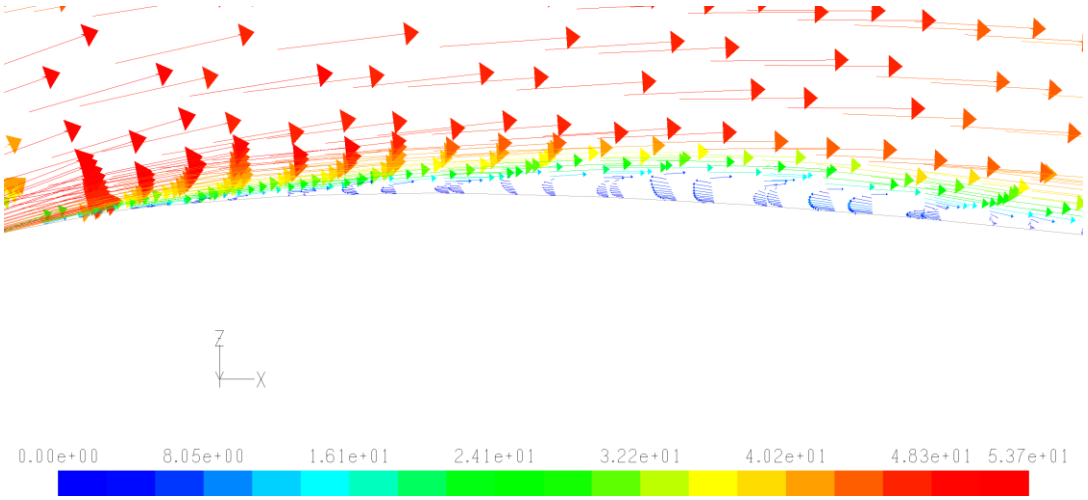

Figure 8.: Velocity vectors in the boundary layer, on the leeward side

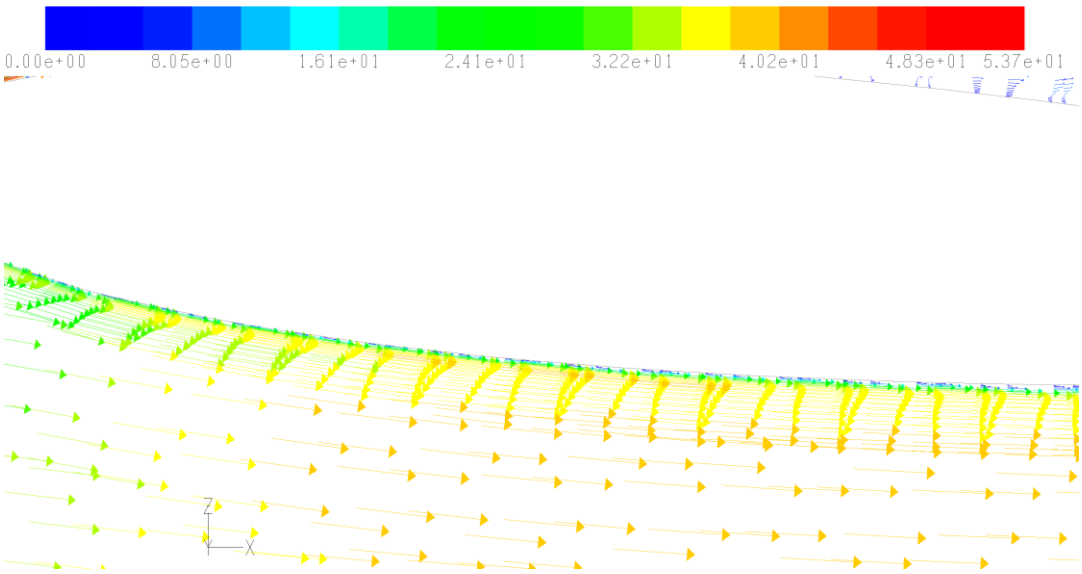

Figure 8.: Velocity vectors in the boundary layer, on the windward side

Observed in Figure 8.23 are the instantaneous vectors of velocity appearing at the tip of bulb in a plane cutting through the keel longitudinally, coloured in terms of velocity magnitude. As per the wake survey, this is from the wingless keel calculations. The vectors are taken at two different times during the simulation, t=0.044s (top) and t=0.062s (bottom). The left pictures are the results from the LES SM case and the right are from the DES R κε simulation.

The calculation results show complex time-dependent flow features in the region adjacent to the end of the bulb. The unsteadiness of the near body-wake flow is clearly well captured. Two counter-rotating core vortices are visible, although for the LES run at 0.044s the second vortex at the bottom is not as pronounced as the top one. At 0.062s, both LES and DES agree well with the flow separation and re-circulation, although the vortices are stronger for LES than those shown under DES. Velocity vectors direction and strength are concurring well.

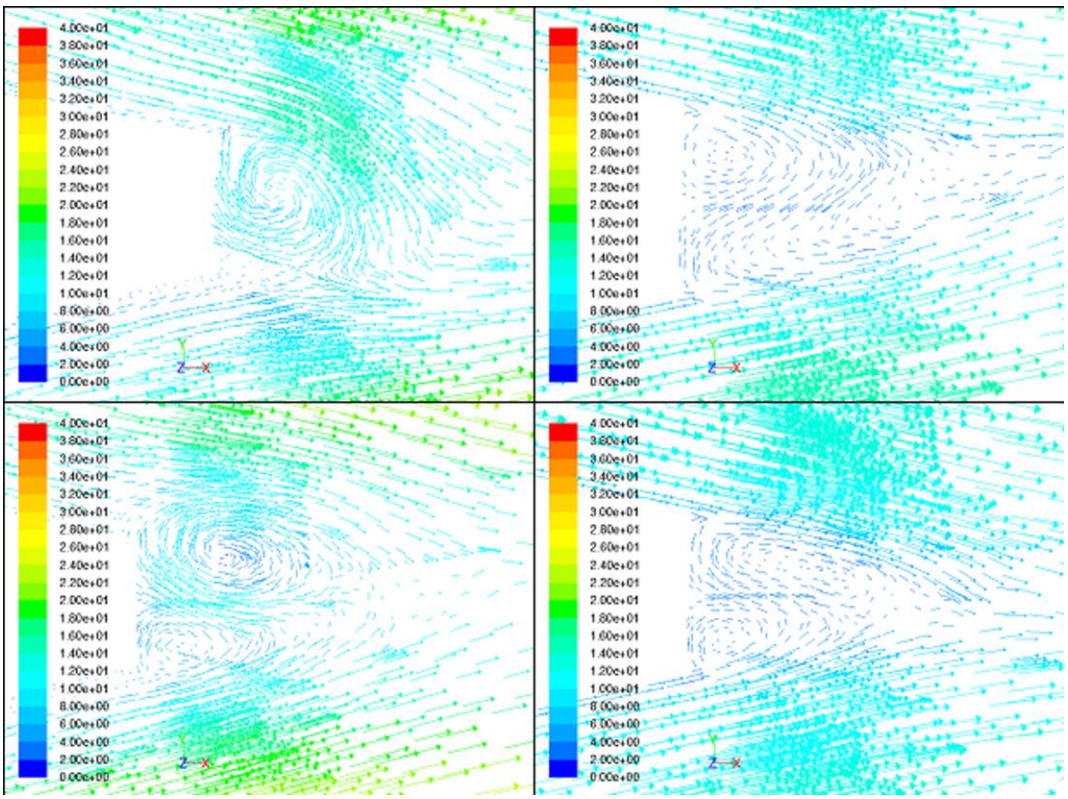

Figure 8.: Instantaneous velocity vectors past the bulb, coloured by velocity magnitude. Left: LES SM; right: DES R κε. Top: t=0.044s; bottom: t=0.062s

Example of the contours of the wall shear stress for DES and LES are depicted in figure 8.24. The top picture (a) shows the contours with DES Rκε, in the middle, the mean contours for LES SM model (b) are observed and on the bottom the instantaneous LES SM values (c). The value of the wall shear stress is found to be the lowest at the trailing edge of the fin keel and about three quarters of the length of the bulb, in the suction side, for the SM model. For the DES model, the lowest value is at the end of the bulb. The highest values of stress for all models are located at the nose of the bulb and at the leading edge of the fin keel. Instantaneous flow shows a high level of unsteadiness behind the fin-bulb intersection and at the after part of the bulb, with fluctuations changes in the force occurring.

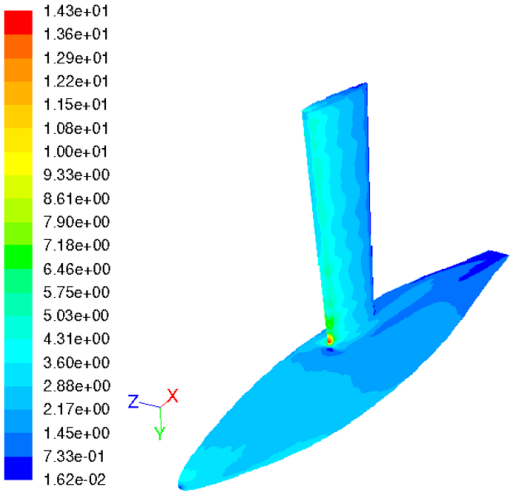

(a)

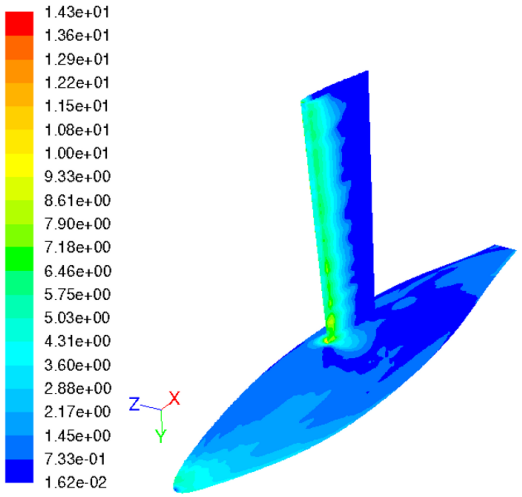

(b)

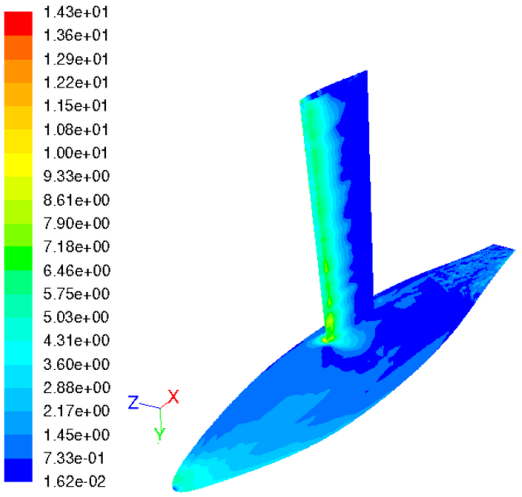

(c)

Figure 8.: Contour plot of wall shear stress on the keel

The LES model shows the natural laminar-to-turbulent flow transition rather smoothly and accurately. The DES model is behaving more in full turbulent flow mode. Looking at the velocity vectors at three different locations along the bulb, through a cut plane taken along the length of the body, the laminar-turbulence transition is observed (figure 8.25). The laminar boundary layer is no longer able to maintain attached flow at the wall and consequently separation occurs. This causes the boundary layer to transit to turbulence and gaining additional momentum, which diffuses back into the turbulent boundary layer allowing it to reattach to the wall.

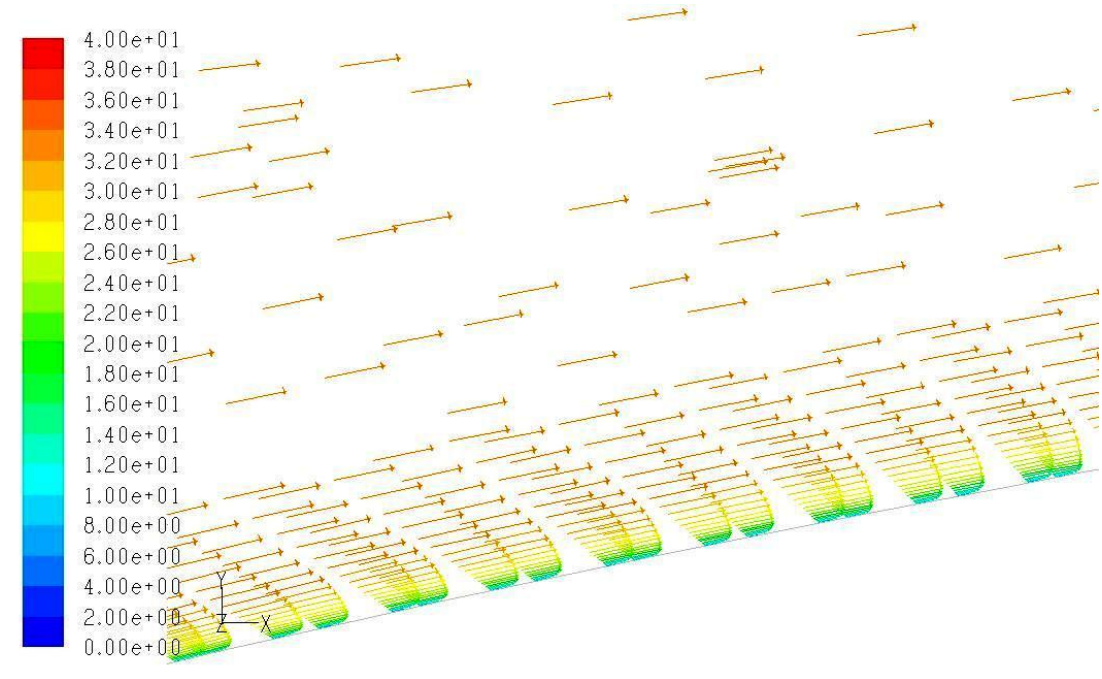

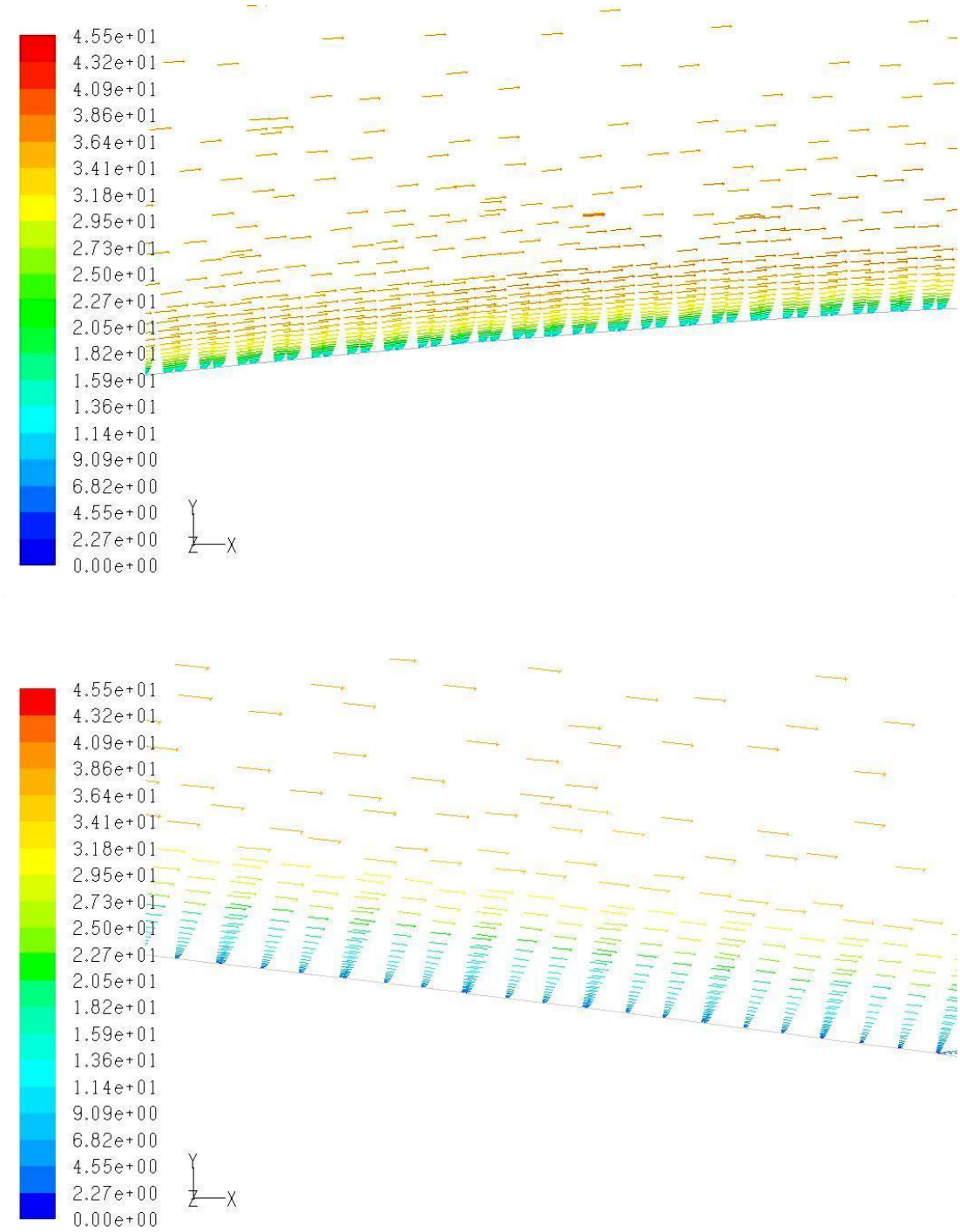

Figure 8.: Velocity vectors profile along the bulb in the boundary layer with LES model. Top to bottom: fore, middle and after position

8.8 Sensitivity Analysis of numerical parameters

A sensitivity study was undertaken for the CFD calculations. Three areas were targeted: time-step dependency, Sub-grid scale (or RANS) model dependency and sub-filter constant (C_s and C_{des}) dependency. Mesh dependency was neither investigated nor other discretization schemes. The results presented here are for the case without winglets.

Table 8.8 summarises the modified parameters during the study for the LES on the keel with 1.4 million cells. The last two columns indicate the absolute error compared to the experimental measurements. As can be seen, values of lift and drag coefficients are still acceptable up to a time-step of 0.001. Beyond this value, the error becomes important and may not be considered reasonable. A time-step equivalent to a value of CFL smaller than one does not increase the accuracy of the results. An upper limit when results are not acceptable is identified, after this value because of too high error. It could be of benefit for longer flow times to increase the time-step after convergence and relevant integrals have been monitored accordingly, but only for qualitative results. For quantitative data, values must be kept close to CFL = 1. Of course, time-step is also dependent on the mesh size, so a finer mesh with require a smaller time-step to keep CFL number at unity.

Several values for the Smagorinsky constant C_s have been tried with results showing that this constant is closely linked to the mesh resolution near the wall and to the filter function of LES. If the grid is fine enough, and when accuracy matters the most, then it may be necessary to use a lower value. However, the standard value of 0.1 is universally used is still very accurate at this stage.

A series of SGS models have also been compared, including the WALE (Nicoud and Ducros, 1999) and the TKE (Kim and Menon, 1997) models, further defined in the Appendices. All sub models perform well; in fact, it is interesting to notice that the difference is very small in lift and small in drag predictions. WALE and TKE are

adapting better to the fluctuations near the wall and can be a good alternative to the SM model.

Table 8.: Numerical sensitivity for LES

Influence of Cs				
Cs	C_L	C_D	%err L	%err D
exps	0.0630	0.0058	-	-
0.1	0.0634	0.0057	0.67	2.08
0.01	0.0634	0.0058	0.56	0.86
0.5	0.0648	0.0061	2.86	5.17
1	0.0651	0.0081	3.30	39.66
Influence of Δt				
Δt	C_L	C_D	%err L	%err D
exps	0.0630	0.0058	-	-
7.1E-06	0.0634	0.0057	0.67	2.08
1.0E-06	0.0634	0.0057	0.57	1.21
1.0E-05	0.0639	0.0057	1.43	2.07
1.0E-03	0.0644	0.0056	2.22	2.76
1.0E-02	0.0659	0.0064	4.57	10.34
Influence of SGS				
SGS	C_L	C_D	%err L	%err D
exps	0.0630	0.0058	-	-
SM	0.0634	0.0057	0.67	2.08
DSM	0.0642	0.0057	1.92	1.78
WALE	0.0634	0.0055	0.63	4.83
TKE	0.0628	0.0056	0.32	3.72

In Table 8.9, the results of lift and drag for the modified parameters of the DES simulation are presented. The last two columns indicate the absolute error compared to the experimental measurements. Results are especially sensitive to the subgrid-scale (RANS) model, and to the value of C_{des}. It is noticed that the two other sub scale models perform better in that given situation. The SST model is able to predict the transitional flow better around the keel and should be considered as a candidate for future simulations. It is widely used in the CFD industry and perhaps was ought to be applied in the current thesis. The SA model is also good, whereas as seen earlier it can underperform for other simulations.

For the time-step sensitivity, a magnitude of the order of 10^{-5} is giving reasonable results although it is not recommended to use higher steps as the solution may be compromised and diffusivity observed during the re-runs was large.

A smaller value of C_{des} gives better results for the case study. It is something though that requires further thought and it is not possible to further comment at this stage. A more refined grid sensitivity study should confirm this.

Table 8.: Numerical Sensitivity for DES

Influence of Cdes				
Cdes	C_L	C_D	%err L	%err D
exps	0.0630	0.0058	-	-
0.61	0.0670	0.0047	6.38	18.48
0.3	0.0625	0.0056	0.79	3.45
0.5	0.0621	0.0050	1.40	13.79
1	0.0570	0.0043	9.52	25.86
Influence of Δt				
Δt	C_L	C_D	%err L	%err D
exps	0.0630	0.0058	-	-
1.0E-06	0.0655	0.0051	3.95	11.32
1.0E-05	0.0675	0.0050	7.07	14.36
5.4E-05	0.0670	0.0047	6.38	18.48
1.0E-03	0.0699	0.0074	10.88	27.76
1.0E-02	0.0735	0.0075	16.65	29.54
Influence of SGS				
SGS	C_L	C_D	%err L	%err D
exps	0.0630	0.0058	-	-
R κ-ε	0.0670	0.0047	6.38	18.48
SA	0.0610	0.0054	3.17	7.67
k-ω sst	0.0654	0.0061	3.81	5.17

8.9 Chapter Summary

In this chapter, LES and DES were applied to the flow around an International America's Cup Class keel and compared to data from wind-tunnel model. A series of adapted, unstructured grids were created ranging in size from half a million cells to

nearly four million. Several configurations were simulated. Results were compared in terms of global forces, wake flow and other qualitative observations.

Quantitative results show both agreement and discrepancy with experimental results. Qualitative results show good agreement in terms of wake, vortices, main flow features Mesh size and near-wall resolution were critical in the results obtained. Furthermore a sensitivity study of some numerical parameters showed that other models may predict the forces more accurately.

The following chapter will form a basis for discussion of the overall thesis and its key findings.

"*The purpose of computing is insight not numbers.*"
C. Hastings

"*Discussion is an exchange of knowledge; argument is an exchange of ignorance.*"
Robert Quillen

9 Discussion

This chapter begins with a review of the thesis with the main points of debate rising from the outcome of the results; it then presents the contributions and research achievements followed by the challenges encountered and the limitations of the work. Finally, it outlines some recommendations for future research to guide future activities in the field.

9.1 Review of the thesis

The primary aim of the dissertation was to investigate the use of LES and DES as tools for the prediction of the flow and the forces around marine bodies, in particular to validate against experimental data, through application and use of commercial state-of-the-art software. The research questions devised at the beginning of this thesis were to find out if advanced numerical models could provide adequately accurate prediction of forces and flow around a yacht keel to match experimental data:

"Can advanced numerical models based on Large Eddy Simulation and Detached Eddy Simulation help in obtaining acceptably accurate predictions of forces and flow around a competitive yacht keel? How do these results compare to those from other methods and against experimental data? Can we assess the use of such advanced models and propose a generic approach?"

Looking back at the work accomplished in the current thesis, it was demonstrated that advanced modelling of turbulent flow through the use of LES and DES models is applicable to complex flows such as that around a sailing yacht keel. However, a more thorough investigation of certain parameters dependent or linked to those

methods is required in order to fully exploit their capabilities and capacities in predicting a better outcome of results than RANS models, closer to experimental values for the example followed in the present work, and reduce the error margin between the measured wind-tunnel values and the CFD-predicted results.

The practicality and possibility of their use, in view of a future application into the field, has been demonstrated, and conclusions drawn from the results are that the level of maturity of LES and DES has not yet reached the acceptable levels to be practically employable in yachting, to the contrary of RANS methods that are now considered mature enough to be trusted and applied. As seen from the current study, numerical results can differ even when the experimental conditions are reproduced to a high level of fidelity.

It is acknowledged that this study was an initial step into the implementation of LES and DES into the field of yacht hydrodynamics, and was not focused as much into the detailed technical parameters influencing the use of the two models, but rather more on the practicality and possibility of their use, in view of a future application into the field. It is observed that from the examples of the more theoretical flows presented here (airfoil, spheroid) and other widely available in literature (e.g. channel flows, backward facing step, Ahmed body), the methods are very suitable and adapted to the use of aero- and hydrodynamic predictions. The flow around a yacht, however, can be classified more as a complex, practical type of flow rather than theoretical. In this instance, the level of maturity of LES and DES has not yet reached the acceptable levels to be practically employable, and coupled with some issues linked to the numerical simulations, and discussed in this chapter, were incorrect and influential enough to not make it possible to fully extract the potential of LES and DES.

Verification and validation of turbulent flow is hitherto still a challenging topic in engineering and hydrodynamics, more so that it is unpredictable in nature, chaotic in behaviour and random in formation, which makes it difficult to predict. Good quality of experimental data for validation is paramount as an endorsement for a more

thorough evaluation of both mathematical and numerical models in naval and marine related problems.

The excellent experimental set-up, post-processing and data developed by VPI on the 6:1 prolate spheroid is an example of a successful case when key components such as the forces, the surface pressure or the near wall separation were perfectly usable for building a strong case of numerical validation. On the other hand, the database from Chalmers Technical University was not sufficient to grasp the fundamentals required for an advanced analysis of LES and DES applications; hence, the author recognizes the limitations of this case study. For a RANS application, a set of lift and drag coefficients supported by a set of wake flow measurements of nominal velocities are sufficient to build a case for this numerical method. It would have been appropriate to have a better database of results to compare the LES and DES models with, particularly for issues such as the near-wall interaction and surface flow of the keel. This is pointed out in the recommendations for future work. Based on the qualitative results obtained of the surface flow and near-wall flow, it is concluded that both methods are predicting main features satisfactorily, with an advantage towards LES.

As indicated by Georgiadis et al. (2010), the wider problem when implementing LES and DES is not in selecting the model inside the solver of the CFD program, but most importantly it is a matter of ensuring the correct settings and steps are applied. These are principally the grid-resolution, the spatial and temporal schemes, the boundary conditions, and time for the simulation to run long enough. All of the above influence the flow quantities, the scalars, the residuals of convergence and the variation of the variables. In the case of this thesis, the main issues encountered were the computational power, the grid resolution and the simulation time, which are believed to have been the major influences on the results; since for the other parameters it is observed from the simple validation cases that there was little influence on the results. With the more complex shape of the fully-winged keel, the mesh generation, the grid size and the running time were found to be the most difficult issues to deal with. Complex engineering problems such as submarine hydrodynamics are at present dealt with meshes of size close to 6.5 million cells with

LES, Alin et al. (2007). At the time the main calculations were taking place, it was not possible to generate meshes of such size. Clearly, the author believes this has influenced a possible better prediction of the forces acting on the keel, and the flow around and behind the geometry. The issue of the high Reynolds number is also a parameter that may have influenced the simulations. For the simple models, very good correlation between experiments and the CFD results were found for Re up to 4.2 million. For the yacht keel, the Reynolds number was based on the bulb's length; it is difficult to account for the Re num. of the other components.

Georgiadis et al. (2010) also discussed that in some cases RANS-based models tend to perform better than LES for some engineering quantities, such as mean flow profiles and overall viscous drag. This argument is however debatable as it can be seen from the two RANS-based studies of the same keel geometry that the global components of lift and drag yielded contradictory results. Ambrogi et al. (2008) reported a domain of 7 million cells yielded a 23% error in lift and 8% error in drag for the same geometry, with and without winglets. It may well be possible that LES and DES require a transition time before being considered as a practical alternative to RANS models for yacht hydrodynamics. The current thesis tends to confirm this. Additionally, a more advanced grid is necessary rather than a single-block volume mesh such as the ones generated herein for complex flows. The author acknowledges that should this opportunity is given, a multi-block mesh will be considered instead.

Unlike in RANS, a grid convergence and a sensitivity study are usually not feasible in LES. Due to the large grid sizes involved and due to the use of unstructured, hybrid grids and adaptive mesh refinements that can bring complications (e.g. mesh irregularities, distortion, stretching…), it is difficult to investigate the uncertainty of the mesh, the sensitivity to the grid resolution and to the linked parameters, as indicated by Fureby and Bensow (2008), and Georgiadis et al. (2010). Achieving grid independence may not be convenient for problems of naval interests such as a sailing yacht flow with unstructured meshes. Preferably, a painstaking LES and DES simulation should encompass sensitivity not only to grid density, but also to grid stretching, time discretization, subgrid-scale modelling, boundary condition, domain

size and other factors and parameters. A trade-off must be applied between focusing on the exactitude and strictness of the simulations and delivering a more flexible and practical engineering solution that can be used for decision-making purposes. As the use of LES and DES will increase, this issue will become more important in the future. The thesis proceeded towards an examination of modelling parameters potentially affecting the solution, and an identification of the sources of errors in the results. More emphasis is put in the literature on the fine resolution close to the near-wall in LES rather than grid uncertainty and convergence studies. Near-wall region is important, with y^+ values below five preferable (Fureby and Bensow, 2008). The use and application of wall models similar to those existing for RANS simulations is also a topic which will be recommended for future work.

The decision of utilizing hybrid and adapted unstructured meshes was supported by the several reasons. Firstly, the complexity of the mesh that needed to be created and the small enclosed domain around the keel that represented the wind-tunnel section of the experiments quickly pointed towards the unstructured solution of most of the domain. Secondly, the problems encountered during the initial stages of the meshing process of the keel geometry obtained by Chalmers Technical University in the IGES file (problems in curvatures, splines, overlaps, gaps…) meant the decision was taken to minimize further problems that would have appeared during the generation of the volume mesh in the latter stages of the meshing process. Thirdly, the angle of yaw present in the experimental tests and reproduced in the CFD did not allow creating a symmetrical mesh around the model, which would have simplified the process. Finally, since a single-block mesh was outlined from the start, it was easier to follow the unstructured approach rather than the structured approach that in most of the cases require a multi-block frame, although in many cases more accurate. The unstructured mesh allowed for more flexibility, particularly when using the TGrid® tool. However, the limited computational resources did not allow for meshes above 4 million cells, and moreover, problems persisted with the grid topology and the changing cell size and volume, as explained in chapter 9. As shown by Tucker and Lardeau (2009), cell topology can have a dramatic numerical influence in resolving turbulent flow features. The numerical discretization and grid are closely coupled

and it is necessary to know how a particular grid will react with a particular solver. In this present study, the unstructured meshes coupled with the chosen solver demonstrated a higher accuracy for LES compared to DES. For the DES simulations, the grids were likely not perfect around the RANS to LES transition region at the interface. Some of the grids were more appropriate to LES application rather than DES and this too have influenced the outcome of some of the forces prediction, whilst others were too generalist and unsuited for the method (by generalist, it is meant that the grids were not clearly characteristic of either LES or DES meshes). Again it is advised that further work is carried out on these issues.

Addad et al. (2008) indicated the importance of obtaining a fine grid resolution not only normal to the wall (y^+) but also in the stream wise direction when creating an optimal unstructured mesh for applying LES. This was demonstrated on simple channel flows for Reynolds number lower than 1,000. In more technical papers using LES and DES, this is taken into consideration; and it is something ought to be addressed in the future application of the author of the thesis.

Kornhaas et al. (2008) studied the influence of two numerical parameters on LES in terms of quality and efficiency. The non-dimensional time-step and the convergence criterion based on the CFL number were investigated and their influence on the results in terms of computational time and mean-values checked. The simulations of a 2-dimensional hill flow indicated that the convergence criterion was not influencing the results, although the higher the CFL number, the difference in the results increased. On the other hand, a large time-step was not beneficial because of the increase in error in the results. These findings are in line with the current indications obtained from the sensitivity studies of chapter 9 on the same parameters.

Ghorbaniasl and Lacor (2008), on looking at the effects of grid irregularities on the results of LES simulations of turbulent channel flows for low Reynolds number (180), found that some sub-grid scale models behave better than others do. The wall-adapting local eddy-viscosity (WALE) model of Nicoud and Ducros (1999) and the variational multi-scale model of Hughes et al. (2001) were not affected by the sudden

changes in cell distribution and stretching of the mesh, while the Smagorinsky-based models yielded worse results in these conditions. It was found that the latter models require a smoother stretching particularly in the region of the boundary layer expansion, in the outer-layers. Some of the meshes of the current study could not follow those guidelines for various reasons. This is a clear indication that the mesh is the main influence on the differences in results recorded in the simulation presented in chapter 9 as for the calculations of chapter 8 on the simple validation cases these differences were not present.

It is recommended that further work should be directed towards a more accurate comparison of the wake flow away from the body. The current results show small differences with the values obtained during the wind tunnel measurements. This is due to a number of factors: an insufficient grid resolution is present in the wake of the model at the given location. A high-accuracy description of this flow is nonetheless very challenging due to the large mesh-size requirement needed along this region, on top of the mesh needs near the keel, which was not possible at the time of the computations. However many positives can be drawn from the fact that the differences were not too high. Streamwise resolution needs to be higher; refinement in the wake is important to get a good prediction of side force for a yacht and lift-induced drag, particularly if it is a competitive yacht. Near-wake qualitative results obtained are considered to be good and demonstrate the pertinent use of LES and DES for this kind of applications. As the flow continues further downstream then the resolution weakens and the good predictions fade. Hence the wake survey is not so accurate. It is noticed that for Werner (2007) a cross-plane of 100 cells is sufficient to show the wake features, as presented in her paper, for simple RANS models. This seems not possible in LES and DES. More cells are needed in the wake.

Finally, it is also of importance to note that no ‘artificial’ means have been used for the transition from laminar to turbulent flow. Figures 8.20 to 8.22 shows that transition can be quite accurately modelled; future studies must recreate appropriate laminar conditions on the keel to highlight any differences occurring from the fully turbulent calculations. However, simulations from the prolate spheroid validation indicate that only small changes were observed between the two conditions.

9.2 Contributions of the present work

Better understanding of the application of LES and DES to yacht hydrodynamics: Although the majority of the numerical investigations on America's Cup keel have focused on the use of the potential flow theory for inviscid flow and the application of RANS-based models for viscous flow for the prediction of the forces and the flow around a yacht, there have only been a handful of published investigations based on more advanced models. Using a LES and a DES model, the present work has added to the understanding of these methods by identifying the possibilities and limitations of each of the methods.

9.3 Challenges encountered and limitations

Since this work is focused on advanced turbulence modelling methods, the grids used for the simulations have had to be very fine, and in the cases when this was not possible, they had to be as refined as permissible, in order to get a reasonable resolution of the near-wall solution, wake effects and farfield. This has meant that grid sizes of about 60,000 for 2-dimensional cells have been used during the airfoil simulations and grids ranging from 550,000 up to 4 million cells for the three dimensional simulations of the spheroid and the America's Cup keel. Therefore, one of the major challenges encountered in the course of this thesis was the large computation time and resources required for the viscous flow CFD calculations. This is considering that hundreds of runs were performed to acquire as much data as presented in chapters 8 and 9 about the assessed quantities, scalars, variables, etc.

The cleaning of the geometry was amongst the most difficult and time-consuming tasks of this thesis. Although imported as an IGES file, the problems in compatibility were numerous and healing, repairing, modifying and applying tolerances to the CAD surface took a lot of time and frustration.

The requirement for fine meshes implied the set-up of very low time-steps, of the order of 10^{-5} seconds even for the simple cases, to avoid diffusivity in the simulations and erroneous results, which in the worst cases led to no-run at all because the problem was diverging dramatically.

Extensive use of the Faculty of Engineering High-performance Computing facility has been made, without which it would not have been possible to conduct the simulations in the present way (lower computational resources would have required another strategy, possibly no-use of the LES and DES or something else). However, the benefit of increased computational power and speed was not fully exploited because of the extensive need and use of power of LES and (to a certain extent) DES.

In addition, limitations set by the computing officer in the available nodes per user of the HPC added a further limitation. FLUENT users were limited to a maximum of eight nodes at any time, on top of the queuing system in application which allowed only a given number of jobs to be run at any time to ensure control of licenses and traffic.

9.4 Recommendations for future research

Given the time frame and resources available for the work presented herein, it is acknowledged that only a very limited portion of the problem of LES and DES applications to yacht hydrodynamics and their impact and influence on the prediction of the flow and global forces has been studied. A more detailed investigation of the problem will be essential and it will be very interesting to see progress and results of further studies on the following linked areas:

- Better use of the near-wall functions for DES and near-wall treatment for LES, such as the Piomelli model (Piomelli and Balaras, 2002) or other model. Other SGS models for LES and RANS model for DES as investigated in the sensitivity study should be considered.

- Possibly perform new experimental measurements which will be specifically directed for validation of flow with LES and DES; with data such as near-flow separation, surface pressure & skin-friction coefficients, velocities, etc.
- Tests were carried on static bodies fixed in space. It can be more realistic to have fully unsteady conditions encountered in real-life, e.g. upwind, downwind, heeling conditions, etc.
- Repeat CFD on larger grids, above 3-4 million cells up to 10 million cells using the latest High-Performance Computing facilities.
- Generate a more meticulous mesh; possibly make use of parameterisation of variables.
- Meshing strategy: multi-block, structured grids should be investigated. Similarly, overset & overlapping grids can be a possible outcome for further research.
- Introduce the laminar zones for the DES calculations
- Investigate the influence the inlet turbulence parameters may have on the LES and DES computations and on the results.
- Extend the domain of the wind-tunnel and investigate if wider dimensions are influencing the results.
- Finally, assess the numerical and mathematical methods in other conditions such as massively separated flow, heeling conditions of yacht, sail design.

"*New opinions often appear first as jokes and fancies, then as blasphemies and treason, then as question open to discussion, and finally as established truths*"
George Bernard Shaw

"Out of damp and gloomy days, out of solitude, out of loveless words directed at us, conclusions grow up in us like fungus: one morning they are there, we know not how, and they gaze upon us, morose and gray. Woe to the thinker who is not the gardener but only the soil of the plants that grow in him"
Friedrich Nietzsche

10 Conclusions

The work presented in this thesis has focused on the use of LES and DES turbulence-based models for describing the key features of the flow around bodies of naval hydrodynamic interest, through comparison of the case studies with experimental results. The marine bodies were a NACA 0012 profile section, a prolate spheroid of 6:1 length-to-breadth ratio and an International America's Cup Class appended keel.

LES and DES provide two suitable solutions that can be implemented for the simulation of the turbulent flows under a range of condition, to examine the complex flow features linked to marine hydrodynamic. It is necessary to examine the problem further to have full confidence in their capabilities when applied to advanced cases such as that of a keel hydrodynamic. The initial steps undertaken in this thesis have been encouraging.

- All physical phenomena such as turbulent flows, separation, pressure and friction changes have been modelled successfully when compared with available wind-tunnel results. It has been shown that adapted structured and unstructured grids are capable of dealing with challenging high Reynolds number flows, such as that around the keel.

- Smaller mesh size, and higher density and computational resources are required in the more complex case of the America's Cup keel to fully realise the potential of the LES and DES.

- The developed numerical solution proved to be accurate when applied to a number of standard 'validation' cases. The higher numerical models are sufficiently powerful enough to resolve the turbulence characteristics of the flow.

- Valuable information about the flow around the America's Cup keel has been collected for future applications (e.g. instantaneous values of velocities, surface streamlines indicating separation and complexity of the problem) and when investigating local flow characteristics (e.g. at winglets).

LES and DES models offer considerable potential for accurate analysis of competitive sailing configurations. Improvements in the mesh size, SGS models and near-wall modelling are required to obtain better quantitative results; the present thesis has identified specific areas for further study.

"*We are not certain, we are never certain. If we were we could reach some conclusions and we could, at last, make others take us seriously.*"
Albert Camus

11 References

Addad, Y., Gaitonde, U., Laurence, D., Rolfo, S., 2008, 'Optimal Unstructured Meshing for Large Eddy Simulations', in *Quality and Reliability of Large-Eddy Simulations*, ERCOFTAC Series, Springer

Alin, N., Berglund, M., Fureby, C., Lillberg, E., Svennberg, U., 2007, 'Complex Engineering Turbulent Flows', in *Implicit Large Eddy Simulation – Computing Turbulent Fluid Dynamics*, Cambridge University Press

Ambrogi, M.M., Broglia, R., Di Mascio, A., 2008, 'Numerical Simulation of a flow Around an America's Cup Class Keel', *Proceedings of the 18th International Offshore and Polar Engineering Conference*, Vancouver, Canada

America's Cup Class Rules, Version 5.0, 15 December 2003

Ansys Advantage, 2007, ANSYS Salutes Winner Alinghi of the 32nd America's Cup, retrieved from http://anss.client.shareholder.com/releasedetail.cfm?releaseid=390859

Axfors, B., and Tunander, H., 2011, 'Investigation of Keel Bulbs for Sailing Yachts', *Master Thesis*, Chalmers University of Technology

Azcueta, R., 1996, 'Numerical Calculation of the Viscous Flow around a Sailing Yacht', Diploma Thesis, *University of Hamburg*, Germany

Azcueta, R., 2002, 'RANSE Simulations for Sailing Yachts Including Dynamic Sinkage & Trim and Unsteady Motions in Waves', *Proceedings of the first High Performance Yacht Design Conference*, Auckland, NZ

Barber, K. M., and Simpson, R. L., 1991, 'Mean Velocity and Turbulence Measurements of Flow around a 6:1 Prolate Spheroid', *AIAA* Paper 91-0255

Barth, T.J. and Jespersen, D., 1989, 'The Design and Application of Upwind Schemes on Unstructured Meshes', *Technical Report AIAA-89-0366*, AIAA 27th Aerospace Sciences Meeting, Reno, Nevada

Blazek, J., 2001, 'Computational Fluid Dynamics: Principles and Applications', *Elsevier Science Ltd*, Oxford England

Böhm, C., Graf, K., 2008, 'Validation of RANSE Simulations of a Fully Appended ACC V5 Design Using Towing Tank Data', *Proceedings of the First Conference on Innovation in High Performance Sailing Yacht*, Lorient, France

Boppe, C. W., 1988, 'Elements of Hull Optimization and Integration for Stars and Stripes', *Proceedings of the Symposium on Hydrodynamic Performance Enhancement for Marine Applications*, Rhode Island, USA

Boppe, C. W., Rosen, B. S., Laiosa, J. P., 1987, 'Stars & Stripes '87: Computational Flow Simulations for Hydrodynamic Design', *Proceedings of the eighth Chesapeake Sailing Yacht Symposium*, Annapolis, USA

Boussinesq, J., 1877, 'Théorie de l'écoulement tourbillant (Theories of swirling flow)', *Mém. prés. par div. savants à l'Acad. Sci. Paris*, Vol.23

Bowler, G. R., Honey, R., 1987, 'KZ 3 & 5 – the First Fibreglass 12 metres', *Proceedings of the Conference on Yacht Technology*, pp. 39-44

Braun, J.B., and Imas, L., 2008, 'High Fidelity CFD Simulations in Racing Yacht Aerodynamic Analysis', *Proceedings of the Third High Performance Sailing Yacht Conference*, Auckland, NZ

Burgess, C. P., 1935, 'The America's Cup Defender', *SNAME Transactions*, Vol. 43, pp. 43-70

Caretto, L. S., Gosman, A. D., Patankar, S. V. and Spalding, D. B., 1972, 'Two Calculation Procedures for Steady, Three-Dimensional Flows with Recirculation', *Proceedings of the Third International Conference on Numerical Methods in Fluid Dynamics*, Paris, France

Chance Jr., B., 1987, 'the Design and Performance of Twelve Meter Yachts', Proceedings *of the American Philosophical Society*, Vol. 131 (4), pp. 378-396

Chesnakas, C. J. and Simpson R. L., 1996, 'Measurements of the turbulence structure in the vicinity of a 3-D separation', *Journal of Fluids Engineering*, 118: 268-275

Chesnakas, C. J. and Simpson R. L., 1997, 'Detailed investigation of the three dimensional separation about a 6:1 prolate spheroid', *AIAA Journal*, 35 (6), pp. 990-999

Coiro, D. P., Nicolosi, F., De Marco, A., Scherillo, F., Maisto, U., 2005, 'Induced Drag of an America's cup Yacht's Fin-Bulb-Winglet: Numerical and Experimental Investigation', *Proceedings of High Speed Marine Vehicle*, Napoli, Italy

Constantinescu, G. S., Pasinato, H., Wang, Y.-Q., Forsythe, J. R., Squires, K. D., 2002, 'Numerical Investigation of Flow Past a Prolate Spheroid', *Journal of Fluids Engineering* (Transactions of the ASME). Vol. 124, no. 4, pp. 904-910

Constantinescu, G.S., Squires, K.D., 2003, 'LES and DES investigations of turbulent flow over a sphere at Re =10,000, *Flow, Turbulence Combustion* 70(1–4), 267–298.

Constantinescu, G., 2004, 'Turbulent Flow (058-268) Lecture Notes', the University of Iowa, IIHR Hydroscience & Engineering

Coudray, T., de Jouëtte, C., Le Buhan, P., Scolan, Y.M., 1995, 'Apports de quelques outils numériques pour la conception et l'amélioration des performances de voiliers de type Coupe America', *5^{e} Journées de l'Hydrodynamique*, Rouen, France

Coudray, T., Ogden, E.A., Bouvet, L., Nivelt, B., 1994, 'A French challenge for the 1995's America's Cup', *Proceedings of the 13th International HISWA Symposium on Yacht Design and Yacht Construction*, Amsterdam, NL

Cowles, G., Parolini, N., and Sawley, M.L., 2003, 'Numerical Simulation Using RANS-Based Tools for America's Cup Design', *Proceedings of the 16th Chesapeake Sailing Yacht Symposium*, Annapolis, USA

Davidson, K. S. M., 1936, 'Some Experimental Studies of the Sailing Yacht', *SNAME Transactions*, Vol. 44, pp. 288-334

Dawson, C. W., 1997a, 'Method for solving ship wave problems', *Proceedings of the 2nd International Conference on Numerical Ship Hydrodynamics*, pp. 305–318

Dawson, C. W., 1977b, 'Numerical solutions of transient three-dimensional ship-wave problems', *Proceedings of the second International Conference on Numerical Ship Hydrodynamics*

DeBord Jr., F., 1985, 'America's Cup 1987-the Role of the Tank Test', SNAME

DeBord Jr., F., 1987, 'Review of the Current State-of-the-art for Sailing Yacht Model Tests and Future Challenges Facing Testing Facilities', *18th International Towing Tank Conference*, Kobe, Japan

Debord Jr., F., Kirkman, K., Savitsky, D., 2004, 'The Evolving Role of the Towing Tank for Grand Prix Sailing Yacht Design', *Proceedings of the 27th American Towing Tank Conference*, St John's, Canada

Debord, F., Reichel, J., Rosen, B., and Fassardi, C., 2002, 'Design Optimization for the International America's Cup Class', *SNAME Transactions*, Vol. 110, pp. 31–53

Detomi, D., Parolini, N., Quarteroni, A., 2009a, 'Numerical Models and Simulations in Sailing Yacht Design', *Computational Fluid Dynamics for Sport Simulation*, Springer Edition

Detomi, D., Parolini, N., Quarteroni, A., 2009b, 'Mathematics in the Wind', *Monografías de la Real Academia de Ciencias Exactas, Físicas, Químicas y Naturales de Zaragoza*, (31), 35-56

Fassardi, C., 2002, 'Tank Testing and Data Analysis Techniques for the Assessment of Sailboat Hydrodynamic Characteristics', *Proceedings of the first High Performance Yacht Design Conference*, Auckland, NZ

Ferziger, J.H., 1993, 'Subgrid scale modelling, Large Eddy Simulation of Complex Engineering and Geophysical Flows', *Cambridge University Press*

Ferziger, J.H., Peric, M., 2002, 'Computational Methods for Fluid Dynamics', *Springer-Verlag*, Berlin Heidelberg, Third Edition

Flay, R.G.J. and Vuletich, I.J., 1995, 'Development of a wind tunnel test facility for yacht aerodynamic studies', *Journal of Wind Engineering and Industrial Aerodynamics*, Vol.58, Issue 3, pp. 231-258.

Fluent Inc, FLUENT 6.2 User's Guide, 2005, ANSYS FLUENT Inc.

Fluent Inc, GAMBIT 2.4.6 User's Guide, 2006, ANSYS FLUENT Inc.

Freer, C., 1986, 'the Twelve-Metre Yacht: Evolution and Design 1906-1987', *Adlard Coles Nautical*

Fureby, C., Bensow, R. E., 2008, 'LES at Work: Quality Management in Practical Large-Eddy Simulations', in *Quality and Reliability of Large-Eddy Simulations*, ERCOFTAC Series, Springer

García-Espinosa, J., Luco-Salman, R., Salas, M., López-Rodríguez, M., Oñate, E., 2002, 'An Advanced Finite Element Method for Fluid Dynamic Analysis of America's Cup Boats', *Proceeding of the first High Performance Yacht Design Conference*, Auckland, NZ

Georgiadis, N.J., Rizzetta, D.P., Fureby, C., 2010, 'Large-Eddy Simulation: Current Capabilities, Recommended Practices, and Future Research', *AIAA Journal*, Vol. 48, Issue 8, pp. 1772-1784

Germano, M., Piomelli, U., Moin, P., Cabot, W.H., 1996, 'Dynamic Subgrid-Scale Eddy Viscosity Model', Summer Workshop, *Center for Turbulence Research*, Stanford, CA

Ghorbaniasl, G., Lacor, C., 2008, 'Sensitivity of SGS Models and of Quality of LES to Grid Irregularity', in *Quality and Reliability of Large-Eddy Simulations*, ERCOFTAC Series, Springer

Giorgetti, F., 2007, 'History and Evolution of Sailing Yachts (From Technique to Adventure)', *White Star*

Graf, K., Wolf, E., 2002, 'CFD Investigations and Design Integration for IACC Yachts', *Proceedings of the First High Performance Yacht Design Conference*, Auckland, NZ

Graf, K., Böhm, C., Renzsch, H., 2009, 'CFD and VPP Challenges in the Design of the New AC90 America's Cup Yacht', *Proceedings of the 19th Chesapeake Sailing Yacht Symposium*, Annapolis, Maryland

Gregory, N. and O'Reilly, C. L., 1970, 'Low-Speed Aerodynamic Characteristics of NACA 0012 Aerofoil Sections, including the Effects of Upper-Surface Roughness Simulation Hoar Frost', *NASA R&M 3726*

Hess, J. L., Smith, A. M. O., 1967, 'Calculation of potential flow about arbitrary bodies', *Progress in Aerospace Sciences*, Vol. 8, pp. 1–138

Hsiao, C.-T., and Chahine, G.L., 2004, 'Numerical Study of Cavitation Inception due to Vortex/Vortex Interaction in a Ducted Propulsor', *Proceedings of the 25th Symposium on Naval Hydrodynamics*, St John's, Canada

Hsiao, C.-T., and Chahine, G.L., 2008, 'Scaling of Tip Vortex Cavitation Inception for a Marine Open Propeller', *Proceedings of the 27th Symposium on Naval Hydrodynamics*, Seoul, Korea

Hughes, T. J. R., Mazzei, L., Oberai, A. A., Wray, A. A., 2001, 'the multiscale formulation of large eddy simulation: decay of homogeneous isotropic turbulence', *Physics of Fluids*, Vol. 13(2), pp. 505–512

Instituto Valenciano de Investigaciones Economicas, 2007, 'Economic Impact of the 32nd America's Cup Valencia 2007', Final report, *University of Valencia'*

Issa, R.I., 1986, 'Solution of Implicitly Discretized Fluid Flow Equations by Operator Splitting', J. Comp. Phys., 62: 40-65

International Service of the Swiss Broadcasting Corporation, Swissinfo, 2007, Alinghi retain America's Cup in photo finish, http://www.swissinfo.ch/eng/specials/americas_cup/Alinghi_retain_Americas_Cup_in_photo_finish.html?cid=970286, 03 July 2007, last accessed on 08 Dec 2012

Johnson, F.T., Tinoco, E.N., Jong Yu, N., 2005, 'Thirty years of development and application of CFD at Boeing Commercial Airplanes, Seattle', *Computers & Fluids* 34: 1115–1151

Jones, P., and Korpus, R., 2001, 'International America's Cup Class Yacht Design Using Viscous Flow CFD', *Proceedings of the 15th Chesapeake Sailing Yacht Symposium*, Annapolis, USA

Kim, S.-E., 2004, 'Large Eddy Simulation Using Unstructured Meshes and Dynamic Subgrid-Scale Turbulence Models', *AIAA Paper 2004-2548*, 34th Fluid Dynamics Conference and Exhibit, Portland, USA

Kim, W.-W., and Menon, S., 1997, 'Application of the localized dynamic subgrid-scale model to turbulent wall-bounded flows', *AIAA Paper 1997-0210*, 35th Aerospace Sciences Meeting, Reno, USA

Kornhaas, M., Dorte C. Sternel, D. C., Schafer, M., 2008, 'Influence of Time Step Size and Convergence Criteria on Large Eddy Simulations with Implicit Time Discretization', in *Quality and Reliability of Large-Eddy Simulations*, ERCOFTAC Series, Springer

Korpus, R., 2004, 'Reynolds-Averaged Navier Stokes in an Integrated Design Environment', *Proceedings of the First International Yacht Design Symposium*, Madrid, Spain

Kotapati-Apparao, R. B. and Squires, K. D., 2003, 'Prediction of a prolate spheroid undergoing a pitch up maneuver', *AIAA Paper 2003-0269*, 41st Aerospace Sciences Meeting and Exhibit, Reno. USA

Kreplin, H. P., Meier, H. U. and Vollmers, H., 1984, 'Wall shear stress measurements on an inclined prolate spheroid in the ONERA F1 wind tunnel-data', *Report DFVLR-IB* 222-84 A 34

Kreplin, H. P., Vollmers, H. and Meier, H. U., 1982, 'Measurements of the wall-stress on an inclined prolate spheroid', *Z. Flugwiss. Weltraumforsch.* 6, 248

Kreplin, H. P., Vollmers, H. and Meier, H. U., 1984, 'Wall shear stress measurements on an inclined prolate spheroid in the DFVLR F1 3 m low speed wind tunnel', *Report DFVLR-IB* 222-84 A 33

Ladson, C. L., 1988, 'Effects of Independent Variation of Mach and Reynolds Numbers on the Low-Speed Aerodynamic Characteristics of the NACA 0012 Airfoil Section', *NASA TM 4074*

Larsson, L., 1990, 'Scientific methods in yacht design', Annual Review Fluid Mech., Vol. 22, pp. 349–385.

Le, H., Moin, P., Kim. J., 1997, 'Direct Numerical Simulation of Turbulent Flow Over a Backward-Facing Step', Journal of Fluid Mech., Vol. 330, pp. 349-374

Lee, A., Philpott, R., 1990, 'Laurent Giles: Evolution of Yacht Design', *Adlard Coles Nautical*

Leidel, J., 2010, InsideHPC, CFD Gaining Ground in Formula One Racing, (http://insidehpc.com/2010/03/08/cfd-gaining-ground-in-formula-one-racing/), retrieved on 08 Mar 2010; last accessed on 08 Dec 2012

Leonard, B.P., 1991, 'The ULTIMATE Conservative Difference Scheme Applied to Unsteady One-Dimensional Advection', Comp. Methods Appli. Mech. Eng., 88, 17-74

Lilly, D.K., 1967, 'The Representation of Small-Scale Turbulence in Numerical Simulation Experiments', *Proceedings of the IBM Scientific Computing Symposium on Environmental Sciences*, New York, USA

Lilly, D.K., 1992, 'A Proposed Modification of the Germano Subgrid-Scale Closure Model', *Physics of Fluids*, 4: 633-635

Meier, H. U. and Kreplin, H. P., 1980, 'Experimental investigation of the boundary layer transition and separation on a body of revolution', *Z. Flugwiss. Weltraumforsch.* 4, 65

Meier, H. U., Kreplin, H. P., and Landhiuser, A., 1986, 'Wall pressure measurements on a 1:6 prolate spheroid in the DFVLR 3 m x 3 m low speed wind tunnel (~ = 10°, U~ = 55 m/s, artificial transition)', *Report DFVLR-IB* 222-86 A04

Milgram, J. H., 1998, 'Fluid mechanics for sailing vessel design', *Annual Review Fluid Mech.*, Vol. 30, pp 613–653

Moser, R.D., Kim, J., Mansour, N.N., 1999, 'Direct Numerical Simulation of Turbulent Channel Flow up to Re_t 5590', *Physics of Fluids*, Vol. 11, Num. 4

New York Times, 2002, YACHT RACING; Playground of Billionaires, by Warren St. John, Published on October 6, 2002

Nicolopoulos, D., Berton, E., Gouvernet, G., Jacques, A., 2009, 'A Hybrid Numerical Method to Develop America's Cup Yacht Appendage's, *Sports Engineering*, Vol.11, No. 4, pp. 177-185

Nicoud, F., Ducros, F., 1999, 'Subgrid-scale modelling based on the square of the velocity gradient tensor', *Flow, Turbulence and Combustion*, vol. 62, pp- 183-200

Official website of the 32nd America's Cup. http://www.americascup.com

Oossanen, P. Van and Joubert, P.N., 1986, 'The development of the winged keel for twelve-metre yachts', *Journal of Fluid Mechanics*, Vol.173, pp. 55-71

Oossanen, P. Van, 1985, 'the Development of the 12 Meter Class Yacht "Australia II"', *Proceedings of the 7th Chesapeake Sailing Yacht Symposium*, Annapolis, USA

Oossanen, P., 1992, ‘Design and Construction of the America’s Cup Yacht ‘Challenge Australia’’, *Proceedings of the 12th HISWA Symposium*, Amsterdam, NL

Pallu de la Barriere, P., 2000, ‘Optimisation des Performances des Voiliers de Compétition en Particulier des ‘Class America’’, *Bulletin de l'Association technique maritime et aéronautique*, Vol. 99, pp. 307-315

Parolini, N., Quarteroni, A., 2005, ‘Mathematical Models and Numerical Simulations for the America’s Cup’, *Computer Methods in Applied Mechanics and Engineering*, Vol. 194, pp. 1001-1026

Patankar, S. V., 1980, ‘Numerical Heat Transfer and Fluid Flow’, *Hemisphere*, Washington, DC

Piquet, J. and Queutey, P., 1992, ‘Navier-Stokes Computations past a Prolate Spheroid at Incidence -I Low Incidence Case’, *Computers and Fluids*, Vol. 21, no 4, pp. 599-625

Piomelli, U. and Balaras, E., 2002, ‘Wall-layer models for large-eddy simulations’, *Annual review of fluid mechanics*, Vol. 34, no. 1, pp. 349-374

Pope, S.B., 2000, ‘Turbulent Flows’, *Cambridge University Press*, First Edition

Porto, A., Frers Jr., G., Hughes, M., 2002, ‘The Extensive Use of a CFD Tool in the Yacht Design Process to Accurately Predict Hull Performance’, *Proceedings of the First High Performance Yacht Design Conference*, Auckland, NZ

Radhakrishnan, S., Piomelli, U., Keating, A., Silva-Lopes, A.S., 2006, ‘Reynolds-averaged and large-eddy simulations of turbulent non-equilibrium flows’, *Journal of Turbulence* 7 (63)

Raymond, J., Finot, J.M., Kobus, J.M., Queutey, P., Delhommeau, G., 2008, 'A Research Program on Performance of Planing Sailing Yachts', *Proceedings of the First International Conference on Innovation in High Performance Sailing Yachts*, Lorient, France

Ranzenbach, R. and Zahn, M., 2005, 'Experimental methods to evaluate underwater appendages', *Proceedings of the 17th Chesapeake sailing yacht symposium*, Annapolis, USA

Reichel, J., Pugh, J., Rosen, B., DeBord Jr., F., 1994, 'Grand Prix Yacht Design with the Aid of Computational and Experimental Techniques', *YachtVision 94*, Auckland, NZ

Rhie, C. M. and Chow, W. L., 1983, 'Numerical Study of the Turbulent Flow past an Airfoil with Trailing Edge Separation', *AIAA Journal*, 21(11):1525-1532

Rhyne, L.C., 1994, 'Product Development with a New Technology – Lessons from the America's Cup', *Journal of Product and Brand Management*, Vol.3, No.3, pp. 39-50

Richards, P.J., Johnson, A., Stanton, A., 2001, '*America's Cup downwind sails – vertical wings or horizontal parachutes?*', *Journal of Wind Engineering and Industrial Aerodynamics*, Vol.89, Issues 14-15, pp. 1565-1577

Rosen, B.S., Laiosa, J.P., Davis Jr., W.H., 2000, 'CFD Design Studies for America's Cup 2000', *AIAA Paper 4339*

Rosen, B.S., Laiosa, J.P., Davis Jr., W.H., Stavetski, D., 1993, 'SPLASH Free-Surface Flow Code Methodology for Hydrodynamic Design and Analysis of IACC Yachts', *Proceedings of the 11th Chesapeake Sailing Yacht Symposium*, Annapolis, USA

Sagaut, P. 2001, 'Large-Eddy Simulation for Incompressible Flows - An Introduction', first ed., *Springer-Verlag*, Scientific Computation series

Salvesen, N., Fritts, M., Meinhold, M., 1988, 'Technology and Design for Stars and Stripes', *Finite Elements in Analysis and Design*, Vol. 4, pp. 79-82

Scuttlebutt, 2002, the design team, in SCUTTLEBUTT No. 1204, http://www.sailingscuttlebutt.com/archived_Detail.asp?key=1244, November 21, 2002, last accessed on 08 Dec 2012

Shan, H., Jiang, L., Liu, C., 1995, 'Direct Numerical Simulation of Flow Separation Around a NACA 0012 Airfoil', *Computers and Fluids*, Vol. 34, Issue 9, pp. 1096-1114

Shur, M., Spalart, P.R., Strelets, M. and Travin, A., 1999, 'Detached-Eddy Simulation of an Airfoil at High Angle of Attack', Proceedings of the 4th International Symposium on Engineering Turbulence Modeling and Experiments, Corsica, France

Simpson, R. L., 'Steady Flow over a 6:1 Prolate Spheroid', *Journal of Fluids Engineering*, [online databank] URL:http://www.aoe.vt.edu/aoe/prolatespheroid

Smagorinsky, J., 1963, 'General Circulation Experiments with the Primitive Equations. I. The Basic Experiment', *Monthly Weather Review*, vol. 91, 99-164

Spalart, P.R., 2000, 'Strategies for turbulence modelling and simulations', *International Journal of Heat and Fluid Flow*, Vol.21, p. 252-263

Spalart, P.R. and Allmaras, S.R., 1994, 'A One Equation Turbulence Model for Aerodynamic Flows', *La Recherche Aerospatiale*, No. 1, pp.5 –21

Spalart, P.R., Jou, W.H., Strelets, M. and Allmaras, S.R., 1997, 'Comments on the Feasibility of LES for Wings, and on a Hybrid RANS/LES Approach', *First AFOSR International Conference on DNS/LES*, Ruston, USA

Stephens II, O. J., 2006, 'A History of Model Testing', *Proceedings of the Classic Yacht Symposium*,

ThinkSpain portal, 2006, FITUR: King underlines importance of 2007 Americas Cup, http://www.thinkspain.com/news-spain/10390/fitur-king-underlines-importance-of-2007-americas-cup, Thursday, January 26, 2006, last accessed on 08 Dec 2012

Thys, M., 2008, 'Performance Evaluation of a Sailing Yacht with the Potential Code *RAPID*', Master Thesis, *ENSTA ParisTech*

Time Magazine, 1977, YACHTING: Defending the America's Cup, Published on Sept. 19, 1977

Tinoco, E.N., Gentry, A.E., Bogataj, P., Sevigny, E.G., Chance, B., 1993, 'IACC Appendage Studies', *Proceedings of the 11th Chesapeake Sailing Yacht Symposium*' Annapolis, USA

Todter, C., Pedrick, D., Calderon, A., Nelson, B., Debord, F., Dillon, D., 1993, 'Stars and Stripes Design Program for the 1992 America's Cup', *Proceedings of the 11th Chesapeake Sailing Yacht Symposium*, Annapolis, USA

Tucker, P.G. and Lardeau, S., 2009, 'Applied Large Eddy Simulation', *Philosophical Transactions of the Royal Society A: Mathematical, Physical and Engineering Sciences*, 367 (1899), 2809-2818

Turnock, S.R., Holroyd, N.J. Date, J.C., 2001, 'Appendage design for the America's Cup using CFD', *European Congress on Computational Methods in Applied Sciences and Engineering* (ECCOMAS--CFD 2001), Swansea, UK

Vandoormall, J.P. and Raithby, G.D., 1984, ‘Enhancements of the SIMPLE Method for Predicting Incompressible Fluid Flows’, *Numerical Heat Transfer*, 7:147-163

Versteeg, H. K. and Malalasekera, W., 2007, ‘an Introduction to Computational Fluid Dynamics: the Finite Volume Method’, *Pearson Education Ltd*, New York

Viola, I.M., 2009, ‘Downwind Sail Aerodynamics: a CFD Investigation with High Grid Resolution’, *Ocean Engineering*, Vol. 36, No. 12, 974-984

Werner, S., Larsson, L., and Regnstrom, B., 2006, ‘A CFD Validation Test Case - Wind Tunnel Tests of a Winglet Keel’, *Proceedings of the Second High Performance Yacht Design Conference*, Auckland, NZ

Werner, S., Pistidda, A., Larsson, L., Regnstrom, B., 2007a, ‘Computational Fluid Dynamics Validation for a Fin/Bulb/Winglet Keel Configuration’, *Journal of Ship Research*, Vol. 51, No. 4, pp. 343-358

Werner, S., Larsson, L., Regnstrom, B., 2007b, ‘Wake survey of a yacht keel for CFD validation and flow analysis’, *Ship Technology Research*, Vol. 54, No 1, pp. 28-42

Wetzel T.G., Simpson R.L., and Chesnakas C.J., 1998a, ‘Measurement of three-dimensional crossflow separation’, *AIAA Journal*, 36 (4), pp. 557-564

Wetzel, T.G., Simpson, R.L., Chesnakas, C.J., 1998b, Unsteady Crossflow Separation Location Measurements on a Maneuvering 6:1 Prolate Spheroid, *AIAA Journal*, Vol. 36, No. 11

Weymouth, G., Hendrickson, K., Yue, D.K. P., O'Shea, T., Dommermuth, D.G., Adams, P., Valenciano, M., 2007, ‘Modeling Breaking Ship Waves for Design and Analysis of Naval Vessels’, *DoD High Performance Computing Modernization Program Users Group Conference*, IEEE

Wikström, N., Svennberg, U., Alin, N., and Fureby, C., 2004, 'Large Eddy Simulation of the Flow Past an Inclined Prolate Spheroid', *Journal of Turbulence*, vol. 5, Issue 29, p. 29

Wright, A., Claughton, A., Paton, J., Lewis, R., 2010, 'Offwind Sail Performance, Prediction and Optimisation', *Proceedings of the Second International Conference on Innovation in High Performance Sailing Yachts*, Lorient, France

Xing, T., Kandasamy, M., Stern, F., 2007. 'Unsteady free-surface wave-induced separation: analysis of turbulent structures using detached eddy simulation and single-phase level set method', *Journal of Turbulence* 8 (44), 1–35

12 Publications

Presented here is a list of journal and conference proceedings of published work from the author of the thesis. Some of the work is not related to the current thesis.

Journal:

D. Mylonas, P. Sayer, "*The Hydrodynamic Flow around a Yacht Keel Based on LES and DES*", Ocean Engineering, 2012, Vol. 46, pp. 18-32

Conference Proceedings:

D. Mylonas, S. Turkmen, M. Khorasanchi, S. Day, "*Smart Materials Application on High Performance Sailing Yachts for Energy Harvesting*", accepted at INNOVSAIL 2013 conference, Lorient

S. Turkmen, D. Mylonas, N. Vardar, "*Numerical Simulation of Flow past a Cavity with Vortex Generators*", Proceedings of INT-NAM 2011, Istanbul

D. Mylonas, P. Sayer, A.H. Day, "*Prediction of Flow around a Yacht Keel Based on LES and DES*", Proceedings of the Second International Conference on Innovation in High Performance Sailing Yachts", Lorient, 2010

D. Mylonas, P. Sayer, A.H. Day, "*New Turbulence Model Applied to Yacht Appendages Hydrodynamics*" Proceedings of the Fourth International Symposium Yacht Design and Production, Madrid, 2010

I. Salas-Jefferson, J. Logan, D. Mylonas, et al., "*America's Cup Yacht Design Process as an Engineering Educational Method for Students*" Proceedings of the 3rd International Symposium on Yacht Design and Production, Madrid, 2008

A. Appendix A: Experimental data for NACA 0012

A.1 Experimental Data from Ladson

Force Coefficients at M= 0.05 for Fixed Transition

$R = 0.70 \times 10^6$

α, deg.	c_d	c_ℓ	c_m	ℓ/d
-4.03	.01121	-.3507	-.0055	-31.29
-1.98	.00857	-.1716	-.0050	-20.03
.00	.00872	-.0094	-.0003	-1.08
2.00	.00847	.1545	.0032	18.24
4.00	.01080	.3283	.0070	30.39
6.06	.01237	.5327	.0025	43.07
8.12	.01450	.6878	.0086	47.43
10.15	.01853	.8030	.0171	43.34
11.12	.02147	.8495	.0200	39.56
12.18	.02716	.8957	.0233	32.98
13.19	.08334	.8918	-.0089	10.70
14.10	.15345	.9391	-.0479	6.12
15.32	.16754	.8626	-.0580	5.15
16.03	.21721	.7506	-.0669	3.46
17.29	.23011	.9005	-.0762	3.91
18.15	.23479	.9382	-.0672	4.00

Force Coefficients at M= 0.15 for Free Transition

$R = 2.00 \times 10^6$

α, deg.	c_d	c_ℓ	c_m	ℓ/d
-4.25	.00730	-.4300	-.0040	-58.90
-2.10	.00620	-.2150	-.0020	-34.68
.00	.00620	.0000	.0000	.00
1.85	.00620	.1940	.0030	31.29
4.25	.00670	.4450	.0040	66.42
6.05	.00870	.6250	.0070	71.84
8.15	.01270	.8550	.0080	67.32
10.15	.01350	1.0450	.0120	77.41
11.15	.01490	1.1350	.0140	76.17
12.10	.01640	1.2180	.0180	74.27
13.08	.01880	1.2900	.0190	68.62
14.25	.02280	1.3620	.0220	59.74
15.25	.02910	1.4080	.0250	48.38
16.25		.7530	-.1060	

$R = 3.94 \times 10^6$

α, deg.	c_d	c_ℓ	c_m	ℓ/d
-4.06	.00701	-.4019	.0022	-57.33
-.04	.00659	-.0033	-.0002	-.50
3.96	.00631	.4203	.0015	66.61
6.00	.00712	.636	.0019	89.33
8.17	.00985	.8657	.0077	87.89
10.02	.00934	1.0629	.0071	113.79
11.07	.01069	1.1622	.0080	108.72
12.08	.01289	1.2489	.0095	96.93
13.37	.01523	1.3587	.0116	89.22
14.10	.01725	1.4215	.0145	82.41
15.14	.02045	1.4844	.0196	72.60
18.09	.22773	1.0946	-.0800	4.81

A.2 Experimental Data from Gregory and O'Reilly

Experimental pressure coefficient at 0, 10 and 15 degrees angle of attack

The data is presented in form of graph in the paper NASA R&M 3726, January 1970 by the authors. The Reynolds number was 2.88 million. There was no fixed transition from laminar to turbulent flow. The data is available for the upper surface only.

0.00		10.00		15.00	
x/c	Cp	x/c	Cp	x/c	Cp
0	1	0	-3.66423	0	-8.65066
0.00235	0.847673	0.002183	-5.04375	0.00243	-10.1789
0.00496	0.456198	0.008734	-5.24068	0.004504	-9.72033
0.005269	0.173569	0.0131	-4.67125	0.008705	-9.04329
0.014241	-0.04441	0.017467	-4.32079	0.012972	-8.67192
0.020934	-0.17528	0.048035	-2.74347	0.016774	-6.16084
0.04735	-0.37265	0.074236	-2.26115	0.046739	-3.99796
0.077944	-0.39639	0.098253	-1.95405	0.076993	-3.16694
0.097619	-0.41941	0.124454	-1.7345	0.096453	-2.68574
0.128166	-0.41887	0.146288	-1.55884	0.146315	-2.05038
0.150001	-0.41109	0.176856	-1.36109	0.174528	-1.83081
0.178387	-0.40294	0.28821	-1.00829	0.287443	-1.23636
0.289702	-0.36672	0.320961	-0.94188	0.317853	-1.12586
0.322431	-0.34712	0.384279	-0.78721	0.380854	-0.9266
0.387891	-0.30791	0.447598	-0.65443	0.443854	-0.72734
0.448983	-0.26841	0.515284	-0.54346	0.509042	-0.59349
0.514442	-0.2292	0.576419	-0.43263	0.576404	-0.45955
0.579902	-0.18999	0.637555	-0.3437	0.635076	-0.34781
0.638834	-0.1591	0.700873	-0.25473	0.698095	-0.23589
0.704317	-0.11463	0.766376	-0.1657	0.761123	-0.16764
0.767593	-0.06528	0.831878	-0.09857	0.8285	-0.09919
0.835236	-0.02621	0.893013	-0.00964	0.893707	-0.05268
0.896305	0.03502	0.958515	0.079384	0.954576	-0.05002
0.959533	0.097857	1	0.124088	1.00022	-0.00436
1.0009	0.173854				

A.3 Numerical results for lift and drag forces with finer mesh

The following tables are the results of the lift and drag coefficients at the two of the three Reynolds numbers studied in chapter 7 under three angles of attack; computed with the refined mesh of approximately 525,000 cells.

Re = 0.7 million					
AoA	4				
	LES SM	LES DSM	DES Rke	DES SA	Exp.
Cd	0.0104	0.0113	0.0107	0.0108	0.0108
Cl	0.3175	0.3141	0.3100	0.3065	0.3283
L/D	30.6176	27.8956	28.8886	28.4201	30.39
AoA	10.0				
	LES SM	LES DSM	DES Rke	DES SA	Exp.
Cd	0.0179	0.0171	0.0176	0.0174	0.01853
Cl	0.8011	0.8065	0.8107	0.8047	0.803
L/D	44.8434	47.1729	45.9686	46.3017	43.34
AoA	15.0				
	LES SM	LES DSM	DES Rke	DES SA	Exp.
Cd	0.1689	0.1670	0.1688	0.1656	0.16754
Cl	0.8654	0.8630	0.8472	0.8470	0.8626
L/D	5.1595	5.1666	5.0201	5.1135	5.15

Re = 2 million					
AoA	4.0				
	LES SM	LES DSM	DES Rke	DES SA	Exp.
Cd	0.0064	0.0069	0.0064	0.0070	0.0067
Cl	0.4355	0.4469	0.4320	0.4311	0.445
L/D	67.6337	65.1437	67.6482	61.7642	66.42
AoA	10.0				
	LES SM	LES DSM	DES Rke	DES SA	Exp.
Cd	0.0137	0.0133	0.0133	0.0135	0.013559
Cl	1.0489	1.0477	1.0436	1.0476	1.045
L/D	76.3103	78.5362	78.6818	77.5498	77.41
AoA	15.0				
	LES SM	LES DSM	DES Rke	DES SA	Exp.
Cd	0.0297	0.0307	0.0279	0.0289	0.0291
Cl	1.4056	1.4264	1.4348	1.4214	1.408
L/D	47.3274	46.5266	51.4712	49.1327	48.38

B. Appendix B: Large Eddy Simulation filters and subgrid-scale models

B.1 Filter Functions

In large eddy simulation only the large scale motions of the flow are solved for by filtering out the small and universal eddies. In practical applications of some SGS models, the grid itself does implicit filtering. The values of velocity on the grid are the filtered values of velocity. However, for some SGS models, such as the Dynamic subgrid-scale model an explicit filtering step is required to compute the SGS stress tensor. Additionally, in the theoretical analysis of LES, filtering a function is defined as convoluting the function with a filtering kernel. Some of the commonly used filters are defined below. In all cases, Δ is the filter width; $G(x)$ is the filtering kernel in physical space and $\hat{G}(k)$ is the filtering kernel in Fourier-wave number space.

There are three filters ordinarily used for spatial filtering in large eddy simulation:

The Box Filter:

The Box filter is the same as the "grid filter" whereby the filter cuts off the values of the function beyond a half filter width away.

$$G(x) = \frac{1}{\Delta} H(\frac{1}{2}\Delta - |x|) \tag{B.1}$$

where H is the Heaviside function,

$$\hat{G}(k) = \sin(\frac{1}{2}k\Delta) / \frac{1}{2}k\Delta \tag{B.2}$$

The Gaussian Filter:

The Gaussian filter is a normalized Gaussian function. The Fourier transform of a Gaussian function is also a Gaussian, hence the $G(x)$ and $\hat{G}(k)$ have very similar forms,

$$G(x) = (\frac{6}{\pi\Delta^2})^{1/2} e^{(-6x^2/\Delta^2)} \quad \text{(B.3)}$$

$$\hat{G}(k) = e^{(-k^2\Delta^2/24)} \quad \text{(B.4)}$$

The Sharp spectral filter:

The filter kernel in physical space is given by:

$$G(x-r) = \frac{\sin(\pi(x-r)/\Delta)}{\pi(x-r)} \quad \text{(B.5)}$$

The filter kernel in spectral space is given by:

$$\hat{G}(k) = H(k-k_c) \quad \text{(B.6)}$$

where $k_c=\pi/\Delta$

B.2 Wall-Adapting Local Eddy –Viscosity Model (WALE)

The WALE model (Nicoud and Ducros, 1999) is a Smagorinsky type model but with a modified dependence on the resolved strain field, which is supposed to provide improved near-wall behaviour. The difference with the previous models comes in the way the eddy viscosity is modelled:

$$\mu_t = \rho L_S^{\,2} \frac{(S_{ij}^d S_{ij}^d)^{3/2}}{(\bar{S}_{ij}\bar{S}_{ij})^{5/2} + (S_{ij}^d S_{ij}^d)^{5/4}} \quad \text{(B.7)}$$

where: L_S and S_{ij}^d (deviatoric part of rate-of-strain tensor) are defined respectively as:

$$L_S = \min(\kappa d, C_w V^{1/3}) \quad \text{(B.8)}$$

and

$$S_{ij}^d = \frac{1}{2}(\bar{g}_{ij}^2 + \bar{g}_{ji}^2) - \frac{1}{3}\delta_{ij}\bar{g}_{kk}^2 \quad \text{(B.9)}$$

With $\bar{g}_{ij} = \dfrac{\partial \overline{u_i}}{\partial x_j}$ (B.10)

The default value of the WALE constant used in the solver, C_w, is 0.325. The rest of the notation is the same as for the Smagorinsky-Lilly model presented in chapter 5. With this spatial operator, the WALE model is designed to return the correct wall asymptotic (y^3) behaviour for wall-bounded flows.

B.3 Dynamic Kinetic Energy Subgrid-Scale Model

The subgrid-scale turbulence can be better modelled by accounting for the transport of the subgrid-scale turbulence kinetic energy. The dynamic subgrid-scale kinetic energy model replicates the model proposed by Kim and Menon, 1997. The subgrid-scale kinetic energy is defined as:

$$k_{sgs} = \frac{1}{2}(\overline{u_k^2} - \bar{u}_k^2) \tag{B.11}$$

which is obtained by contracting the subgrid-scale stress in equation (5.8). The subgrid-scale eddy viscosity μ_t is computed using k_{sgs} as:

$$\mu_t = C_k k_{sgs}^{1/2} \Delta_f \tag{B.12}$$

Where Δ_f is the filter-size computed from $\Delta_f \equiv V^{1/3}$, and V is the cell volume. The subgrid-scale stress can then be written as:

$$\tau_{ij} - \frac{2}{3} k_{sgs} \delta_{ij} = -2 C_k k_{sgs}^{1/2} \Delta_f \bar{S}_{ij} \tag{B.13}$$

K_{sgs} is obtained by solving its transport equation.

C. Appendix C: List of figures for 6:1 prolate spheroid analysis

Surface Pressure

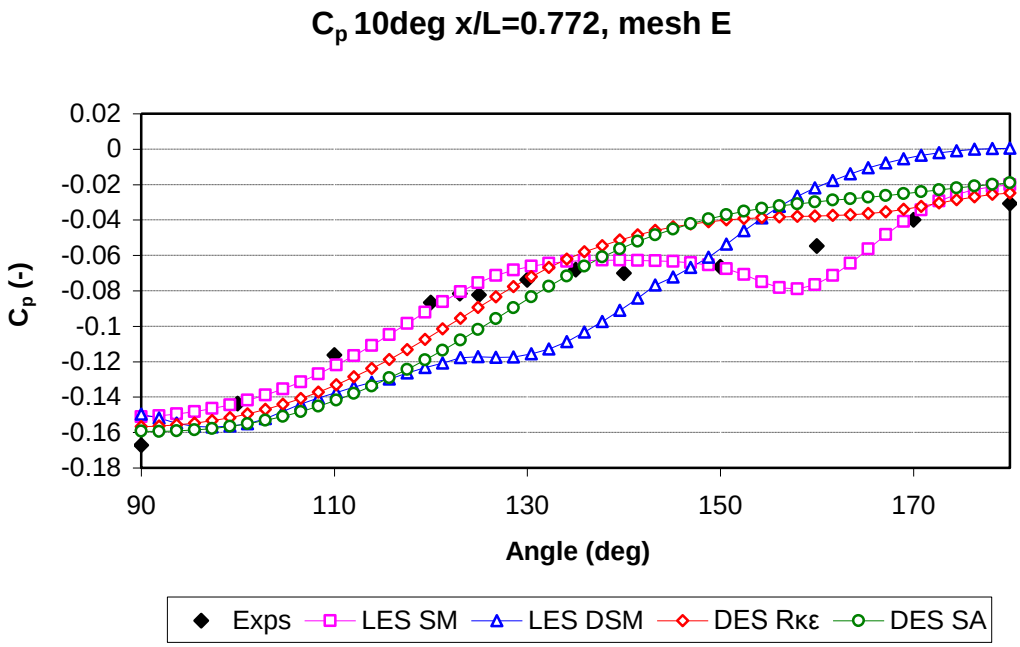

Figure C.: Mean azimuthal (or circumferential) pressure coefficient α=10 deg, x/L=0.772

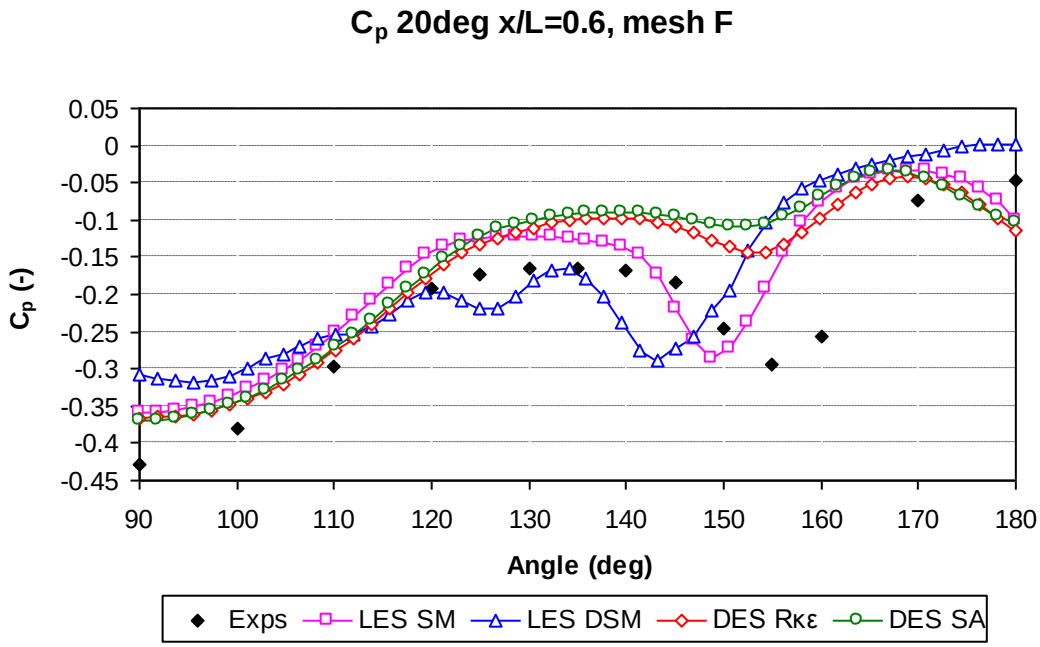

Figure C.: Mean azimuthal (or circumferential) pressure coefficient α=20 deg, x/L=0.6

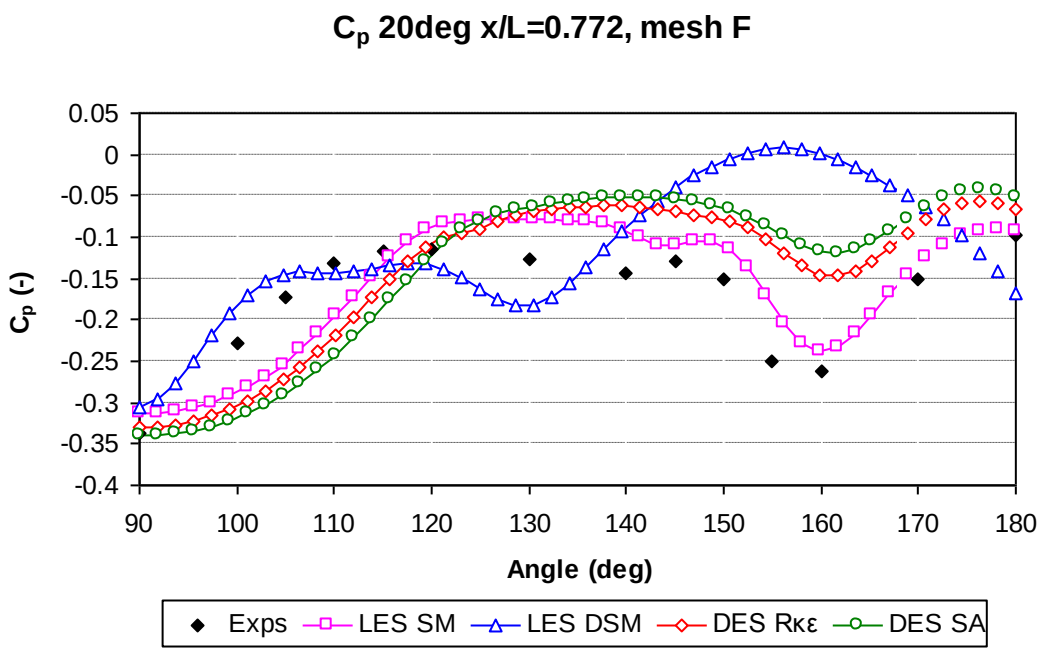

Figure C.: Mean azimuthal (or circumferential) pressure coefficient α=20 deg, x/L=0.772

Surface Skin-Friction

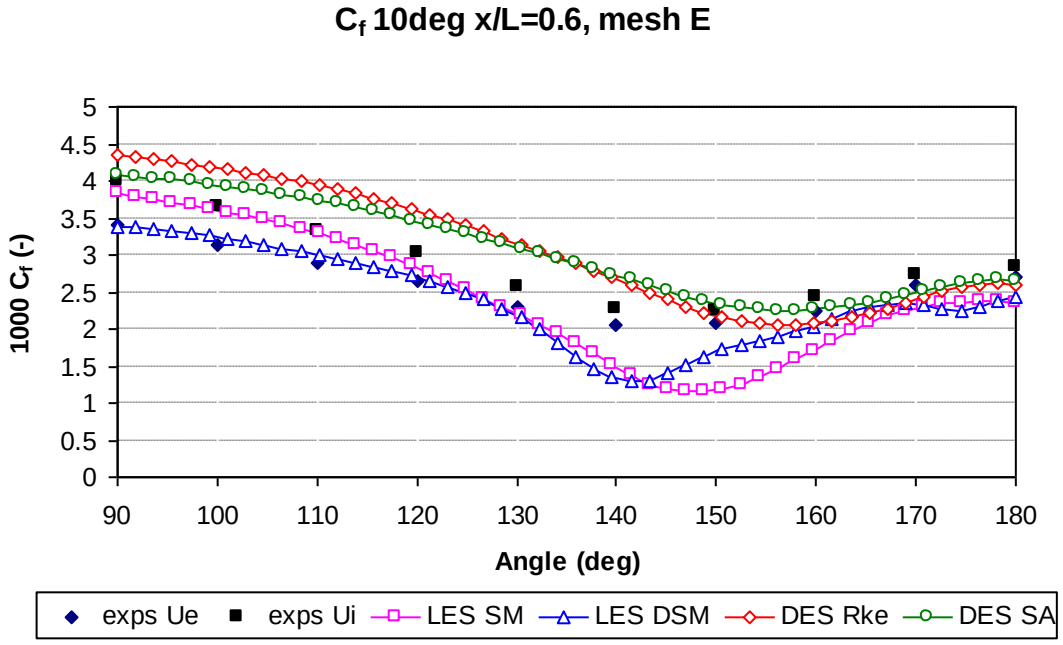

Figure C.: Mean azimuthal (or circumferential) skin-friction coefficient α=10 deg, x/L=0.6

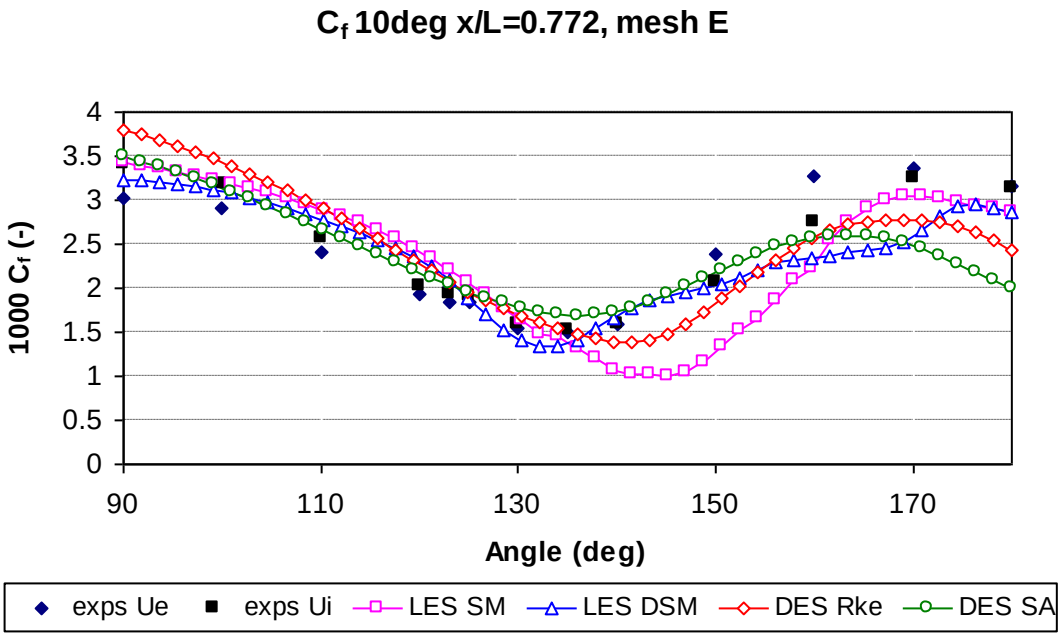

Figure C.: Mean azimuthal (or circumferential) skin-friction coefficient α=10 deg, x/L=0.772

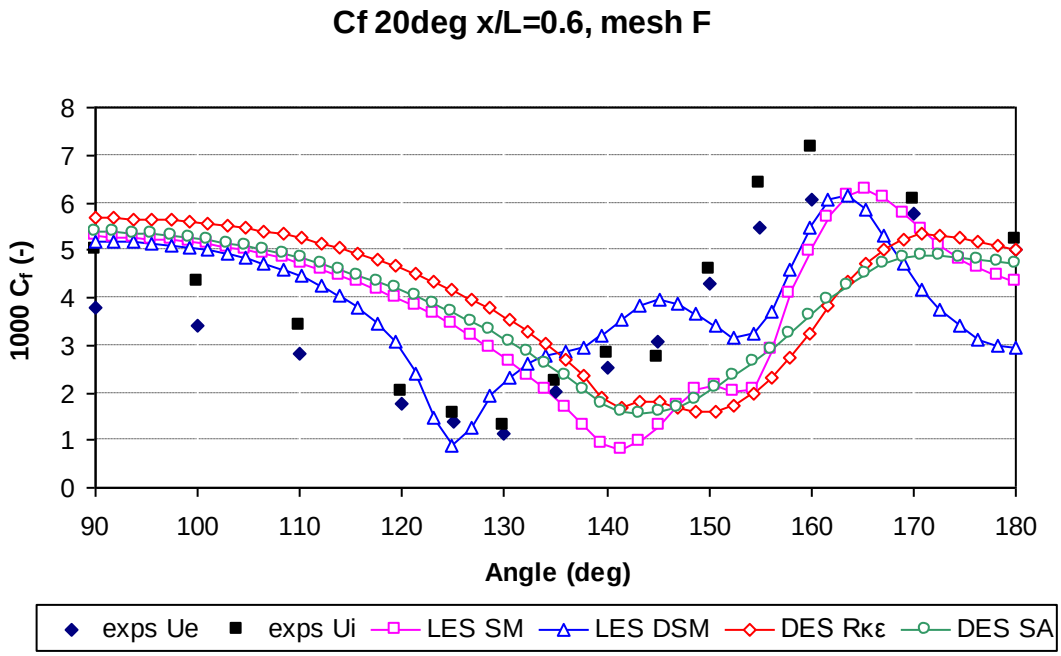

Figure C.: Mean azimuthal (or circumferential) skin-friction coefficient α=20 deg, x/L=0.6

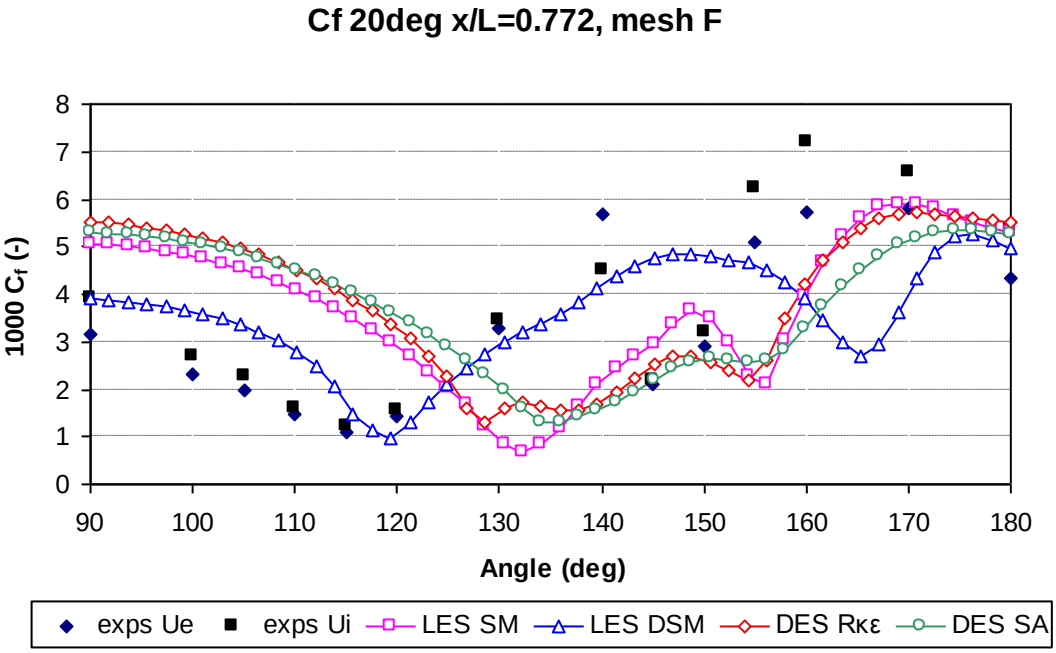

Figure C.: Mean azimuthal (or circumferential) skin-friction coefficient α=20 deg, x/L=0.772

Mean Velocity Profiles

For clarity in the legend of each graph, U/U_{inf} will be referred to as U*, V/U_{inf} as V* and W/U_{inf} as W*. Each letter corresponds to a mesh (A to F), followed by the LES or DES sub-grid model tested. Results are compared against steady-flow measurements from VTI laboratory. Mean velocity profiles are shown for the angles of attack of 10° and 20°, for the position x/L of 0.6 and 0.772 and for 5 different circumferential angles (when data is available).

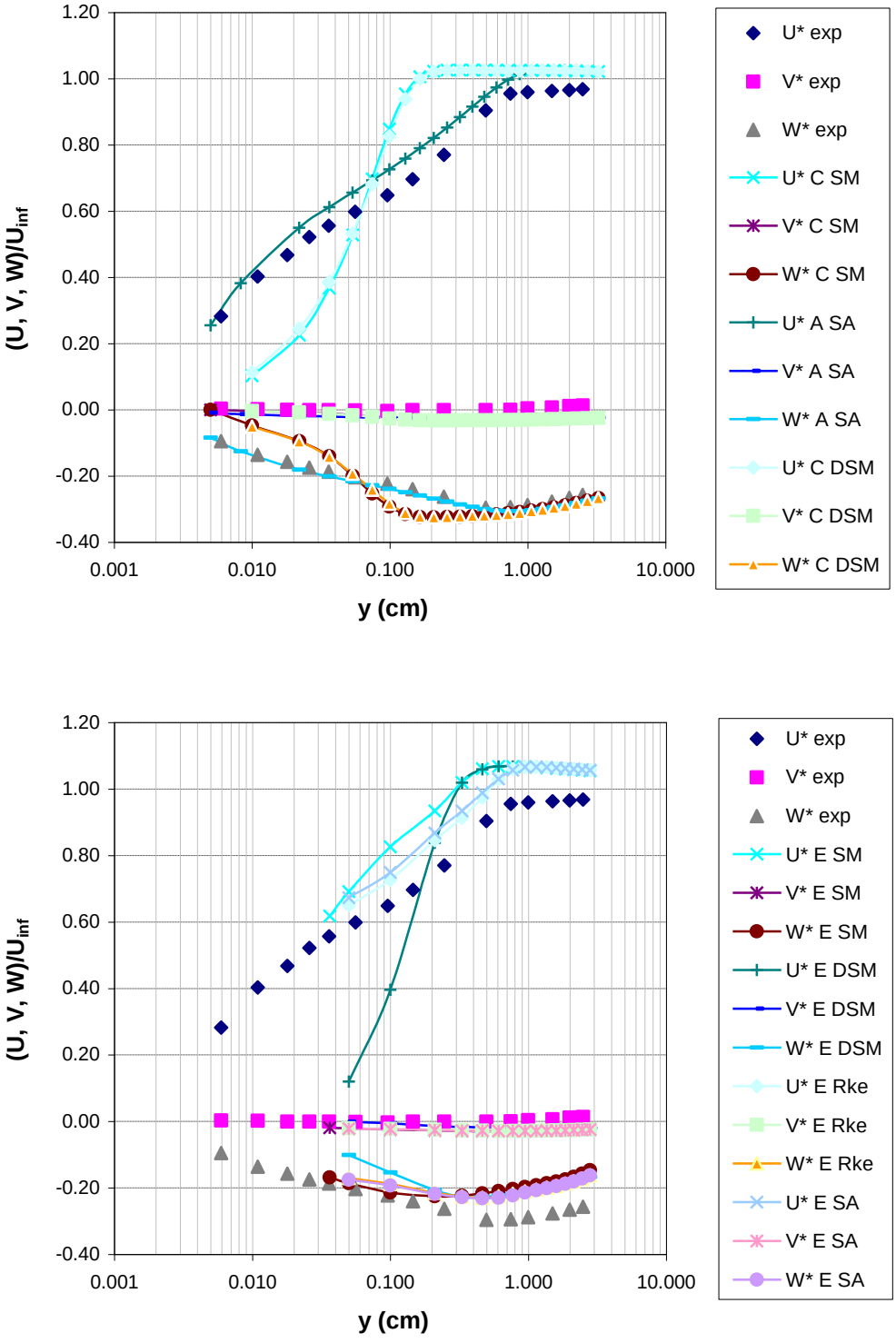

Figure C.: Mean velocity profiles, α=10 deg, x/L=0.6, circumferential 90 deg

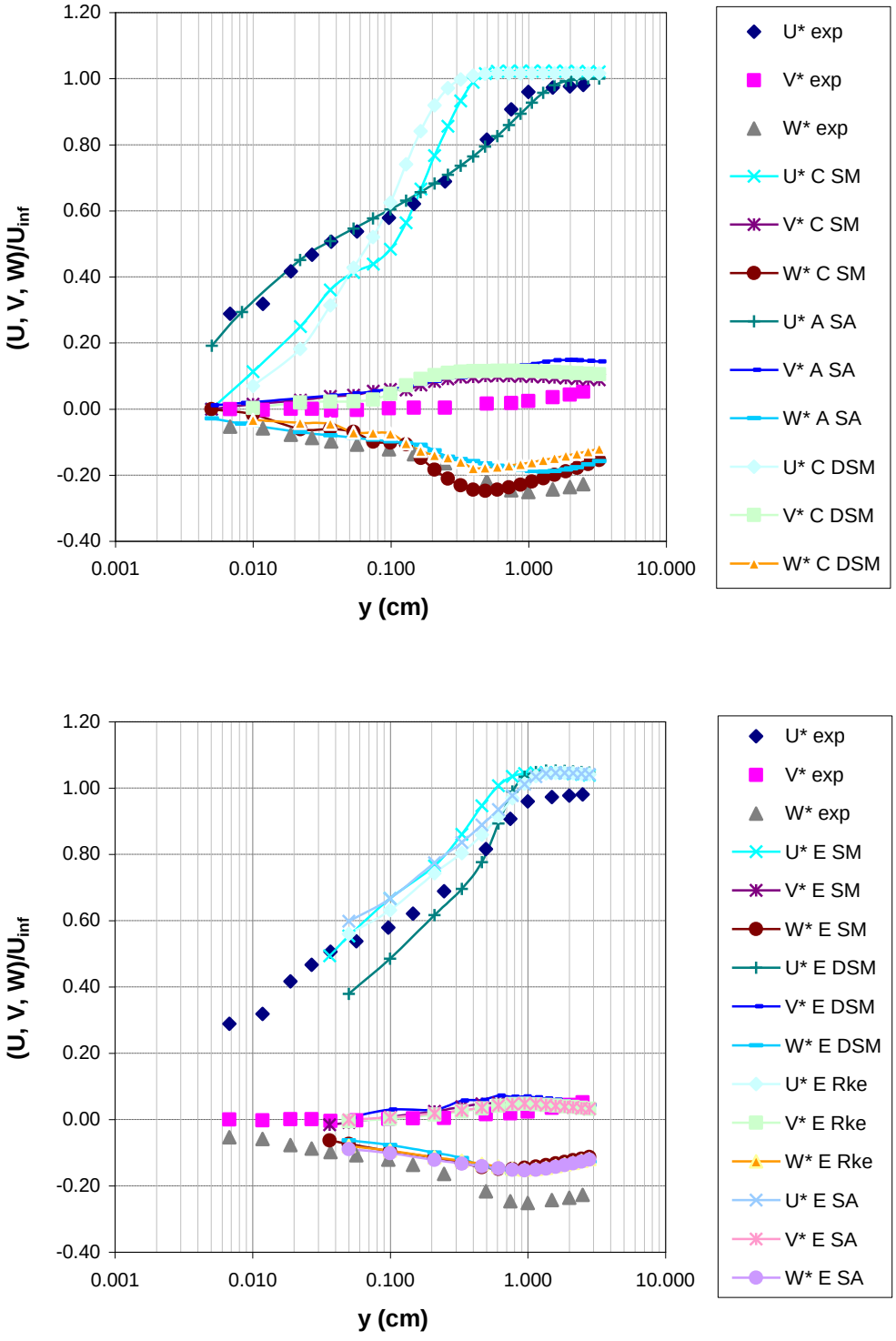

Figure C.: Mean velocity profiles, α=10 deg, x/L=0.6, circumferential 120 deg

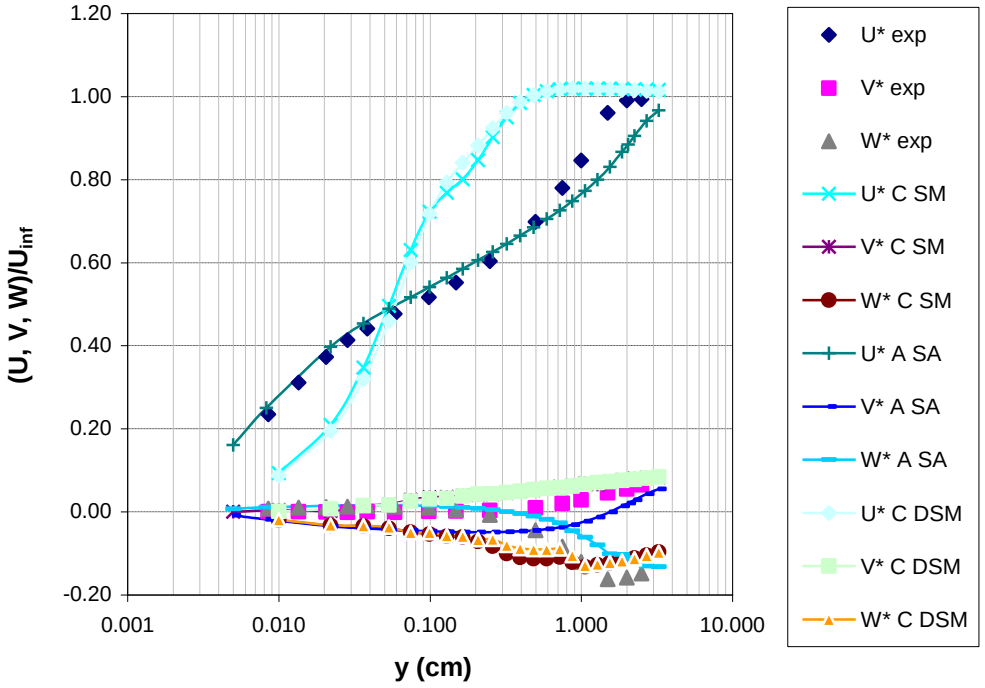

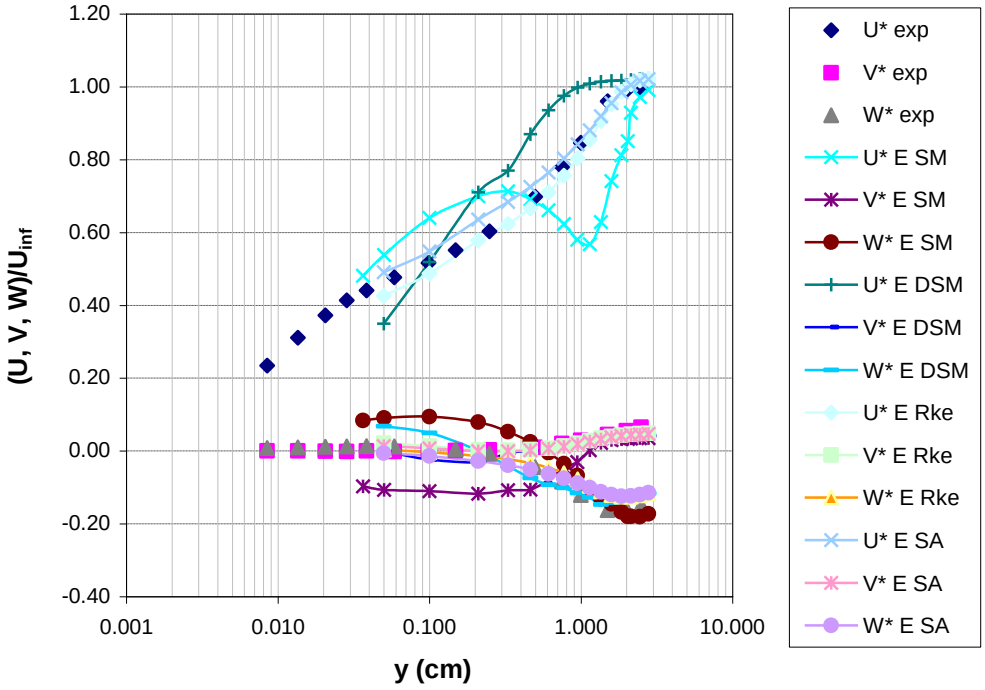

Figure C.: Mean velocity profiles, α=10 deg, x/L=0.6, circumferential 150 deg

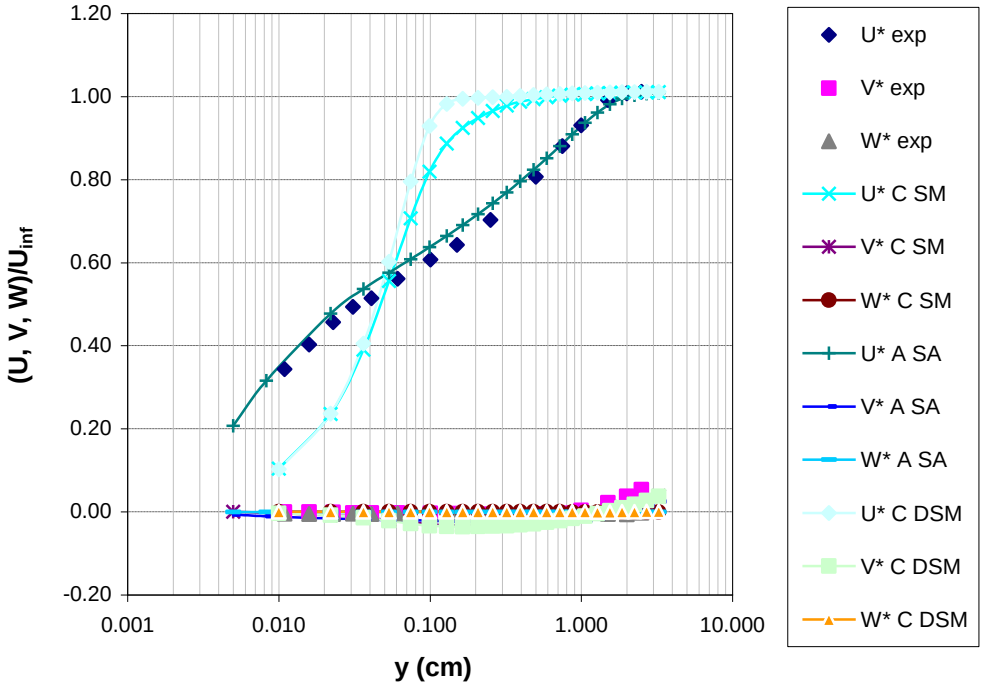

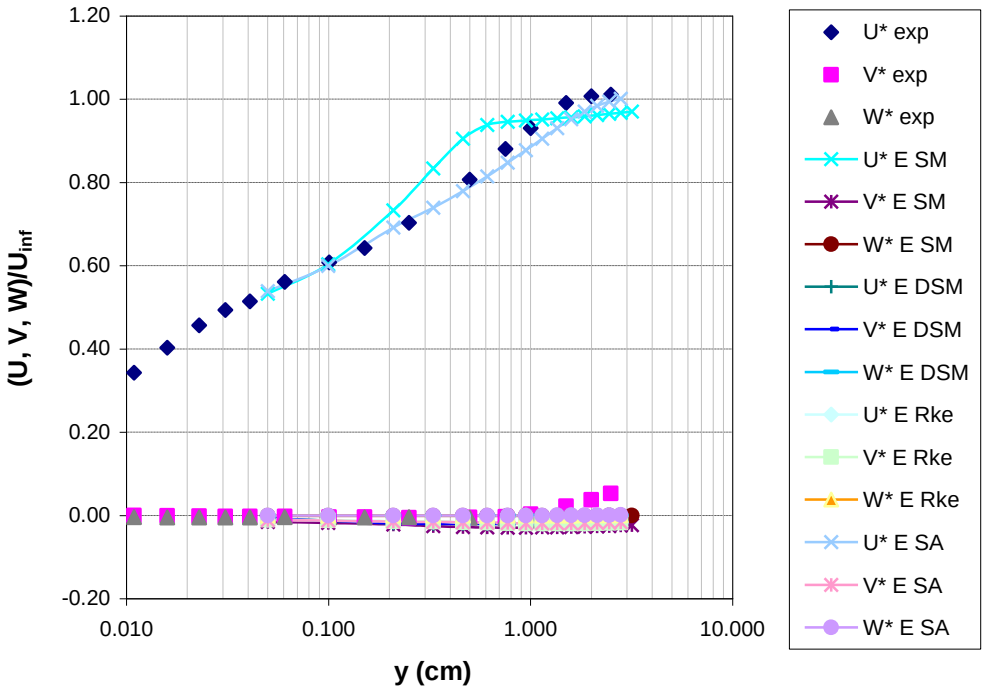

Figure C.: Mean velocity profiles, α=10 deg, x/L=0.6, circumferential 180 deg

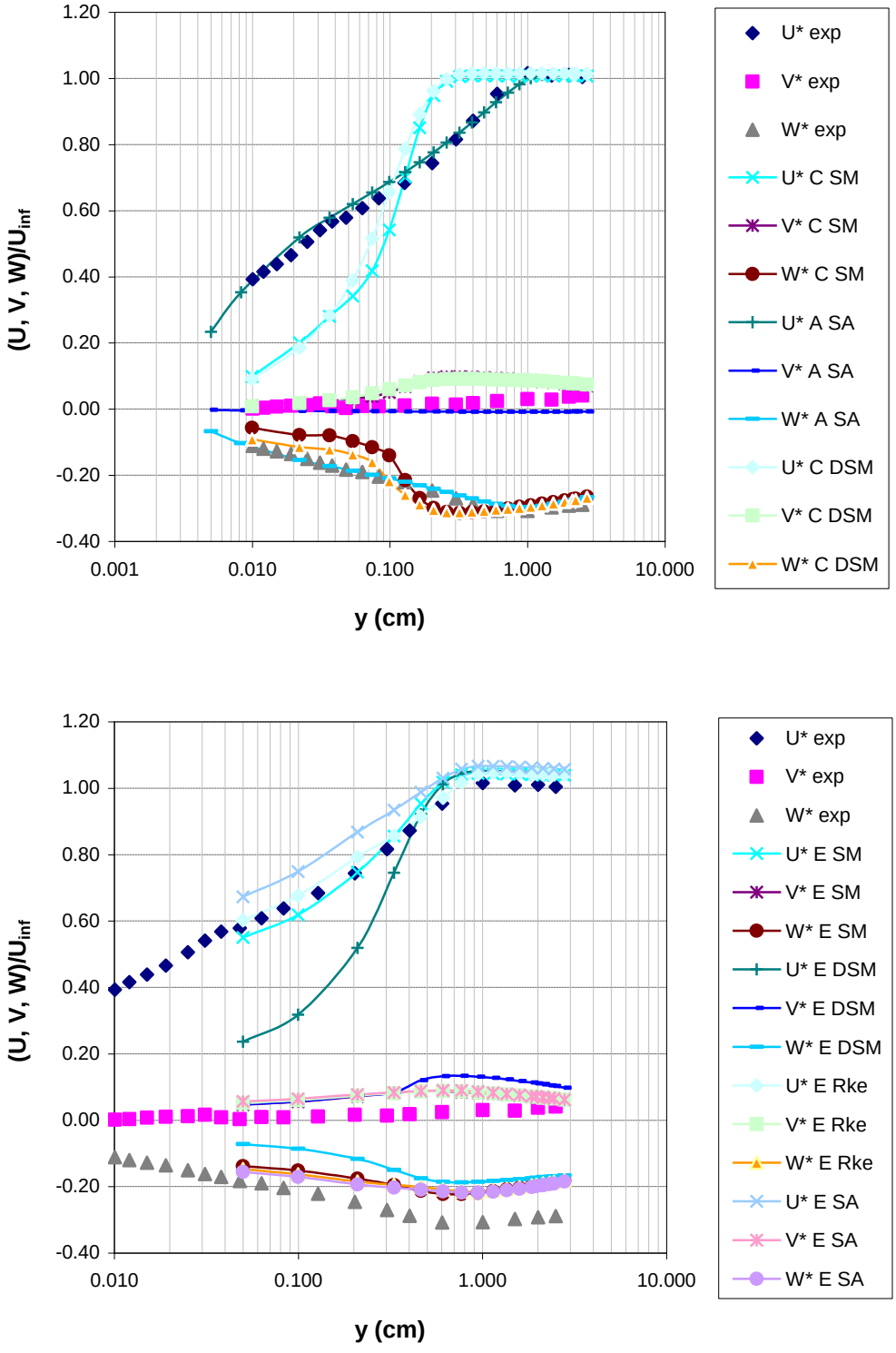

Figure C.: Mean velocity profiles, α=10 deg, x/L=0.772, circumferential 90 deg

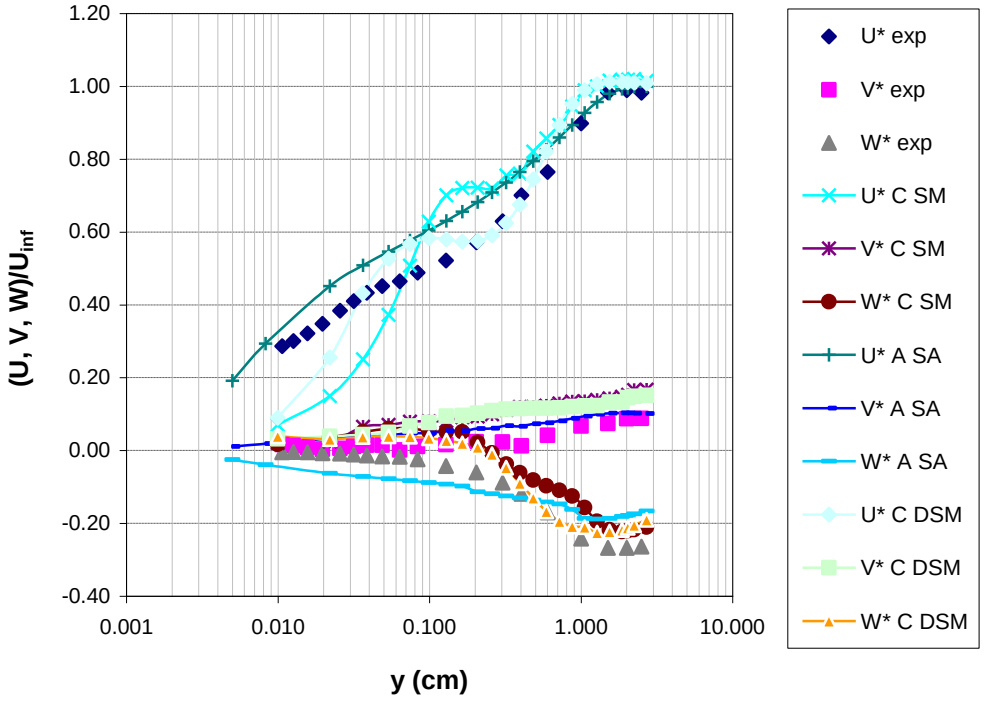

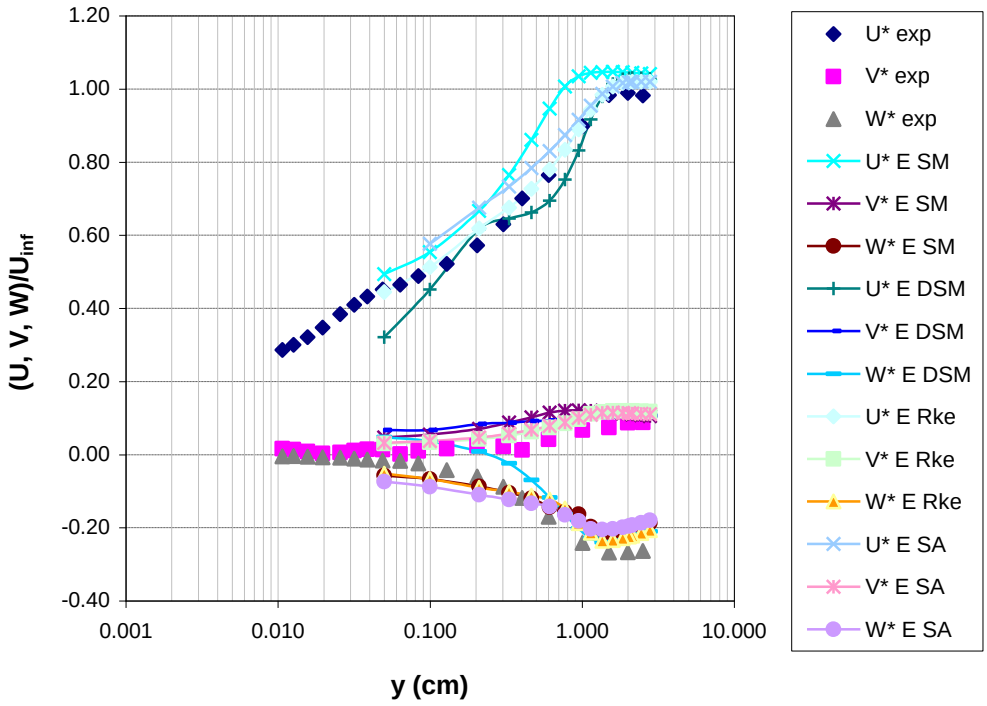

Figure C.: Mean velocity profiles, α=10 deg, x/L=0.772, circumferential 120 deg

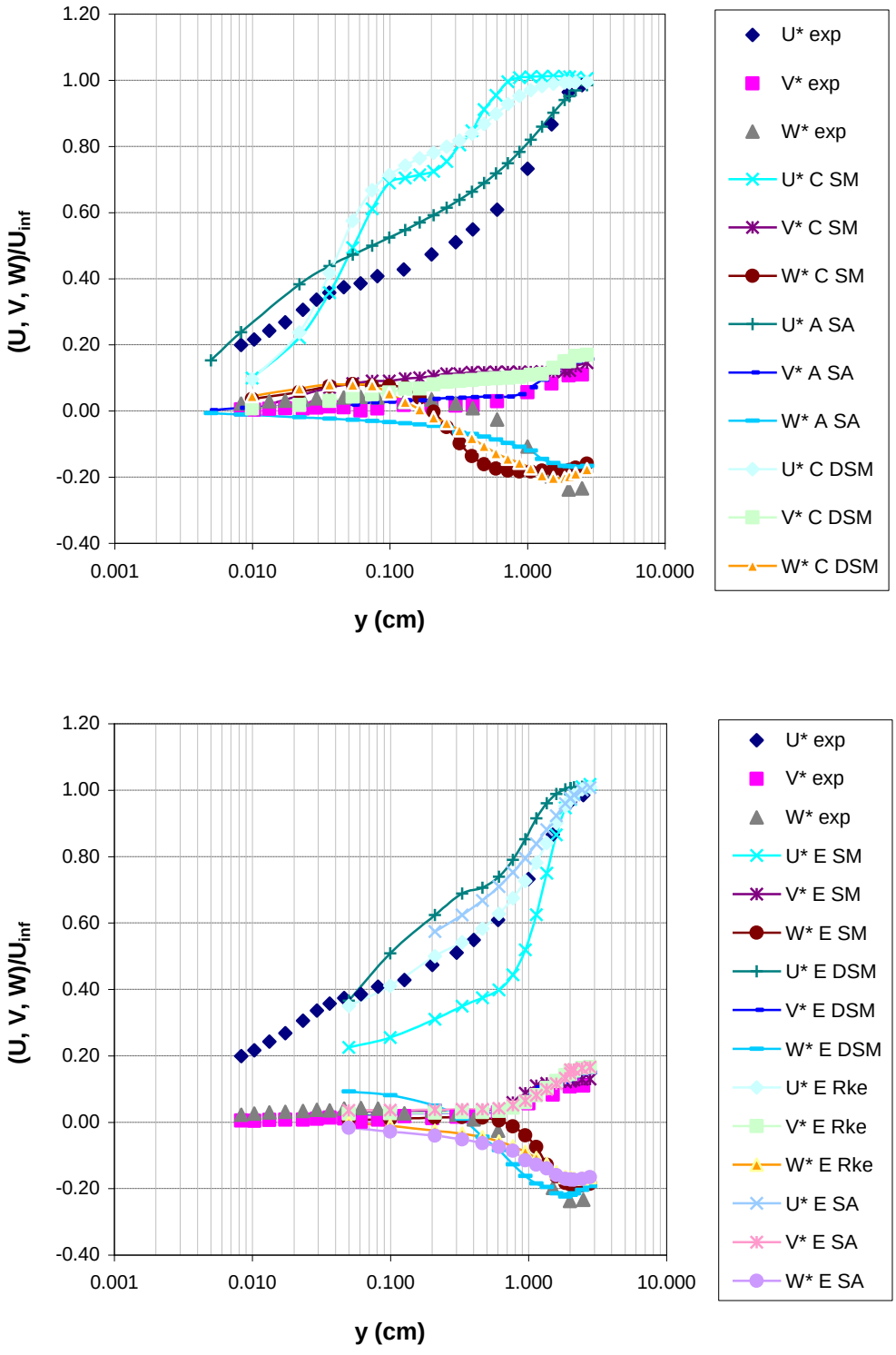

Figure C.: Mean velocity profiles, α=10 deg, x/L=0.772, circumferential 135 deg

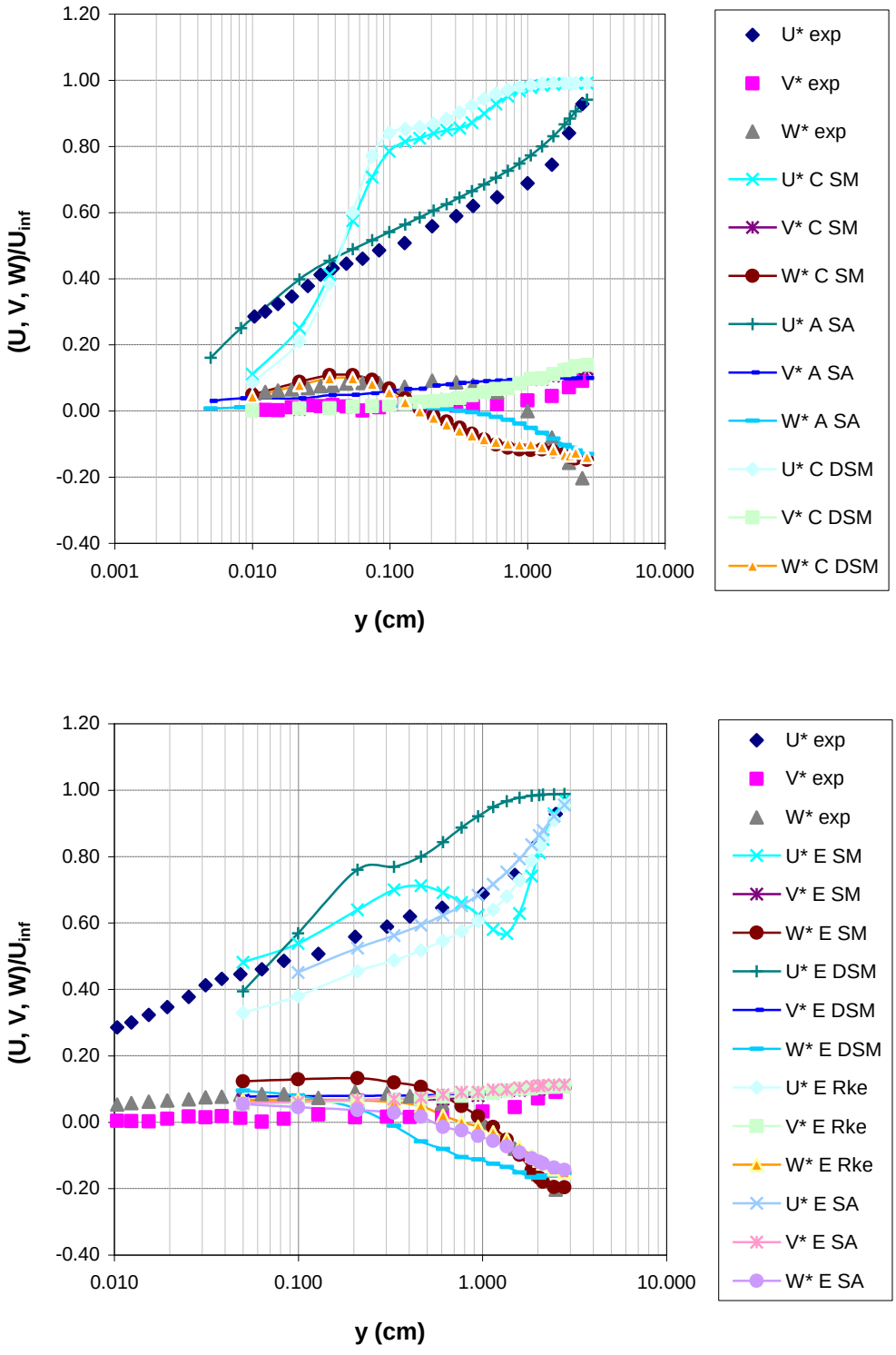

Figure C.: Mean velocity profiles, α=10 deg, x/L=0.772, circumferential 150 deg

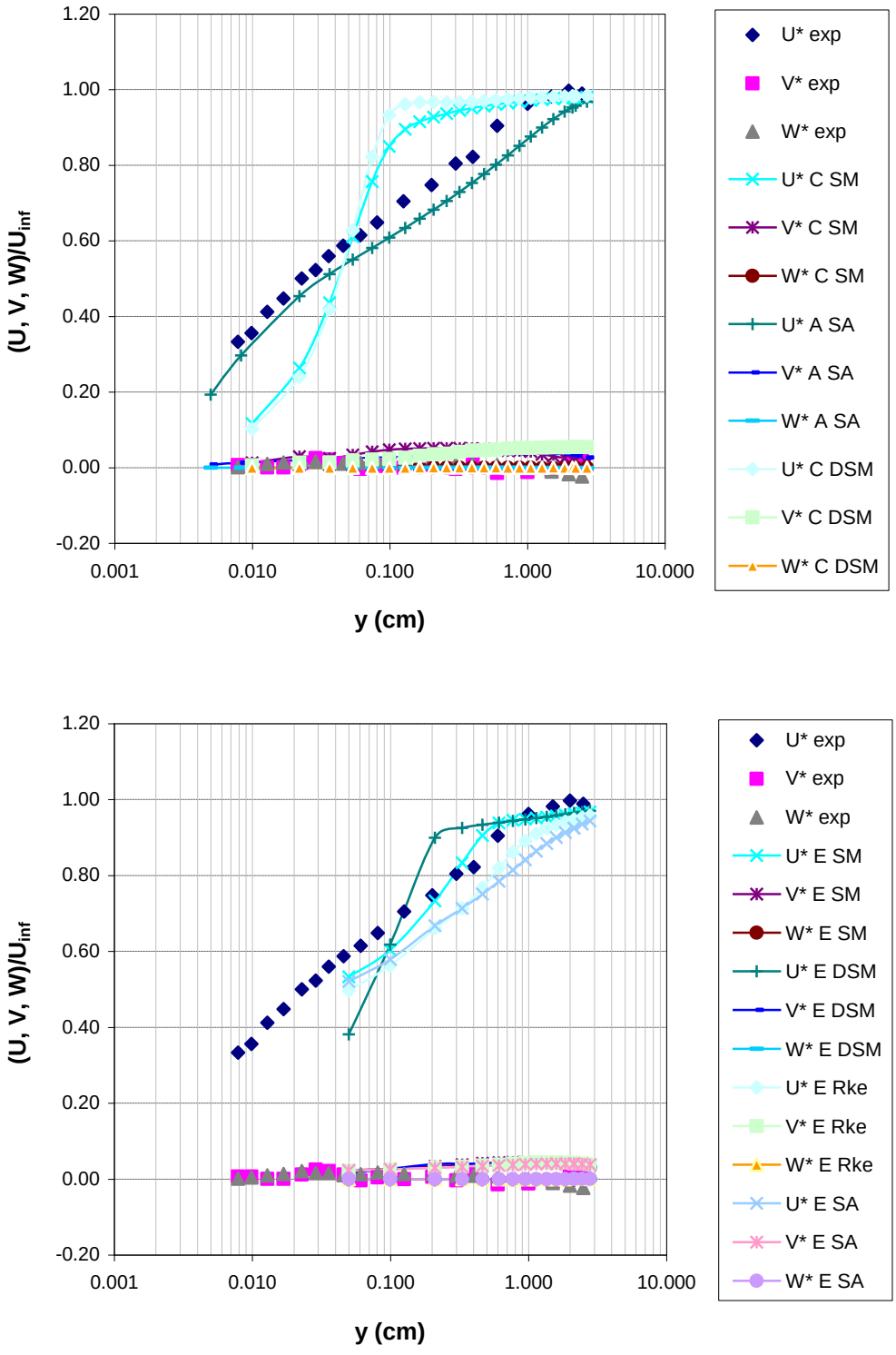

Figure C.: Mean velocity profiles, α=10 deg, x/L=0.772, circumferential 180 deg

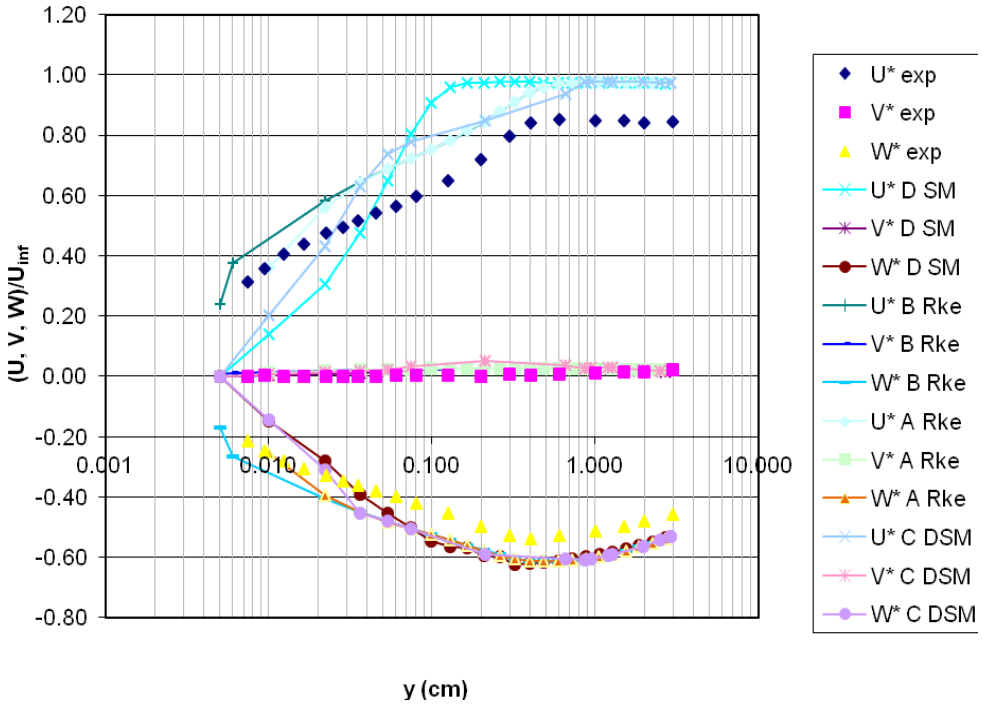

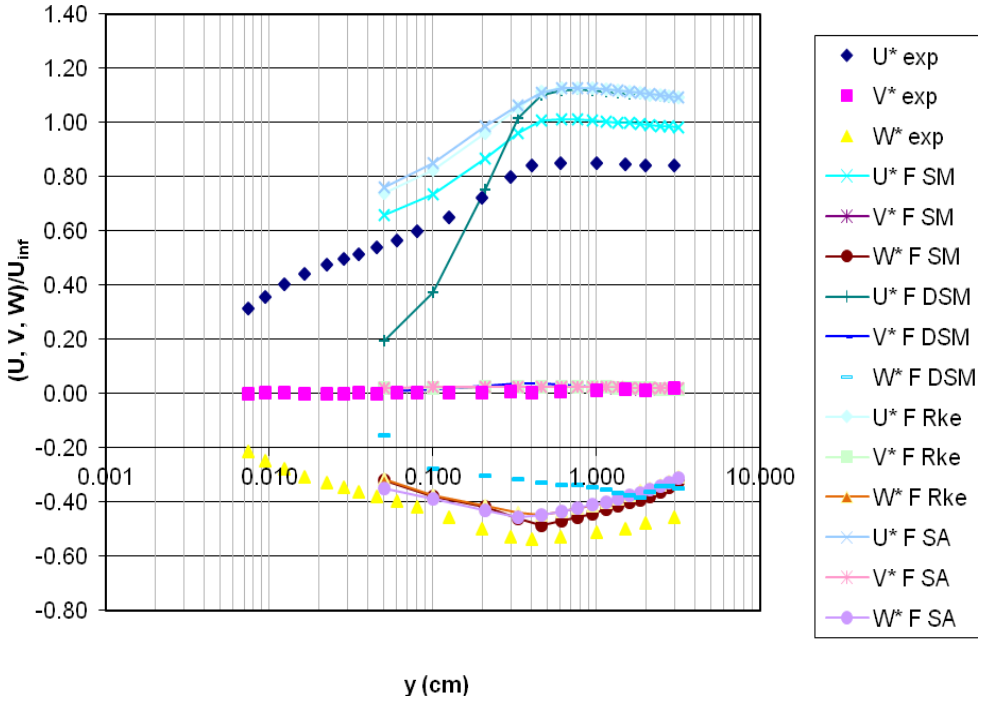

Figure C.: Mean velocity profiles, α=20 deg, x/L=0.6, circumferential 90 deg

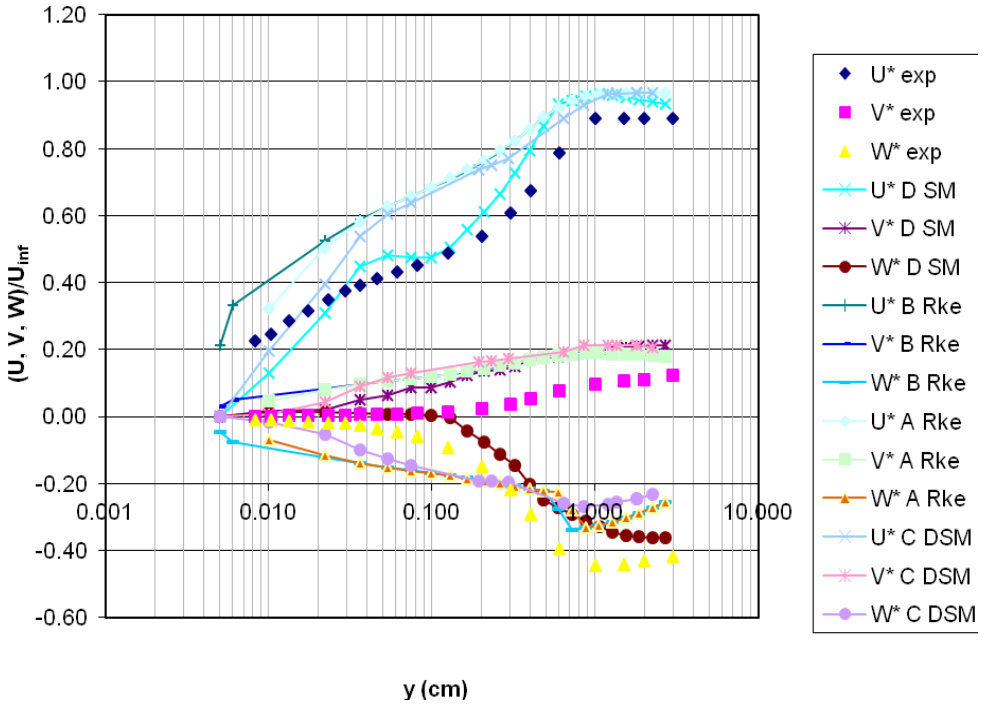

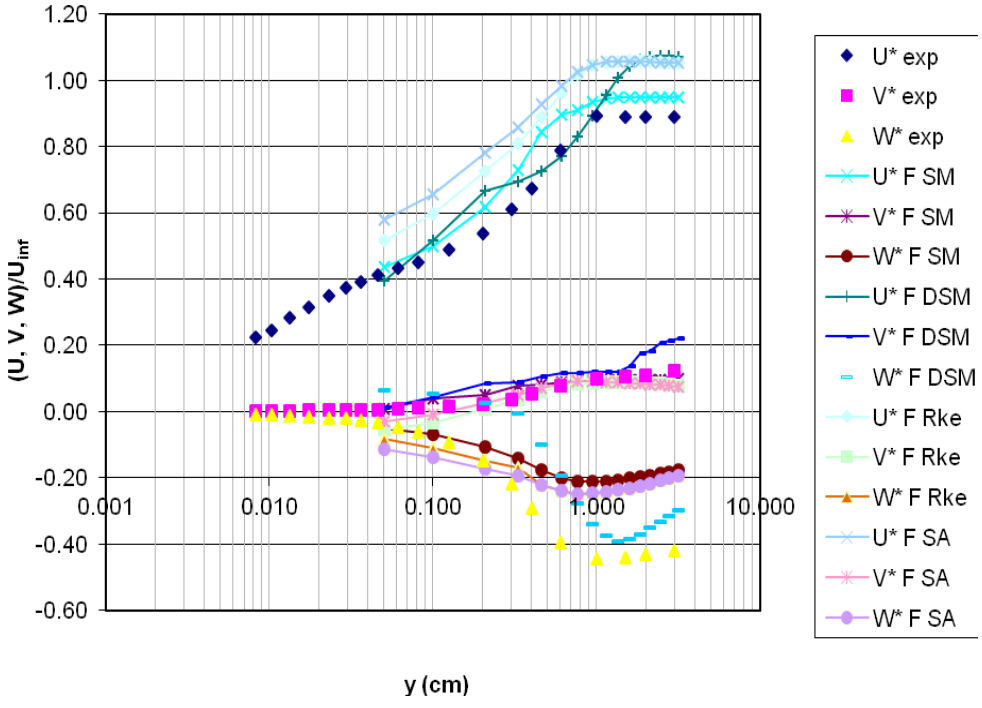

Figure C.: Mean velocity profiles, α=20 deg, x/L=0.6, circumferential 120 deg

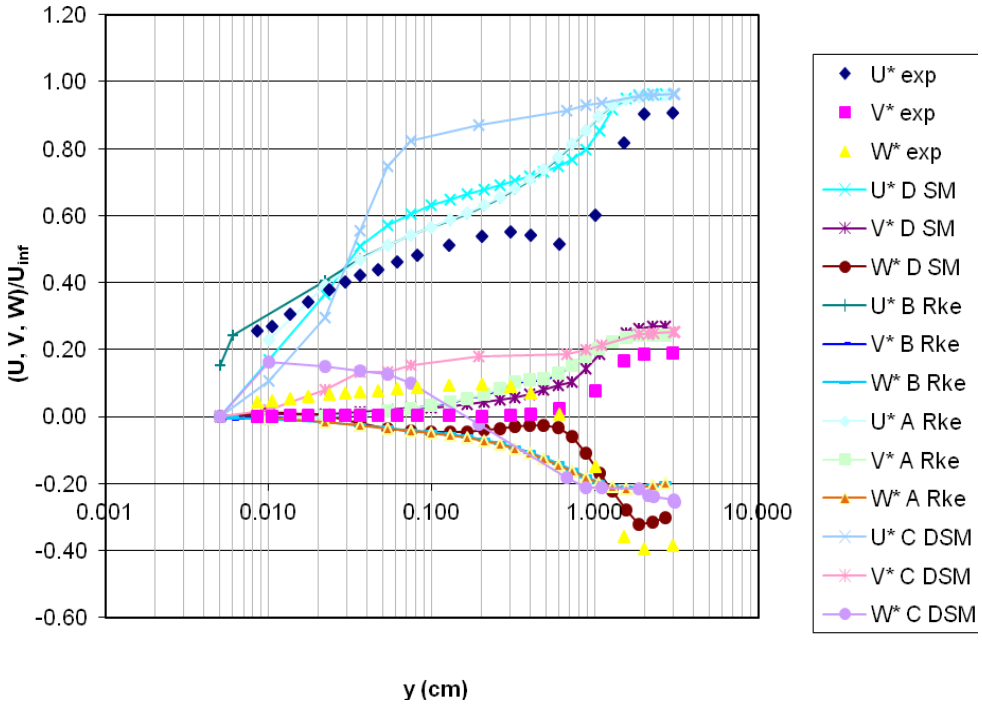

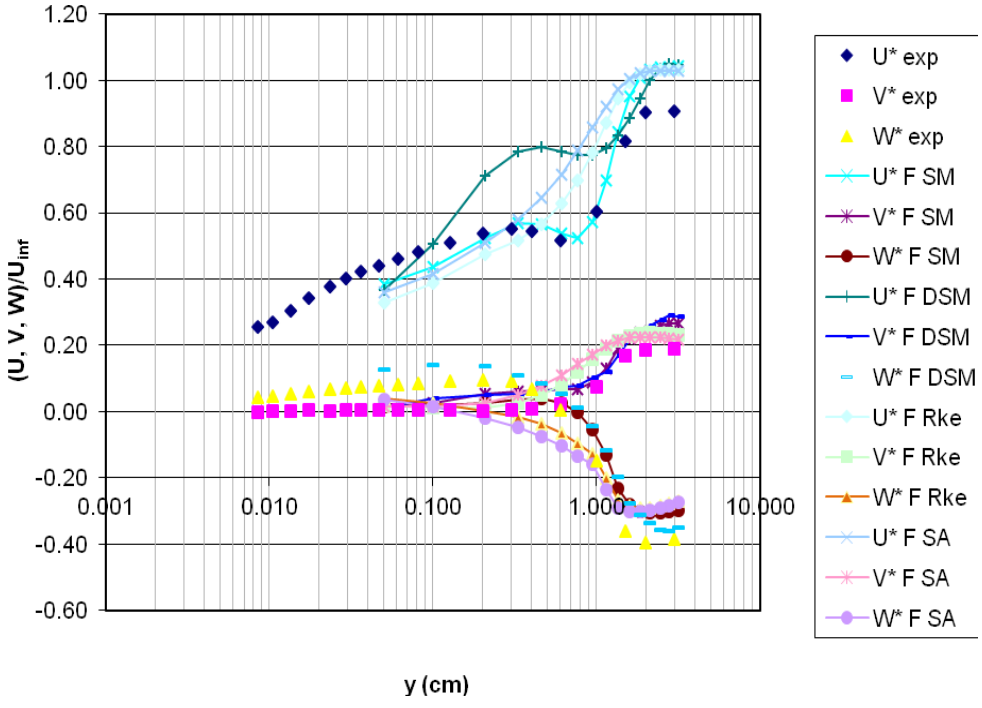

Figure C.: Mean velocity profiles, α=20 deg, x/L=0.6, circumferential 135 deg

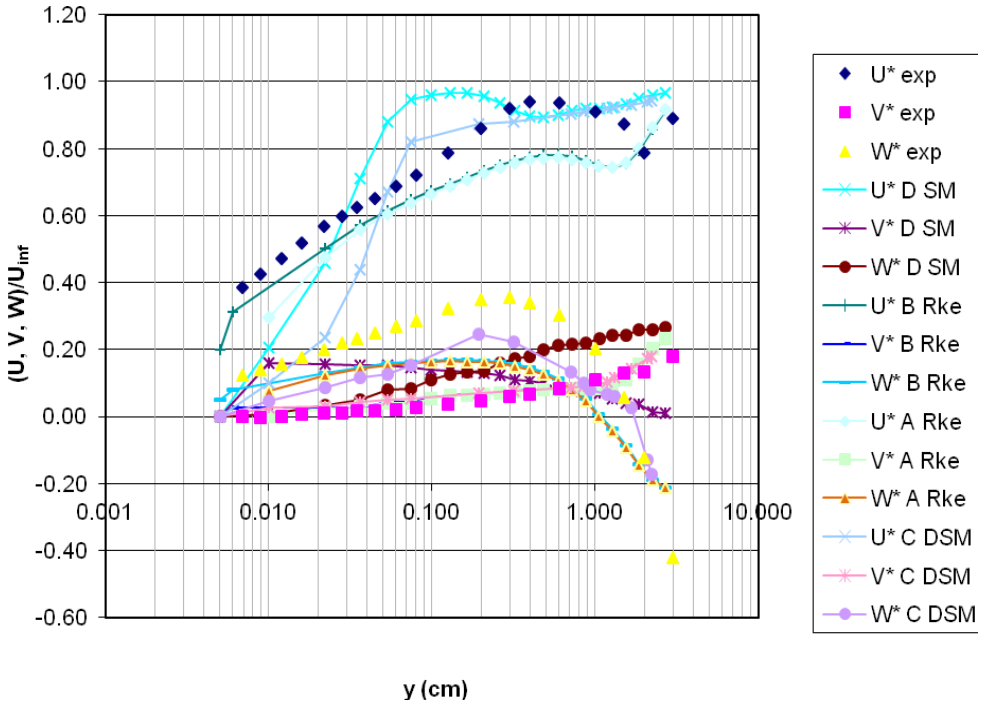

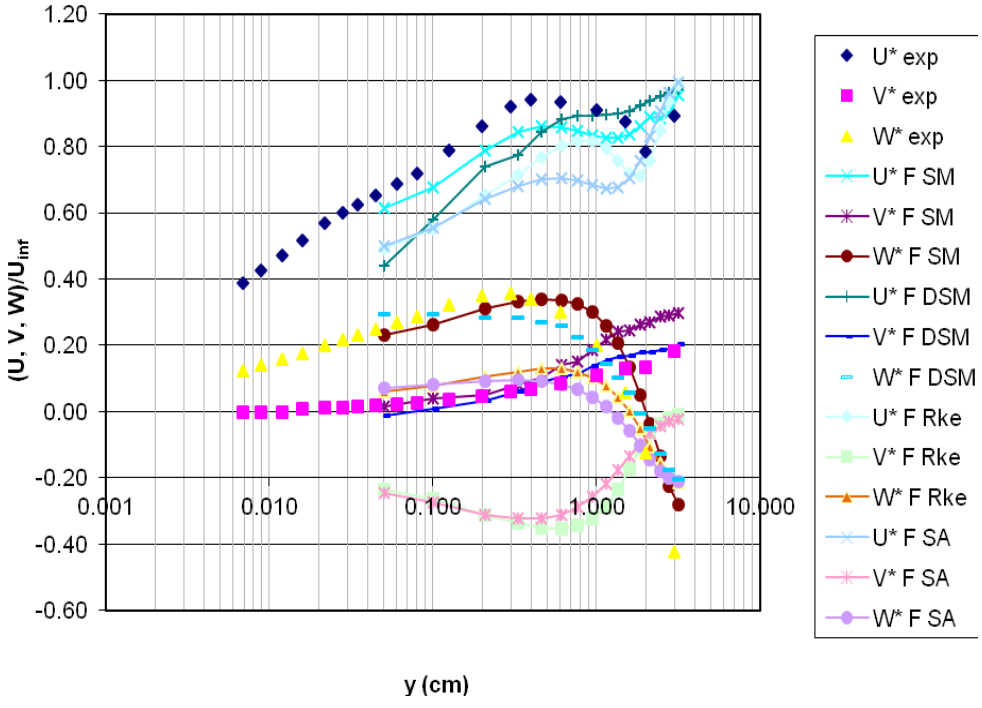

Figure C.: Mean velocity profiles, α=20 deg, x/L=0.6, circumferential 150 deg

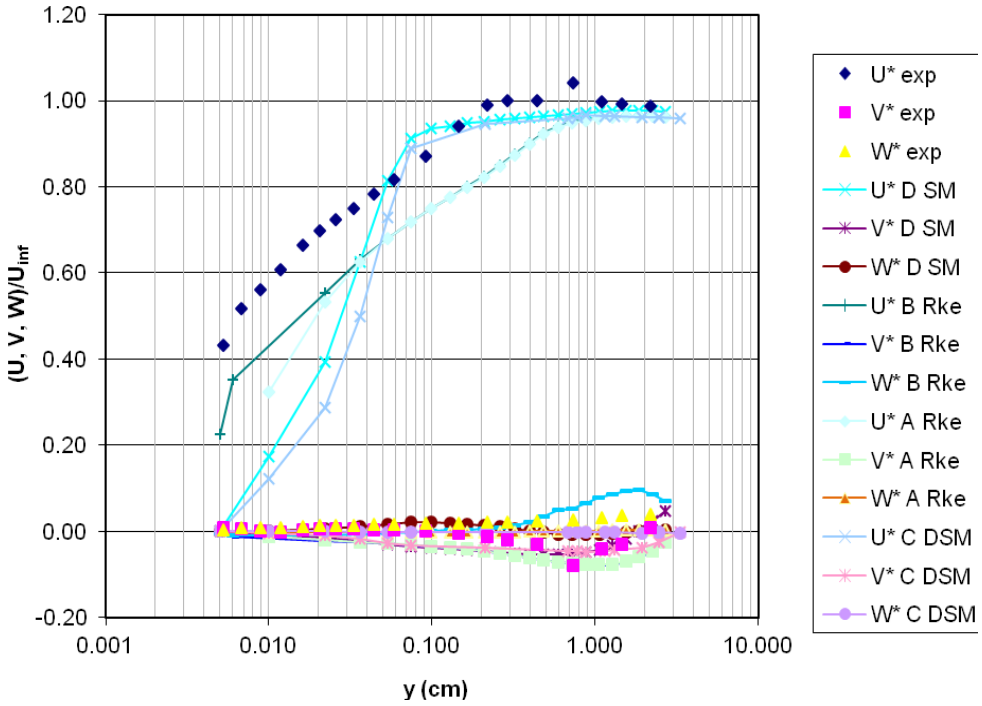

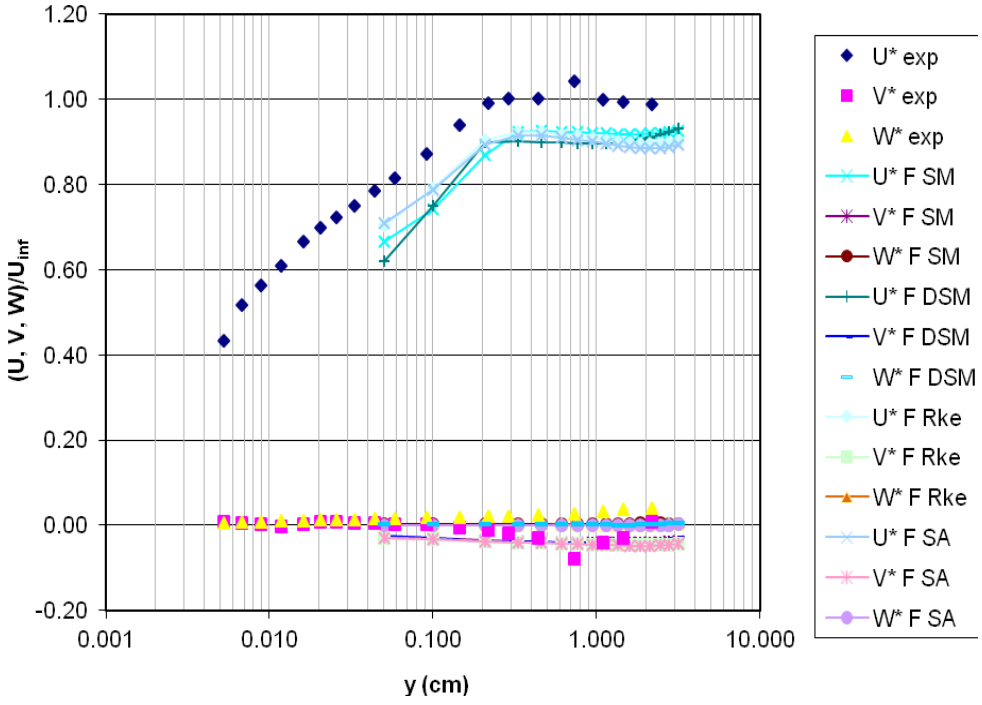

Figure C.: Mean velocity profiles, α=20 deg, x/L=0.6, circumferential 180 deg

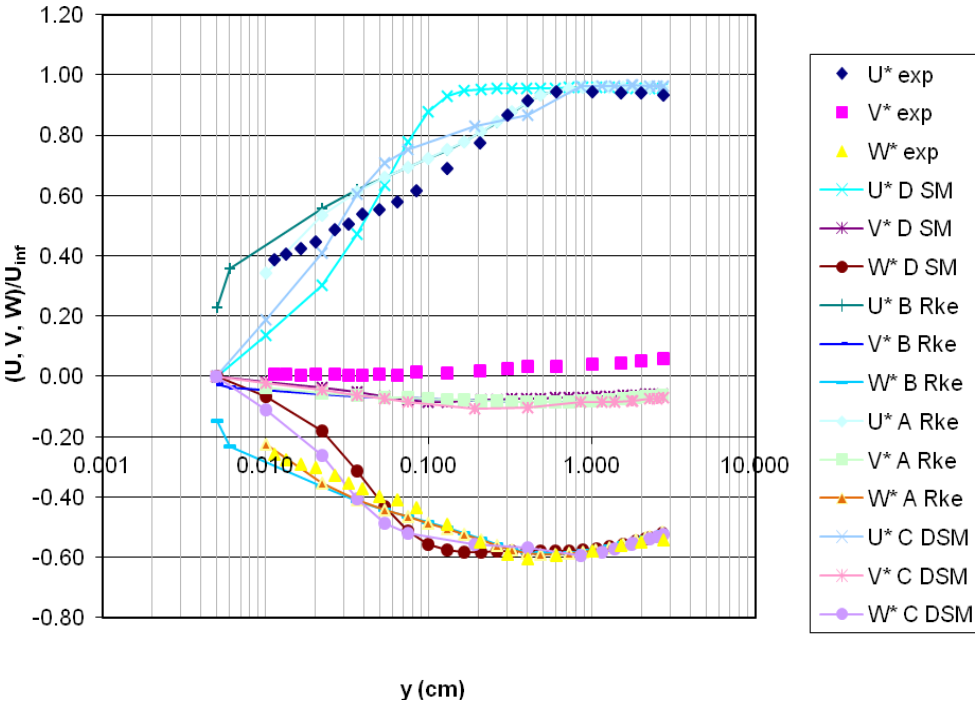

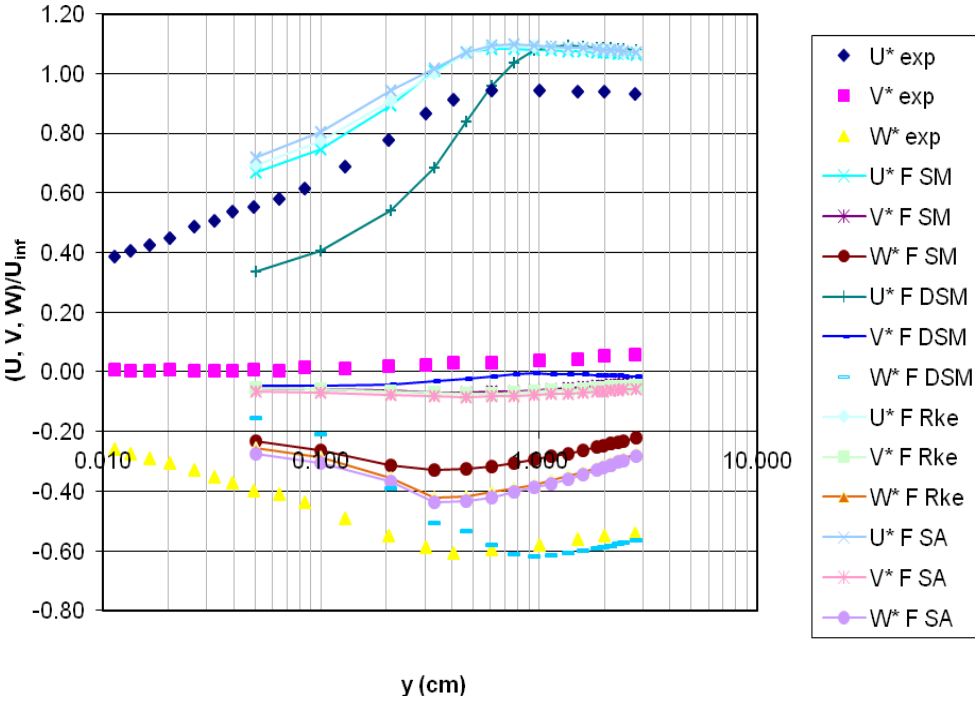

Figure C.: Mean velocity profiles, α=20 deg, x/L=0.772, circumferential 90 deg

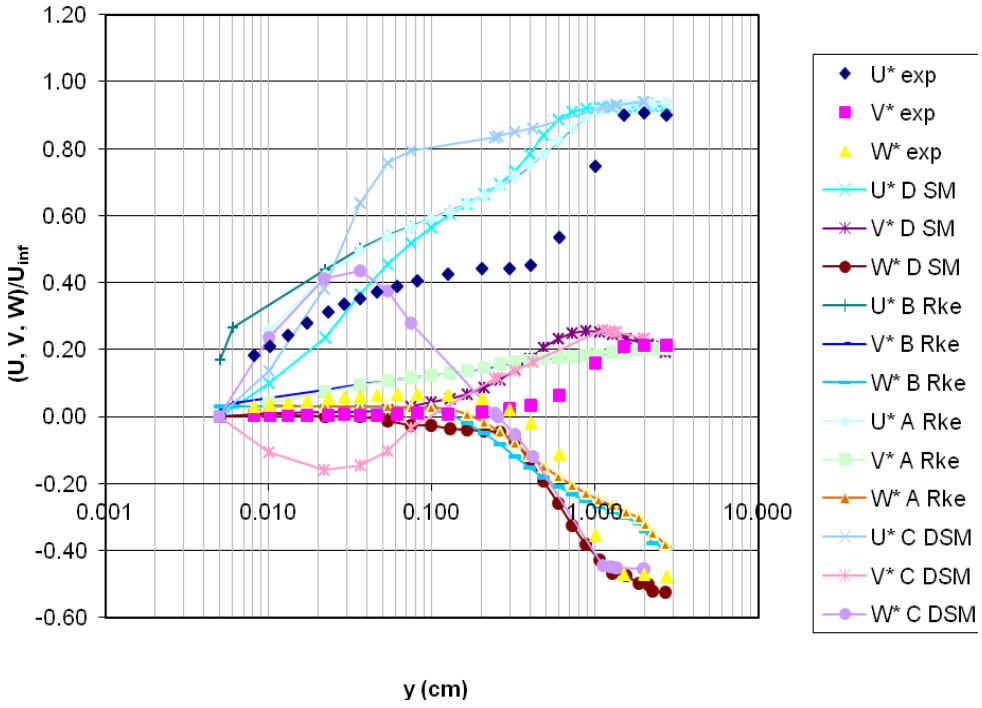

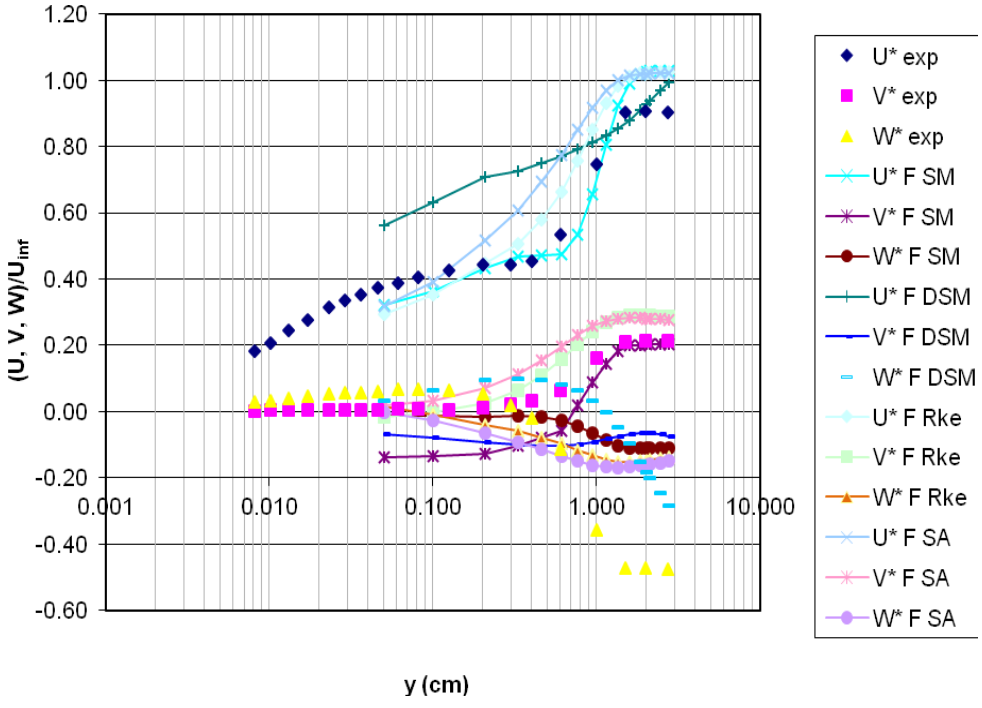

Figure C.: Mean velocity profiles, α=20 deg, x/L=0.772, circumferential 120 deg

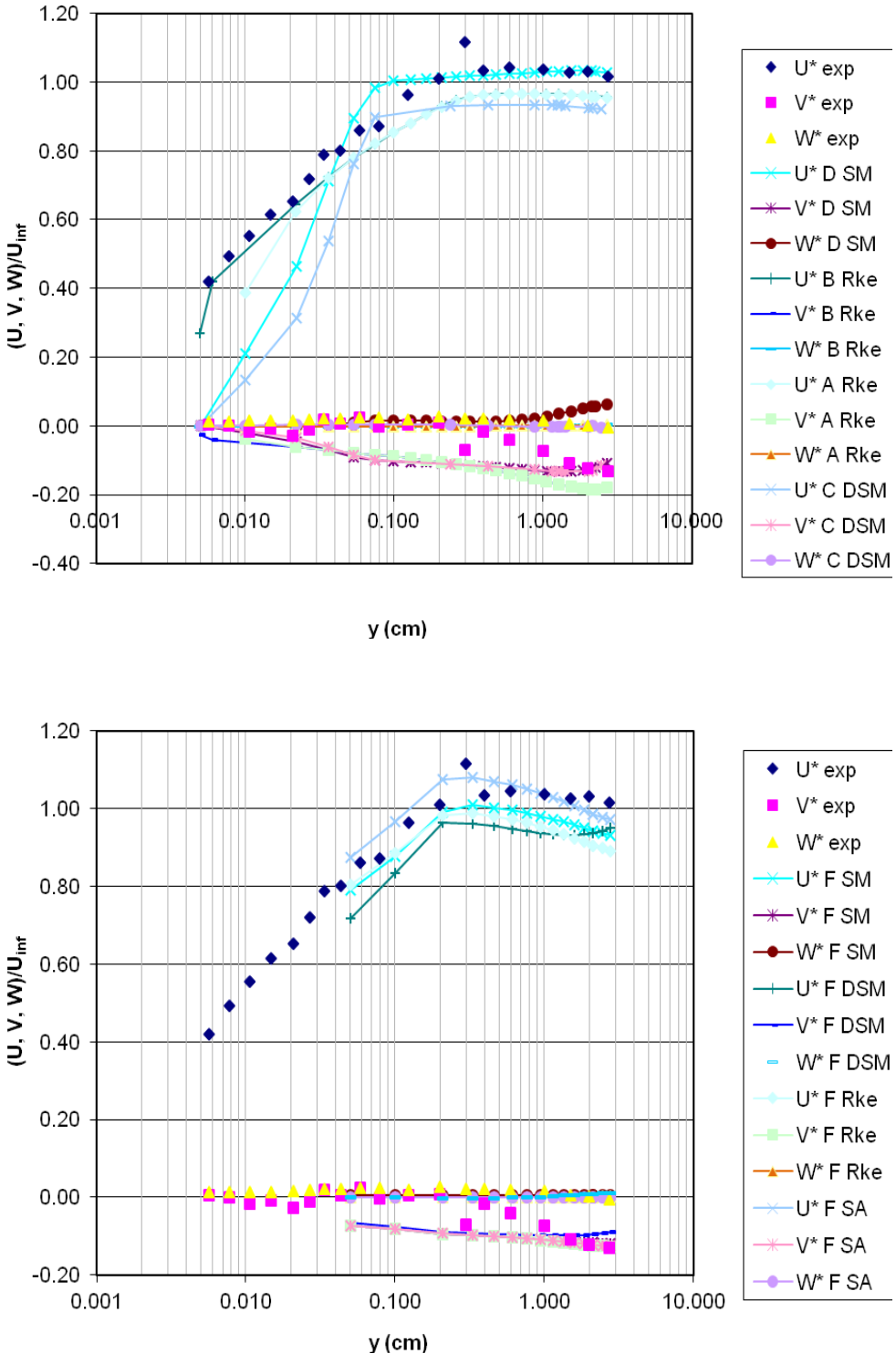

Figure C.: Mean velocity profiles, α=20 deg, x/L=0.772, circumferential 180 deg